Electrokinetic Effects in Power Transformers

TR-113441

Final Report, August 1999

EPRI Project Manager
S. Lindgren

EPRI • 3412 Hillview Avenue, Palo Alto, California 94304 • PO Box 10412, Palo Alto, California 94303 USA
800.313.3774 • 650.855.2121 • askepri@epri.com • www.epri.com

DISCLAIMER OF WARRANTIES AND LIMITATION OF LIABILITIES

ORGANIZATION(S) THAT PREPARED THIS PACKAGE

Department of Electric Power Engineering
Rensselaer Polytechnic Institute

ORDERING INFORMATION

Requests for copies of this package should be directed to the EPRI Distribution Center, 207 Coggins Drive, P.O. Box 23205, Pleasant Hill, CA 94523, (925) 934-4212.

CITATIONS

This report was prepared by

Department of Electric Power Engineering
Rensselaer Polytechinic Institute
110 8th St.
Troy, NY 12180-3590

Principal Investigators
J. Nelson
M. Brubaker

This report describes research sponsored by EPRI.

The report is a corporate document that should be cited in the literature in the following manner:

Electrokinetic Effects in Power Transformers; EPRI, Palo Alto, CA: 1999. TR-113441.

REPORT SUMMARY

Electrokinetic effects such as static electrification can cause catastrophic failures in large forced-oil-cooled power transformers. The development of a network-based theoretical model provides a critical perspective not apparent from previous small-scale laboratory experiments.

Background

In January 1979, a prototype high-voltage dc valve (RP213) developed pinhole leaks in cooling-loop insulators containing flowing refrigerant 113. A subsequent study (EPRI reports EL-4501 and EL-6138) investigated static electrification as a possible explanation for these leaks and developed a number of models. Several 1979 reports from Japan also indicated that abnormally high-velocity oil flow could cause static electrification problems in power transformers. Although U.S. transformers operate with lower flow rates, over a dozen U.S. failures have been associated with the problem since 1982. EPRI has sponsored ongoing research to develop possible solutions, and sponsored workshops in 1986, 1989, 1992, and 1994 to assess results from related EPRI projects (EPRI reports EL-6081, EL-ER-6880, EL-6918, TR101216, TR-102112, TR-104973, TR-105019, TR-111386 and TR-113381).

Objectives

- To combine experimental effects and semi-empirical electrification models to mimic large transformer geometries using a network-based approach.
- To provide a relationship between static electrification in laboratory models and actual power transformers.

Approach

The project team performed experiments to investigate the impact of moisture dynamics upon charge separation. They used additional experiments to examine the impacts of charge separation, deposited charge, and charge accumulation on dielectric integrity. They integrated these results with earlier experimental results to provide necessary empirical inputs for model building. The team developed and empirically calibrated a boundary layer approach for charge separation in a simple transformer duct. They incorporated the single duct model into a network model to approximate the core-form laboratory structure. Having established theoretical and empirical linkage, they investigated a complete transformer winding.

Results

The experiments did not show a dramatic impact of moisture dynamics upon static electrification processes, but very non-uniform moisture distribution was consistently observed. A relatively thin surface layer of cellulose appeared to govern moisture equilibrium with the oil and to be much wetter than the bulk cellulose. Because of laboratory vacuum processing limitations, “wet zones” on the pressboard surfaces were more probable than the “dry zones” that are believed to aggravate static electrification in actual transformers. The experiments confirmed the importance of scale in simulating charge accumulation. Although realistic, the shell-form transformer model structure was not large enough to demonstrate damaging effects of static electrification. The network-based streaming electrification model developed in this study was demonstrated to a first order. Results appear very reasonable and provide a critical perspective that cannot be obtained from smaller structures.

EPRI Perspective

Static electrification continues to be a significant worldwide problem jeopardizing the reliability of large forced-oil-cooled shell-form and core-form transformers. Results from this work support earlier EPRI perspectives. Static discharges in U.S. shell-form transformers can occur at entrances to unintentional oil-flow paths through the major insulation and/or where dc charges exit and accumulate near the higher voltage bushing. Worst-case conditions occur during temperature transients. During start-up, heating of the oil increases charge generation while cold dry pressboard concentrates dc stress. A similar effect probably explains the extreme physical destruction of pressboard components found at the flow-entrance region in an "unfailed" large core-form transformer reported at the 1994 workshop. This report culminates a coordinated effort toward controlling electrification-related transformer problems. What has been learned should lead to overall improvements in transformer design and reliability.

TR-113441

Keywords

Static electrification
Transformer insulation
Transformer faults
Transformer reliability
Substations

ABSTRACT

Charge separation resulting from the convection of insulating oil has been recognized as a threat to large power transformers which require forced cooling. While this phenomenon has been studied extensively, much of the previous work has addressed relatively small-scale laboratory models and simple geometries. Experiments have been performed using realistic geometries to examine the dependence of streaming electrification upon moisture dynamics and recirculating charge. Additional studies have examined the impact of static charging upon the dielectric integrity of a transformer structure. These results are combined with theoretical work in order to bridge the gap between the laboratory and the actual power transformer. An empirically calibrated network-based approach is developed such that a basic duct element model can be used to assemble a realistic transformer geometry. Building upon the foundation laid by previous investigators, static charging behavior is modelled in an actual transformer winding to provide new information which is not apparent from small-scale results.

CONTENTS

LIST OF FIGURES

LIST OF TABLES

1

INTRODUCTION

1.1 Justification for Present Work

A power transformer is an exceedingly complex entity which cannot be viewed merely as an electrical device. The roles played by mechanical and chemical processes must also be considered when evaluating transformer design and operating procedures. Unexpected failure mechanisms may exist as a result of interaction between the electrical, mechanical and chemical domains. A prime example of such a mechanism is the phenomenon of static electrification in forced-oil-cooled power transformers.

Static electrification occurs when chemically produced ions are separated by the flow of insulating oil. As a result, excess charge may accumulate and lead to the development of large static potentials. When these potentials are superimposed upon normal operating voltages, the dielectric integrity of the transformer may be prejudiced. A number of recent transformer failures have been attributed to this phenomenon (1).

An exhaustive amount of research has been undertaken to address the issue of electrification in the transformer context (see Section 2). However, the problem has yet to be satisfactorily understood and eliminated. A clear gap exists between the numerous laboratory and analytical studies performed and the actual phenomenon which occurs in a transformer. The primary goal of the present work is to reduce this gap through experimental and theoretical contributions.

1.2 Objective and Approach

The objective of this work is to provide a relationship between streaming electrification in laboratory models and actual power transformers. Previous experimental results are integrated with new laboratory studies to provide the necessary empirical inputs. A basic theoretical model is then developed for a simple transformer duct. This model is extended to simulate a more complicated structure for additional empirical calibration. Having established theoretical and empirical linkage, a complete transformer winding is investigated. The results provide insight into the importance of scale and operating conditions with regard to streaming electrification.

Large-scale electrification studies using realistic transformer geometries have been recently performed by Lee and Nelson (2). These experiments were continued to provide additional data on a scale which is comparable to a real transformer. The influence of moisture dynamics upon streaming electrification in transformer structures was investigated over realistic thermal cycles. Also, experiments were performed to examine the effects of deposited charge upon the surface breakdown strength of cellulose insulation. In addition, partial discharge measurements have been made in a realistic transformer structure subject to static charging effects. Finally, cumulative charging tests were undertaken to determine the role of entering volume charge upon electrification in a transformer geometry.

In conjunction with the experimental efforts, semi-empirical electrification models were developed for simple transformer ducts. These models were then combined to mimic the larger transformer geometries investigated experimentally using a network-based approach. The network methodology was extended to incorporate these calibrated building blocks into a macroscopic electrification model. This large-scale model serves as the focal point for the work documented in this thesis and has been applied to an actual transformer winding. The results demonstrate the feasibility of the approach and provide useful data for the utility industry.

1.3 Review of Relevant Fundamental Electrification Theory

The separation of electrical charges resulting from one medium moving with respect to another is defined as static electrification. An example of this process is the Van der Graff generator which employs a moving belt to strip charges from a point source. For present purposes, the analogous situation of fluid flow past a solid surface will be considered.

The crucial ingredient for the electrification phenomenon is the presence of dissociable impurities. These impurities will undergo a chemical reaction to form positive and negative ions as shown below:

$$[AB] \rightleftharpoons [A]^{+} + [B]^{-}. \qquad \text{(eq. 1-1)}$$

The actual concentrations of each ionic species will depend upon the nature of the impurities and the reaction rates involved. When the fluid is at rest, equal concentrations of positive and negative ions are present in the bulk of the liquid and charge neutrality is maintained.

However, a mechanism for charge separation is provided by the existence of a solid phase in contact with the fluid. Typically, ions of one species will be chemically adsorbed by the solid surface. Alternatively, ions may be formed or neutralized at the interface via oxidation and reduction processes. In either case, the fluid adjacent to the wall will contain an excess of one ionic species and hence a net electrical charge. The

counter charges of the opposite sign will reside on the solid surface and an electric field will be present at the interface. An illustration of the charge separation process at the solid/liquid interface is shown in Figure 1-1

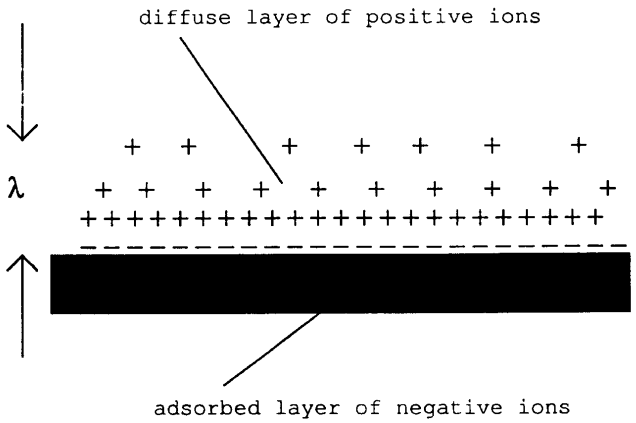

Figure 1-1
An illustration of the charged interface.

Under equilibrium conditions, a balance between electrical and diffusion forces will be achieved and a double layer established at the interface. The charged interface is quantified by the characteristic Debye length and zeta potential. The former parameter is defined as

$$\lambda = \sqrt{\frac{D\varepsilon}{\sigma}} \qquad \text{(eq. 1-2)}$$

where

D = molecular diffusion coefficient [m^2/s]

ε = fluid permittivity [F/m]

σ = fluid conductivity [S/m]

and provides an indication of how far the charged region penetrates into the fluid. The zeta potential gives a measure of the total charge contained in the liquid by application of Gauss's law. If the fluid charge density is q_o, then the zeta potential is expressed in terms of the Debye length and fluid permittivity as

$$\zeta = -\frac{q_o \lambda^2}{\varepsilon} \qquad \text{(eq. 1-3)}$$

These parameters are employed in more detailed descriptions of the charge distribution at the interface.

The classic concept of the double layer was first conceived by Helmholtz (3). His formulation considers the charges to occupy parallel planes as in the case of a simple capacitor. More realistic models recognize the existence of non-uniform charge distributions at the interface. The Gouy-Chapman model (4, 5) assumes that the charge on the solid surface is effectively located in a plane and that the fluid charge occupies a Boltzmann-type (exponential) distribution. When the zeta potential is small, the Debye-Huckel approximation (6) is commonly employed to model the diffuse layer as a linear charge profile.

A further refinement in double layer theory was proposed by Stern (7). The Stern model considers the charges in the fluid to occupy a compact layer very near the wall and a diffuse layer farther away where the Gouy-Chapman result applies. Within the compact region, the charge distribution is determined primarily by ion dimensions. As shown by Grahame (8) for salt solutions in contact with metals, the interface may be described in terms of a triple charge layer. The first layer consists of adsorbed ions on the surface which occupy an inner Helmholtz plane (IHP). The compact layer in the fluid contains ions of the opposite sign which effectively reside in an outer Helmholtz plane (OHP). Finally, the diffuse layer exists beyond the OHP and is comprised of the same ionic species as the compact layer. Grahame's interface model is illustrated in Figure 2.

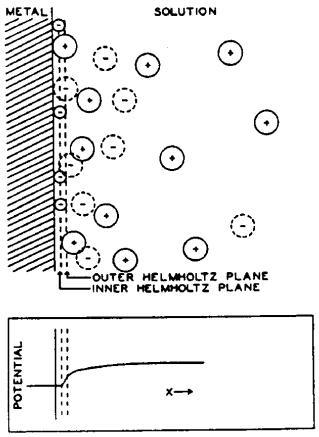

Figure 1-2
The triple layer model of the charged interface after Grahame (8).

Further advancements in describing charged interfaces have occurred within the past 50 years. Bockris et al (9) have developed a detailed model to resolve a number of discrepancies between the Stern approach and empirical findings. Their work provides a complete analysis of various adsorption processes and considers the presence of water

dipoles. In addition, they explain the relationship between the interfacial capacitance characteristic and the charge stored. A complete treatise on modern interface theory is given by Hunter (10).

While more detailed models are available, the Gouy-Chapman theory of the double layer is often used in the context of static electrification. Recognizing that the shear plane is very close to the OHP (10), the ions in the diffuse layer will be most readily transported by fluid motion. Assuming the ions in the compact layer remain stationary, the Gouy-Chapman distribution may be applied to model the diffuse region where the convection of charge is significant. Having acknowledged the existence of the charged interface, the consequences of charge separation occurring as ions in the fluid are convected away from their adsorbed counterparts must be considered.

When ions are being transported by fluid flow, some number of point charges will pass an arbitrary reference point during a given time. The corresponding electrical current is often used as a measure of static electrification. For example, consider the Helmholtz model of the double layer on a flat plate subjected to a laminar flow. As shown in Figure 1-3, the velocity profile near the wall is approximated as being linear by

$$v(y) = \frac{\tau_w}{\mu} y \qquad \text{(eq. 1-4)}$$

where

τ_w = shear stress at the wall [N/m^2]

μ = fluid viscosity [Ns/m]

y = distance from the wall [m].

The streaming current will be the product of the volume flow rate and volume charge density in the Debye layer and the latter may be expressed in terms of the zeta potential via eq. 1-3. The flow rate is obtained by integrating 1-4 over the Debye length and the streaming current per unit width will be

$$I_s = -\frac{\zeta \varepsilon \tau_w}{2\mu}. \qquad \text{(eq. 1-5)}$$

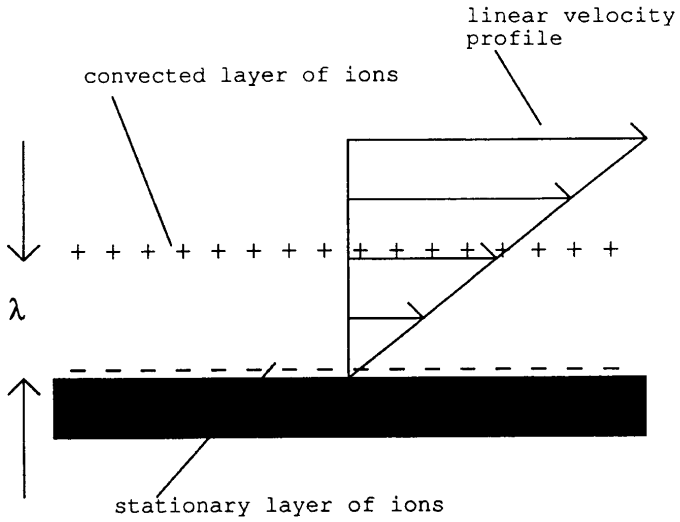

Figure 1-3
Convection of the fluid side of the Helmholtz double layer in a laminar flow.

In general, the streaming current is expressed in terms of the velocity and charge density profiles as

$$I_s = \int_A q\,\bar{v} \bullet dS \qquad \text{(eq. 1-6)}$$

where A is the cross sectional area of the flow at the point of interest.

As convection plays a major part in the charge separation process, the nature of the flow will be of paramount importance. In the case of fully developed laminar flow, molecular diffusion is the primary means by which ions are transported from the wall. Since this process is opposed by the electric field at the interface, the highest concentration of charge is within a few Debye lengths. Typically, the Debye length is quite small (i.e. on the order of microns for transformer oil) relative to the momentum length scale.

In the case of turbulent flow, eddy motion (11) may augment the molecular diffusion mechanism. The limiting factor will be the relationship between the Debye length and the laminar sublayer near the wall. If the Debye layer is contained within the sublayer, molecular diffusion will dominate as in laminar flow. However, if the diffuse layer penetrates the turbulent core, the eddy diffusivity mechanism will be significant. The turbulent Debye length proposed by Gasworth et al (12) now becomes the appropriate length scale for the charge distribution in the fluid. This parameter is obtained by replacing the molecular diffusion coefficient with an appropriate turbulent diffusivity D_T as shown below:

$$\lambda_T = \sqrt{\frac{D_T \varepsilon}{\sigma}}. \qquad \text{(eq. 1-7)}$$

The turbulent Debye length may well be of the same order as the characteristic length of the fluid dynamics problem and a great deal more charge will be entrained in the liquid. The dependence of the charge distribution upon the molecular Debye length and diffusion sublayer thickness is demonstrated by Abedian and Sonin (13) as shown in Figure 1-4.

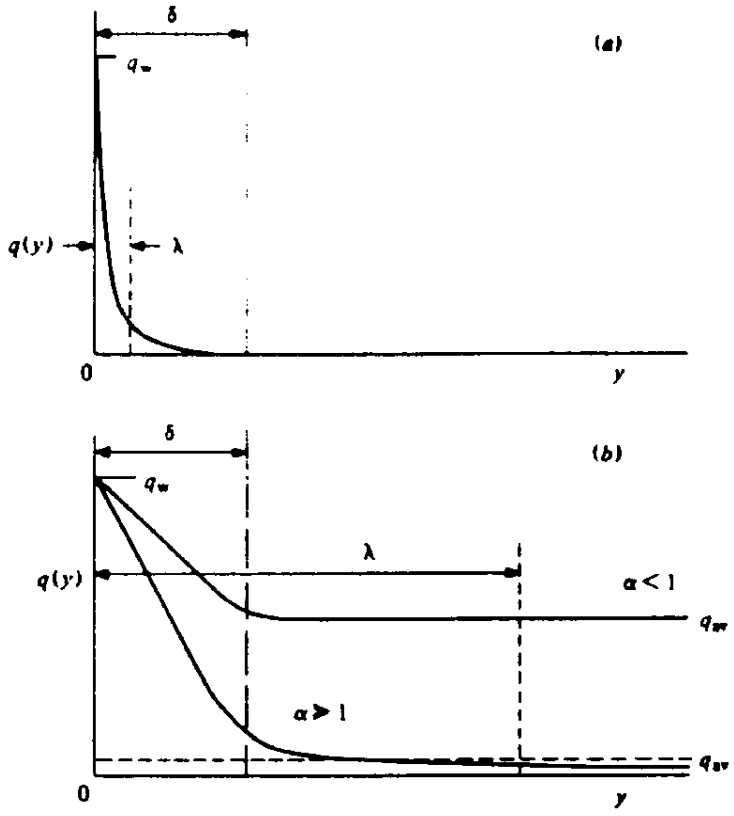

Figure 1-4
Turbulent charge profiles after Abedian and Sonin (13) for (a) $\lambda < \delta$ (b) $\lambda > \delta$. Note that the reference defines δ as the diffusion sublayer thickness.

Regardless of the type of flow which separates the charges, the crucial issue will be how they are subsequently reunited. Ideally, the convected charges will relax to ground potential where they will be met by a leakage current from the surface where their counterparts are trapped. However, in reality this process may be quite complex even if electrification is occurring in a conducting pipe. Further complications will arise when insulating surfaces are involved as in the case of a transformer.

The complete process of static electrification is well illustrated by Klinkenberg (14) in the context of the petroleum industry. His simple model reduces the problem to an RC circuit which demonstrates the separation and recombination of charge. Figure 1-5 depicts the equivalent circuit for electrification which occurs as oil flows through a metal pipe into a large tank. The effective capacitance between the fluid and conducting tank wall is charged by ions separated in the pipe. However, positive and negative charges are allowed to recombine through the leakage resistance R since the oil is not a perfect insulator. In the steady state, the capacitive current will decay to zero and Kirchoff's current law is satisfied as the generated streaming current flows to ground through the leakage resistance. Note that the tank and pipe are at the same electrical potential in this example.

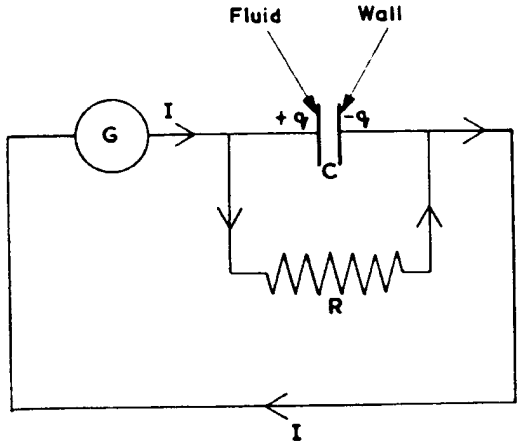

Figure 1-5
Lumped element electrical circuit which demonstrates the electrification process (after Klinkenberg (14)).

1.4 History of Problems

Static electrification hazards exist in a variety of rather diverse applications. In general, problems arise when electrification occurs on an isolated surface where the charges held by adsorbed ions cannot easily be conducted to ground. Alternatively, when convected charges are deposited on an insulating surface, a similar situation results. In either case, very large static potentials may be generated. When the corresponding electric field reaches sufficient magnitude, a flashover may occur to ignite the surrounding medium or initiate a dielectric failure. While the examples in this section focus upon electrification resulting from the flow of liquids, the phenomenon can also occur during the transport of solid materials (15).

While the electrical double layer will exist at nearly any solid/fluid interface, low-conductivity (i.e. dielectric) fluids pose the greatest threat. The reason for this

becomes obvious upon considering the relationship between conductivity and the Debye length in eq. 1-2. In aqueous (conducting) solutions, the Debye length will be on the order of angstroms and thus very little charge can be convected. However, in dielectric fluids where conductivities may range from 1×10^{-1} S/m to 1×10^{-15} S/m (16), the corresponding Debye lengths will be on the order of microns to millimeters. Under these conditions, ions will be much more readily transported by the flow. The low conductivity also discourages relaxation of charge to ground.

The petroleum industry has a long history of electrification problems related to the processing and transport of low-conductivity hydrocarbons. Explosions resulting from static discharges in the presence of volatile fuels instigated much of the early research in static electrification (17). The filling of tanker trucks has been recognized as a particularly hazardous operation as discharges may ignite vapors in partially filled tanks (18). In addition, dangerous levels of charge may be generated during filtration since the filter presents a large surface area to the flow (19). Some measure of success in reducing electrification in petroleum applications has been achieved through the use of additives which increase conductivity in conjunction with proper grounding (14).

Many liquids used for refrigeration systems (i.e. freon) are dielectric in nature and thus prone to electrification (12). Hence, the circulation of coolants through insulating tubes can result in unexpected static potentials which are not considered by the designer. However, since the insulating qualities of refrigerants are not critical, electrification problems can be inhibited by the use of additives as in the case of petroleum products.

The phenomenon of static electrification has been recognized as a threat to forced-oil-cooled power transformers only within the past 20 years. In the late 1970's, electrification problems in EHV transformers were first reported in Japan (20, 21, 22). Improved insulation processing techniques which increase the resistivity of oil and cellulose through the reduction of water also limit the leakage of static charge. In conjunction with the increased oil flow velocities required for the cooling of higher kVA rated transformers, static fields sufficient to cause dangerous discharging activity may result. A number of recent transformer failures in the U. S. have been attributed to the electrification phenomenon (1, 23). Numerous investigations have greatly enhanced understanding of the electrification process in a transformer environment, but the problem remains unresolved.

1.5 Application to Transformers

A transformer consists of a magnetically permeable core wound with conductors through which a current is passed to induce a magnetic flux in the core. Proper insulation must be employed to isolate the windings from each other and the core. In the case of large power transformers (e.g. 500 MVA), heating of the copper winding conductors becomes significant and forced cooling must be employed to prevent

thermal damage. The coolant must have both sufficient heat transfer and electrical properties as in the case of transformer oil. As the low-conductivity oil circulates through the transformer hydraulic circuit, charge separation will occur as described in the previous sections. Under the right conditions, static charge levels may become substantial enough to precipitate a catastrophic failure.

The most common EHV transformers are of the core-form and shell-form varieties. The core-type transformer windings are typically configured with groups of turns arranged in disks or layers. Static electrification occurring in a core-form transformer is demonstrated by Shimizu et al (21) as shown in Figure 1-6. Positive charges are separated by flow in the windings and relax in the plenum and cooling loop. A similar illustration is provided for a shell-form transformer by Tamura et al (24) as depicted in Figure 1-7. The shell-type windings consist of large "pancakes" which are separated by cooling ducts. While static charging problems have been documented in both types of transformers, electrification failures are more prevalent in shell-form designs.

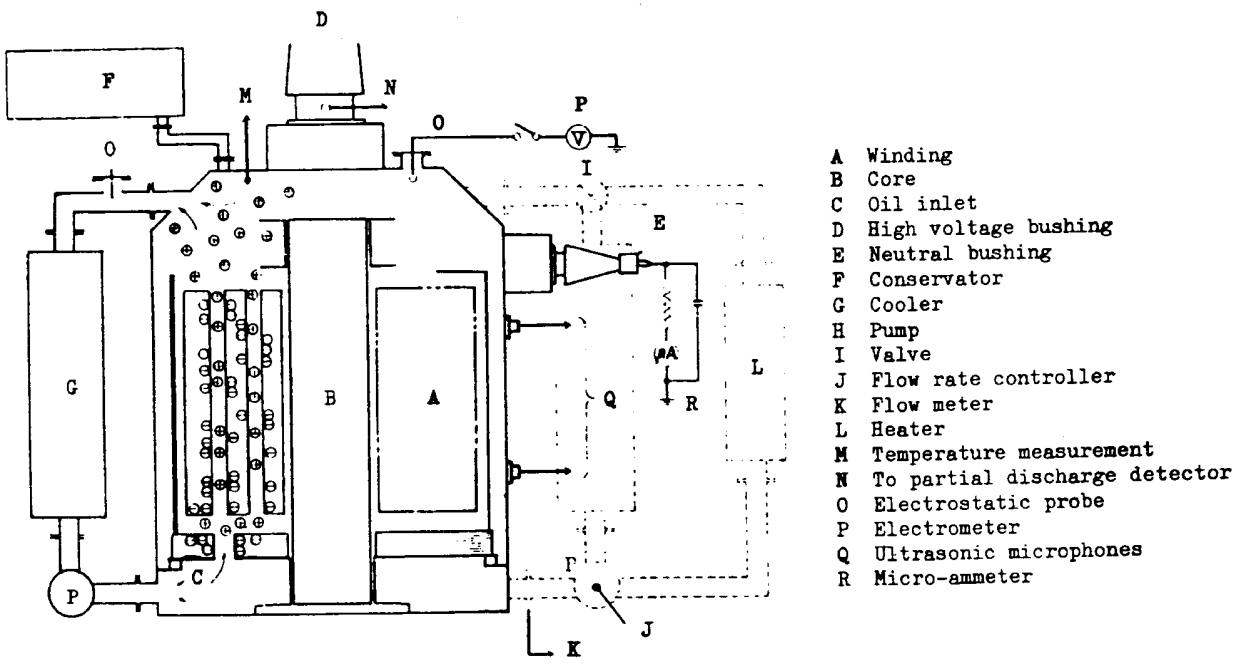

Figure 1-6
Charge separation in a core-form transformer after Shimizu et al (21).

The common trademarks of static electrification are electrical discharging (22), carbonized tracking on pressboard surfaces (21) and "wormholes" below the surface of cellulose insulation. These effects are all believed to result from static charge accumulation in regions where normal operating stresses are high. Static discharges are often detected prior to failures and are analogous to a capacitor which is charged until a flashover occurs between the plates. Surface and sub-surface tracking are typically

observed on the insulation structure during subsequent teardowns. Unfortunately, photographs of such phenomenon in transformer components are regarded as proprietary information by manufacturers and cannot be shown here.

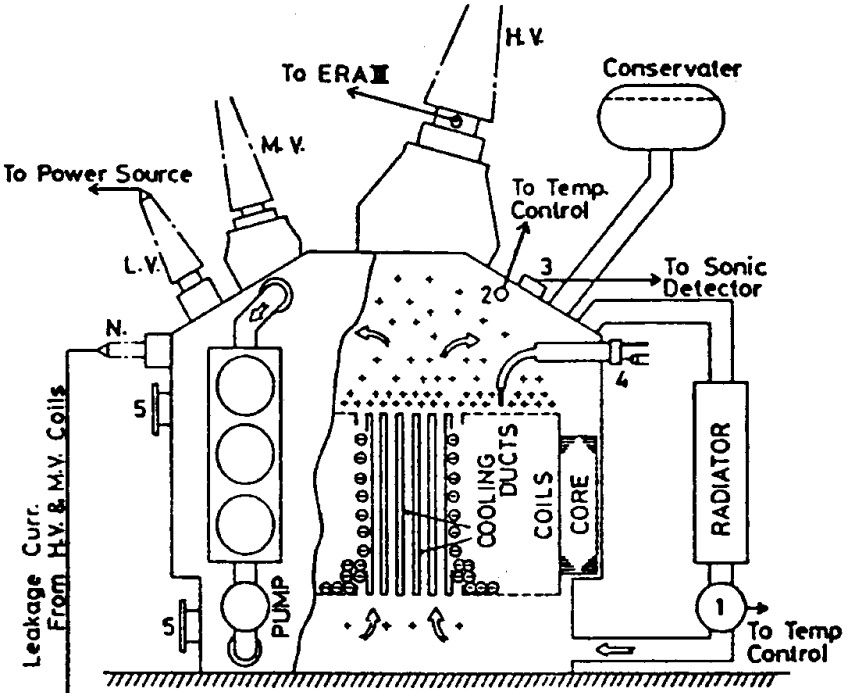

Figure 1-7
Charge separation in a shell-form transformer after Tamura et al (24).

The electrification process in transformers is governed by a number of competing parameters. The AC electric fields present at oil/cellulose interfaces have been shown to enhance the charge separation process (25, 26, 27). As the convection of ions gives rise to the phenomenon, flow velocities and Reynolds numbers also play an important role in static charging (12, 25, 28). In addition, the oil temperature which influences conductivity, viscosity, and ion concentrations is recognized as a critical variable (25, 29). Moisture levels in the oil and cellulose components of transformer insulation will affect conductivity and hence leakage resistances (26, 30). Furthermore, low moisture levels in oil which do not substantially alter the conductivity have been found to reduce static charging (31). Static electrification may also be linked with electrohydrodynamic effects which involve fluid motion resulting from electric fields acting on entrained charges and have been shown to influence dielectric breakdown (32).

1.6 Previous Work

Earlier technical reports in this series (25, 26) have outlined much of earlier work on the characteristics and analysis of streaming electrification with particular relevance to

transformers. Reiteration of this material would not seem appropriate here. However, for completeness, many of the salient references which underpin the earlier work have been included in the biography. In particular, these may be categorized as: experimental streaming electrification in dielectric fluids (33, 44), electrification in transformer geometries (45, 56), the development of charge measurement techniques (57, 59), and theoretical models (60 - 72). Subsequent sections of this research report will make use of many of these references in commenting on the significance of the findings.

2

EFFECTS OF MOISTURE DYNAMICS ON STATIC ELECTRIFICATION

2.1 Introduction

Varying amounts of water will always be present in the oil and cellulose components of transformer insulation. The latter material is hydrophilic in nature and will thus contain a much larger fraction of moisture by weight than the oil. Typically, pressboard will absorb between 0.1 and 7.0 percent water while transformer oil can accommodate moisture levels ranging from 1.0 to 50.0 parts per million (ppm) at room temperature. The distribution of moisture between the oil and pressboard at a given temperature is defined by the empirically determined Norris curves (73). These characteristics are based on the data of Fabre and Pichon (74) and are illustrated in Figure 2-1 for various temperatures.

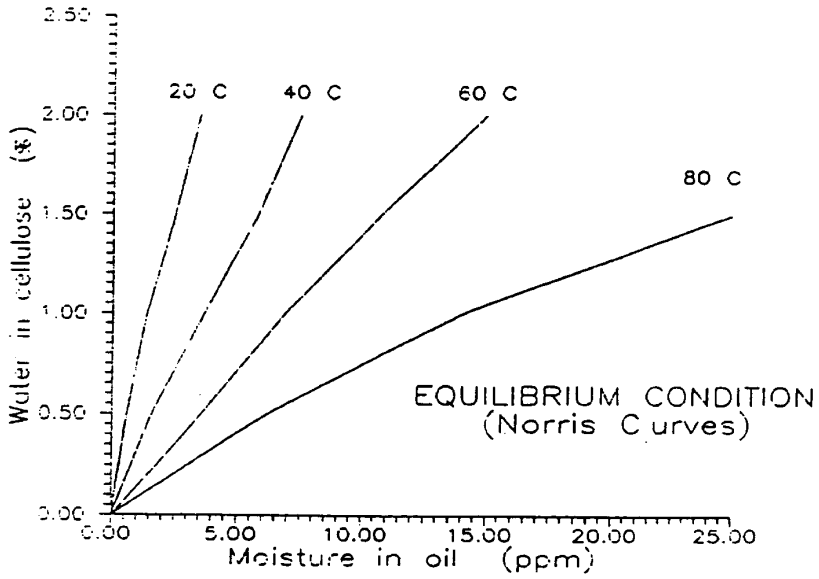

Figure 2-1
The Norris curves used for predicting the moisture equilibrium between oil and cellulose.

In the context of static electrification, moisture contained in the oil and cellulose may be quite important. The resistivity of pressboard is a strong function of moisture (75, 76, 77) and governs the leakage of static charge to ground. Hence, dry pressboard will hold more charge and thus lead to higher potentials resulting from flow electrification. The influence of water in the oil upon the electrification process may also be significant. Water molecules can dissociate to form H^+ and OH^- ions (16) which may participate in the electrification process. Alternatively, the water may act in concert with other dissociable impurities which produce ions. However, as moisture levels exceed approximately 10.0 ppm (25, 78), the streaming current is typically reduced. When free water droplets are present, the oil conductivity will increase such that the charge relaxation time is reduced.

The Norris curves predict the amounts of water residing in the components of an oil/cellulose system under equilibrium conditions. However, a change in operating temperature will create a dynamic situation while a new equilibrium point is established. Recognizing that the temperature of a transformer will fluctuate dramatically during service, the issue of moisture dynamics must be addressed with regard to static electrification. Recent electrification failures have occurred within hours or days after the units were brought on line (23). As the time constants associated with moisture equilibration are of the same order, the process has been identified as a possible catalyst for static charge. This Chapter documents large-scale experiments performed to investigate this hypothesized relationship between insulation moisture dynamics and the streaming electrification phenomenon.

2.2 Experimental Facilities

2.2.1 Fluid Loop

The moisture dynamics experiments discussed in this Chapter were performed using the fluid loop pictured in Figure 2-2. This facility provides a realistic range of oil flow rates and temperatures for investigating electrification in various structures. The relaxation tank dimensions were selected to ensure that all entering charges will be effectively trapped. Hence, all charge densities observed in the measurement section may be directly correlated with charge separation in the generating section. The smaller tank provides an expansion volume and allows for degassing or drying of the oil using an external vacuum. As illustrated, the loop is instrumented such that the oil temperature, volume flow rate, and moisture content may be monitored. An Absolute Charge Sensor (ACS) and Tandem Chamber Monitor (TCM) are installed downstream of the generating section to provide a measure of the volume charge density exiting the test structure.

2.2.2 Moisture Meters

Two different methods were used to determine the water content in the transformer oil used. On-line readings were provided by a specially modified HY-CAL™ sensor mounted in the relaxation tank. This sensor is described by Oommen (79) and makes use of a polyamide film which readily absorbs moisture. The capacitance of the film is strongly related to the ambient relative humidity and thus provides a measure of the moisture present in the oil. The HY-CAL™ meter calibration was found to be changed if the sensor tip and

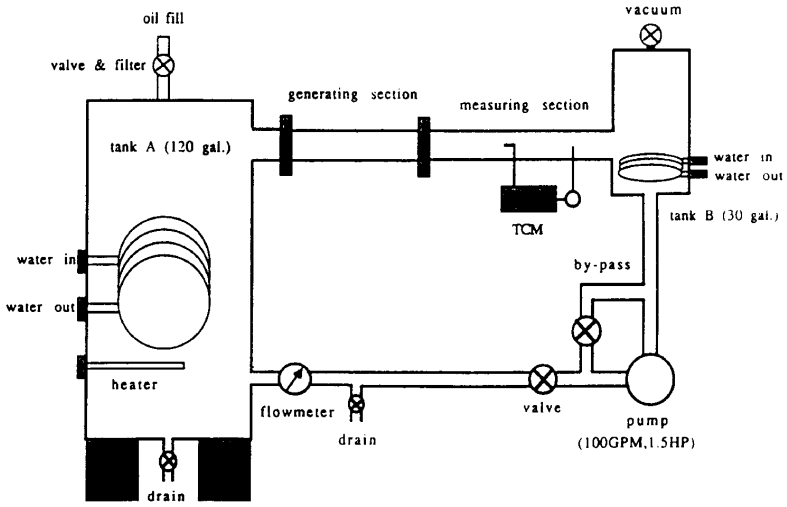

Figure 2-2
The fluid loop facility used for studying electrification.

driving electronics were at different temperatures as shown in Table 2-1. However, at a fixed temperature, the instrument will give stable trend information which was quite useful for these experiments.

Table 2-1
Effect of temperature difference between driving electronics and sensor on the calibration of the HY-CALTM probe.

Electronics Temperature [°C]	Sensor Temperature [°C]	Output Current [mA]
22	22	4.67
40	22	4.70
50	22	4.73
60	22	4.84

An alternative measurement of the oil water content was provided by a Mitsubishi CA-06 colometric moisture meter. This instrument titrates water based upon the reactions shown below (80):

$$n\,I_2 + S\,O_2 + H_2\,O \rightarrow 2\,H\,I + S\,O_3 \qquad \text{(eq. 2-1)}$$

$$2\,I^- - 2\,e \rightarrow I_2 \qquad \text{(eq. 2-2)}$$

Transformer oil is injected directly into the anode reagent and eqs. 2-1 and 2-2 are balanced by the flow of electrical current between the anode and cathode of the test cell. The amount of current required provides a measure of the moisture contained in the sample. This instrument can be calibrated using precise water samples and is considered to be more accurate in terms of absolute magnitude than the HY-CAL™ sensor. The Mitsubishi meter was also calibrated against the more primitive volumetric Karl Fisher method (ASTM D1533) and good agreement was obtained to within 2 ppm in saturated oil. The addition of a VA-06 vaporizer unit allows the Mitsubishi instrument to determine moisture levels in solid samples of pressboard. The samples were shredded and baked at 150°C to extract the water which is conveyed to the titration cell by dry nitrogen.

2.2.3 Transformer Models

The moisture dynamics experiments were performed using two different transformer models in the generating section of the fluid loop. These models are representative sections of transformer geometry fabricated by EHV Weidmann to industrial specifications. Note that while the transformer models were constructed largely of pressboard, the more significant volume of cellulose placed in the relaxation tank was assumed to dominate the moisture equilibrium process.

The core-form model schematic is depicted in Figure 2-3. Two passes of an annular disk-type winding are represented. The copper winding conductors are bundled into groups and covered with oil impregnated paper with the conductors of each disk section electrically connected. Each "turn" may thus be energized with respect to neighboring turns or an external ground plane. Alternatively, the winding sections could be grounded through an electrometer to provide a measure of streaming current. The model was encased in Spauldite™ and clamped into the fluid loop using specially made flanges.

A schematic of the shell-form model is shown in Figure 2-4. Sections of two parallel "pancake" windings are separated by duct structures comprised of 90° spacer blocks. Similar to the core-form model, each winding is made of copper conductors bundled together and wrapped with oil impregnated paper. The conductors of each "turn" were again electrically connected to one another. An external bushing was provided to attach an AC source or electrometer. As before, a Spauldite™ casing was used to contain the model and facilitate installation in the fluid loop via special flanges.

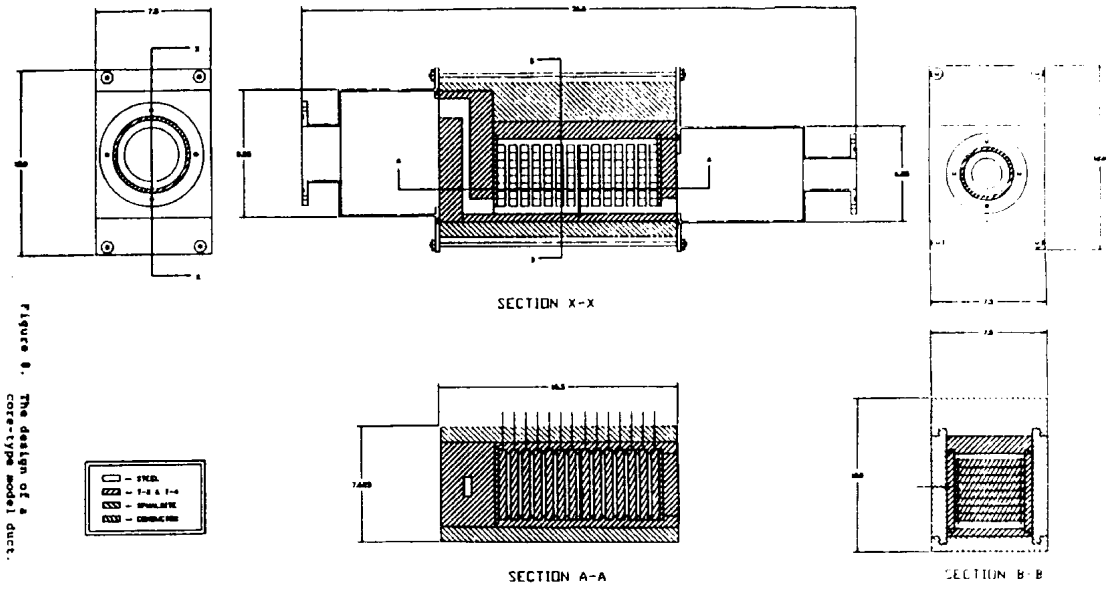

Figure 2-3
Schematic of the core-form transformer model.

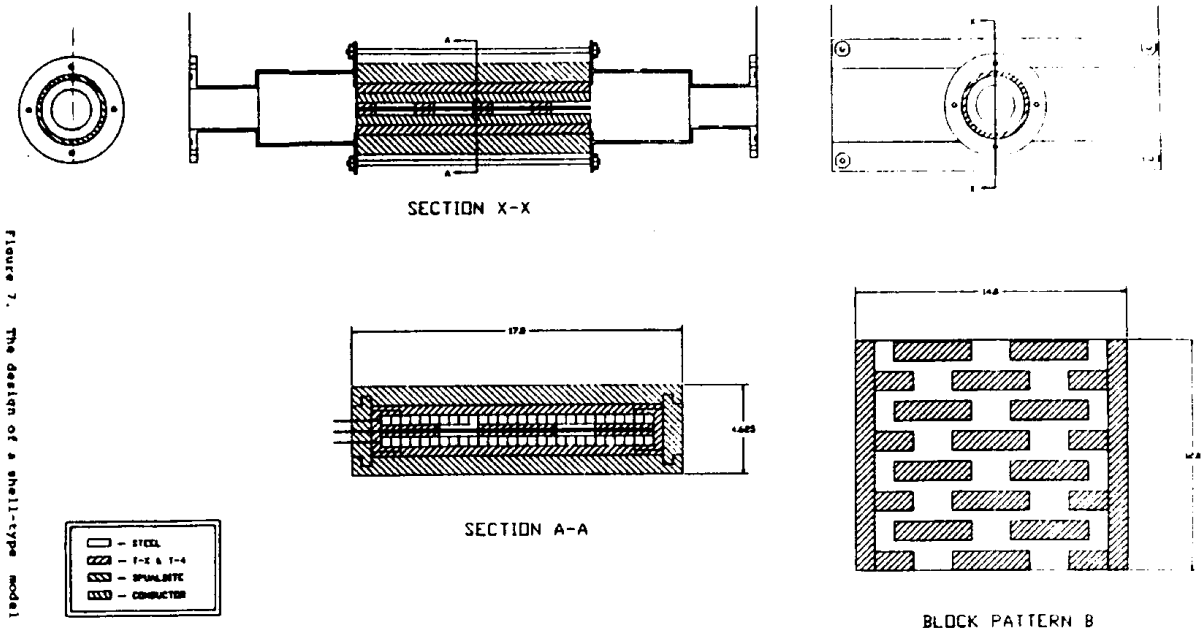

Figure 2-4
Schematic of the shell-form transformer model.

2.3 Methodology

2.3.1 Preparation of Insulation Components

The oil and cellulose used for this experiment were processed in accordance with industrial standards. The Shell DIALA-A transformer oil was heated to 60°C in the fluid loop and circulated through the degassing chamber at a low flow rate. A vacuum was applied to extract the water vapor from the oil after it was sprayed through a perforated pipe section into the tank. Over a period of several weeks, the oil moisture content was reduced from 50.0 ppm (saturated) to approximately 1.0 ppm as measured by the Mitsubishi meter. Typically, the oil used to fill a new transformer will contain between 1.0 and 10.0 ppm water.

The pressboard used for these experiments was supplied by EHV Weidmann in unimpregnated form. Equal amounts of high and low-density (T4™ and HI-VAL™) were used. The volume of pressboard was chosen such that the volume ratio of oil to cellulose was 8:1 which is representative of an actual transformer (81). The cellulose sheets were cut into sections having approximate dimensions of 76.2 cm by 43.18 cm by 0.32 cm to facilitate batch drying in a vacuum oven. Seven batches of pressboard were processed using the following procedure (75, 82):

1. 12 hours at 80°C with no vacuum.

2. 7 days at 120° with approximately 500 microns of vacuum applied (a cold trap was required to prevent water damage to the pump).

3. Cool under vacuum and seal in plastic.

This process resulted in pressboard moisture levels on the order of 0.2 percent which exceeds the typical specification of 0.1 percent (75). However, this was deemed acceptable since the pressboard was not going to be subject to electrical stress. After all seven batches of cellulose had been dried, each was returned to the oven, heated to 80°C and impregnated with dry transformer oil from the fluid loop. The impregnation was performed under vacuum and the boards were submerged in oil for 12 hours.

Having prepared the oil and pressboard insulation, the latter was placed in the relaxation tank of the fluid loop. The boards were arranged as shown in Figure 2-5 to provide the greatest surface area in contact with the oil and ensure proper circulation. Sacrificial samples of cellulose were suspended from fittings in the top of the tank for subsequent moisture measurements. Upon completion of assembly, the oil and pressboard moisture contents were found to be approximately 5.0 ppm and 0.3 percent respectively. The increased moisture levels are attributed to unavoidable exposure to air during the assembly process.

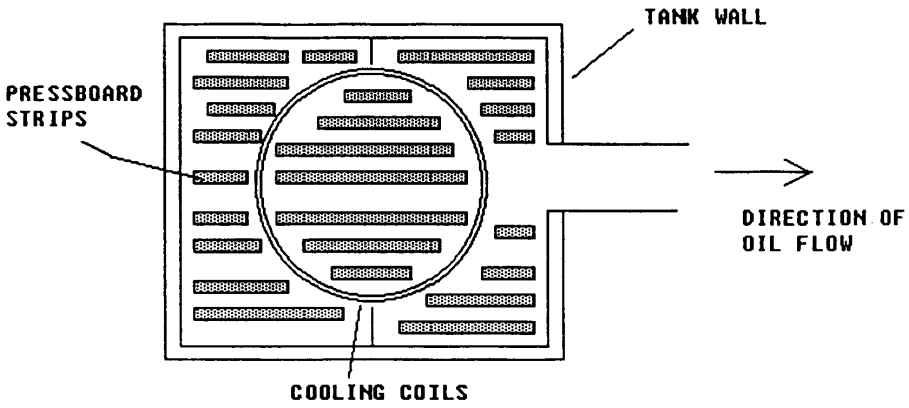

Figure 2-5
Orientation of the bulk pressboard in the relaxation tank.

2.3.2 Thermal Cycles

The oil and cellulose system was subjected to three stages of a transformer service life as follows:

1. Step 1: initial equilibrium (20°C).

2. Step 2: start up (20°C to 60°C).

3. Step 3: shut down (60°C to 20°C).

The first step was intended to allow for moisture equilibrium between the oil and cellulose after a transformer has been processed in the field. The second segment simulated the thermal transient associated with energization and loading of the unit. Upon completion of the transient, the operating temperature was held at 60°C such that a new moisture equilibrium could be achieved. The final step of the experiment required cooling the system to mimic the effect of de-energizing the transformer. The temperature was restored to 20°C and held constant until moisture equilibrium was obtained.

During the thermal cycles explained above, the system parameters were closely monitored. Oil moisture, temperature and conductivity were all measured with respect to time. The oil was circulated regularly to facilitate measurements of streaming electrification and ensure that the system was well-mixed. Also, the water content of the cellulose was examined regularly. Measurements were made at a frequency determined by the rate of change of the oil moisture content. Initially, data was taken on an hourly basis and later on a weekly basis near the end of each cycle. The fluid loop was kept sealed during the experiment except for very brief intervals when oil and pressboard samples were removed.

2.4 Core-Form Model Results

2.4.1 Step 1 (Initial Equilibrium)

Recognizing that changes in oil moisture levels are insignificant relative to the water content for the bulk cellulose for the volume ratio selected, the latter value may be used to predict the final equilibrium point. Figure 2-6 depicts the "load-line" corresponding to 0.3 percent moisture in the paper on the Norris curves. At 20°C, the oil moisture is expected to reach an equilibrium level of less than 1.0 ppm.

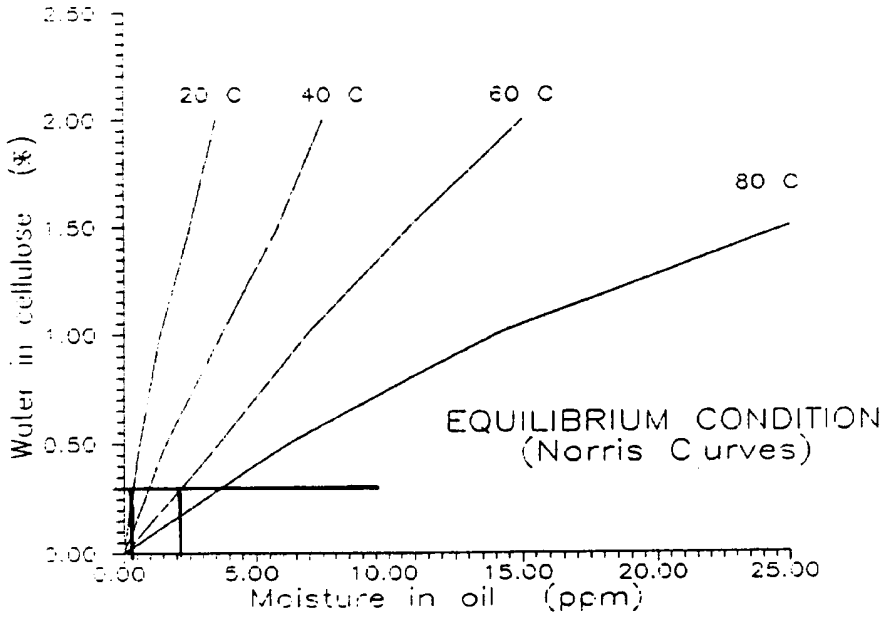

Figure 2-6
Norris curves showing predicted oil moisture equilibrium points based on a constant water level in the cellulose for the core-form experiments.

As shown in Figure 2-7, the oil moisture drops from 5.0 ppm and exhibits a time constant on the order of 120 hours. Over the course of 1600 hours, the rate of change decreases and an asymptote of approximately 1.0 ppm is approached. While the HY-CAL™ sensor and calibrated Mitsubishi meter depict nearly identical trends, the values given by the former were shifted in absolute magnitude. Recognizing that 1.0 ppm is very close to the detection threshold of either instrument, the final results are considered to be acceptable. Note that the water content of the pressboard samples examined did not vary significantly from the initial value of 0.3 percent.

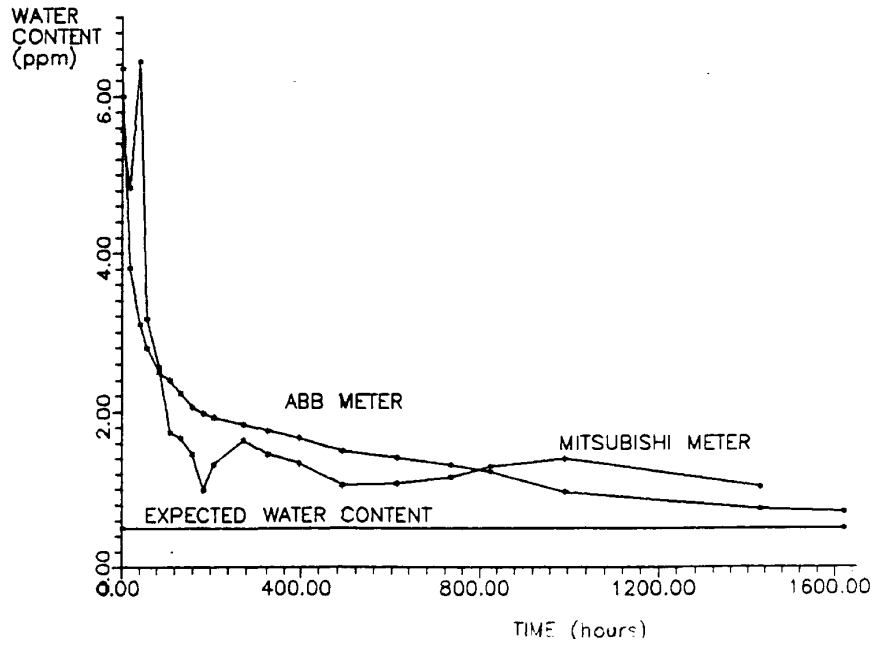

Figure 2-7
Oil moisture measured with respect to time during initial equilibrium (core-form).

The oil conductivity is illustrated with respect to time in Figure 2-8. This data was taken using an EMCEE model 3000 DC conductivity meter to analyze oil samples from the main tank. The slight decrease in oil conductivity during initial equilibrium is not unreasonable as the oil moisture is also reduced. Water content is known to influence the conductivity of dielectric fluids (16), but the relationship for transformer oil is relatively weak below 10 ppm (25) when all moisture is in solution. Note that the possibility of additional impurities provided by the moisture should also be recognized. The conductivity appears to stabilize in concert with the oil moisture level.

Streaming electrification measurements were performed under various conditions during the initial equilibrium stage. The core-form model casing was covered with aluminum foil on three sides such that realistic electric fields would result when the winding conductors were energized with a power frequency voltage. Figure 2-9 illustrates the charge densities measured downstream of the model outlet. Both the unenergized and 10 kV characteristics were taken at the maximum flow rate of $2.27 \times 10^{-3} m^3/s$. As expected, (25, 29, 48), the application of an AC electric field augments the charge separation process. Since the TCM error margin is approximately $\pm$ 1.0 $\mu C/m^3$, the fluctuations in the charge density measurements are not considered particularly significant. However, the decrease in oil moisture does appear to somewhat influence the electrification process in the core-form model with the charge density initially decreasing in concert with moisture during the first 100 hours. Note that this is the opposite of the effect previously discussed above 10 ppm where added moisture reduces static charging.

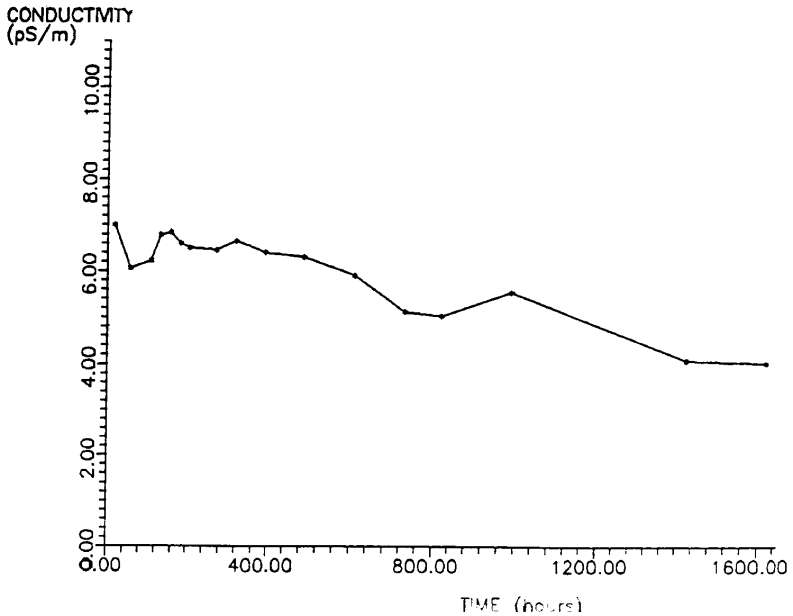

Figure 2-8
Oil conductivity measured with respect to time during initial equilibrium (core-form).

2.4.2 Step 2 (Start Up)

Upon completion of initial equilibrium, the system temperature was increased from 20°C to 60°C. The transient was applied over a 12 hour period as shown in Figure 2-10. Measurements were taken during the temperature transient and continued once 60°C had been achieved. The Norris curves of Figure 2-6 predict approximately 2.5 ppm in the oil at equilibrium. Based on sacrificial bulk cellulose samples, the pressboard moisture level remained at 0.3 percent.

In order to attain the expected equilibrium point, moisture was transferred from the cellulose to the oil. As demonstrated in Figure 2-11, the amount of water in the oil does increase and ultimately exceeds the predicted value. The Mitsubishi meter data is believed to be more accurate since the HY-CAL™ sensor calibration is temperature dependent (see Table 2-1). In this case the HY-CAL results have not been shifted since the temperature calibration problem adds an additional scaling factor. While the oil moisture content appears to reach an equilibrium, the final value approaches 5.0 ppm after 700 hours rather than the expected 2.5 ppm. This discrepancy may be partially explained by a non-uniform moisture distribution in the cellulose which is addressed in Section 2-6.

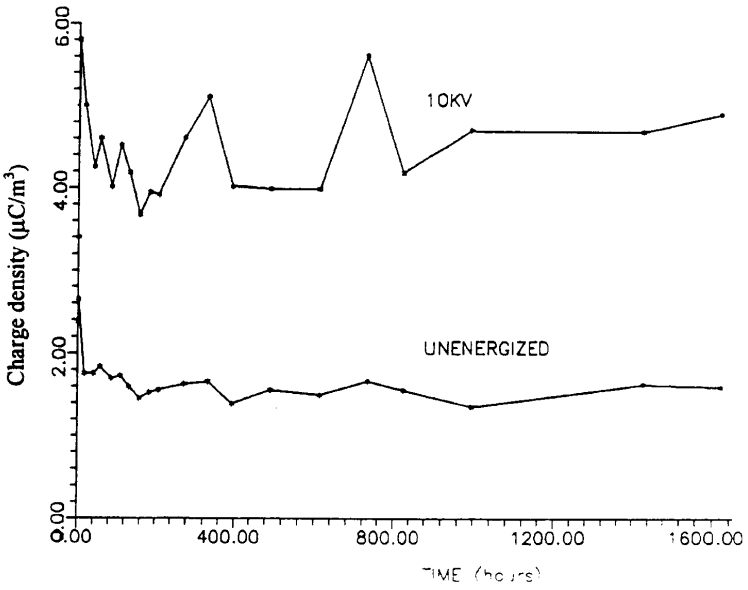

Figure 2-9
Volume charge density generated by flow electrification at 2.27 x 10^{-3} m^{-3}/s with respect to time during initial equilibrium (core-form).

The oil conductivity initially increases with temperature as shown in Figure 2-12. While the accompanying increase in oil moisture could enhance the conductivity, the expected temperature dependence appears to dominate. The results of initial equilibrium indicate that a change of 5.0 ppm in the oil moisture corresponds at most to a change of 3.0 pS/m and is probably less if there is no free water. Typically, the conductivity of a dielectric fluid will obey an Arrhenius relationship with temperature (83). The conductivity may be expressed in terms of an activation energy as

$$\sigma = \sigma_o \exp\left[- \frac{W_\sigma}{k\,T} \right] \qquad \text{(eq. 2-3)}$$

where

σ_o = constant [S/m]

W_σ = activation energy [J]

k = Boltzmann constant (1.38×10^{-23}) [J/°K]

T = temperature [°K].

The validity of eq. 2-3 has been demonstrated for transformer oil (25, 29, 48) and will be further discussed later in a theoretical context.

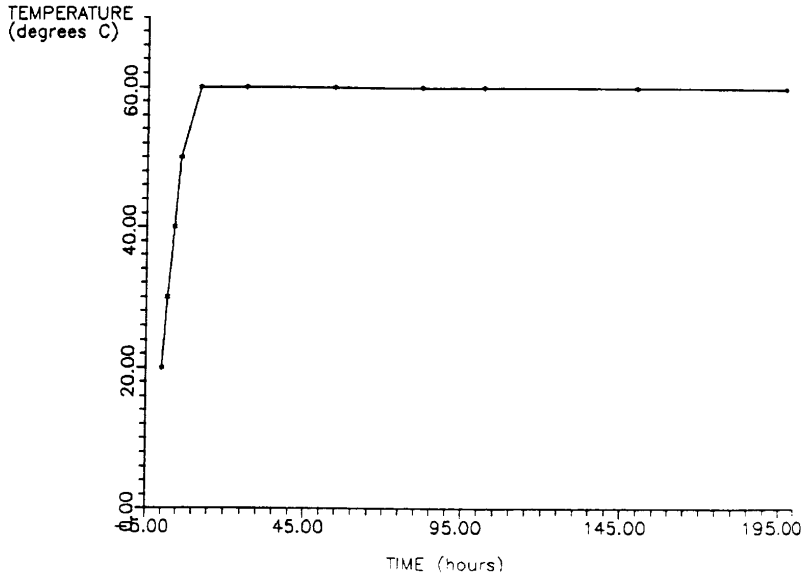

Figure 2-10
Oil temperature measured with respect to time during start up (core-form).

The oil conductivity appears to stabilize for nearly 20 hours after the desired temperature was reached prior to a gradual increase. This effect was not expected since the oil temperature remained at 60°C. After 400 hours, a maximum of 24.0 pS/m is reached which is nearly double the original value of 12.2 pS/m first achieved at 60°C. This effect may be attributed to contamination resulting from degradation of the epoxy used to assemble the core-form model. In addition, oxidation of the oil may have occurred with the copper sections in the fluid loop providing the necessary catalyst. Compounds resulting from oxidation may dissociate in the oil with the resulting ions augmenting the conductivity (16, 84). However, the contamination hypothesis is more plausible given the fact that 60° is probably too low for oxidation to occur in transformer oil (85). Regardless of the cause for the conductivity increase, the effect upon streaming electrification provides some interesting results.

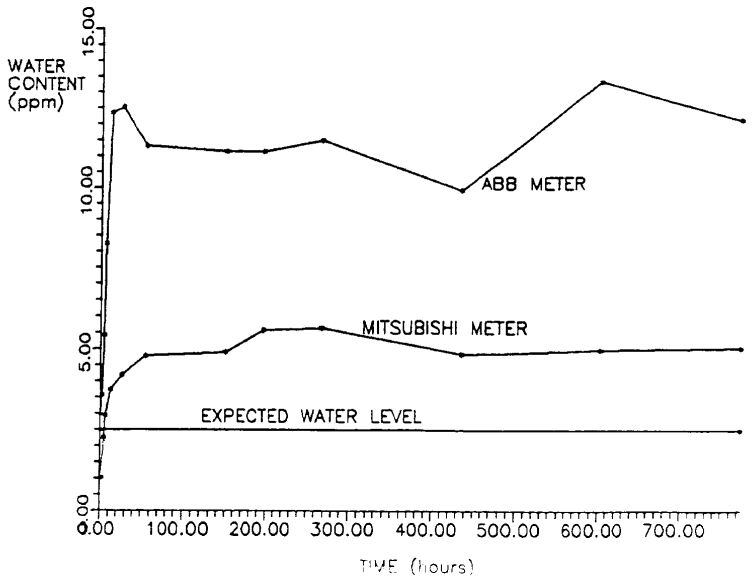

Figure 2-11
Oil moisture measured with respect to time during start up (core-form).

Initially, the charge density exiting the model increased with temperature as shown in Figure 2-13. This relationship between electrification and temperature has been well documented (25, 26, 45) and depends on several parameters. Note that the temperature effect appears to dominate over any influence of increasing moisture. The concentration of dissociated ions in the oil is expected to increase with temperature (16) and has been postulated to follow an Arrhenius dependence (45, 29) similar to eq. 2-3. The kinematic viscosity will decrease logarithmically with temperature (26, 83) to give higher Reynolds numbers which increase charge separation (29, 48). Also, the molecular diffusion coefficient for ions in the oil will rise with temperature (83) which aids in the transport of ions from the oil/cellulose interface. The oil conductivity usually provides two behavior regimes for static electrification. Below a given threshold, the streaming current will increase with conductivity while above this threshold the converse is true. The electrification process is ultimately dictated by the competition between the generation and relaxation mechanisms. During the temperature transient, the increasing charge densities signify the low-conductivity regime.

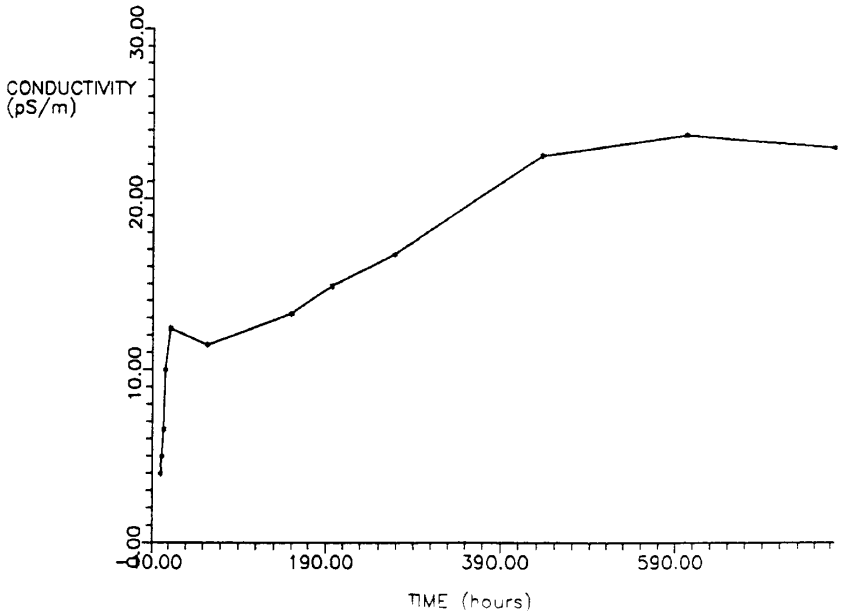

Figure 2-12
Oil conductivity measured with respect to time during start up (core-form).

Once 60°C is reached, the charge density appears to follow the oil conductivity for the next 80 hours. However, once the conductivity reaches approximately 15.0 pS/m (100 hours), the impact of AC energization begins to diminish. As the conductivity continues to increase, the high-conductivity regime is entered and relaxation begins to dominate. The charge density characteristic declines and ultimately stabilizes once the oil conductivity stops rising. While this effect would be anticipated, the application of AC electric fields would still be expected to produce higher charge densities.

The data shown in Figure 2-13 was taken at a volume flow rate of $2.27 \times 10^{-3} m^3/s$. In the axial ducts where energization will be most significant, the corresponding Reynolds numbers at 60°C indicate turbulent flow (26). Under these conditions, large AC electric fields will act to inject charges into the turbulent core of the flow (48). Positive ions will be transported during the appropriate part of the 60 Hz cycle as determined by their mobility. Under turbulent conditions, the eddy diffusivity will prevent removal of these ions from the core region during the opposing half cycle and a net positive charge in the oil will result. As demonstrated in Sections 4 and 5, the energization phenomenon may be effectively considered as field transport of ions from the fluid side of the Debye layer. The model works quite well when the oil conductivity obeys the expected Arrhenius temperature relationship. However, some additional postulates must be offered to explain these results.

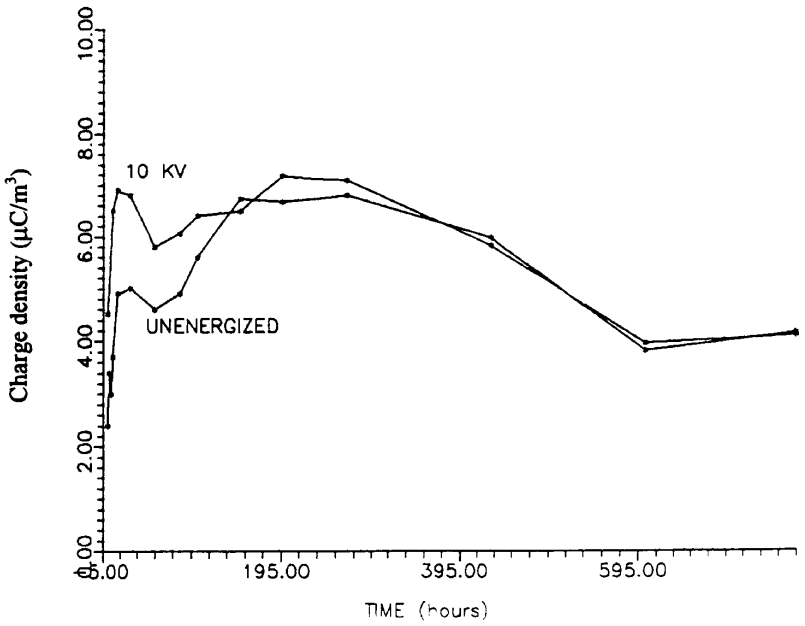

Figure 2-13
Volume charge density generated by flow electrification at 2.27 x 10^{-3} m^{-3}/s with respect to time during start up (core-form).

Figure 2-13 appears to indicate that the unenergized charge density increased to approach the 10 kV curve over a 200 hour period. This would indicate that the low-conductivity electrification regime exists below 15 pS/m. Hence, the added carriers acted to supply the static charging process. Accepting that these new carriers could have much different parameters from the intrinsic ions present at lower temperatures, several scenarios may be considered. A much less mobile positive species would greatly reduce the effect of AC energization. However, a lower mobility also implies a lower diffusion coefficient by the Einstein relation. This would indicate a smaller Debye length and predict a decline in the unenergized charge density which is not apparent from the results.

Typically, the negative species in the double layer is assumed to achieve a strong chemical bond to the cellulose and eventually discharge to ground once the corresponding countercharge in the fluid is swept away. However, in the present case, the behavior of the negative species may not have been the same. The added species may form a much weaker surface bond with the insulation surface such that field transport into the turbulent core occurred during the negative half cycle. This negative injection may have neutralized the AC transport of positive ions from the Debye layer without influencing the unenergized case. Another possibility would be field-induced dissociation of ions which resulted in a higher conductivity and hence a lower generated volume charge in the oil under energized conditions. Unfortunately, this hypothesis would be much more plausible under DC conditions rather than for power frequency voltages.

2.4.3 Step 3 (Shut Down)

After nearly 700 hours at 60°C, the system temperature was reduced to 20°C over a 24 hour period as shown in Figure 2-14. Measurements were taken during the transient and continued after 20°C was attained.The moisture level in the pressboard remained at approximately 0.3 percent. Hence, the Norris curves indicate a final equilibrium point for the oil moisture of less than one ppm as per initial equilibrium.

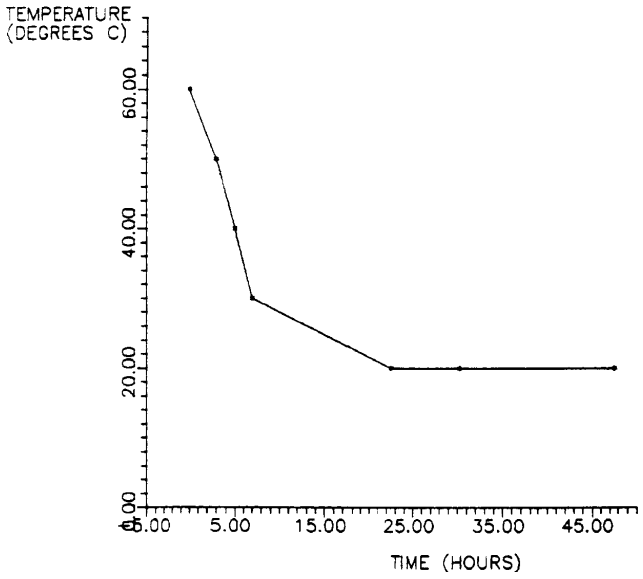

Figure 2-14
Oil temperature measured with respect to time during shut down (core-form).

The oil moisture content dropped in conjunction with the temperature reduction as shown in Figure 2-15. The HY-CAL™ sensor and Mitsubishi meter both indicate a final equilibrium point of nearly 2.5 ppm in the oil. However, this value clearly does not agree with the Norris curves. A discussion of this discrepancy is provided in Section 2.6. Note that the agreement between the moisture meters at 20°C occurred with no adjustment to the HY-CAL™ probe calibration. Scaling to the Mitsubishi results is not appropriate during temperature transients due to the additional calibration shift in the HY-CAL sensor.

Reducing the oil temperature produced a corresponding drop in the oil conductivity. As illustrated in Figure 2-16, the conductivity ultimately reaches a value of 6.0 pS/m at room temperature. This indicates that the contamination observed at 60°C did not permanently

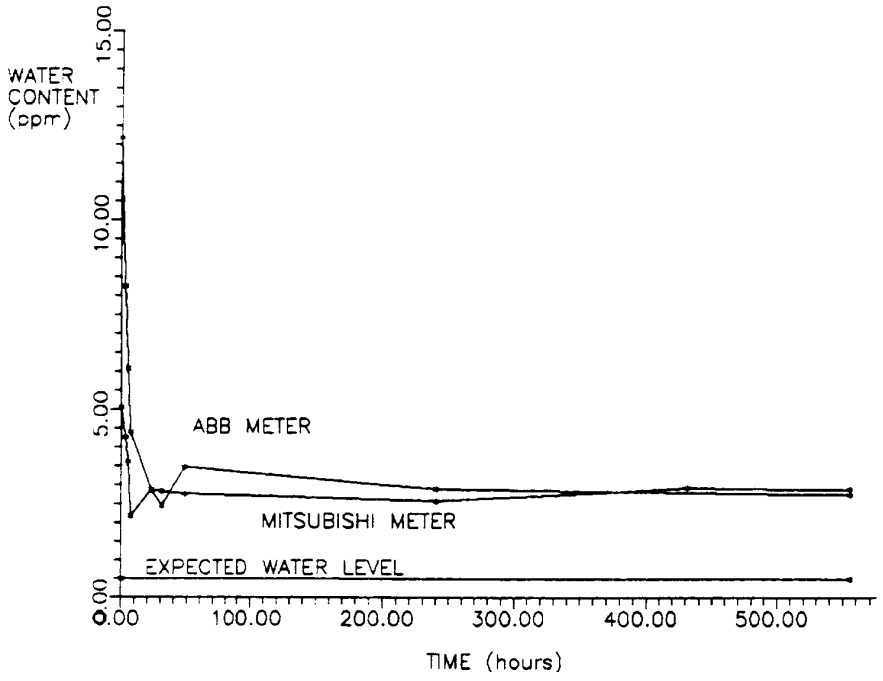

Figure 2-15
Oil moisture measured with respect to time during shut down (core-form).

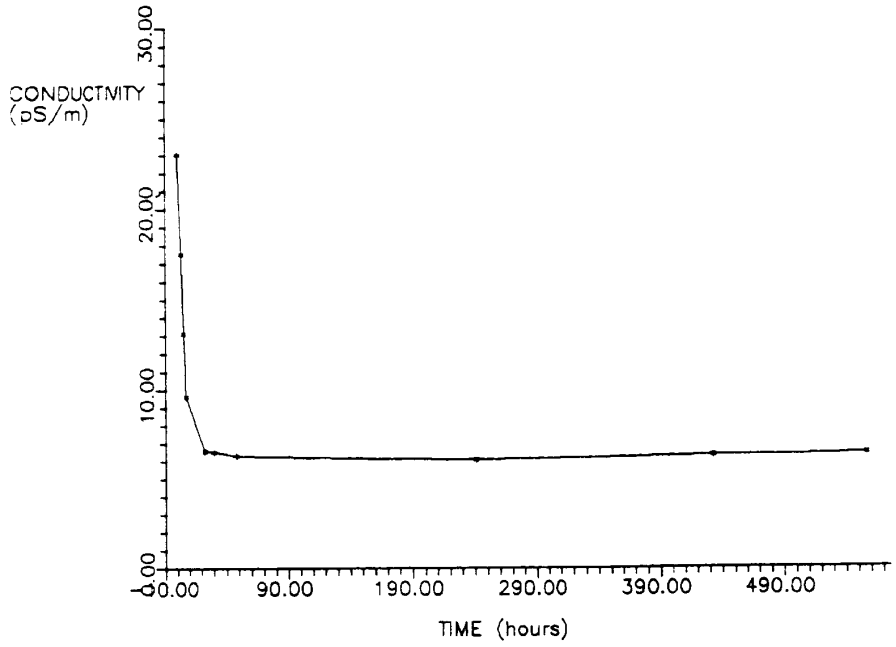

Figure 2-16
Oil conductivity measured with respect to time during shut down (core-form).

change the resistivity of the oil. Hence, the supply of dissociable contaminant(s) would appear to be available only at high temperature. This is reasonable if the contamination theory is accepted, particularly if an adhesive from the transformer model is suspected. An improperly cured adhesive could conceivable soften and go into solution after a prolonged period at 60°C. Furthermore, when the oil was cooled, the contaminant could have precipitated out of solution and thus ceased to influence the conductivity.

The charge generated in the core-form model was found to decrease as the oil temperature was reduced. As depicted in Figure 2-17, the influence of AC energization again becomes evident once the conductivity drops below 15.0 pS/m. As the oil temperature stabilizes at 20°C, both the unenergized and 10 kV results appear to become essentially constant in time. Although there is some indication of a minimum at approximately 200 hours in the electrification and moisture results, this trend must be considered insignificant with respect to measurement error margins. A clear relationship between generated streaming current and oil water content is not demonstrated during this phase of the experiment. However, due to several competing mechanisms (i.e. conductivity, dissociation rates) the moisture effect could be hidden.

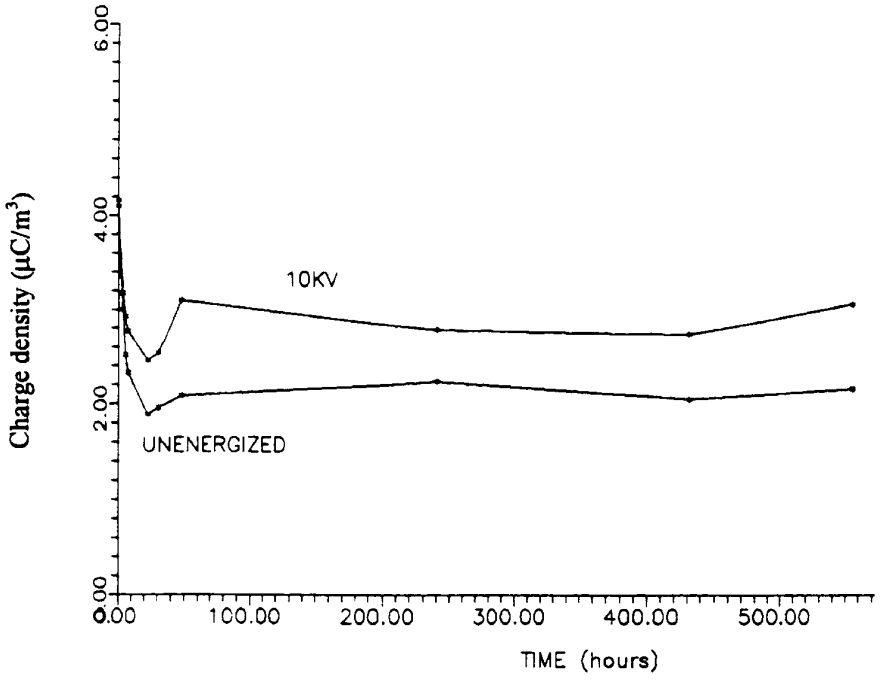

Figure 2-17
Volume charge density generated by flow electrification at 2.27 x 10^{-3} m^3/s with respect to time during shut down (core-form).

2.4.4 Summary

Three temperature cycles were investigated in a large-scale system having a realistic ratio of oil to cellulose. While the moisture dynamics data follow the predicted trends, the final equilibrium points do not always coincide with the Norris curves. The best agreement was obtained during initial equilibrium at 20°C. During the second and third cycles, the oil moisture remained higher than expected. Moisture dynamics within the bulk cellulose resulting from ambient humidity exposure may explain these results and is discussed further in Section 2.6.

This experiment would suggest two regimes of behavior for the relationship between electrification and oil moisture content. As discussed previously, moisture levels above 10 ppm tend to reduce the amount of charge separated. However, at very low moisture levels, the converse effect is somewhat apparent in the results of this section (see Figure 2-9). Hence, the break-point between the high and low moisture regimes might fall at approximately 5 ppm. Some additional discussion of this effect is provided in Section 2.6.

The most critical factor during temperature cycling would appear to be the oil conductivity. Due to unexpected contamination, the conductivity achieved a value more than twice that predicted by the Arrhenius temperature relationship. As a result, AC energization ceased to enhance charge separation at 15 pS/m and the observed charge density declined until the conductivity finally stabilized. This effect is tentatively attributed to different ion parameters for the positive and negative species supplied by the contaminant at high temperature. In particular, negative ions which were weakly adsorbed by the cellulose may have negated positive ion transport under turbulent AC energized conditions.

2.5 Shell-Form Model Results

2.5.1 Preliminary Findings

A new supply of Shell DIALA-A transformer oil was obtained in response to concerns about the apparent contamination problems during the core-form experiments. The original oil was drained from the fluid loop with the bulk pressboard left in place. Before refilling, a more powerful pump was installed to provide a higher range of oil flow rates. The new oil was found to have a moisture content of 7.0 ppm upon arrival and did not become appreciably wetter during the filling process. With the pressboard still in the system, the oil could not be dried and the initial equilibrium measurements were started immediately.

Analysis of bulk moisture samples in the main tank indicated that the moisture content was still on the order of 0.3 percent. Hence, a final equilibrium value of less than 1.0

ppm was expected in the oil as in the core-form experiment. However, as shown in Figure 2-18, an asymptote of nearly 5.0 ppm was approached after 500 hours. This was attributed to possible moisture contamination of the bulk cellulose surfaces when the oil was removed from the system. Despite the fact that air was introduced through a desiccator, the cellulose

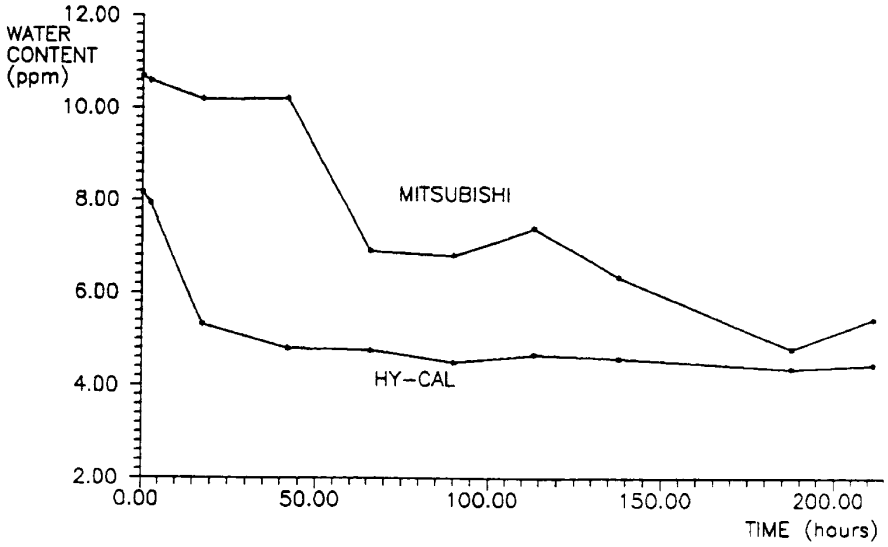

Figure 2-18
Oil moisture measured with respect to time during the first initial equilibrium test using the shell-form model.

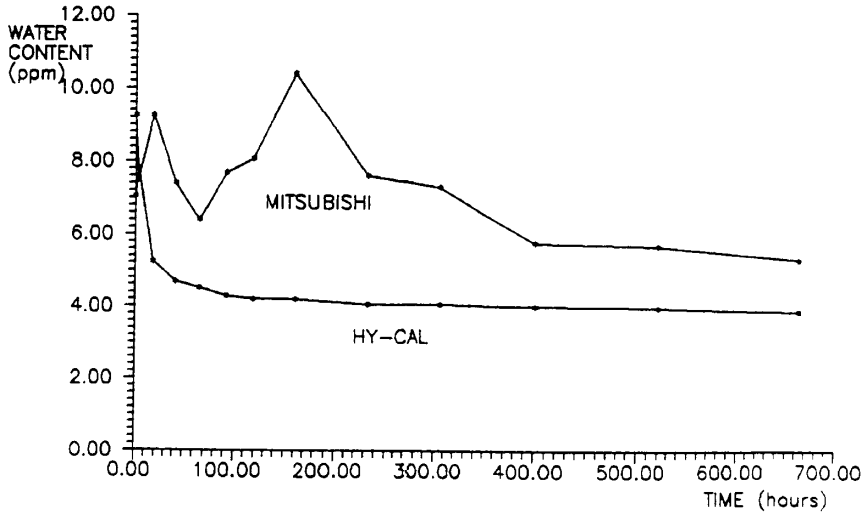

Figure 2-19
Oil moisture measured with respect to time during the second initial equilibrium test using the shell-form model.

surfaces may have been exposed to ambient humidity. While impregnated cellulose will not absorb moisture as readily as in the unimpregnated state, substantial surface moisture contamination may have occurred.

The oil was again removed from the system and a vacuum was applied for 12 hours in an attempt to remove the suspected surface moisture from the cellulose. After refilling, the initial equilibrium process was begun a second time. As illustrated in Figure 2-19, the oil moisture approached 4.0 ppm but failed to achieve the desired equilibrium point. Subsequent measurements of the cellulose demonstrated a non-uniform moisture distribution. A thin "wet-zone" near the surface is believed to have dominated the equilibrium process as discussed in Section 2.6.

2.5.2 Step 1 (Initial Equilibrium)

In order to better replicate the core-form experiment, new pressboard was obtained. The cellulose was sectioned, dried and impregnated using the process outlined in Section 2.3.1 and the oil was dried. Upon final assembly, the oil moisture was determined to be 7.0 ppm with approximately 0.4 percent water in the pressboard. As shown in Figure 2-20, the oil moisture dropped to nearly 2.0 ppm during initial equilibrium. The Norris curves shown in Figure 2-21 predict a final equilibrium point of nearly 1.0 ppm based on the measured water level in the paper with an assumed homogeneous distribution.

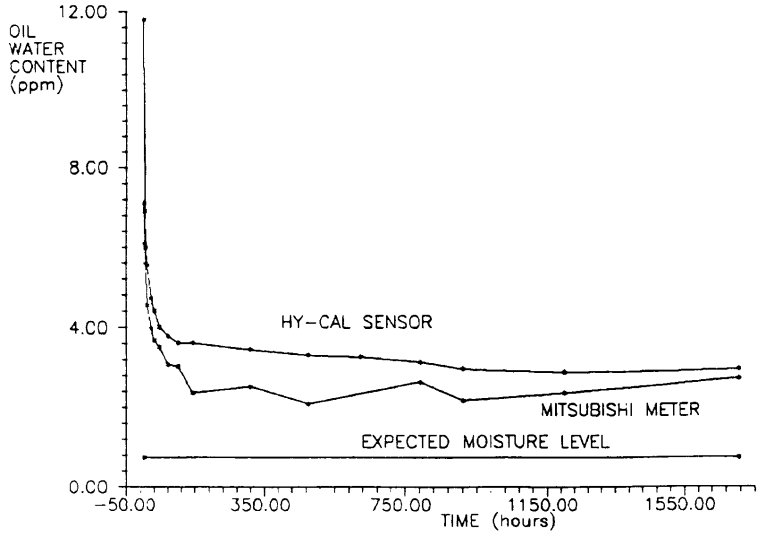

Figure 2-20
Oil moisture measured with respect to time during initial equilibrium (shell-form).

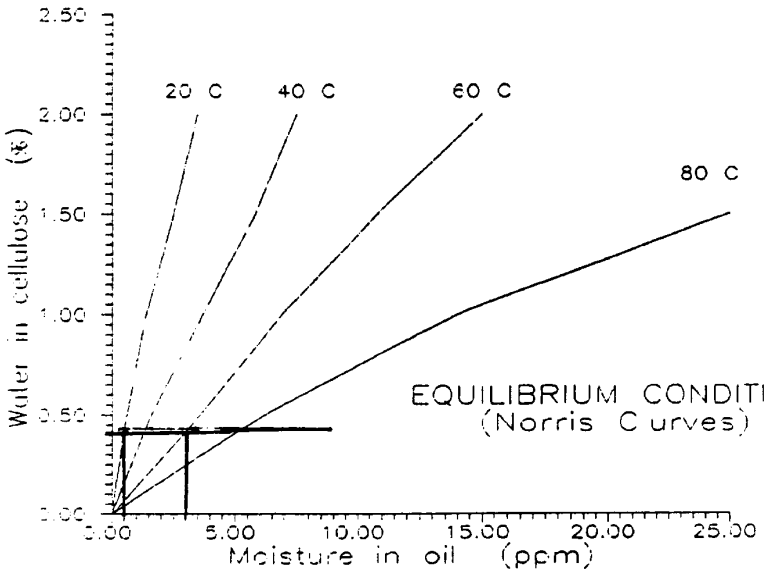

Figure 2-21
Norris curves showing predicted equilibrium points for the shell-form moisture dynamics experiment.

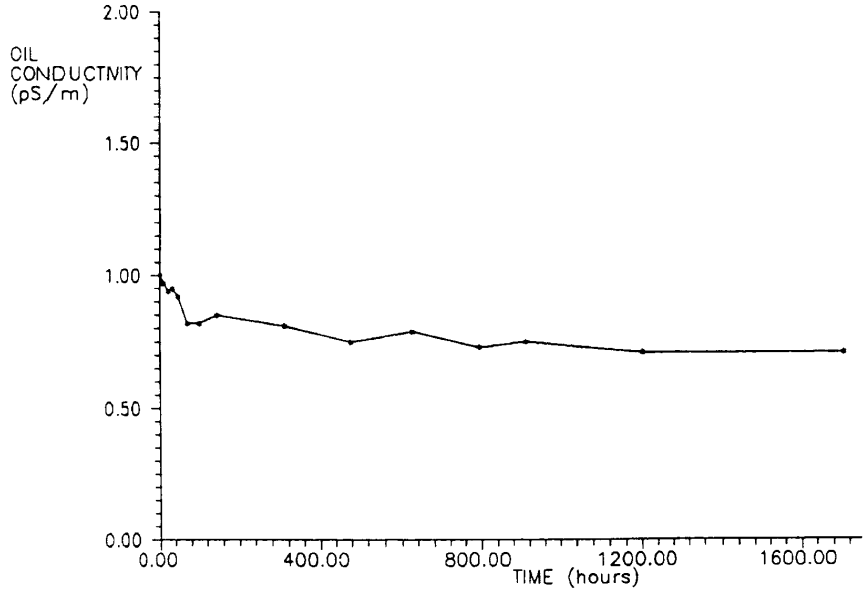

Figure 2-22
Oil conductivity measured with respect to time during initial equilibrium (shell-form).

The new oil initially had a conductivity of 1.0 pS/m. As illustrated in Figure 2-22, the conductivity gradually declined to a value of 0.75 pS/m over a period of 1600 hours. As in the case of the core-form experiments, this behavior is reasonable given the weak relationship between moisture and conductivity in relatively dry oil. The change of nearly 25 percent is consistent with the previous result.

Electrification measurements were taken using both an ACS and TCM as shown in Figure 2-23. The AC voltage was applied across the two pancake windings in the model. While there is an unresolved discrepancy of 3.0 $\mu C/m^3$ under energized conditions, both meters provide similar trends in the charge density. The fluctuations are not considered significant relative to the recognized error margins of $\pm$ 1.0 $\mu C/m^3$. In accordance with the core-form tests, little correlation between moisture and electrification is evident during initial equilibrium. As observed previously, the TCM readings do initially appear to drop in concert with the oil moisture.

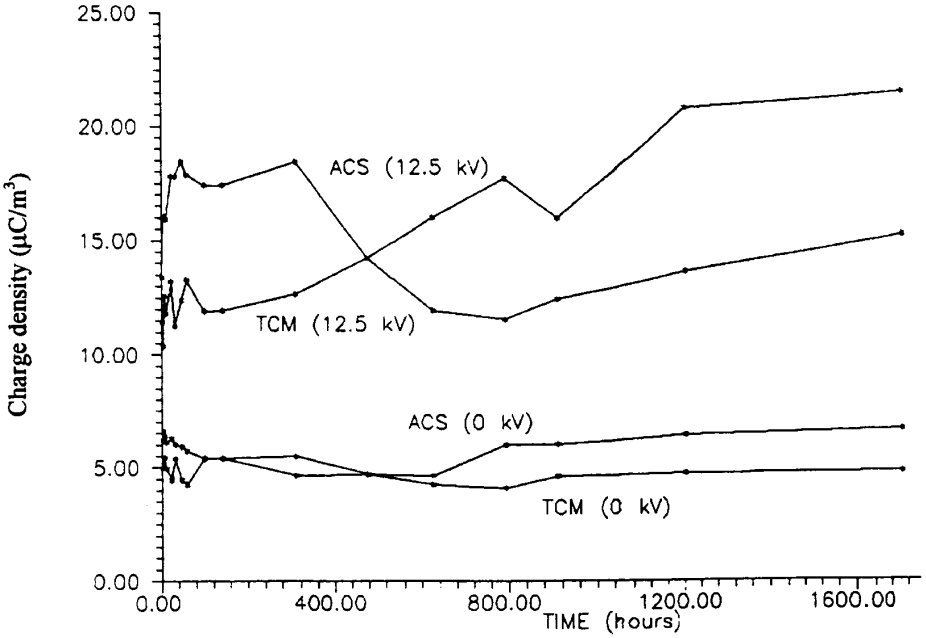

Figure 2-23
Volume charge density generated by flow electrification at 2.27 x $10^{-3}m^3/s$ with respect to time during initial equilibrium (shell-form).

2.5.3 Step 2 (Start Up)

Following initial equilibrium, the oil temperature was raised from 20°C to 60°C as shown in Figure 2-24. With the moisture content in the pressboard remaining at 0.4 percent, an equilibrium point of 3.0 ppm is expected. However, Figure 2-25

demonstrates that the oil moisture ultimately reaches a value of 5.0 ppm based on the Mitsubishi meter. The decline

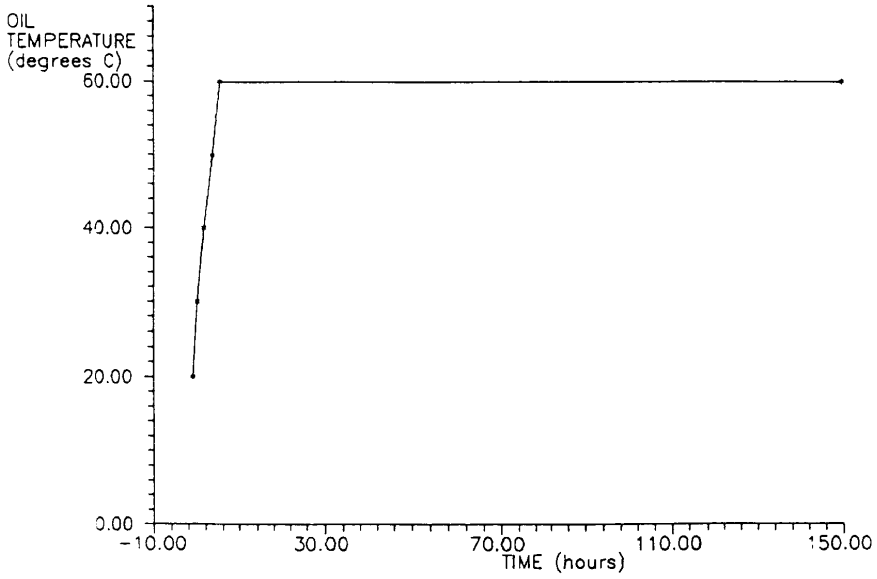

Figure 2-24
Oil temperature measured with respect to time during start up (shell-form).

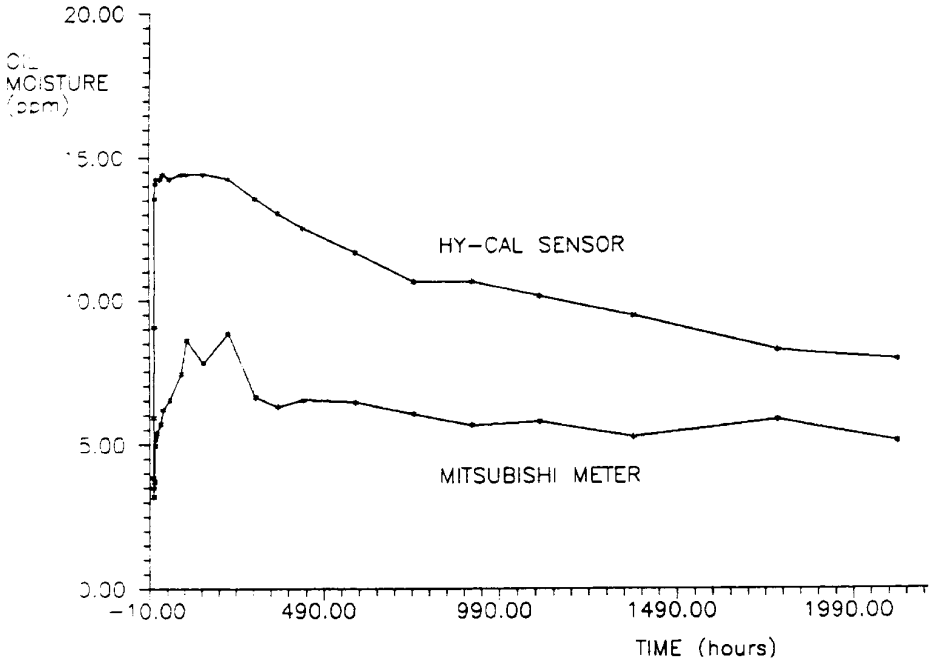

Figure 2-25
Oil moisture measured with respect to time during start up (shell-form).

shown in the HY-CAL™ sensor data is attributed to drift in the sensor calibration. As previously mentioned, the absolute magnitude discrepancy can be partially accounted for by the increased temperature.

The oil conductivity was monitored using the EMCEE DC meter with additional data provided by the TCM. As shown in Figure 2-26, both readings show similar trends, but differ in magnitude. This is explained by recognizing that the instruments sample at different locations in the fluid loop. The oil tested in the EMCEE meter is drawn directly from the relaxation tank using a port in close proximity to the heating element. The cell was pre-heated to the tank temperature to improve accuracy. In contrast, the TCM probe is installed downstream of the tank in a section of copper pipe. Assuming some heat transfer from the oil to the copper piping and aluminum chambers of the TCM, the temperature will be lower than that in the main tank. Recognizing the Arrhenius relationship of eq. 2-3, the temperature difference probably was responsible for the discrepancy. This explanation is supported by the fact that good agreement is obtained between the EMCEE meter and TCM when the entire fluid loop is at room temperature.

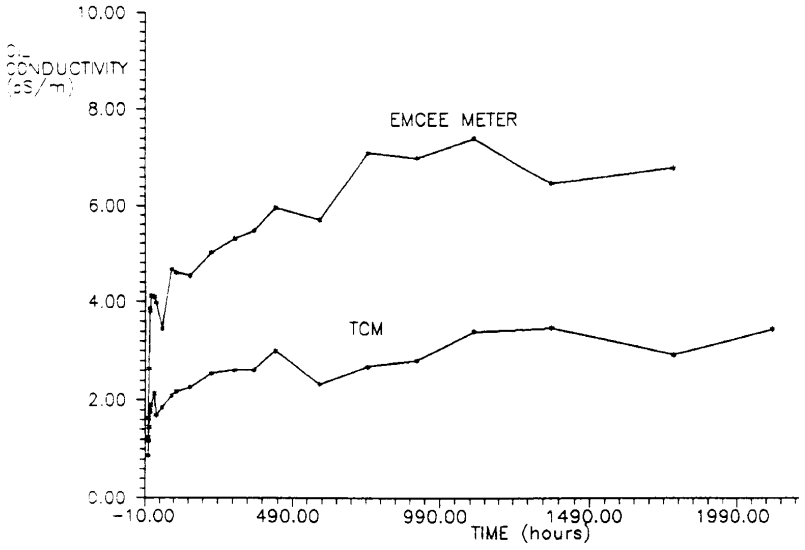

Figure 2-26
Oil conductivity measured with respect to time during start up (shell-form).

The behavior of the oil conductivity may be readily compared to that observed during start up in the core-form experiments. Initially, the conductivity tracks the temperature transient as expected. Once 60°C was achieved, a gradual increase due to oxidation or more likely contamination from the adhesives in the shell-form model is evident. However, the peak value of conductivity is about 7.0 pS/m as opposed to the previous result of 24.0 pS/m. In view of the fact that the impurity content of the new oil could be much different, these results are not unreasonable.

The electrification process was quantified in terms of the measured volume charge density exiting the shell-form structure as illustrated in Figure 2-27. During the temperature transient, the increase in charge density with and without energization indicates the low-conductivity regime. The continued increase with conductivity while the temperature remained at 60°C shows that the additional ions were enhancing charge generation more significantly than relaxation. The apparent decrease in charge density after 1300 hours occurred despite the fact that the conductivity remained stable. This may indicate some change in the oil/cellulose interface chemistry which altered the adsorption and desorption processes that supply the double layer. The difference between the ACS and TCM readings can be partially attributed to the influence of pressure on the ACS bellows. Note that the conductivity increase beyond the Arrhenius predicted level was not severe enough to limit the effect of AC energization as previously observed.

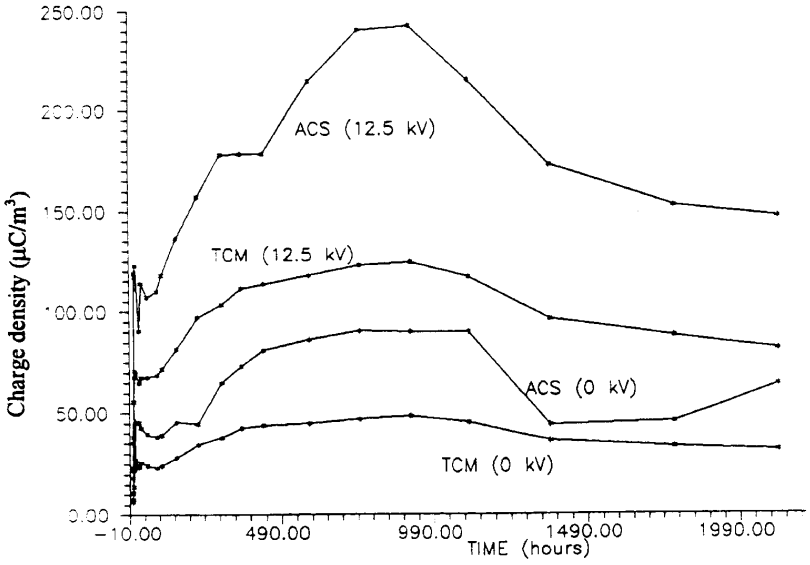

Figure 2-27
Volume charge density generated by flow electrification at 2.27 x 10^{-3} m^3/s with respect to time during start up (shell-form).

2.5.4 Step 3 (Shut Down)

After nearly 2000 hours at 60°C, the system temperature was reduced to 20°C as depicted in Figure 2-28. The HY-CAL™ sensor and Mitsubishi meter readings are seen to agree once the oil was cooled as shown in Figure 2-29. The final equilibrium point for the oil moisture approaches 2.0 ppm once 20°C is attained which corresponds with initial equilibrium. However, a value of approximately 1.0 ppm is predicted by the Norris curves given that the cellulose moisture remained at 0.4 percent.

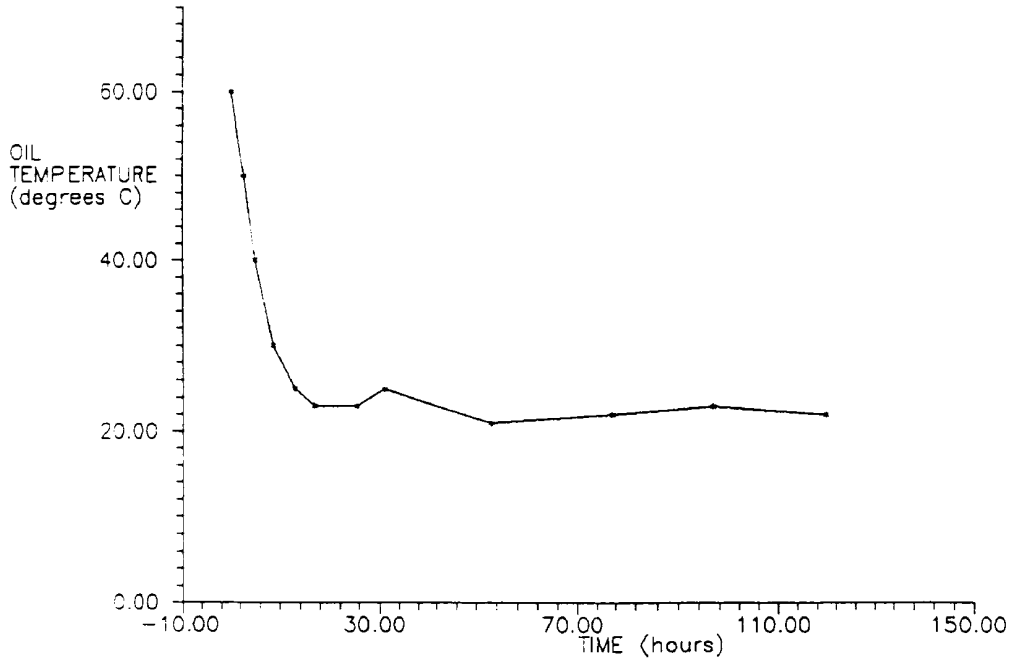

Figure 2-28
Oil temperature measured with respect to time during shut down (shell-form).

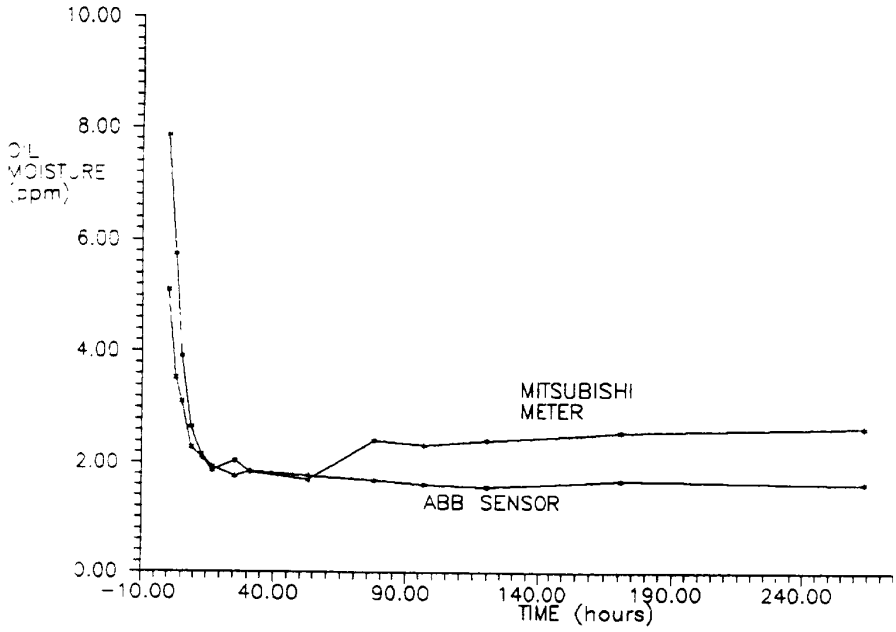

Figure 2-29
Oil moisture measured with respect to time during shut down (shell-form).

The oil conductivity decreased with temperature as expected and returned to approximately 1.0 pS/m. As demonstrated in Figure 2-30, the EMCEE and TCM results follow the same trend and agree fairly well at room temperature. As in the core-form tests, the apparent contamination effect evident at 60°C was not permanent and the original conductivity was restored at room temperature. This supports the hypothesis that the contaminant(s) can only remain in solution at higher temperatures.

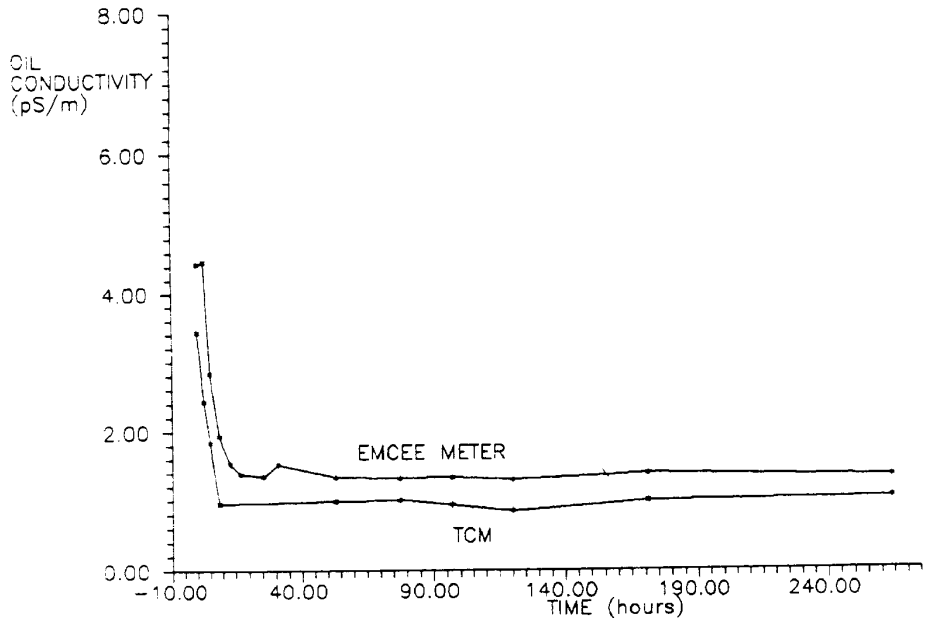

Figure 2-30
Oil conductivity measured with respect to time during shut down (shell-form).

As the oil temperature and hence conductivity are reduced, the amount of charge separated in the shell-form model drops accordingly. Figure 2-31 shows the ACS and TCM measurements over time with and without AC energization of the model. The charge densities ultimately return to their original levels observed during initial equilibrium. While there is still some question as to the true magnitude of the volume charge density in the oil, both instruments provide very similar trend information. The question becomes whether moisture effects on electrification can be decoupled from the influence of temperature and conductivity changes. As discussed in Section 2.6, surface moisture in the wet-zone may interact with the Debye layer to influence the supply of ions.

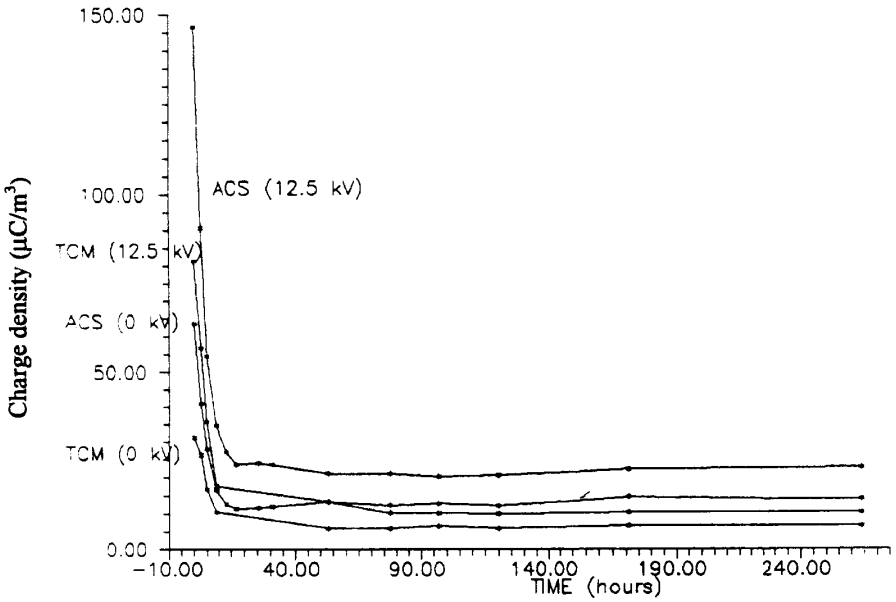

Figure 2-31
Volume charge density generated by flow electrification at 2.27 x 10^{-3} m^3/s with respect to time during shut down (shell-form).

2.5.5 Summary

The moisture dynamics experiments were repeated using a shell-form model in conjunction with new cellulose and oil. As in the core-form tests, the oil moisture followed the expected trends when the temperature was changed, but did not match the equilibrium values predicted by the Norris curves. As in the core-form experiments, the oil conductivity exceeded predicted values during the high temperature step. In this case, the effect was much less pronounced and did not have as severe an impact on generated charge densities. There was some correlation between charge and moisture in dry oil (less than 5.0 ppm moisture), but no moisture effect was obvious during temperature cycling.

2.6 Discussion of Moisture Equilibrium

In view of the results obtained during the core- and shell-form experiments, additional discussion of moisture dynamics is warranted. This section considers the discrepancies in the oil and cellulose water levels indicated by the Norris curves. Classification of water in the cellulose and the existence of non-uniform moisture distributions are addressed. The relationship between charge density and moisture is also considered here.

The moisture contained in pressboard will be present in various states. In general, primary bound, secondary bound, free, and bulk water are recognized (86, 87). The primary bound water is essentially part of the cellulose structure. Secondary bound water will be hydrogen-bonded to the OH groups present at the surface of cellulose fibers (75). The free and bulk water are absorbed by the cellulose and are not chemically bound. The former exists in multilayers on the fiber surfaces while the latter will occupy the pores in the pressboard structure.

In order to understand the meaning of equilibrium in an oil/cellulose system, the state of water in the latter component which governs the process must be identified. When unimpregnated pressboard is dried, the free and bulk water are easily removed. However, secondary bonding between the water and cellulose will ensure a residual level of moisture (75). Gervais et al (88) have demonstrated that only primary and secondary bound water will be present in impregnated cellulose (which has not been aged) containing less than 1.0 percent moisture. However, free water might be supplied by the oil or be released from the cellulose when the temperature is raised. The primary bound water is assumed to be divorced from the equilibrium process.

The type of moisture detected in a cellulose sample will be determined by the temperature setting of the Mitsubishi VA-06 vaporizer unit. A temperature of 150°C was used to extract the majority of free and secondary bound moisture from the sacrificial pressboard samples analyzed. Excessive temperatures must be avoided to prevent degradation of the cellulose which will release the primary bound water. Other researchers (89) have determined that the optimal vaporizer temperature range is between 100°C and 200°C. Hence the selected temperature of 150°C is expected to provide an accurate measure of the moisture in pressboard samples.

Assuming that the measurement techniques for oil and pressboard moisture are valid, the Norris curves are somewhat suspect. However, similar equilibrium curves generated by Oommen (90) do not support this assertion. Rather, the possibility of a non-uniform moisture distribution in the pressboard is suggested. This hypothesis is strengthened by considering the moisture diffusion equation given by Howe (91) for free water as

$$\frac{\partial C_M}{\partial t} = D_p \nabla^2 C_M \qquad \text{(eq. 2-4)}$$

where

C_M = moisture concentration

D_p = diffusion coefficient for water in pressboard [m^2/s].

At room temperature, D_p has been estimated (92) to be on the order of 1.34×10^{-13} m^2/s. The corresponding diffusion time constant for the 0.32 cm thick pressboard used in these experiments will be approximately 3239 hours. This is probably optimistic for bound water where the diffusion coefficients may be concentration dependent (93). In view of this time scale, a non-uniform moisture distribution in the bulk pressboard becomes feasible. At higher temperatures, correspondingly larger diffusion coefficients will reduce the time required for equilibrium.

Crude sectioning of pressboard samples using a razor blade did indicate a non-uniform moisture distribution. As illustrated in Figure 2-32, a thin surface layer may contain considerably more moisture than the bulk of the sample. The actual surface moisture is expected to be much higher than indicated, but limitations on sectioning forced an effective average over a larger thickness. If the total specimen were vaporized, only the bulk moisture content by weight would be apparent. However, the wetter surface layer will be in contact with the oil and thus dominate the equilibrium process. The existence of such a "wet-zone" on the surface of impregnated cellulose has been postulated by other researchers (92). Additional measurements of the cellulose used in the moisture experiments have shown that the surface may be up to an order of magnitude wetter than the bulk. In one case, a surface moisture of 9.0 percent was measured in a sample having a bulk moisture content of 0.4 percent.

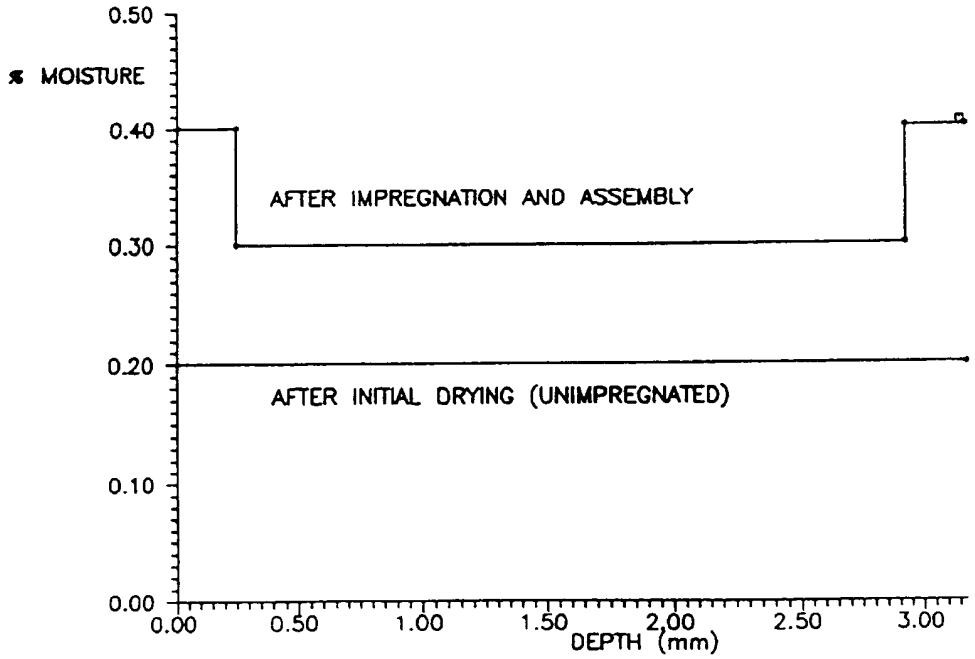

Figure 2-32
Moisture distribution in an oil impregnated pressboard sample.

Recognizing the fundamental limitations of the present techniques for moisture profiling in cellulose, a rigorous quantitative analysis of these experiments cannot be justified. However, some general qualitative conclusions can be readily drawn. Accepting theoretical and empirical evidence supporting the existence of a wet-zone at the cellulose surface, the traditional interpretation of the Norris curves can be challenged. A general explanation for the experimental results may thus be developed.

Both the core-form and shell-form experiments consistently demonstrated oil moisture levels in excess of those values predicted by bulk cellulose measurements. One possible reason for this might have been the release of moisture from the transformer models. However, the exposed pressboard surface of the models was significantly less than that presented by the bulk pressboard in the relaxation tank. Hence, the latter is assumed to have dominated the process of moisture equilibrium. The presence of a wetter cellulose surface layer which governs the equilibrium process would thus seem a more likely explanation.

A brief exposure of the bulk cellulose to ambient humidity was inevitable during the assembly of these experiments. This exposure could well have resulted in the establishment of a wet layer on the surfaces of the impregnated pressboard sheets. Now consider a "layer of influence" in the cellulose which governs the initial time constant for moisture equilibrium. In other words, this layer would rapidly absorb moisture from the oil over the first 100 hours of initial equilibrium (step 1). Once this layer had equilibrated with the oil, moisture transfer is then controlled by bulk diffusion within the cellulose which is much slower. If the influence layer and bulk cellulose were initially at the same moisture level, then the ideal Norris curve predictions would hold true. However, in the present case, ambient moisture added to the surface layer during assembly may have increased the water content in the influence layer. Hence, the oil moisture asymptotes observed during step 1 of the experiments were always in excess of the levels predicted by the bulk cellulose measurements.

This same reasoning may be readily applied to the situation of increased temperature (start up). In this case, the influence layer is releasing moisture into the oil and the time constant is closer to 50 hours presumably due to temperature enhanced diffusion coefficients. After this point, the continued moisture transfer is much slower with bulk diffusion dominating the process. In the experiment, the oil moisture at 60°C was consistently in excess of the values predicted by bulk cellulose samples. This is understandable in terms of the original surface moisture contamination previously suggested. The influence layer is assumed to have been wetter than the bulk before the temperature was raised. Note also that the influence layer is probably thicker at high temperature due to the expected Arrhenius dependence of the moisture diffusion coefficients upon temperature.

During the final phase of the experiments (shut down), the oil released moisture back into the pressboard. As per initial equilibrium, the influence layer is expected to absorb moisture during the first 100 hours until bulk diffusion begins to limit the process. It is interesting to note that the final step oil moisture levels are in excess of the step 1 values, particularly for the core-form case. If the 60°C influence layer were thicker than the 20°C influence layer this result might make sense. In other words, more moisture is released at high temperature than can readily be re-absorbed within the low-temperature time constant. This hypothesis is quite relevant for a real transformer which has not been properly dried. The water released into the oil after loading (and hence heating the unit) could pose a very real threat for reduced temperature conditions. If the cellulose was not able to re-absorb sufficient moisture during a temperature drop, free water could precipitate from the oil with potentially disastrous consequences. Free water or sufficient water in solution can both dramatically reduce the breakdown strength of insulating oils (25, 94).

Having provided a possible explanation for the moisture dynamics results, further comment is needed regarding the moisture relationship with streaming electrification. The present results do not indicate that moisture transients provide a dramatic enhancement to the charging process. However, there is some evidence that there are two moisture regimes which influence the process differently. The high moisture (above 10 ppm) in oil has been well demonstrated to reduce the charging tendency (31). However, the lower moisture levels examined in these experiments hint at the opposite effect. Below approximately 5.0 ppm, charging would appear to decrease with decreasing moisture content during equilibrium with the cellulose. Two different scenarios are proposed to explain this behavior.

The first concept involves the surface wet-zone (i.e. influence layer) and the supply region concept described in Section 4. The double layer is assumed to be distributed over the interface where cellulose fibers and molecular chains extend into the oil. Assuming this region also covers part of the surface wet-zone, cellulose moisture could influence the properties of the supply region. As the oil is dried, the supply region/influence layer takes on water. If the supply region effective moisture content exceeds 10 ppm, then the amount of charge in the Debye layer might be reduced by the same mechanism observed in bulk oil for the high moisture regime. If the moisture concentration at the interface became sufficiently large, local free water could also act to increase the apparent local conductivity and hence reduce the Debye length. Note that the water dipoles in the supply region are assumed to be randomly oriented such that there is no local permittivity enhancement acting to increase the double layer thickness.

The second possibility for explaining the lower moisture regime again relates to the cellulose water content. Recognizing that the cellulose conductivity increases with moisture, the corresponding leakage resistance will decrease. As the oil dries and the cellulose takes on moisture, the leakage resistance could decrease to the point that adsorbed ions would have a higher probability of discharging before attracting counter

charges to the interface. This would depend on the degree of local dissociation and availability of nearby positive ions to neutralize the adsorbed species. Obviously, this theory would be best realized on the thin paper covering the winding conductors which represent the DC ground plane.

While moisture dynamics per se do not appear to provide a substantial catalyst for streaming electrification failures, insulation moisture remains an important parameter. It is interesting to note that some of the first electrification failures occurred after the implementation of improved transformer drying techniques (i.e. vapor phase drying). However, this may simply be due to the increased leakage resistances expected in drier cellulose insulation. As discussed in later chapters, this effect is very critical in governing the static potentials achieved in a forced-oil-cooled power transformer subject to streaming electrification.

3

INFLUENCE OF STATIC ELECTRIFICATION UPON THE DIELECTRIC INTEGRITY OF TRANSFORMER INSULATION

3.1 Introduction

While understanding the process of streaming electrification is clearly vital, a practical investigation must also consider the consequences of charge separation in an insulating system. In the transformer context, the obvious concern becomes the mechanism(s) by which static charges compromise dielectric strength. This section documents experiments performed to quantify the influence of streaming electrification upon partial discharge behavior and impulse breakdown in a transformer environment. The results of cumulative charging tests are also presented.

3.2 Impact of Streaming Electrification upon Partial Discharge Behavior in a Shell-Form Geometry

3.2.1 Introduction

Partial discharging in an insulating system is a most undesirable occurrence. These localized breakdowns will damage the insulation and may ultimately initiate dielectric failure (75, 94). Also, partial discharges will create gas bubbles in a liquid insulant (95) which may have a substantially lower dielectric strength. In a forced-oil-cooled transformer, these bubbles may accumulate to form large gas pockets in the oil where a breakdown can occur (23). Recognizing these potential hazards, minimal partial discharge levels are critical for good transformer designs.

The partial discharge phenomenon is effectively described in terms of a local capacitance which discharges when a given voltage threshold is exceeded. Discharging can occur under both AC and DC conditions with the former generally causing more damage to the insulation (95). In a transformer where electrification is present, both scenarios are possible. The 60 Hz energizing voltage will cause discharging during the

parts of the AC cycle when the inception threshold is surpassed. In contrast, the static potentials generated by streaming electrification will take much longer to reach the discharge inception voltage because they are dependent upon the RC time constant of the structure. Other investigators have reported large intermittent discharges in actual transformers which were attributed to static charge buildup (21, 22, 24, 28). When the static and power frequency voltages are superimposed, the partial discharge inception voltage may be more readily exceeded.

3.2.2 Experimental Apparatus

3.2.2.1 Partial Discharge Detection Equipment.

Partial discharge experiments were undertaken using a shell-form model with a 90° blocking pattern as the test specimen. Measurements were made using an ERA model 3 detector described by Kreuger (96) in a straight detection configuration (94, 95). As shown in Figure 3-1, the shell-form structure is represented by the terminal capacitance C_s. The series combination of a blocking capacitor C_B and detection impedance Z is connected in parallel with the specimen. Discharges originating in the model will circulate through this branch along with calibration pulses coupled through C_q. The calibration pulse height is adjusted to fit the observed partial discharges, providing a measure of their apparent magnitude. Note that Z and C_q are selected based on the capacitance C_s. The values of the elements in the circuit of Figure 3-1 are given in Table 3-1.

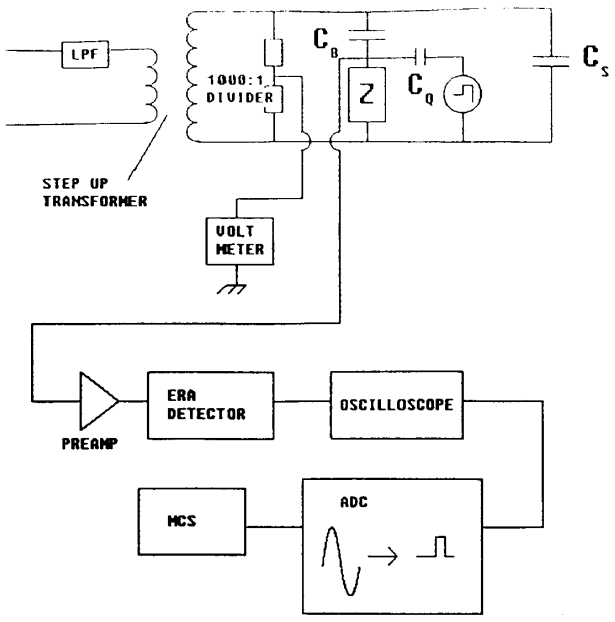

Figure 3-1
Partial discharge detection scheme.

The output signal is taken from the detection impedance, amplified and sent to the ERA detector for display on an elliptical time base. In addition, the amplified signal is fed through an analog-to-digital converter which transforms the bipolar discharge pulses into logic pulses. These logic signals are coupled to a multichannel scaler such that partial discharge repetition rates can be determined. The base rate count resulting from the calibration pulses is subtracted from the total count to obtain the true repetition rate over the dwell time selected.

Table 3-1
Values of the elements in the partial discharge detection circuit.

Element	Value/Description
C_s	280.0 pF
C_B	4.0 nF
C_q	50.0 pF
Z	ERA type 3

3.2.2.2 Modifications to Shell-Form Model.

Lee and Nelson have previously made partial discharges in a shell-form model subject to electrification (26). However, AC effects were found to dominate over static behavior at relatively low voltages. This was attributed to the presence of sharp edges on the ends of the winding conductors which enhanced the local electric fields. In order to rectify this difficulty, discharge shields were installed on the winding ends of the model.

The discharge guards were made from aluminum cylinders that were milled flat on one side. As shown in Figure 3-2, the guards are attached to the winding faces using copper pins. A conducting (copper-filled) epoxy was applied to ensure that all of the conductors in a given winding were electrically connected. The epoxy also provided additional mechanical support to hold the shields in place. Recognizing that the electric field will be inversely proportional to the radius of curvature, the curved faces provided by the discharge guards are clearly superior to the original geometry.

Additional modifications were made in the external connections for the winding conductors. The original leads were made of thin wire which could easily discharge as a result of enhanced local electric fields. These leads were replaced with copper tubing having a much larger radius of curvature. A new Spauldite™ container was machined to accommodate the modified shell-form model and facilitate installation in the fluid

loop. The new container was assembled using dove-tail joints to prevent the failure under pressure suffered by the previous casing.

3.2.3 Methodology

A variety of tests were performed to determine the effects of streaming electrification upon partial discharge behavior in the modified shell-form model. The AC inception voltage was measured as a function of temperature and flow rate. In addition, the impact of accumulated surface charge upon the AC inception voltage was examined. Partial discharge

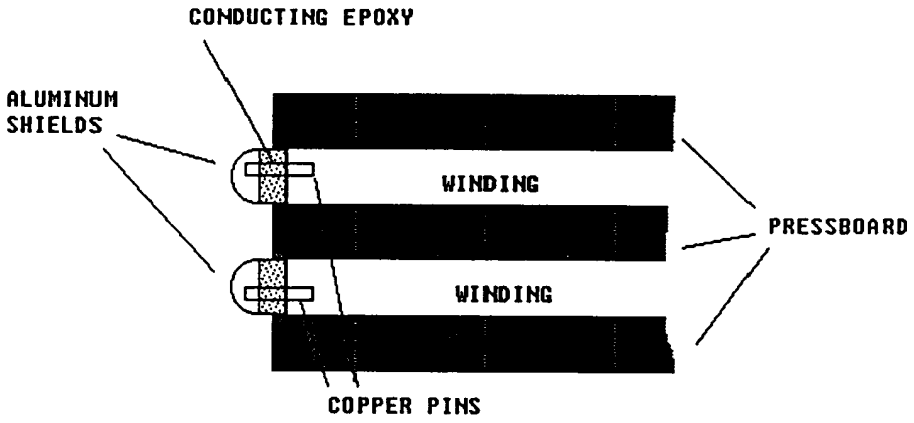

Figure 3-2
Application of discharge shields to the shell-form model windings.

magnitudes and repetition rates were observed at high temperature (60°C) where large amounts of charge were produced by flow electrification. Long sampling times of up to 10 minutes were used for measuring static discharging to ensure proper averaging. Note that these experiments were performed during the start up segment of the shell-form moisture dynamics experiments. Acoustic measurements were also attempted as documented in Appendix B.

3.2.4 Results

Other investigators have determined that breakdown voltage can be directly correlated with the flow velocity of a liquid dielectric (32). With this in mind, preliminary experiments were performed to examine the effect of oil flow rate upon the AC discharge inception voltage. The results at 20°C and 60°C are shown in Figure 3-3. Based on this data, the inception voltage for the shell-form model does not appear to be

sensitive to oil velocity. These measurements were taken over a very short time period such that the streaming potentials in the model did not develop significantly.

In order to determine the regions of static and AC-dominated discharge behavior, the test voltage was varied from zero to 15.0 kV (rms). When AC activity was minimal, observations were taken over a ten minute period to provide a good average static discharge magnitude. As illustrated in Figure 3-4, the static and AC regimes are clearly evident over a range of flow rates. These results are similar to those of Lee and Nelson (26) which are presented in Figure 3-5. However, the addition of the discharge shields has shifted the cutoff threshold for the AC-dominated regime from 6.0 kV to 9.0 kV. Discharges were observed during the positive and negative half-cycles of the 60 Hz voltage.

As expected, the recorded partial discharge repetition rates also illustrate the static and AC regimes. Figure 3-6 depicts repetition rates as a function of applied voltage for various flow rates. Under static conditions, the discharge frequency is on the order of 10^{-2} Hz.

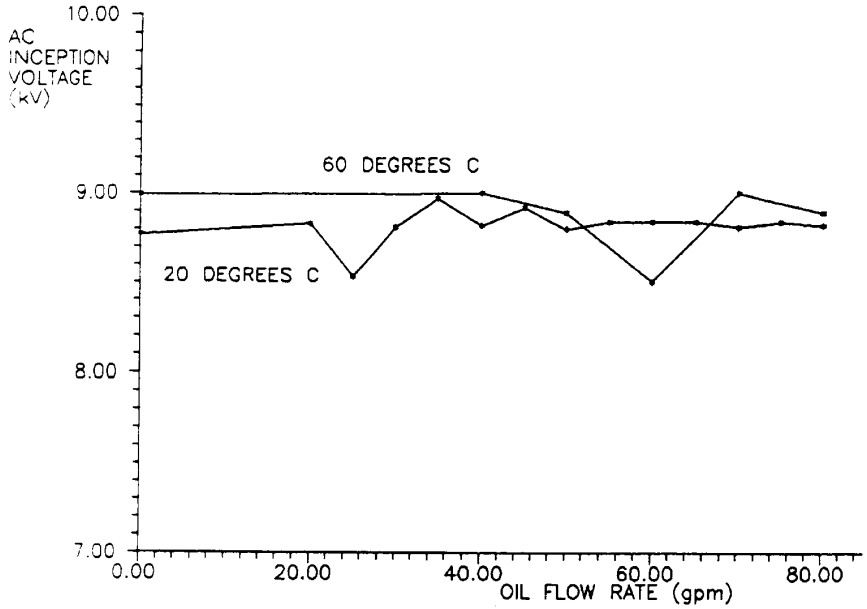

Figure 3-3
AC partial discharge inception voltage as a function of oil flow rate.

In contrast, up to 10^3 discharges per second are evident when AC behavior dominates. This is explained by the longer times required to charge the model surfaces by electrification. In the AC regime, charge is supplied by the source through capacitive

divider action and partial discharges become more frequent as the test voltage exceeds the inception threshold for longer portions of the 60 Hz cycle (95).

A final test was performed to demonstrate the effect of accumulated static charge upon the AC inception voltage. Two scenarios were investigated over a range of oil temperatures. For the first experiment, the inception threshold was measured with no oil flow. The oil was then circulated for 30 minutes at 5.05×10^{-3} m^3/s to separate static charge in the shell-form model. After turning off the pump, the new AC inception voltage subject to static charging was measured. The second experiment was undertaken in the same manner except that the measurements before and after charging were taken with the oil flowing at 5.05×10^{-3} m^3/s. The results of these experiments are presented with respect to temperature in Figure 3-7.

Regardless of whether the oil was flowing through the model during the measurement, the AC inception voltage is shown to be reduced by the presence of accumulated static charge. Typically, the original inception voltage was restored over time as the model surfaces discharged. This occurred through small discharges over roughly 30 minutes or more quickly via larger bursts of partial discharges. For all cases, the AC inception voltages are shown to be reduced as the oil temperature is raised.

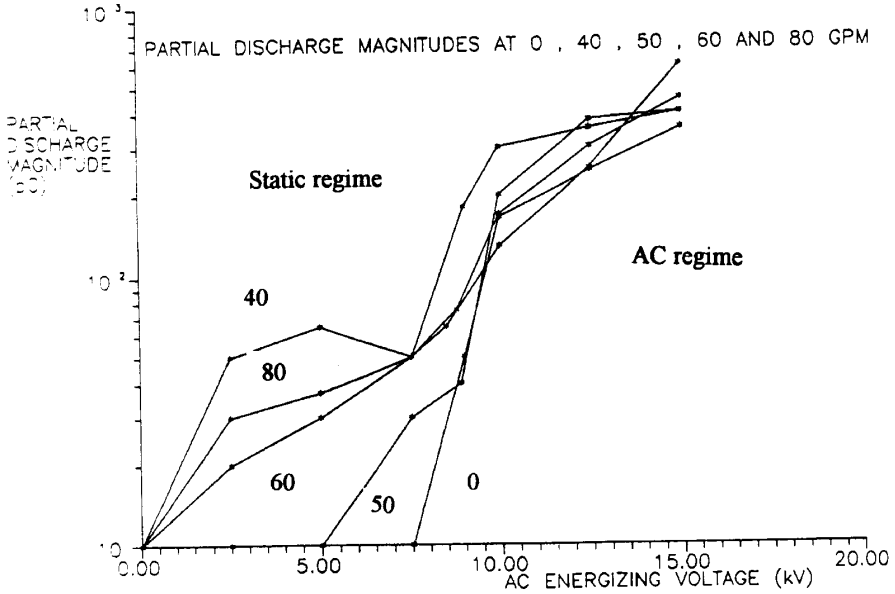

Figure 3-4
Average partial discharge magnitudes in the shell-form model with respect to applied AC voltage.

3.2.5 Summary

Partial discharging in the shell-form model was investigated subject to streaming electrification. While a regime of static discharge behavior is apparent, the frequency and magnitude of AC discharges are much more significant. Upon inspection of the model, no visible damage was evident as a result of either type of partial discharge. However, the buildup of static charge in the model was found to reduce the AC inception voltage. Recognizing the statistical nature of the partial discharge phenomenon and the complex structure of the shell-form model, no analysis beyond the qualitative discussion presented can be justified for these experiments.

A basis for appreciation of the results is provided by considering the industry standards for partial discharge in a large power transformer. Unfortunately, the American specification dictated by the IEEE (97) is expressed in terms of a radio interference voltage (RIV) measurement technique. The detection bandwidth is quite narrow and a direct correlation

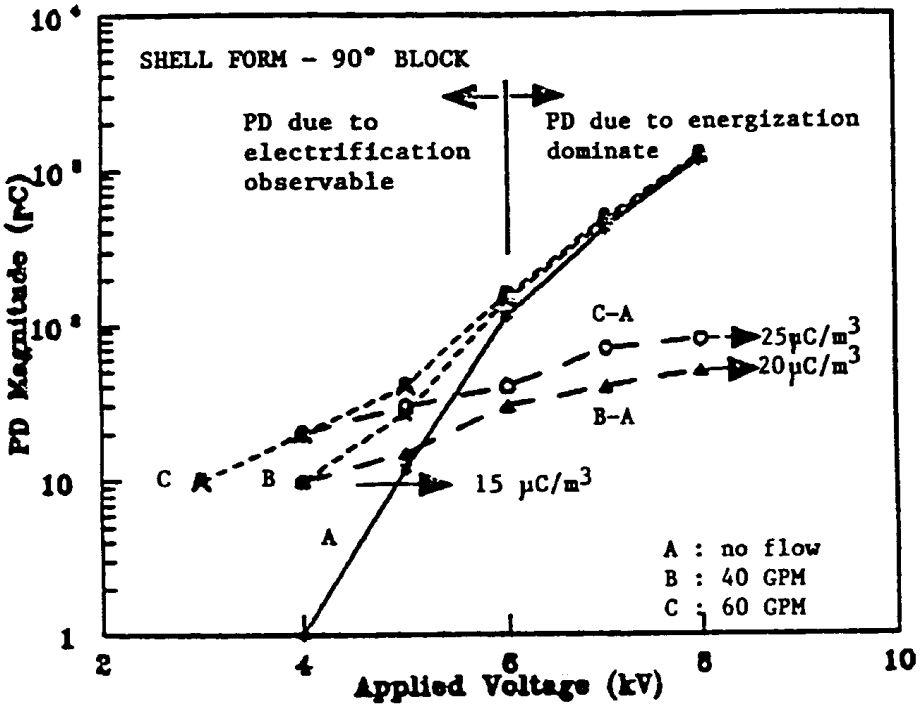

Figure 3-5
Partial discharge magnitudes in the shell-form model observed by Lee and Nelson (26).

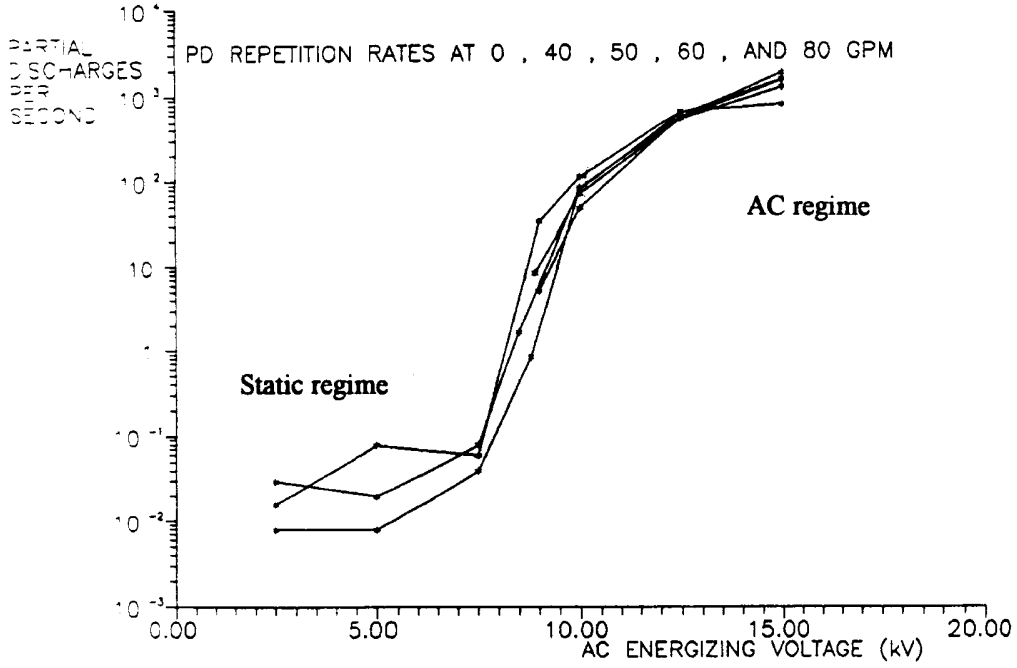

Figure 3-6
Partial discharge repetition rates measured in the shell-form model with respect to applied voltage.

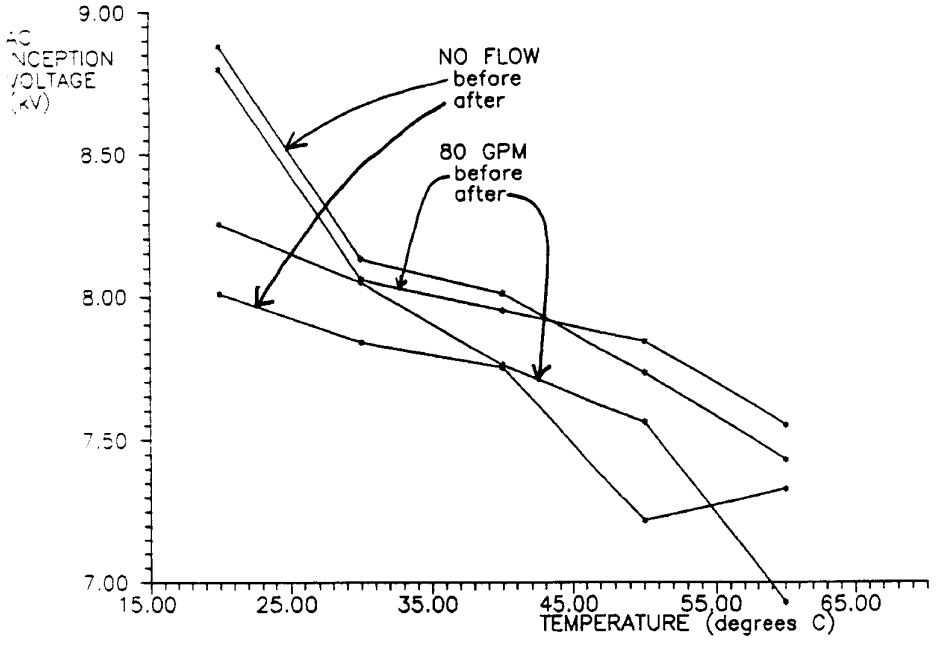

Figure 3-7
AC inception voltage dependence on temperature and static charge in the shell-form model.

between μV and pC is not obvious. However, the corresponding European specification given by the IEC (98) dictates a maximum value of 300 pC during overpotential testing. The partial discharge magnitudes observed in these experiments as a result of streaming electrification did not exceed 100 pC and therefore would not be considered a threat to transformer integrity during factory tests.

One should not dismiss the static discharge effect when considering scale differences between the model and an actual shell-form transformer. The sheer size of the insulation in a power transformer will provide much longer leakage paths to ground for static charge. In particular, the full-length pressboard washers which separate the high and low voltage coils are very well insulated from ground. Significant discharge damage has been observed on the ends of these washers in the lower plenum region of some transformers which allegedly failed due to streaming (23). The total flow rates in such transformers is typically on the order of 4000 gpm as opposed to 80 gpm in the RPI fluid loop. Hence, while the oil velocity may be realistic, the effective volume is not. This issue is further discussed in Section 6 which provides an analysis of a full-scale structure.

Another important issue is the direction of the applied electric field during AC energization. On the full-length pressboard washers previously discussed, there will be a tangential E-field component. The discharge damage is observed to propagate from the edges of the washers as the effective electrode is extended by carbonization of the insulation (99). This propagation generally follows the direction of the tangential stress leading away from the leading edge of the washer in the lower plenum region (see Figure 1-7). The lack of a tangential electric field and a large charge accumulation surface like the high-low washer obviously limits the ability of the laboratory model to mimic the effects seen in the actual transformer case.

The present experiment has provided further demonstration of the effects documented by Lee and Nelson (26). Discharges caused by static buildup clearly demonstrate different behavior from their AC dominated counterparts with much slower repetition rates and lower magnitudes. The former effect is attributed to the time constant(s) associated with flow electrification charging of the model surfaces. The latter result indicates that the damage observed in actual transformers may not be the result of single, high-energy fast events, but rather a gradual degradation of the insulation due to small local discharges. A simple order of magnitude scaling of the model results by a factor of 50 (accounting for flow volume differences) would indicate that discharges in excess of the acceptance threshold (300 pC) are quite plausible in a real transformer.

3.3 The Role of Static Charge in Determining the Breakdown Strength of a Pressboard Surface

3.3.1 Introduction

As a result of static electrification within transformer structures, insulating surfaces are expected to become charged. Regardless of whether such charge is deposited by the relaxation process or left behind as a result of charge separation (generation), an electric field will be present. When this DC field component is superimposed upon operating stresses, tangential electric field strengths may exceed design margins and initiate creep failures. Previous studies by Lee and Nelson (25) found that the impulse breakdown voltages for pressboard surfaces under oil were reduced by up to 10 percent by the presence of static charge. The fluid loop depicted in Figure 2-2 was used to continue these studies on a larger scale.

3.3.2 Experimental Apparatus

3.3.2.1 Test Cell.

A special test cell was manufactured to facilitate these experiments. As illustrated in Figure 3-8, the cell consists of a Teflon™ pipe housing brass electrodes which flank rings of pressboard. The impulse voltage is provided to the central continuous ring through an external bushing. A section of cellulose is stressed by grounding the appropriate discrete outer electrode and applying the desired impulse to the center electrode. Five grounding electrodes are provided for each of two pressboard test rings such that a total of 10 breakdowns may be performed without refitting the cell.

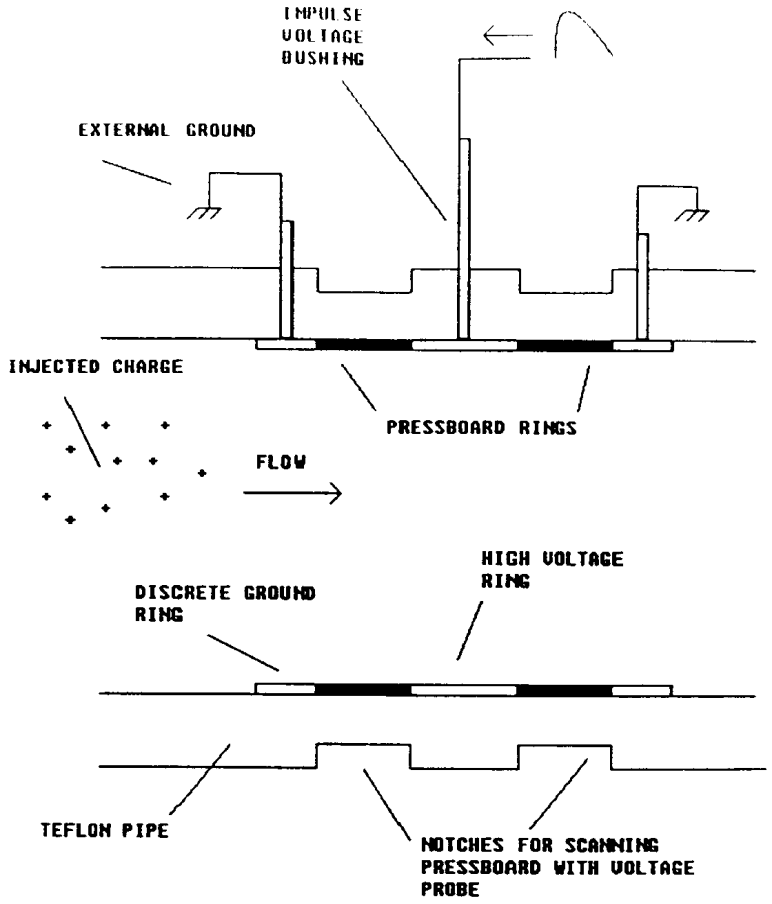

Figure 3-8
Diagram of the impulse breakdown cell.

Slots were milled into the Teflon™ pipe opposite the pressboard rings to allow external potential measurements using a Monroe 1015B non-contacting probe. Recognizing that the probe effectively detects the image charges on the outside of the pipe, the corresponding surface charge density on the inner pressboard ring may be estimated based on a suitable capacitance. A measure of the volume charge density flowing through the cell was provided by a TCM installed immediately downstream.

3.3.2.2 Charge Injector.

A DC charge injector was provided to ionize the flowing oil upstream of the breakdown cell. The injector was designed by Lee (26) and is illustrated in Figure 3-9. This device consists of an array of energized razor blades embedded in Spauldite™ pipe in an annular configuration with respect to a grounded pipe. Positive or negative voltages up to 20 kV are used to energize the blades. The injector charging characteristics are illustrated in Figure 3-10 and demonstrate that negative injection is much more efficient.

This may result because electrons are more easily injected by the divergent fields to rapidly form ions in the oil by attachment. In theory, thermionic injection of electrons (94) provides a basic explanation of the charge injector. While this statement is readily made, the actual process may be much more complicated.

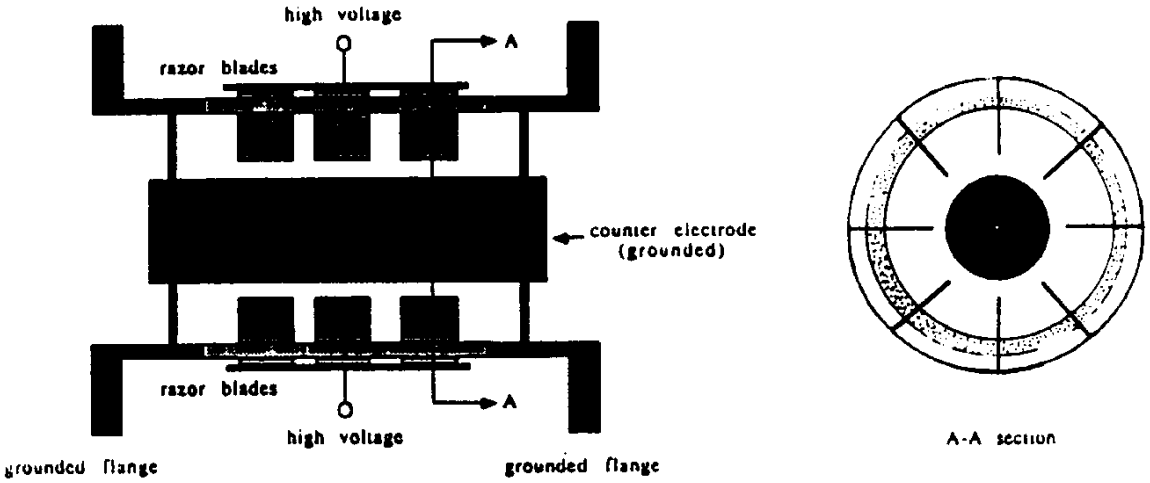

Figure 3-9
DC charge injector used to ionize flowing oil.

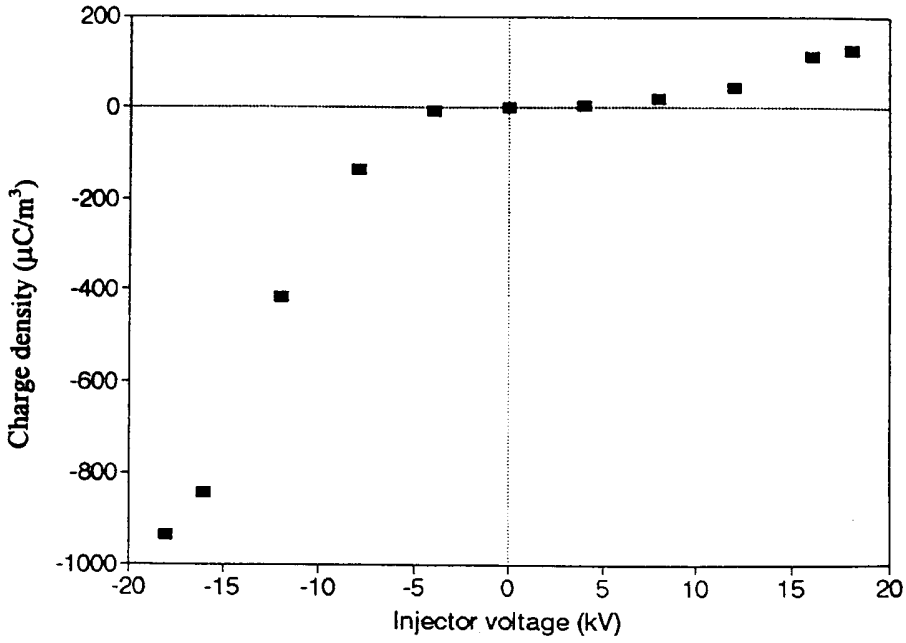

Figure 3-10
Charge injector characteristics based on downstream TCM measurements.

In practice, the processes involved with a point-cylinder (i.e. point plane) geometry are not trivial. A similar geometry has been studied by other investigators (100) who recognized electron/hole emission, ion injection, field-enhanced dissociation and electrohydrodynamic motion. These researchers primarily considered electric fields in a stationary hydrocarbon liquid which were believed to be insufficient for electron conduction from the knife edge. Their results are explained in terms of ionic transport and do not show the same degree of polarity dependence as the present experiment.

A more fundamental treatment by Lewis (101) contrasts cathode and anode processes for electrodes in hydrocarbons. He indicates that thermionic emission requires the formation of a double layer at the electrode/fluid interface to lower the potential barrier. In this case, the availability of counter charges (probably ions) in the fluid will determine the efficiency of the injection process. In the present case, more readily available positive ions in the oil may have provided for enhanced electron transfer under negative point conditions. Such electrons would readily attach to any electronegative species in the oil to form negative ions.

3.3.2.3 Impulse Generator.

A standard double-exponential voltage impulse (102) was used for these experiments. The impulses were supplied by the Goodlet type generator (103) shown in Figure 3-11. A step-up transformer and rectifier provide the DC voltage for charging the capacitor bank in parallel. Once the desired voltage is achieved, a solenoid is activated to trigger the air gaps and effectively sum the capacitor voltages and currents to create the impulse.

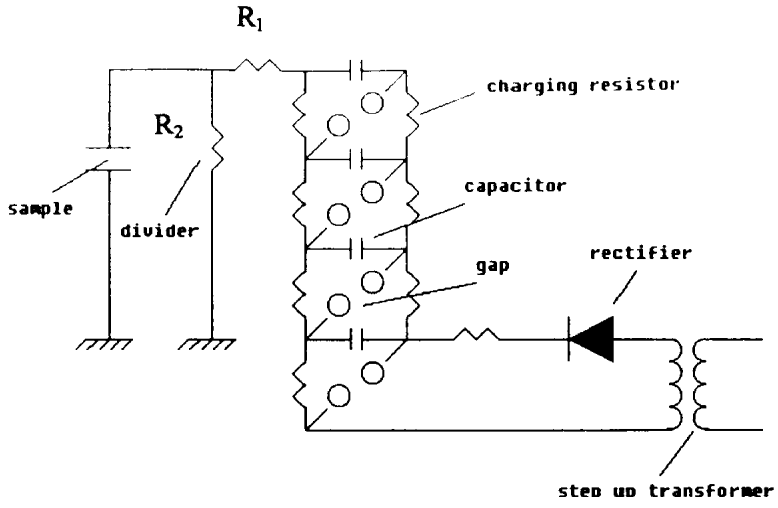

Figure 3-11
Impulse generator used for dielectric integrity studies.

The impulse waveshape is determined by the equivalent circuit shown in Figure 3-12. The capacitances C_1 and C_2 are characteristics of the impulse generator and test circuit respectively. The resistors R_1 and R_2 are thus specified to provide the respective rise and tail times of the wave. The values of the elements used are given in Table 3-2. These values correspond to a time-to-crest of 33.0 nanoseconds and a time-to-one-half-peak of 36.0 microseconds.

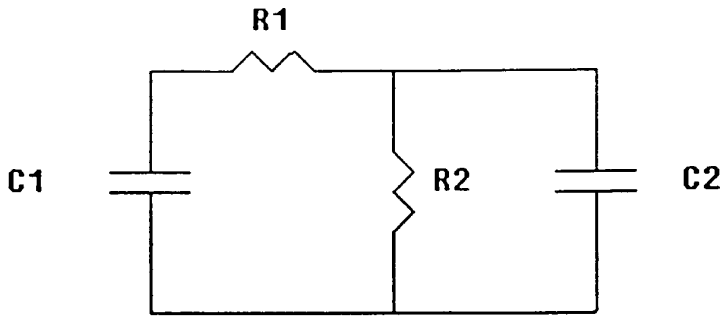

Figure 3-12
Equivalent circuit for impulse generator.

Table 3-2
Values of the elements in the impulse generator equivalent circuit.

Element	Value/Description
C_1	12.5 nF (impulse generator)
C_2	58 pF (stray) + 12 pF (sample) = 70 pF
R_1	50 Ω
R_2	3970 Ω

Figure 3-13 shows the predicted and measured waveforms for a typical negative impulse. The actual impulse has a slower rise time and smaller magnitude than predicted. These differences are attributed to stray inductance in the test circuit which was found to be on the order of 40.0 μH. However, sufficient agreement was obtained that the given waveshape is acceptable. The fast rise-time was selected such that ions on the test surfaces would not migrate in the applied field prior to breakdown. An estimation of the migration distance x may be calculated as

$$x = bEt_c \qquad \text{(eq. 3-1)}$$

where

b = ion mobility [m^2/Vs]

E = electric field [V/m]

t_c = time to crest [s].

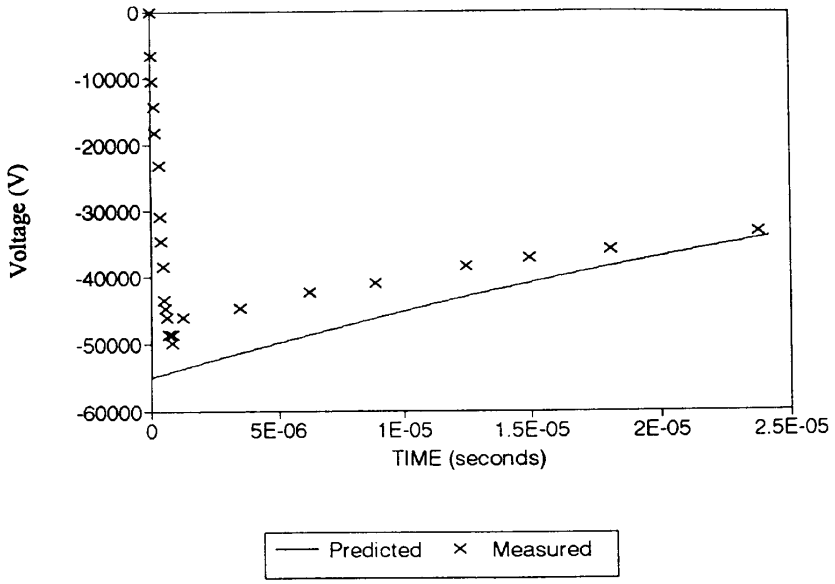

Figure 3-13
Predicted and measured impulse waveforms.

The mobility of ions in transformer oil is on the order of 5×10^{-10} m^2/Vs at room temperature (25). For a voltage of 100 kV applied across the 3.0 mm wide pressboard sample ring, the migration distance during a 1.0 microsecond rise-time will be on the order of 1.67×10^{-4} mm. Hence, the charge distribution on the test surface was assumed to be unperturbed prior to breakdown.

3.3.3 Methodology

The complete apparatus for the impulse testing of charged surfaces is illustrated in Figure 3-14. Initial experiments were performed to quantify charge deposition on the cellulose sample rings. Breakdown tests were then undertaken using both positive and negative polarity impulses to interrogate the test surfaces. Base cases were established with no flow or injection to facilitate comparison with results for charged surfaces and flowing oil.

The process of electrical breakdown in liquids is highly complicated due to the large number of influencing factors and mechanisms involved (104). In the case of the

present experiments, the introduction of pressboard surfaces and irregularities in the test electrodes provide even more uncertainties (105, 106, 107). Therefore, efforts were directed toward defining the breakdown probability distribution rather than a single mean value of breakdown voltage. At each voltage, a fixed number of impulses were applied to virgin samples such that the probability of failure could be determined. Once a given sample

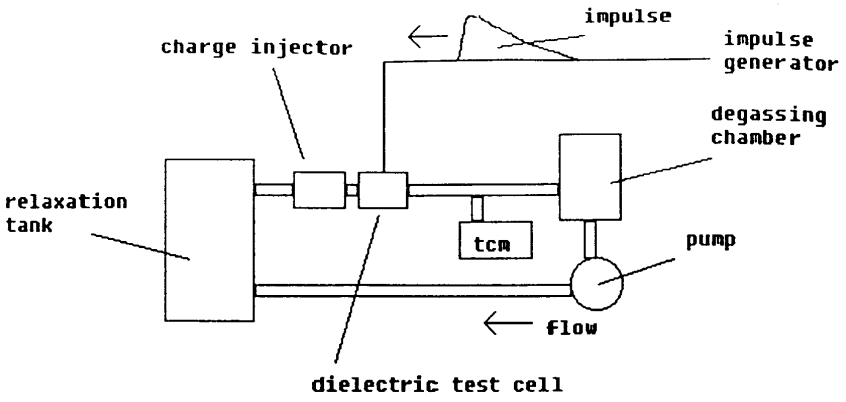

Figure 3-14
Diagram of the fluid loop configuration for impulse breakdown tests.

flashed over, it was not used again. However, samples which did not fail were allowed to relax for several minutes and reused. This method was deemed necessary since only 10 sections could be broken down before the cell had to be drained and fitted with new cellulose rings.

The sample rings consisted of 40.0 mil (1.02 mm) thick HI-VAL™ pressboard supplied by EHV Weidmann. Batches of strips 3.0 mm wide were cut and placed in an aluminum form having an inner circumference equal to that of the test cell. The rings were left in the form during dryout and impregnation to ensure that they held the proper curvature. Note that the samples were prepared in accordance with the procedures discussed in Section 2.3.1. Each experiment utilized rings from the same batch to ensure consistency.

3.3.4 Results

Preliminary tests were undertaken to quantify the surface charges developed on the pressboard test rings. The results for positive and negative injection are displayed in Figures 3-15 and 3-16 respectively. For both cases, the measurements represent the steady state mean surface charge density at a flow rate of $1.89 \times 10^{-3} m^3/s$. The charge densities are related to the observed external static potentials using an effective

capacitance derived by finite element analysis. As expected based on the charge injector characteristics of Figure 3-10, higher negative surface charge densities are evident. With -20 kV injection, the dynamic range of the static probe was exceeded and the final point of Figure 3-16 had to be extrapolated. Since higher negative surface charges could be attained, negative injection was used in the impulse breakdown experiments. The system parameters are given in Table 3-3.

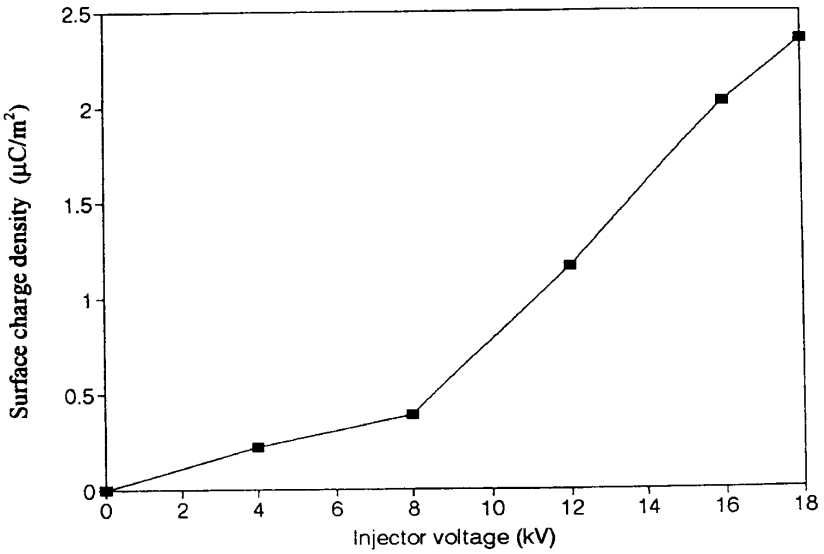

Figure 3-15
Surface charge density as a function of injector voltage (positive injection) with a flow rate of 1.89 x 10^{-3} m^3/s.

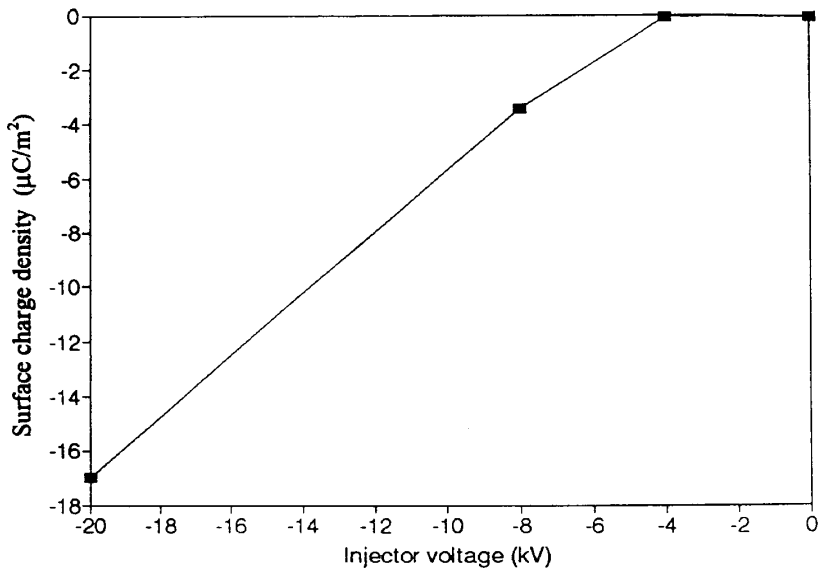

Figure 3-16
Surface charge density as a function of injector voltage (negative injection) with a flow rate of 1.89 x 10^{-3} m^3/s.

Table 3-3
System parameters used for dielectric integrity studies.

Parameter	Value and Units
oil moisture content	7.5 ppm
oil conductivity	2.62 pS/m
oil temperature	25°C
pressboard moisture content	0.5 percent

Breakdown tests were first performed using a negative impulse. Base cases (no flow or injection) were alternated with static charge tests (flow and injection) in an attempt to identify difference between the probability distributions. The maximum injector voltage of -20 kV was used for the static charge tests. A flow rate of 6.4×10^{-4} m^3/s was chosen to ensure laminar flow and provide longer residence times for the charged oil in the test cell and maximize the amount of charge relaxed onto the test surfaces. The raw data and fitted normal distributions (108) are shown in Figure 3-17. Recognizing the ± 2.0 kV firing error in the impulse generator and the scatter of the data, the influence of static charging seems minimal. However, the breakdown probability distribution exhibits the expected characteristic as the voltage magnitude is increased (94).

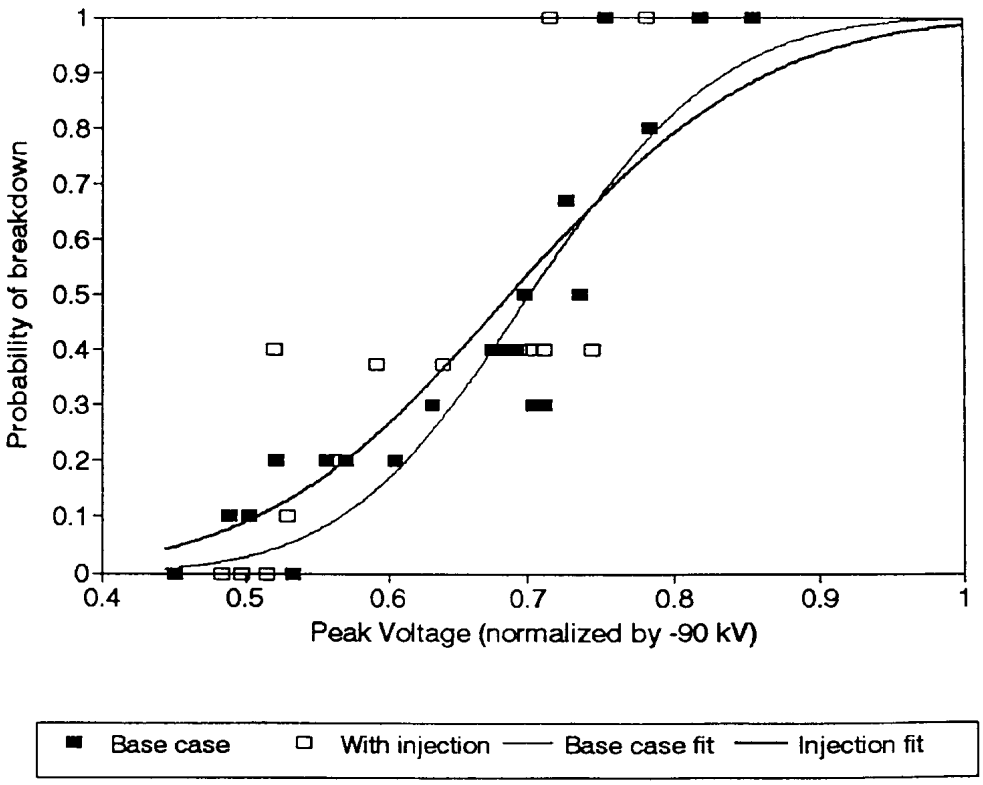

Figure 3-17
Impulse breakdown results for negative impulses with and without negative surface charge.

Upon completion of the negative impulse tests, the generator was reconfigured for the opposite polarity. Positive impulse tests were then performed using the same methodology to compare breakdown with and without static charge. The corresponding raw data and normal fits are depicted in Figure 3-18. The breakdown strength actually appears to be improved somewhat for the static charge case. However, this effect could have resulted from the oil flow alone as documented by other researchers (32, 104). The impact of static charge does not appear to be significant and shifts the breakdown distribution by less than 10 percent as previously observed by Lee and Nelson (25).

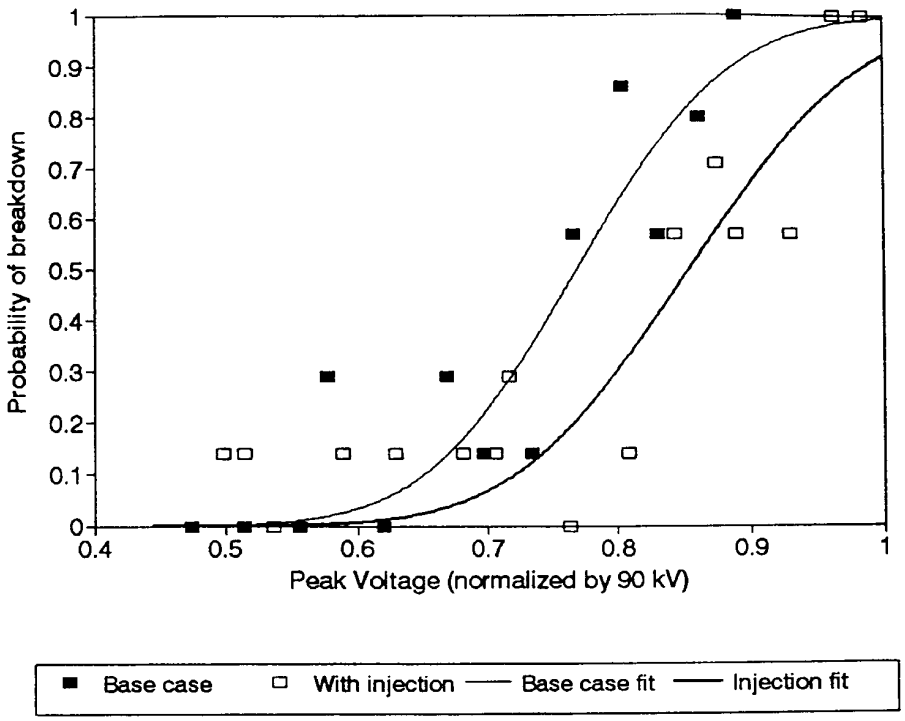

Figure 3-18
Impulse breakdown results for positive impulses with and without negative surface charge.

3.3.5 Summary

Large-scale tests were performed to evaluate the impact of deposited static charge on the electrical breakdown strength of a cellulose surface. The results indicate a minimal effect for the geometry used for both positive and negative impulses subject to negative charge. Limitations in the magnitude of the available impulses prevented the use of larger sample surfaces which would have held more charge. In order for the experiment to be useful, the pressboard surface gap must be small enough to allow breakdown without static charge present such that a base case can be established.

The electric field present across the pressboard sample rings may be readily estimated given the peak impulse voltage and electrode spacing. In the case of positive voltage, the apparent 50 percent probability breakdown level is estimated from Figure 3-18 as 72 kV. The corresponding voltage (see Figure 3-17) is 68 kV. The respective fields across the 3 mm wide samples would thus be 24 kV/mm for positive and 22.8 kV for negative. These values are close enough together that the test cell appears to have been relatively symmetric. The voltage distribution resulting from the maximum negative surface charge of Figure 3-16 is given in Figure 3-19. The corresponding electric field is shown in Figure 3-20 and the calculated peak is on the order of 1 kV/mm. The impulse breakdown strength thus should not have been significantly influenced by the surface charge which is consistent with the results.

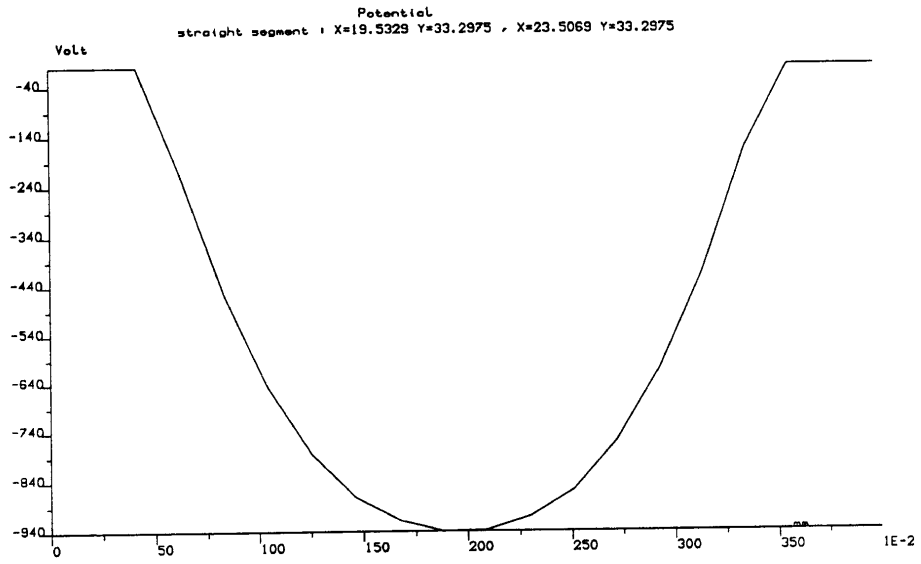

Figure 3-19
Static potential distribution on pressboard test surface.

These experiments again raise the issue of laboratory versus actual transformer scale. A larger surface with higher leakage resistance to ground for deposited charge would obviously provide a more significant static electric field. However, recent findings indicate that the coupling between electrification and transformer failure may not be so direct. The theory advanced by Moore (23, 99) suggests that electrification damage in the lower plenum of the transformer may initiate the actual failure in the upper plenum. The local discharge damage discussed in the previous section would tend to generate bubbles and/or carbon particles which will be convected through the transformer windings by flowing oil. These entities then emerge into the upper plenum and may be swept into high stress regions

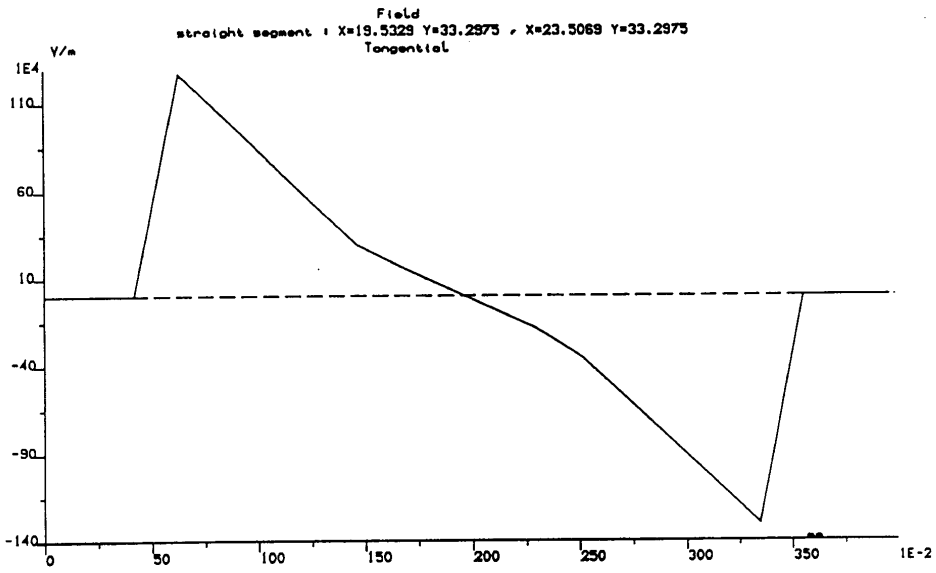

Figure 3-20
Static tangential electric field on pressboard test surface.

to compromise dielectric integrity such that catastrophic failure occurs. Thus, one should bear in mind that the electrification threat may be more complex than surface charge simply reducing the local dielectric strength.

An additional question is the difference between surface charge relaxed from flowing oil and adsorbed ions left behind on cellulose when their counter species is convected from the double layer. A recent paper by Jia-Xiang et al (109) demonstrates an effect of streaming electrification on creep breakdown in the latter case. The AC and DC (both polarities) creep strengths of a needle-plane geometry are shown to be reduced by more than 20 percent due to charge separation on a pressboard sheet attached to the plane electrode. The former issue has been studied by Lee and Nelson (25) and in the present work without demonstrating a dramatic effect upon dielectric strength under impulse. In this case, the two effects could have been supporting one another with negative charge left by electrification augmented by the relaxing charge which was probably dominant. The different surface charging mechanisms will most likely result in different surface charge distributions. This would appear to be true from the results of Jia-Xiang et al who also seem to have found that streaming effect on creep discharge depended on where the electrodes were placed. Note that their test specimens were much larger than those used for the present work.

3.4 Cumulative Charging Tests

3.4.1 Introduction

When electrification occurs in transformers, the generated charges will propagate through the structure. The entrained charge in the oil will induce counter charges on solid surfaces and hence establish an electric field which leads to relaxation subject to mobility (i.e. relaxation time). Conceivably, this field might influence the Debye layer and thus the charge separation process at the interface. In order to address this issue, cumulative charging tests were performed using the shell-form model.

3.4.2 Methodology

A bypass section was installed in the fluid loop as shown in Figure 3-21. This modification allows the relaxation tank to be removed from the hydraulic circuit via control valves. Hence, the charge generated in the model can be fed directly back into the structure if desired. Measurements were taken with and without the relaxation tank in the loop to determine the impact of inlet charge upon flow electrification in the shell-form model. The inlet and outlet volume charge densities were monitored using the ACS and TCM respectively. The model windings were alternatively energized with an AC voltage or grounded through an electrometer to provide a measure of streaming current.

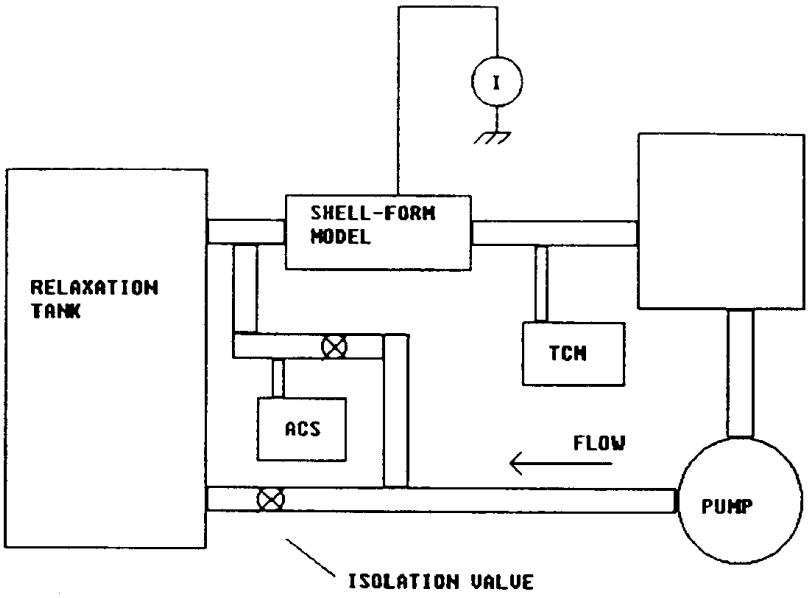

Figure 3-21
Fluid loop configuration used for cumulative charging tests.

3.4.3 Results

Initial measurements were taken with the shell-form model windings attached to an AC voltage source. The TCM (outlet) and ACS (inlet) results are shown with respect to time in Figure 3-22. Note that the electrometer could not be connected with the windings

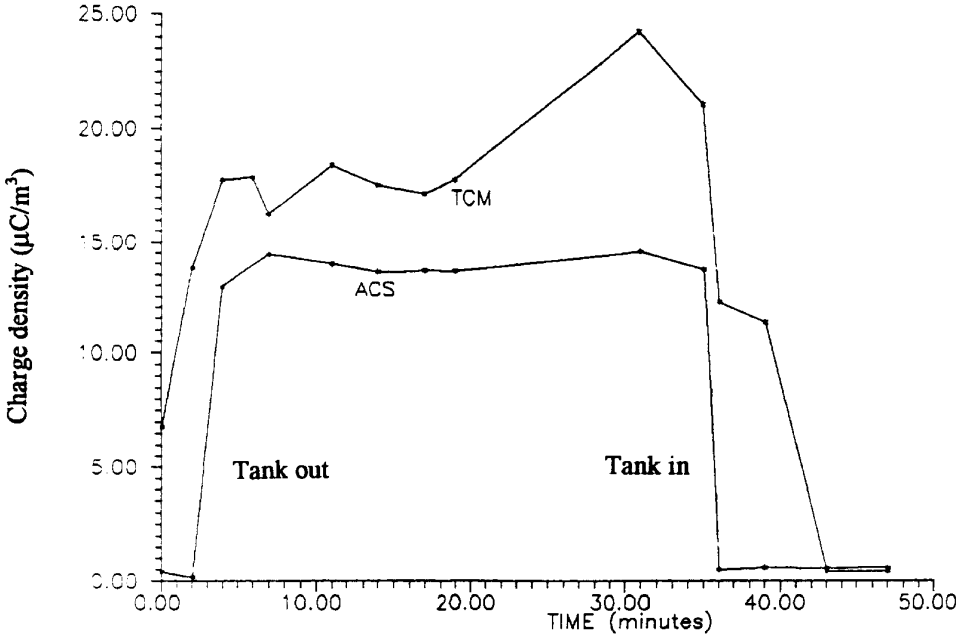

Figure 3-22
Inlet and outlet charge density with respect to time during the first cumulative charging experiment.

energized. The flow was started at 5.05×10^{-3} m^3/s with the relaxation tank in the loop and the ACS detected no charge as expected. After a few minutes, the relaxation tank was switched out and the ACS reading jumped to 14.0 $\mu C/m^3$. The TCM data subsequently shows the original outlet value of 7.0 $\mu C/m^3$ augmented by the inlet charge density to attain a new value of 18.0 $\mu C/m^3$. Both readings remained stable until the windings were energized after several minutes. The TCM results show the expected increase in charge density with applied electric field. However, the ACS clearly does not indicate any feedback from the outlet. This probably demonstrates that the degassing chamber is sufficient to relax the charges exiting from the model. The measured charge density at the model inlet is assumed to originate in the pump where significant charge separation can occur (110).

Another experiment was run with the model windings attached to an electrometer to facilitate streaming current measurements. The corresponding inlet, outlet and calculated volume charge densities are given in Figure 3-23. Over the duration of the

experiment, frictional heating occurred with the relaxation tank out of the loop as shown in Figure 3-24. The sharp drops in oil temperature are associated with switching the relaxation tank back in to supply a large volume of colder oil.

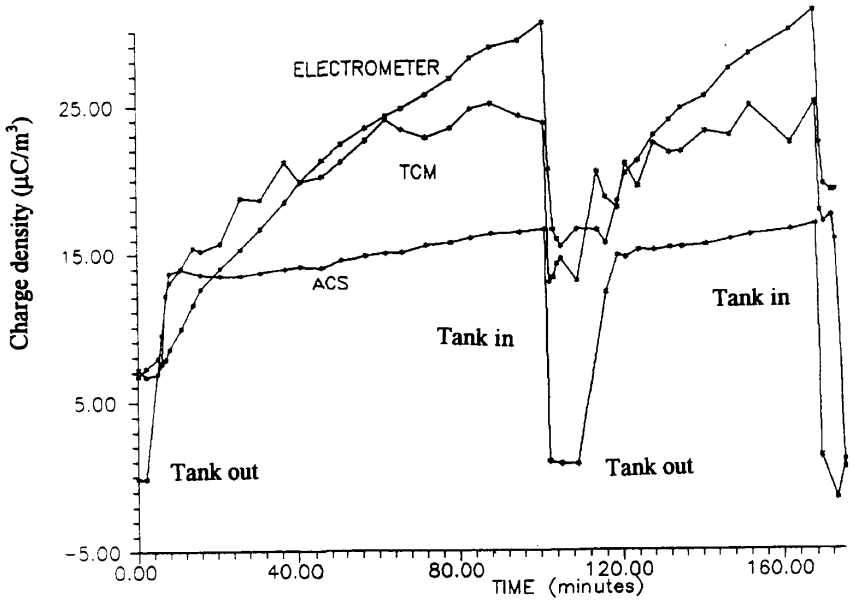

Figure 3-23
Inlet and outlet charge density with respect to time during the second cumulative charging experiment.

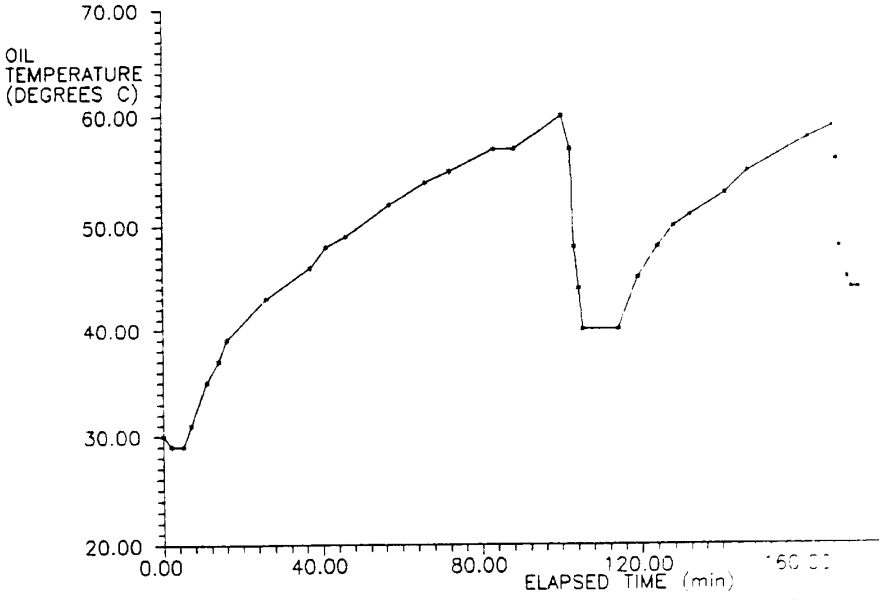

Figure 3-24
Oil temperature with respect to time during the second cumulative charging test.

Initially, the relaxation tank was left in and the ACS shows no charge in the oil at the model inlet. Both the TCM and electrometer indicate about 7.0 $\mu C/m^3$ at the outlet. After five minutes, the relaxation tank was removed and the ACS reading increased to 14.0 $\mu C/m^3$. All charge density measurements are seen to increase as the oil temperature was raised by frictional heating. The expected rise in charge density with temperature is demonstrated by the TCM and electrometer results.

After 100 minutes, frictional heating had raised the system temperature to 60°C and the relaxation tank was switched back in. The ACS reading immediately dropped to near zero as previously observed. In addition, the large volume of cooler oil in the tank quickly reduced the system temperature and hence the amount of charge separation in the shell-form model. After 10 minutes, this cycle was repeated with very similar results. Based on this data, the inlet charge density does not appear to influence electrification in the model and frictional heating was found to be the dominant parameter. The residence time for charged oil in the model was small relative to the dielectric relaxation time and influent charge could not relax sufficiently to influence the measured streaming current.

3.4.4 Summary

The cumulative charging tests show that significant charge feedback is not possible in the fluid loop. While some inlet charge was observed, this was probably generated in the pump. Any changes in the charge density exiting the model were not apparent in the inlet measurements. Furthermore, the presence of charge in the oil entering the shell-form model did not appear to influence the streaming electrification process within the limits of the experiment.

These results are supported to some degree by the results of Zahn and Washabaugh (111) who similarly found that charge generation in a filter was not influenced by influent charge. Rather, they demonstrate cumulative charging in a recirculatory system when the residence time for the oil in the non-charging sections of the system is reduced. This would indicate (as does the present work) that the superposition of relaxation and generation would appear to be valid. The theoretical models discussed in the remaining sections make use of this assumption and a very weak coupling between inlet charge and generation is predicted. Section 6 illustrates that recirculated charge can be advantageous in the transformer context via relaxation acting to reduce surface counter charges when oil residence times are sufficiently long.

4

A SEMI-EMPIRICAL MODEL FOR STATIC ELECTRIFICATION IN A TRANSFORMER DUCT

4.1 Introduction

In order to model streaming electrification in an actual transformer, the various single elements comprising the structure must first be described. The most prevalent such elements will be the rectangular ducts through which transformer oil is circulated to cool the windings. In the context of the present work, a theoretical duct model which incorporates the crucial physics of charge separation without excessive computation is essential. This Chapter presents a novel approach to this problem and provides some experimental justification for the method.

4.2 Boundary Layer Approach

A wide variety of streaming electrification models are available, but the majority of these approaches are applicable only to very specific cases. For example, the Abedian and Sonin model (13) describes charging in developed turbulent pipe flows. Unfortunately, the transformer problem requires a method which recognizes a wide dynamic range of flows including laminar and turbulent conditions. Furthermore, the influence of transverse AC electric fields must also be considered. The empirical models of Lee and Nelson (25) and Tanaka et al (29) have attempted to address these issues. However, these approaches do not adequately consider the spatial development of separated charges in the duct. In addition, the role of energization under turbulent flow conditions is neglected.

A boundary layer approach is desirable in that a local length scale is provided for interpreting the behavior of the charge distribution. The charge density profile is defined in terms of this parameter which varies as a function of distance from the inlet. This type of integral solution method is commonly used for analyzing both flow (112) and heat transfer (113) problems. A two-dimensional situation is reduced to a one-variable approximation which can be more easily solved with a minimal cost of accuracy. Such a simplification is clearly advantageous to offset the complications presented by the range of flow conditions, energization and temperature effects.

By comparing the charge boundary layer with other length scales, the significance of key electrification mechanisms may be assessed. In the case of turbulent flow, the charge distribution will be severely altered if the ion layer penetrates into the turbulent core. Under energized conditions, the charge profile will be augmented by a transport length based on the ion mobility and electric field characteristics. For either scenario, the charge boundary layer thickness provides a direct indication of the appropriate physical model required. These models are detailed in the following sections assuming a steady state with regard to time.

4.2.1 Boundary Conditions

Boundary conditions for static charging are as plentiful as the various solution methods. The arguably complete formulation of Walmsley (69) offers the disadvantage of computational complexity. Indeed, a finite element approach is required to treat the basic spatial development problem alone. However, the fluxes of each ionic species at the wall might well be reduced to a single net flux as postulated by Koszman and Gavis (61, 62, 63) and later Gavis (64). This assumption would seem reasonable since there is ample evidence that the moving dielectric fluid obtains a net charge.

As ions of one species are adsorbed at the interface, an excess concentration of the opposing sign is created in the fluid. The resulting gradient establishes a diffusion flux of ions from the wall into the liquid. Schön (36) first demonstrated the viability of this boundary condition experimentally and assumed that the flux was independent of position. The constant current density approach has been successfully applied to transformer duct models by Lee and Nelson (25) and Tanaka et al (29). Their empirical results indicate that the magnitude of the injected current depends upon the flow velocity in addition to the ion concentration.

In the case of a cellulose duct, some rationalization for the velocity dependence of the wall charge gradient may be found by considering the nature of the surface. As depicted in Figure 4-1, cellulose fibers will extend into the oil from the bulk material. In the presence of this non-ideal interface, the positive ions could be attracted by their counter charges bound to the fiber surfaces and effectively held in place. However, when the oil is flowing, ions are broken free to diffuse as drag forces become sufficient to overwhelm electrical attraction. The ideal oil/pressboard interface is thus transformed into a three-region system as illustrated in Figure 4-2.

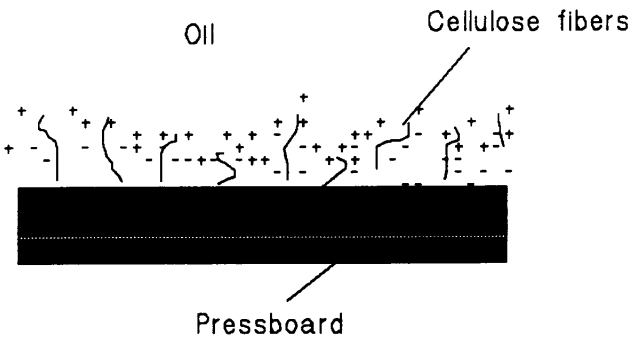

Figure 4-1
Visualization of the actual oil/cellulose interface.

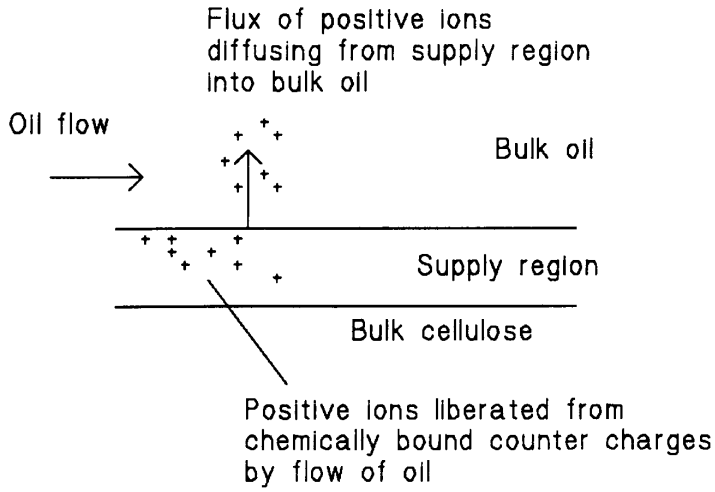

Figure 4-2
Illustration of the solid, supply region and liquid interface.

The interface is now defined as the "supply region" where positive ions are liberated by the flow such that they can diffuse into the bulk oil. The charge density gradient is given in the form

$$q'(0) = q'(0)_o V^a \qquad \text{(eq. 4-1)}$$

where

$q'(0)_o$	=	scaling constant
V	=	oil velocity [m/s]
a	=	empirical constant.

Empirical data indicates that the constant "a" typically ranges from 0.5 to 3 depending upon the materials and flow conditions involved. Following Lee and Nelson (25), a = 1 is assumed for initial purposes. Note that the sign of $q'(0)$ and $q'(0)_o$ will be negative in the given coordinate system to denote a gradient of positive ions from the wall into the oil.

4.2.2 Laminar Flow

Consider the plane channel geometry shown in Figure 4-3. Assuming a fully developed laminar flow, oil velocity profile as derived in Appendix C is

$$v(y) = \frac{3V}{H^2}\left(H y - \frac{y^2}{2} \right) \qquad \text{(eq. 4-2)}$$

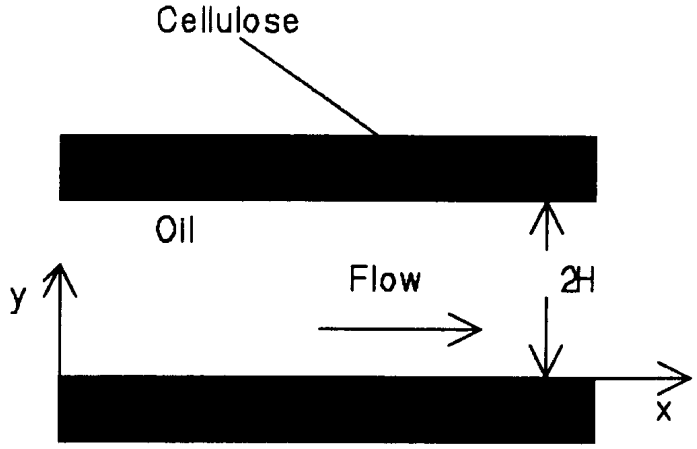

Figure 4-3
Plane channel geometry defined in cartesian coordinates.

V = mean oil velocity [m/s]

H = channel half-height [m].

Under these conditions, no transverse velocity components are available to influence the charge density distribution. Hence, the steady state linear relaxation equation developed in Appendix C may be used as shown

$$D\frac{\partial^2 q}{\partial y^2} - \frac{q}{\tau} - v(y)\frac{\partial q}{\partial x} = 0 \qquad \text{(eq. 4-3)}$$

where

D = molecular diffusion coefficient [m^2/s]

τ = relaxation time [s]

q = volume charge density [C/m^3].

In order to pursue an integral solution of 4-3, the charge profile must be defined in terms of the charge boundary layer thickness $\delta(x)$. An illustration of the evolving charge distribution in the duct is presented in Figure 4-4.

The nature of the charge boundary layer profile may be determined by considering the solution of eq. 4-3 far from the inlet where the convection term vanishes. The fully developed charge distribution is found to have the form

$$q(y) = q(0)\cosh\left(\frac{y}{\lambda}\right) + q'(0)\,\lambda\sinh\left(\frac{y}{\lambda}\right) \qquad \text{(eq. 4-4)}$$

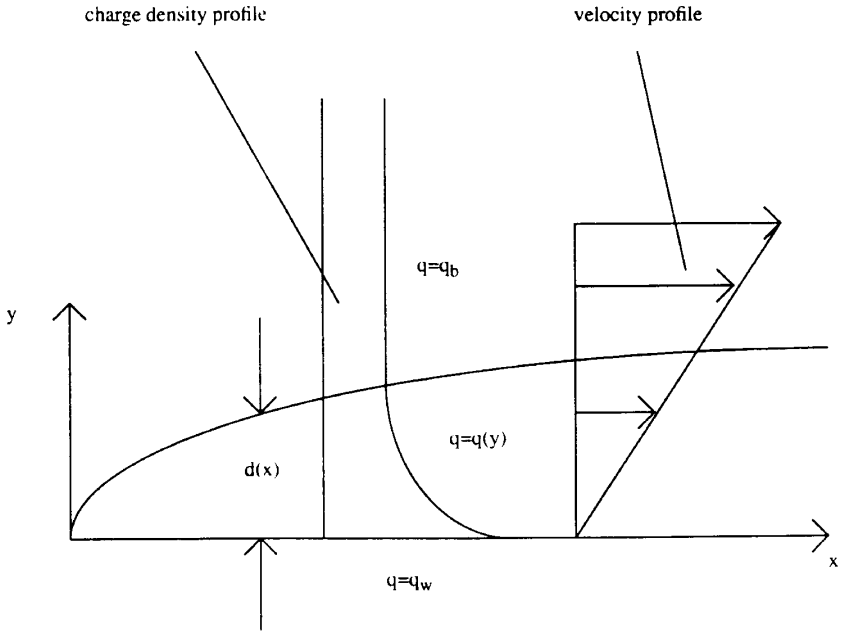

Figure 4-4
Illustration of the spatially evolving charge boundary layer.

where q(0) is the volume charge density in the oil adjacent to the interface. The wall charge gradient $q'(0)$ is the boundary condition of eq. 4-1 and λ is the Debye length given by eq. 1-2. Subject to spatial equilibrium, the net current density at the wall (y=0)

must be zero. Hence, the diffusion and relaxation currents must be equal and opposite such that

$$-\frac{1}{\tau}\int_0^y q(y)\,dy = -D\,q'(0)\,. \qquad \text{(eq. 4-5)}$$

If q^* is the net charge per unit area contained in the fluid, then eq. 4-5 becomes

$$q'(0) = -\frac{1}{\lambda^2}q^* \qquad \text{(eq. 4-6)}$$

with q^* approximated by $q(0)\lambda$. Substituting eq. 4-6 into eq. 4-4 yields the familiar Boltzmann-type distribution described in Section 1, namely

$$q(y) = q(0)\exp\left(-\frac{y}{\lambda}\right). \qquad \text{(eq. 4-7)}$$

Taking a cue from eq. 4-7, a normalized cubic charge profile is proposed such that

$$\theta = A + B\,y + C\,y^2 + D\,y^3 \qquad \text{(eq. 4-8)}$$

with

$$\theta = \frac{q(y) - q_B}{q_W - q_B} \qquad \text{(eq. 4-9)}$$

where

q_B = mean uniform inlet charge density [C/m^3]

q_W = wall charge density [C/m^3].

A set of boundary conditions are now required for eq. 4-8. Four logical constraints are

$$q(0) = q_W \longrightarrow \theta = 1$$

$$q(\delta) = q_B \longrightarrow \theta = 0$$

$$\frac{\partial^2 q}{\partial y^2}\bigg|_0 = 0 \longrightarrow \frac{\partial^2 \theta}{\partial y^2}\bigg|_0 = 0$$

$$\frac{\partial q}{\partial y}\bigg|_\delta = 0 \longrightarrow \frac{\partial \theta}{\partial y}\bigg|_\delta = 0$$

and the resulting profile has the form

$$\theta = 1 - \frac{3}{2}\left(\frac{y}{\delta}\right) + \frac{1}{2}\left(\frac{y}{\delta}\right)^3 \qquad \text{(eq. 4-10)}$$

with q′(0) specified. Note that the same profile is used for the analogous convective heat transfer problem (113) of laminar flow over a flat plate subject to a constant heat flux. The temperature profile is readily defined in terms of a boundary layer. While the charge separation problem is clearly similar, the addition of the relaxation term complicates the integral solution. Far from the leading edge (inlet) the charge boundary layer slope goes to zero while the thermal boundary layer continues to grow.

For $\lambda \ll H$, the velocity profile of eq. 4-2 is approximated as linear in the region of interest by

$$v(y) = \beta y \qquad \text{(eq. 4-11)}$$

where $y \ll H$ and β is the ratio of wall shear stress and oil viscosity given by

$$\beta = \frac{\tau_w}{\mu}_{y=0} \qquad \text{(eq. 4-12)}$$

Noting that

$$\tau_w = -\mu \left.\frac{d[v(y)]}{dy}\right|_0 , \qquad \text{(eq. 4-13)}$$

β is defined in terms of the mean oil velocity and channel half-height as

$$\beta = \frac{3V}{H} . \qquad \text{(eq. 4-14)}$$

Substituting Equations 4-10 and 4-14 into 4-3 and integrating over the boundary layer, δ, yields the boundary layer equation as follows:

First term

$$D \int_0^{\delta} \frac{\partial^2}{\partial y^2} \left[(q_W - q_B) \left(1 - \frac{3}{2}\left(\frac{y}{\delta}\right) + \frac{1}{2}\left(\frac{y}{\delta}\right)^3 \right) + q_B \right] dy$$

$$= \frac{3}{2} \frac{D}{\delta} (q_W - q_B)$$

(eq. 4-15)

Second term

$$\frac{1}{\tau} \int_0^{\delta} \left[(q_W - q_B) \left(1 - \frac{3}{2}\left(\frac{y}{\delta}\right) + \frac{1}{2}\left(\frac{y}{\delta}\right)^3 \right) + q_B \right] dy$$

$$= \frac{3}{8} \frac{\delta}{\tau} (q_W - q_B) + q_B \frac{H}{\tau}$$

(eq. 4-16)

Third term

$$\int_0^{\delta} v(y) \frac{\partial q}{\partial x} = \frac{d}{dx} \int_0^{\delta} v(y)\, q(y)$$

$$\beta \frac{d}{dx} \int_0^{\delta} \left[y(q_W - q_B) \left(1 - \frac{3}{2}\left(\frac{y}{\delta}\right) + \frac{1}{2}\left(\frac{y}{\delta}\right)^3 \right) + q_B \right] dy$$

$$= \beta \frac{d}{dx} \left[(q_W - q_B) \frac{1}{10} \delta^2 \right] + \frac{\beta}{3H} \frac{d}{dx} \left(q_B \delta^3 \right)$$

(eq. 4-17)

Note that Liebnitz's rule has been employed to extract the derivative from the integral sign in the third term.

Recognizing that $q'(0)$ is known, the $(q_W - q_B)$ factor can be eliminated from eqs. 4-15, 4-16 and 4-17 via

$$\left. \frac{\partial q}{\partial y} \right|_0 = - \frac{3}{2} \frac{1}{\delta} (q_W - q_B) \, .$$

(eq. 4-18)

The entering uniform volume charge density q_B will relax over the length of the pipe such that

$$q_B(x) = q_B(0)\exp\left(-\frac{x}{V\tau}\right). \qquad \text{(eq. 4-19)}$$

For a channel of one meter in length with a mean oil velocity of one meter per second and a relaxation time of three seconds, q_B at the outlet will be 30 percent less than the inlet value. This provides a worst case scenario assuming oil at 60°C flowing at relatively low speed and demonstrate that the second term of eq. 4-17 can be safely neglected. The significance of this term is further reduced by the fact that

$$\frac{\delta^3}{H} \gg \delta^2. \qquad \text{(eq. 4-20)}$$

The final form of the charge density boundary layer equation after invoking eq. 4-18 thus becomes

$$-D\,q'(0) + \frac{1}{4}\frac{\delta^2}{\tau}q'(0) - q_B\frac{H}{\tau} - \frac{\beta}{5}q'(0)\,\delta^2\,\delta' = 0 \qquad \text{(eq. 4-21)}$$

Substituting the Debye length relation $\lambda = (D\tau)^{\frac{1}{2}}1$ into eq. 4-21 gives

$$1 + \frac{q_B H}{\lambda^2 q'(0)} - \frac{\delta^2}{4\lambda^2} - \frac{\beta\tau}{5\lambda^2}\delta^2\,\delta' = 0 \qquad \text{(eq. 4-22)}$$

Now introduce the constants

$$k_1 = 1 + \frac{q_B H}{\lambda^2 q'(0)} \qquad \text{(eq. 4-23)}$$

$$k_2 = \frac{1}{4\lambda^2} \qquad \text{(eq. 4-24)}$$

$$k_3 = \frac{\beta\tau}{5\lambda^2} \qquad \text{(eq. 4-25)}$$

to obtain

$$k_1 - k_2\delta^2 - k_3\delta^2\,\delta' = 0. \qquad \text{(eq. 4-26)}$$

The constants are eliminated by transforming eq. 4-22 into dimensionless form by introducing

$$f = \delta \frac{k_2}{k_1} \qquad \text{(eq. 4-27)}$$

$$\eta = \frac{k_2}{k_3}\left(\frac{k_2}{k_1}\right)^{\frac{1}{2}} x \qquad \text{(eq. 4-28)}$$

such that the boundary layer equation becomes

$$1 - f^2 - f^2 f' = 0 . \qquad \text{(eq. 4-29)}$$

This equation was solved numerically using Taylor integration to generate the boundary layer characteristic. The dimensionless charge boundary layer is shown in Figure 4-5 and may be scaled to fit the problem of interest.

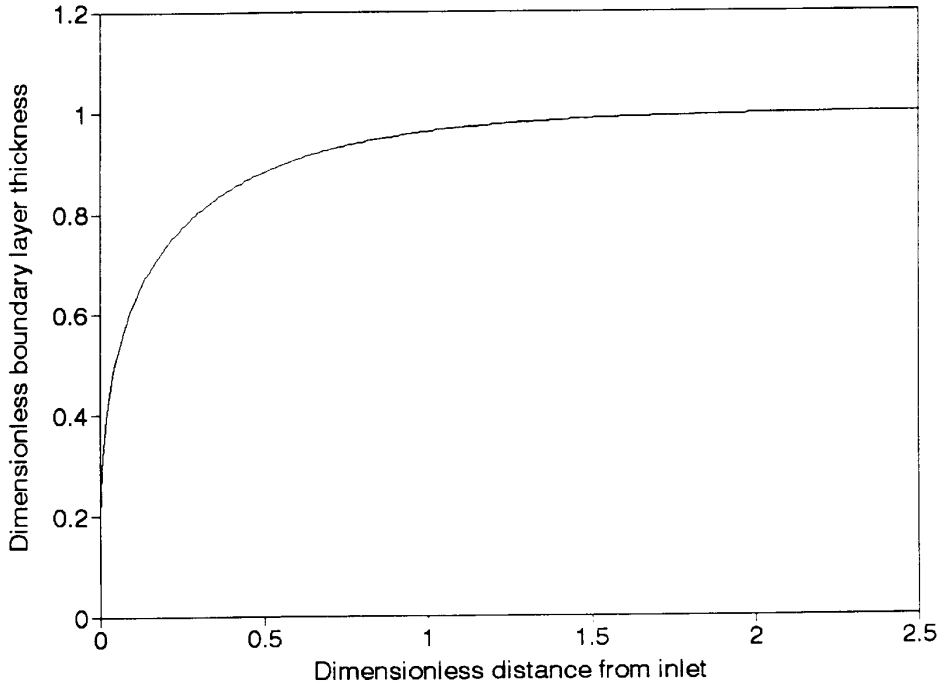

Figure 4-5
Dimensionless volume charge density boundary layer characteristic.

4.2.3 Turbulent Flow

In a power transformer, electrification in turbulent duct flows must also be addressed. Under these conditions, the time-averaged turbulent relaxation equation is shown in Appendix D to be

$$\frac{\partial}{\partial y}\left[(D + D_T) \frac{\partial \bar{q}}{\partial y} \right] - \frac{\bar{q}}{\tau} - V \frac{\partial \bar{q}}{\partial x} = 0 \qquad \text{(eq. 4-30)}$$

where

$\bar{q}$ = time averaged volume charge density [C/m^3]

V = mean flow velocity in the x-direction [m/s]

D_T = turbulent diffusion coefficient [m^2/s].

The oil flow will consist of a turbulent core where the diffusivity mechanism is significant and a laminar region very near the wall where molecular diffusion will dominate the charge transport process.

A diffusion sublayer of thickness Δ is typically defined in which $D_T = D$. Following Abedian and Sonin (13), the diffusion sublayer is given by

$$\Delta = \frac{\beta \nu}{\left(\frac{\nu}{D} \right)^{\frac{1}{m}} v^*} \qquad \text{(eq. 4-31)}$$

where

B = scaling constant

ν = kinematic viscosity [m^2/s]

D = molecular diffusion coefficient [m^2/s]

m = constant.

The quantity v^* is the friction velocity defined as

$$v^* = \left(\frac{\tau_w}{\rho} \right)^{\frac{1}{2}} \qquad \text{(eq. 4-32)}$$

where

τ_w = wall shear stress [kg/m/s^2]

ρ = fluid density [kg/m^3].

The boundary layer formulation is incorporated subject to the relative magnitudes of δ and Δ. For $\delta \le \Delta$, the laminar approach may be used with the β coefficient derived for turbulent flow following Abedian and Sonin (13) as

$$\beta = \frac{.0396\, V^{\frac{7}{4}}}{[d_H]^{\frac{1}{4}}[\nu]^{\frac{3}{4}}} \qquad \text{(eq. 4-33)}$$

where $d_{-H} = 4H$ for a channel of half-height H. However, once $\delta(x) = \Delta$, a two-region problem must be solved. In this case, the bulk charge in the core will be augmented by the turbulent diffusivity mechanism.

The charge residing within the diffusion sublayer will continue to occupy the profile of eq. 4-9 with $\delta = \Delta$. The bulk charge q_B becomes $q_B(x)$ and defines the boundary condition at $y = \delta(x)$. In the turbulent core, a new length scale becomes appropriate based on the mean diffusivity

$$\overline{D_T} = \frac{1}{H}\int_0^H D_T(y)\,dy\ . \qquad \text{(eq. 4-34)}$$

The turbulent Debye length may be thus defined in terms of this parameter as

$$\lambda_T = \sqrt{\frac{\overline{D_T}\,\varepsilon}{\sigma}}. \qquad \text{(eq. 4-35)}$$

Recognizing that λ_T is on the order of H, a well-mixed turbulent core is assumed following Gasworth (12) and Zahn et al (48). Therefore, the bulk charge density has no y-dependence and a simple control volume approach can be adopted outside the diffusion sublayer.

Integrating the relaxation equation over both the sublayer and turbulent core yields

$$-D_{q'}(0) + \frac{1}{4}\frac{\Delta^2}{\tau}q'(0) - q_B\frac{H}{\tau} - \left[\beta\frac{\Delta^2}{2} + V(H-\Delta)\right]\frac{dq_B}{dx_t} = 0. \qquad \text{(eq. 4-36)}$$

This equation has solution

$$q_B(x) = q'(0)\frac{\lambda^2}{H}\left[\frac{1}{4}\frac{\Delta^2}{\lambda^2} - 1\right]\left[1 - \exp\left(-\frac{x_t}{V\tau}\right)\right] \qquad \text{(eq. 4-37)}$$

and assumes that $H \gg \Delta$. The variable x_t defines a coordinate system with the origin at x such that $\delta(x) = \Delta$. Hence the turbulent core model is only invoked once the laminar charge boundary layer has exceeded the diffusion sublayer. The two-region scenario is illustrated in Figure 4-6 for a plane channel geometry.

4.2.4 Influence of AC Energization

In an operating transformer alternating electric fields will be present. The potential drop between the turns of a winding implies that an electric field will exist in the ducts which separate them. Substantial voltages may also exist between the windings and the transformer tank. If the local fields are sufficiently large, the mechanics of the electrification process may be influenced. This issue must be addressed under both laminar and turbulent conditions.

The analysis of this section assumes that the applied electric field is y-directed and hence perpendicular to the flow. For a sinusoidal field having frequency ω, the velocity of an ion will be given as

$$v = bE_o \sin(\omega t) \qquad \text{(eq. 4-38)}$$

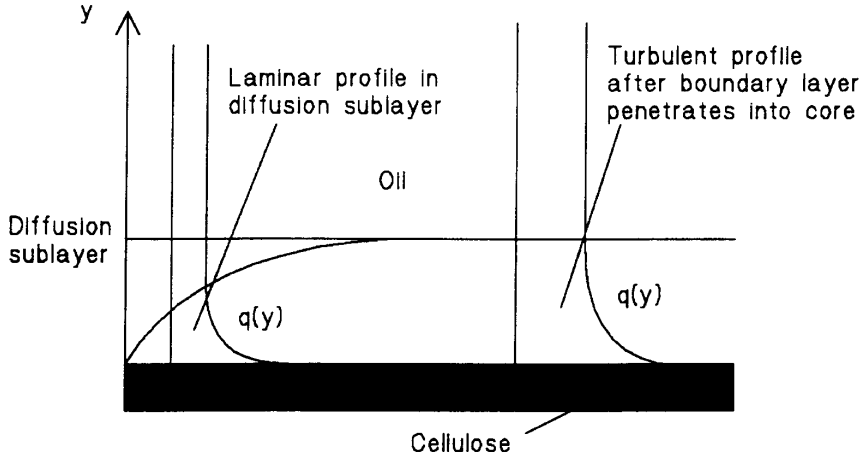

Figure 4-6
Illustration of the two-region charging problem under turbulent conditions once the charge boundary layer penetrates the core.

where b is the ionic mobility of the selected species [m^2/Vs]. Eq. 4-38 may be integrated with respect to time to obtain the ion position (y-axis is perpendicular to the wall)

$$y(t) = \frac{b E_o}{\omega}(1 - \cos(\omega t)) + y(0). \qquad \text{(eq. 4-39)}$$

Assuming that the ion starts from the interface, y(0) = 0 and the time average of eq. 4-39 simply becomes

$$\overline{y(t)} = \frac{b E_o}{\omega} = \delta_e. \qquad \text{(eq. 4-40)}$$

The parameter δ_e provides a length scale for the electrical transport of charge away from the wall. Under laminar conditions, the charge boundary layer thickness will be increased by the applied field such that

$$\delta(x)_{net} = \delta(x) + \delta_e \qquad \text{(eq. 4-41)}$$

Hence, the mean effect will be that the charge profile extends farther into the fluid to provide a larger streaming current without an increase in the fluid velocity. If the flow is turbulent and $\delta_e \leq \Delta$, the boundary layer can penetrate the turbulent core closer to the inlet than under no-field conditions. This will lead to higher charge densities in the oil via eq. 4-37.

A second electrification scenario is possible with an AC electric field applied across a turbulent duct flow. If $\delta_e \geq \Delta$, the field can transport ions from the wall into the turbulent core. The eddy diffusivity mechanism will oppose the removal of ions from the core during the opposing half cycle. Therefore, substantial charging of the core can occur for sufficiently high fields subject to the frequency and ionic mobility.

A model for AC energization charging in a turbulent Couette flow has been postulated by Zahn et al (48). While this approach has been experimentally verified only at frequencies well below 60 Hz, it provides a reasonable basis for the present analysis. The derivation is provided for completeness and is required to formulate the concept in a channel geometry.

Assuming the sinusoidal, y-directed electric field of eq. 4-38, charge will be transported into the core during the appropriate half cycle. A positive ion will cross the diffusion sublayer at time t_1 such that eq. 4-39 satisfies

$$\Delta = \frac{b E_o}{\omega}(1 - \cos \omega t_1) \qquad \text{(eq. 4-42)}$$

or

$$t_1 = \frac{1}{\omega} \cos^{-1}\left[1 - \frac{\Delta\omega}{b\,E_o}\right]. \qquad \text{(eq. 4-43)}$$

The ion velocity will remain positive until time $t_2 = \frac{\pi}{\omega} 2$ and the time window for injection into the core is thus defined. The injected current density may be written as

$$J_{in} = q_{eff}\, b\, E_o \sin(\omega t) \text{ for } t_1 < t < t_2 \qquad \text{(eq. 4-44)}$$

where q_{eff} is the effective volume charge density transported from the wall. Taking the time average of eq. 4-44 gives the mean injected current

$$\overline{J_{in}} = \frac{q_{eff}}{2\pi} b\, E_o \left[2 - \frac{\Delta\omega}{b\,E_o}\right]. \qquad \text{(eq. 4-45)}$$

Recognizing that exactly the same process can act to transport ions from the core to the wall, a rejection current can be derived in the same manner. In this case, the bulk charge density in the core is substituted for q_{eff} to obtain

$$\overline{J_{rej}} = \frac{q_B}{2\pi} b\, E_o \left[2 - \frac{\Delta\omega}{b\,E_o}\right]. \qquad \text{(eq. 4-46)}$$

Applying continuity at the edge of the diffusion sublayer thickness, the net current flowing into the turbulent control volume will be

$$\overline{J_{net}} = \overline{J_{inj}} - \overline{J_{rej}} \qquad \text{(eq. 4-47)}$$

and hence,

$$\overline{J_{net}} = (q_{eff} - q_B) \frac{b\,E_o}{2\pi} \left[2 - \frac{\Delta\omega}{b\,E_O}\right]. \qquad \text{(eq. 4-48)}$$

A control volume representation is easily applied to the present case. The injection current density becomes J_1 with the relaxation current density given by

$$J_2 = \frac{H\, q_B}{\tau} \qquad \text{(eq. 4-49)}$$

for the channel geometry. Solving the current continuity equation gives an expression for the spatial development of the bulk charge density in the core subject to an applied AC field as

$$q_B(x) = \frac{-d\,q'(0)\,A}{\left(A + \frac{1}{\tau}\right)}\left[1 - \exp\left(-x\left[A + \frac{1}{V\tau}\right]\right)\right] + q_B(0)\exp\left[-x\left(A + \frac{1}{V\tau}\right)\right] \qquad \text{(eq. 4-50)}$$

where

$$A = \frac{b\,E_o}{2\pi\,V\,H}\left(2 - \frac{\Delta\omega}{b\,E_o}\right). \qquad \text{(eq. 4-51)}$$

The parameter d is a diffusion thickness which is multiplied by the wall charge gradient to obtain the effective volume charge density available for field transport into the core. Empirical data is required to specify d once an appropriate value of $q'(0)_o$ has been determined. Note that the preceding derivation accounts for half of the channel and that eq. 4-50 must be multiplied by two to obtain the total charge density present in the core. Ion injection from the electrodes and/or cellulose surface is not considered in this analysis.

4.2.5 Temperature Dependence

A transformer in the field experiences a wide range of operating temperatures. The oil temperature is influenced by load, ambient temperature and the operation of the cooling system. All of the parameters which govern the streaming electrification process are temperature sensitive. The net effect on charge separation is ultimately governed by competition between several mechanisms.

Conveniently, the critical transformer oil properties typically obey an Arrhenius relationship with respect to temperature expressed in terms of an activation energy. The conductivity data of Lee and Nelson (25) follows the form

$$\sigma = \sigma_o \exp\left[-\frac{W_\sigma}{k\,T}\right] \qquad \text{(eq. 4-52)}$$

where

σ_o	=	constant = 2.35 x 10^{-6} [S/m]
W_σ	=	activation energy = 5.37 x 10^{-20} [J]
k	=	Boltzmann constant
T	=	temperature [^{o}K].

The kinematic viscosity of the same oil exhibits the opposite behavior with temperature such that

$$\nu = \nu_o \exp\left[\frac{W_\nu}{k\,T}\right] \qquad \text{(eq. 4-53)}$$

and

ν_o = 7.527×10^{-11} [m^2/s]

W_ν = 5.22×10^{-20} [J].

Following Adamchewski (83), the ion mobility will generally be inversely proportional to the oil viscosity by

$$b = \frac{K}{\nu} = \frac{K}{\nu\,\rho}. \qquad \text{(eq. 4-54)}$$

Lee (25) estimates b to be on the order of 5.0×10^{-10} m^2/Vs at 25°C. In accordance with this assumption, the ion mobility to be used for the positive species has the form

$$b = b_o \exp\left[-\frac{W_b}{kT}\right] \qquad \text{(eq. 4-55)}$$

where

b_o = 1.63×10^{-4} [m^2/Vs]

W_b = $W_\nu = 5.22 \times 10^{-20}$ [J].

The molecular diffusion coefficient remains to be defined. Incorporating the Einstein relation,

$$D = \frac{k\,T}{e^-}\,b \qquad \text{(eq. 4-56)}$$

where e^- is the electronic charge in Coulombs. Hence, the diffusion coefficient becomes

$$D = D_o\,T \exp\left[-\frac{W_D}{kT}\right] \qquad \text{(eq. 4-57)}$$

with

$$D_o = 1.4 \times 10^{-8} \text{ [m}^2\text{/s]}$$

$$W_D = W_b = 5.22 \times 10^{-20} \text{ [J]}.$$

Note that this approximation has assumed univalent positive ions for the species present in the oil.

The chemical processes which supply dissociated ions to the double layer will also be temperature dependent. Oommen (45) and Tanaka et al (29) both assume that the number of ions available obey an Arrhenius temperature relationship. Hence, the wall charge gradient boundary condition is tentatively postulated to follow a similar dependence, namely

$$q'(0)_o = q'(0)_\infty \exp\left[-\frac{W_q}{k\,T} \right]. \qquad \text{(eq. 4-58)}$$

The scaling constant $q'(0)_\infty$ and activation energy W_q are determined empirically in the next section.

4.3 Calibration with Experimental Data

4.3.1 Review of Experiments

This section compares the present theoretical approach with the experimental data of Lee and Nelson (25). Their apparatus consisted of the small fluid loop shown in Figure 4-7.

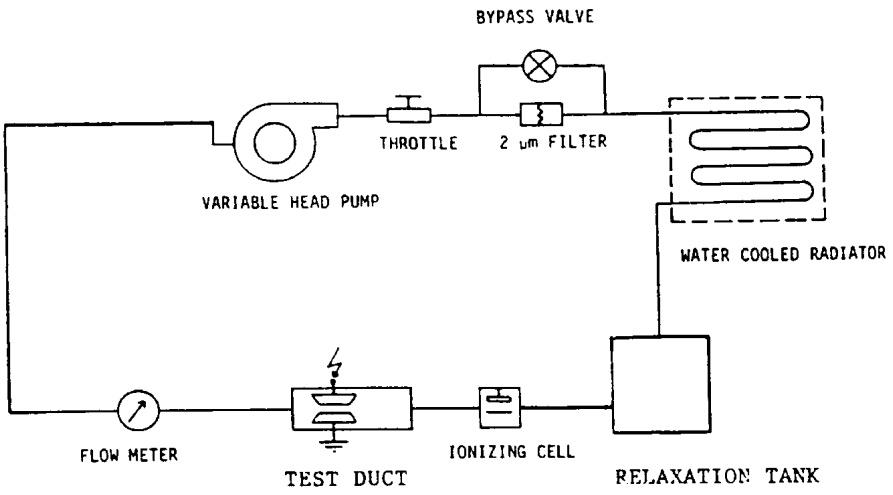

Figure 4-7
The fluid loop used by Lee and Nelson (25) for electrification measurements.

The square pressboard duct used to generate charge is illustrated with appropriate dimensions in Figure 4-8. Note that the material parameters presented in the previous section correspond to the mixture of Exxon Univolt and Shell Diala-A used for these experiments. However, the parameters are not expected to vary significantly for transformer oil meeting the same specifications.

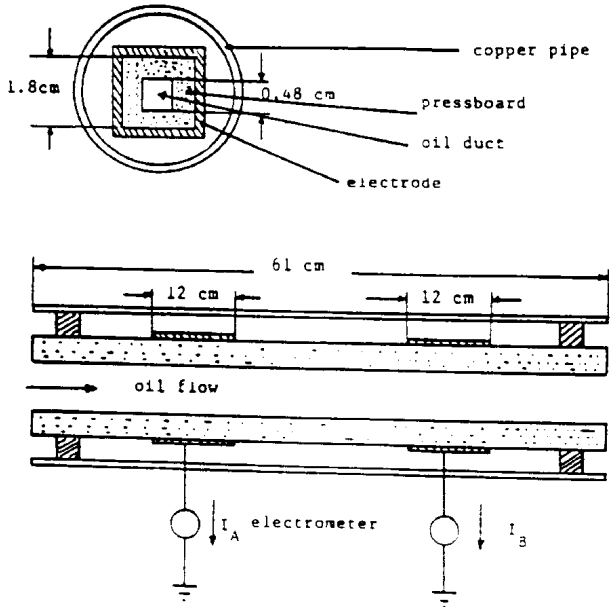

Figure 4-8
Square pressboard duct used by Lee and Nelson (25).

The experimental data was obtained under laminar flow conditions. Hence, the charge boundary layer thickness was on the order of the Debye length which is significantly less than the hydraulic diameter of the duct. The geometry can thus be reasonably approximated by unfolding the duct to obtain a single flat plate. Recognizing that the duct length (60 cm) is much greater than the hydraulic diameter (.48 cm), the flow will be fully developed based on the criterion given by Schlicting (112), namely

$$L_d = \frac{25}{R_e} \qquad \text{(eq. 4-59)}$$

At 25°C, a typical Reynolds number of 500 indicates laminar flow with a development length on the order of 5 cm.

The oil temperature was regulated using a thermocouple-controlled heating tape applied to a section of copper tubing. The flow rate was controlled via a throttling valve and measured using a ball-type gauge. Streaming current measurements were taken from a metal foil on the outside of the duct. A Faraday cage was necessary to shield the apparatus from external sources due to the extremely low currents being measured. The test duct was also equipped with copper plates on two sides to facilitate energization.

4.3.2 Electrification as a Function of Flow

The measurements of Lee and Nelson are presented in terms of streaming currents. Hence, the charge density profiles of the previous section must be integrated via eq. 1-6 to facilitate comparison. For laminar flow over a pressboard plate, integrating the product of eq. 4-9 and the laminar velocity profile over the boundary layer yields

$$I(L) = -\frac{2}{15} W \beta q'(0) \delta(L)^3 \qquad \text{(eq. 4-60)}$$

at the channel outlet (x = L). The parameter W denotes the plate width which will be 4s for the square duct having sides of length s. The boundary layer thickness is determined by scaling the characteristic of Figure 4-5 by the parametric transformations defined in eqs. 4-27 and 4-28. Note that there is no term required to account for the bulk charge since no inlet charge density was present for these experiments. A relaxation volume upstream of the test duct ensured that zero inlet charge was present.

With $q'(0)_o$ set to -2.91×10^5 C/m^4 at 25°C, a reasonable fit is obtained for laminar flow as shown in Figure 4-9. Having empirically specified the boundary condition at one oil velocity, the experimental and theoretical results agree fairly well. Unfortunately, the highest velocity examined experimentally was below 1 m/s which corresponds to a laminar Reynolds number.

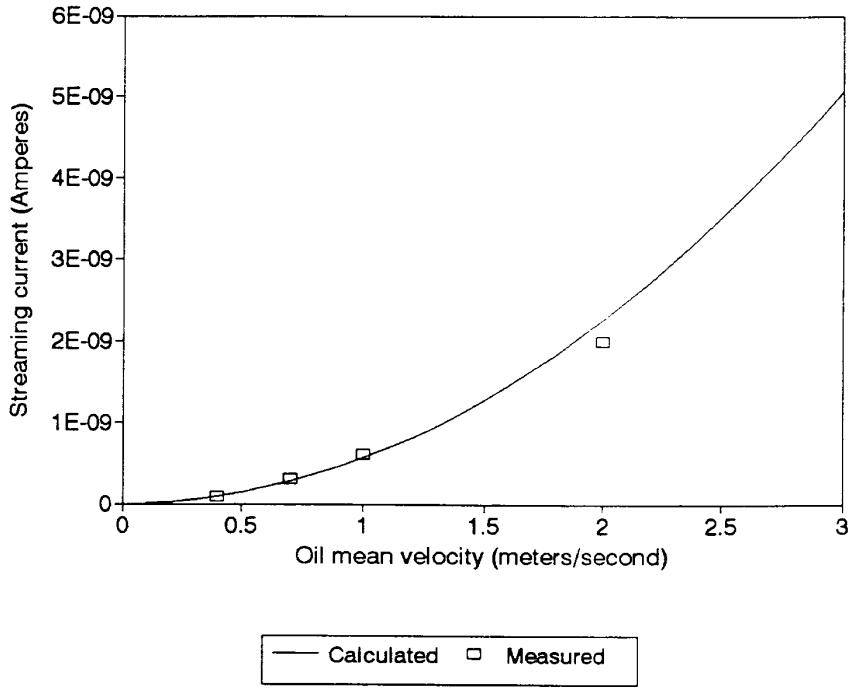

Figure 4-9
Predicted and measured values for streaming current as a function of oil velocity with laminar flow.

In order to demonstrate the turbulent charging characteristic, a plane channel geometry is required. This results from the fact that the turbulent Debye length will be on the order of the channel height. For consistency, a channel having height s and width s will be used. Integrating the turbulent charge density expression of eq. 4-37 with no inlet charge gives

$$I(L) = -\frac{2}{15}\beta W q'(0)\Delta^3 + \left[\beta W \Delta^2 + 2 V W (H - \Delta)\right] q_B \qquad \text{(eq. 4-61)}$$

where

$$q_B = q'(0)\frac{\lambda^2}{H}\left[\frac{1}{4}\frac{\Delta^2}{\lambda^2} - 1\right]\left[1 - \exp\left(\frac{x_t - L}{V\tau}\right)\right]. \qquad \text{(eq. 4-62)}$$

The variable x_t denotes x where $\delta(x) = \Delta$ and the charge boundary layer penetrates the turbulent core. If $x_t > L$, then eq. 4-60 is used with β given by eq. 4-33.

The exiting streaming current is shown over a wide range of velocities in Figure 4-10. A large discontinuity is evident as the flow transitions to turbulence and δ exceeds Δ. A

similar effect was found by Tanaka et al (29) in their studies of oil flowing through pressboard pipes. The much larger streaming current is to be expected under turbulent conditions due to the eddy diffusivity mechanism which acts to distribute ions over a greater cross section of the flow.

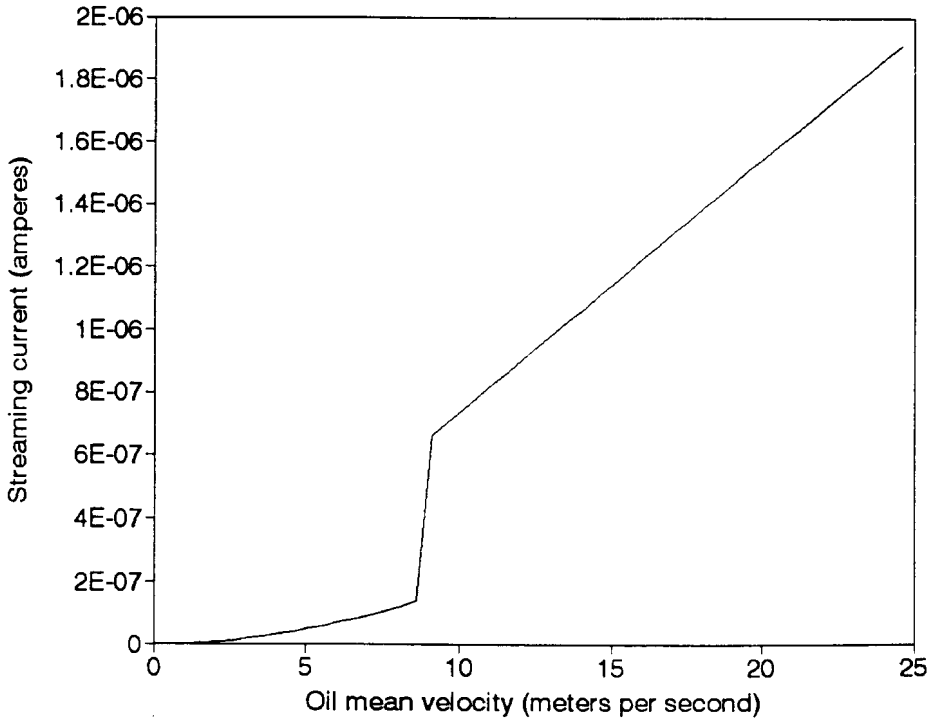

Figure 4-10
Streaming current predicted at the duct outlet under laminar and turbulent flow conditions.

4.3.3 Electrification as a Function of AC Energization

With an alternating voltage applied to the test duct under laminar flow conditions, the charge density at the duct outlet is integrated to obtain

$$I(L) = -\frac{2}{15} W \beta q'(0) (\delta(L) + \delta_e)^3. \qquad \text{(eq. 4-63)}$$

This has the same form as eq. 4-60 except that the charge boundary layer is augmented by the ion transport length δ_e. Figure 4-11 shows that the theory provides a reasonable fit with the results of Lee and Nelson under laminar conditions.

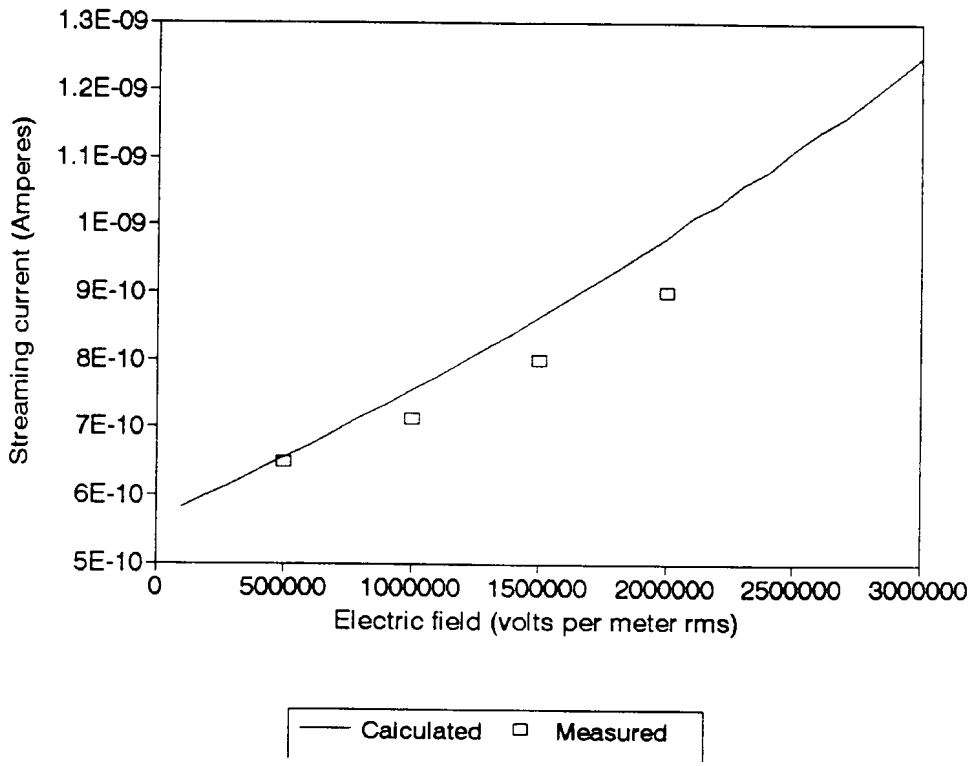

Figure 4-11
Measured and predicted streaming current as a function of applied AC field for laminar flow.

Although no experimental data is available for the geometry of interest, the impact of AC energization in conjunction with turbulent Reynolds numbers must also be addressed. If the transport length does not exceed the diffusion sublayer thickness, the streaming current equations described in the previous sections apply. As for laminar flow, the boundary layer thickness must be adjusted to account for the AC field transport length. However, for a sufficiently large applied field, charge transport into the core of the flow will occur and eq. 4-50 must be integrated to obtain the streaming current as

$$I(L) = -\frac{2}{15}\beta W q'(0)\Delta^3 + \left[\beta W \Delta^2 + 2 V W (H - \Delta)\right] q_B \qquad \text{(eq. 4-64)}$$

where

$$q_B = -\frac{d q'(0) A}{A_2}\left[1 - \exp(-L A_2)\right] \qquad \text{(eq. 4-65)}$$

and

$$A = \frac{b E_o}{2\pi V H}\left(-\frac{\Delta\omega}{b E_o}\right) \qquad \text{(eq. 4-66)}$$

$$A_2 = A + \frac{1}{V\tau} \qquad \text{(eq. 4-67)}$$

The wall charge gradient is converted to an effective charge density via multiplication by the parameter d. In this case, d was assumed to be equal to the diffusion sublayer thickness Δ. The streaming current as a function of the alternating electric field magnitude is shown in Figure 4-12. As expected, a large jump occurs when the field becomes sufficiently large that the electrical transport length exceeds the diffusion sublayer thickness. Below this threshold (which is of the same order of magnitude as experienced in transformer ducts), the only effect of energization is to force the charge boundary layer to penetrate the turbulent core closer to the inlet.

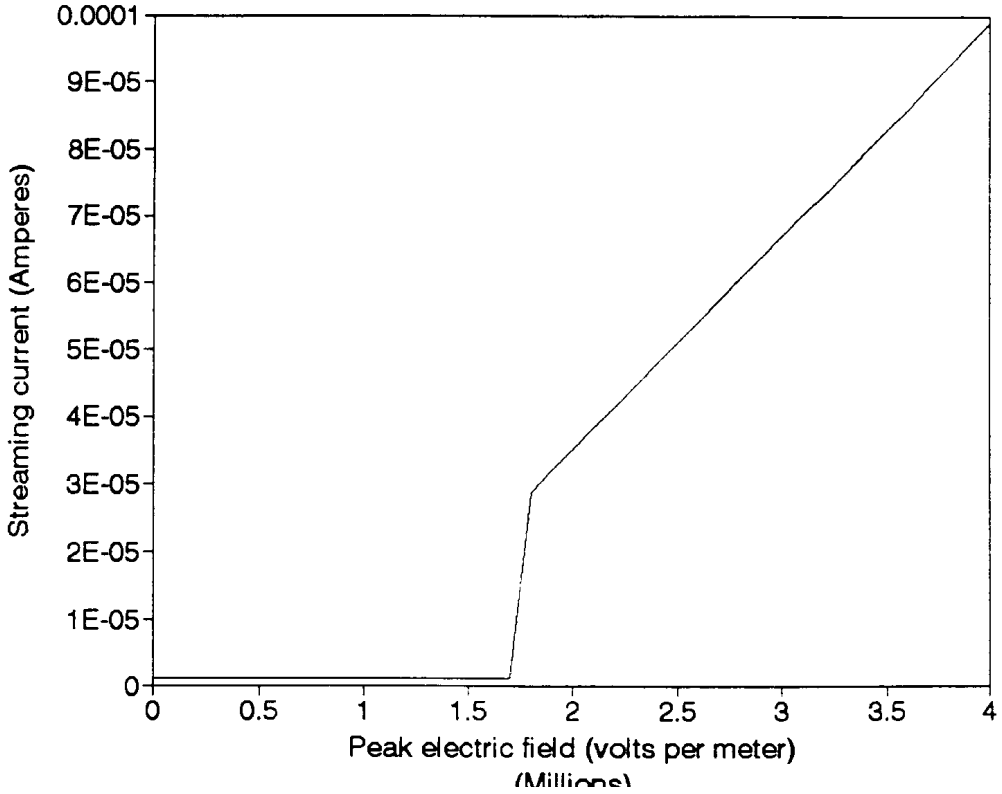

Figure 4-12
Streaming current under turbulent flow conditions as a function of applied AC electric field.

4.3.4 Electrification as a Function of Temperature

The Arrhenius parameter relationships derived in the previous section are now used to model the dependence of streaming current upon oil temperature. The boundary condition $q'(0)_o$ scaling constant and activation energy W_q to fit the experimental data are 1.432×10^{-8} C/m^4 and 2.505×10^{-20} J respectively. The fit was obtained under the assumption that the other temperature dependencies were correctly accounted for. Figure 4-13 shows a comparison of the measured and calculated results at two different velocities. The discrepancy in magnitude at the higher velocity is believed to be the result of experimental error. Recall that good agreement for streaming current as a function of velocity was demonstrated at 25°C.

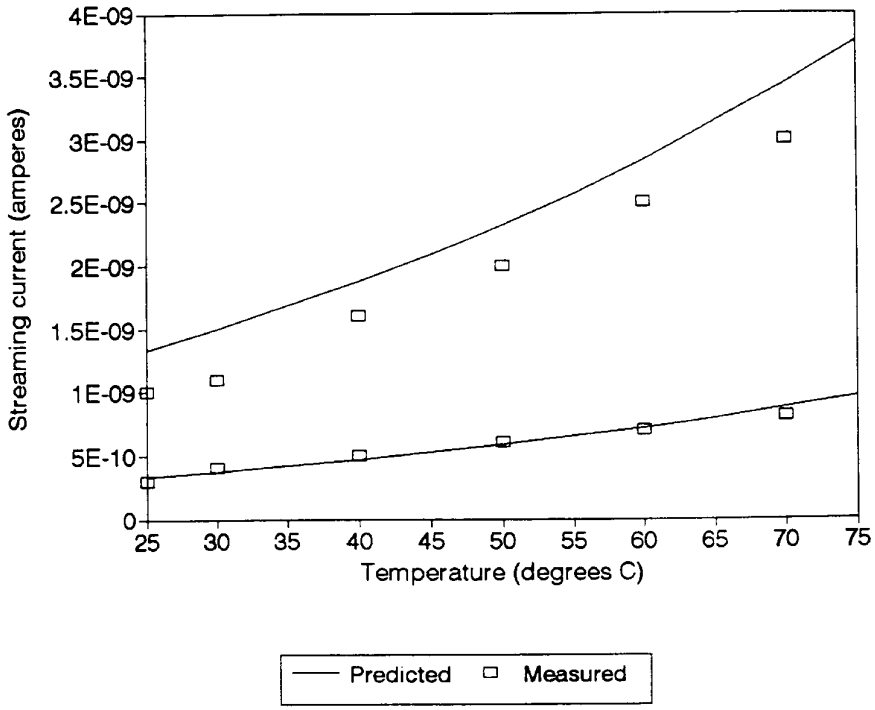

Figure 4-13
Theoretical fit and experimental results for streaming current as a function of oil temperature (oil velocities of 0.7 m/s and 1.4 m/s).

4.4 Summary

The single duct electrification theory has been derived and compared with experimental findings. While empirical results are not available for all cases of interest, a basic understanding of the critical physics has been demonstrated. Having successfully modelled streaming electrification in a simple geometry, the next step will be to address a more complicated structure. The methodology presented in this Chapter will provide the basis for the ultimate goal of a macroscopic approach.

5

A NETWORK-BASED STREAMING ELECTRICFICATION MODEL FOR A CORE-FORM TRANSFORMER STRUCTURE

5.1 Introduction

The single-duct electrification model developed in the previous Chapter must now be incorporated to examine a more realistic geometry. A section of a core-form transformer winding may be easily constructed using simple duct elements. Having established the appropriate terminal characteristics for these elements, a mathematical equivalent streaming electrification model can be defined. Hence, static charge densities may be predicted at the desired nodes in the system.

The concept presented here represents an extension of the methodology originally suggested by Roach and Templeton (66). Their model applies Kirchoff's continuity law to the streaming currents flowing through the various sections of a power transformer. The present approach offers a number of improvements by recognizing different flow regimes, energization effects and static potentials. A flow model is also implemented to provide the required inputs for the electrification solver.

The network formulation is a powerful tool in that the terminal characteristics of a transformer structure may be determined. This structure may then be reduced to a single element and used to assemble a more complex geometry. In this manner, a full-scale transformer structure can be simulated on a macroscopic level without excessive computational requirements.

5.2 Network Based Flow Model

Oil flow distributions in transformer winding structures have been studied by numerous investigators. The flow model presented in this Chapter is not intended to exceed the level of previous work. Rather, an engineering model is assembled to facilitate a case analysis of streaming electrification. Incorporating the flow model

removes the restriction of studying only those structures which have previously been solved. Similarly, any desired driving

flow rates may be selected to allow a more complete analysis. Note that the fluid model emphasizes the macroscopic flow distributions in a transformer geometry which are critical data for the streaming electrification model.

5.2.1 Hydraulic Resistance Models

Consider a simple duct of length L through which a volume flow rate Q is sustained. Defining the inlet and outlet pressures P_1 and P_2 respectively, the duct may be represented by a hydraulic resistance R_H as shown in Figure 5-1. The hydraulic resistance is defined as

$$R_h = \frac{P_1 - P_2}{Q} \qquad \text{(eq. 5-1)}$$

which has a direct electrical analogy with voltage and current introduced in place of pressure and flow rate. Under steady state conditions, the hydraulic resistance provides an effective network element to represent the duct. The task remains to define this element as a function of geometry, fluid parameters and flow regime.

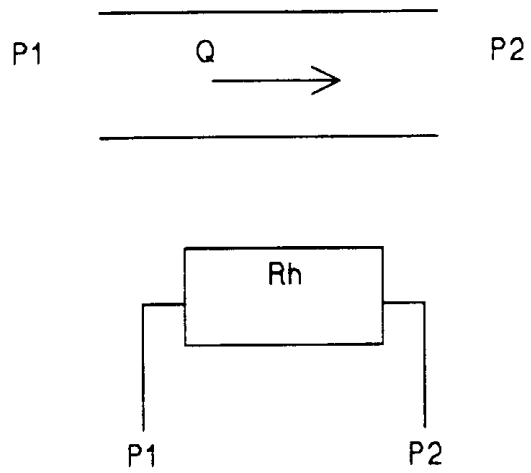

Figure 5-1
Equivalent representation of a pipe by equivalent hydraulic resistance.

For a circular pipe, a no-slip condition at the wall imposed on the Navier-Stokes Equations yields the follow expression for velocity profile (112) (see Appendix C):

$$v(r) = \frac{R^2}{4\mu}\left(-\frac{dP}{dz}\right)\left[1 - \frac{r^2}{R^2}\right] \qquad \text{(eq. 5-2)}$$

This expression assumes fully developed laminar flow and the variables are defined as

v	=	axial z-directed velocity [m/s]
R	=	pipe radius [m]
μ	=	fluid viscosity [Ns/m^2]
P	=	pressure [N/m^2]
z	=	axial distance [m]

The negative sign denotes a favorable pressure gradient such that the flow is in the positive z-direction.

Integrating eq. 5-2 over the pipe radius provides the volume flow rate

$$Q = \int_0^R v \, dr = \frac{\pi R^4}{8\mu}\left(-\frac{dP}{dz} \right). \qquad \text{(eq. 5-3)}$$

Approximating the pressure gradient by

$$-\frac{dP}{dz} = \frac{P_1 - P_2}{L} \qquad \text{(eq. 5-4)}$$

where L is the pipe length, the laminar hydraulic resistance is given via eq. 5-1 as

$$R_h = \frac{8\mu L}{\pi R^2}. \qquad \text{(eq. 5-5)}$$

This expression may be generalized for ducts of non-circular cross section by defining a hydraulic diameter

$$d_H = \frac{4 A_c}{C_c} \qquad \text{(eq. 5-6)}$$

where A_c is the cross sectional area of the flow and C_c is the wetted periphery. The general form of eq. 5-5 thus becomes

$$R_h = 40.74 \frac{\nu \rho L}{d_H^4} \qquad \text{(eq. 5-7)}$$

where the kinematic viscosity, ν, has been incorporated as the ratio of the absolute viscosity μ and density ρ.

The validity of 5-7 is determined based on the Reynolds number defined as

$$R_e = \frac{V\, d_H}{\nu} \qquad \text{(eq. 5-8)}$$

where V is the mean flow velocity. For $R_e \leq 2000$, laminar flow is assumed in a straight duct.

In the case of turbulent flow, the hydraulic resistance becomes non-linear and a friction factor must be incorporated. The Blasius formula (112)

$$\frac{P_1 - P_2}{L} = \frac{\lambda_f \rho V^2}{2\, d_H} \qquad \text{(eq. 5-9)}$$

where

$$\lambda_f = \frac{.3164}{R_e^{\frac{1}{4}}} \qquad \text{(eq. 5-10)}$$

provides an empirical friction factor for turbulent flow. Noting that the flow rate and mean velocity correlate for pipe flow as

$$V = \frac{4\, Q}{\pi\, d_H^2}, \qquad \text{(eq. 5-11)}$$

eq. 5-9 becomes

$$I_{out} = q_{in}\, Q \exp\left(-\frac{L}{V \tau} \right). \qquad \text{(eq. 5-12)}$$

and the hydraulic resistance is found to be

$$R_h = \frac{.4429\, (L \rho)^{\frac{4}{7}} \nu^{\frac{1}{7}}}{d_H^{\frac{19}{7}}} (P_1 - P_2)^{\frac{3}{7}} \qquad \text{(eq. 5-13)}$$

for turbulent flow ($R_e > 2600$). As for laminar flow, the use of a hydraulic diameter allows for ducts of non-circular cross section. In the context of this work, all ducts will be treated as circular pipes to simplify flow modelling.

The hydraulic resistance for the transition region ($2000 < R_e < 2600$) remains to be defined. In the absence of specific data, the characteristic will be interpolated between

the laminar and turbulent regimes. Using eqs. 5-7 and 5-13 to determine the pressure drop and corresponding hydraulic resistances, the appropriate slope and intercept are determined. The transition region model is thus found to be

$$R_h = 3.85 \times 10^{-4} \frac{1}{\nu\, d_h} (P_1 - P_2) + 16.1 \frac{\nu\, \rho\, L}{d_H^4}. \qquad \text{(eq. 5-14)}$$

The hydraulic resistance formulations defined thus far apply only to straight ducts. Additional models will be needed to consider the bends and junctions which serve as connecting points for assembling a large structure. Unfortunately, data for the required hydraulic resistances in the desired range of Reynolds numbers is not readily available. The results of Jamison and Villemonte (114) for oil in metal pipe networks are the most appropriate. Their empirical findings in the range of $10 < R_e < 10000$ offer at least some information about the losses in elbows and tees. Some justification for applying their data to core-form transformer winding ducts is provided by Oliver (115).

The equivalent hydraulic networks for dividing and combining tee junctions are shown in Figure 5-2. Following Allen and Childs (116), the junction losses have been inserted into the combining or dividing branches. Adopting the curve fitting results of Oliver (115) for the data of Jaimison and Villemonte (114) to the present nomenclature, the following hydraulic resistance formulas are obtained:

Combining tee

$$R_{h\,1\text{-}m} = 636.62 \frac{\nu\, \rho}{d_H^3} \left[10.65 - 19.76 \frac{Q_1}{Q_m} + 11.2 \left(\frac{Q_1}{Q_m} \right)^2 \right] \qquad \text{(eq. 5-15)}$$

$$R_{h\,2\text{-}m} = 4647.32 \frac{\rho\, \nu}{d_H^3} \qquad \text{(eq. 5-16)}$$

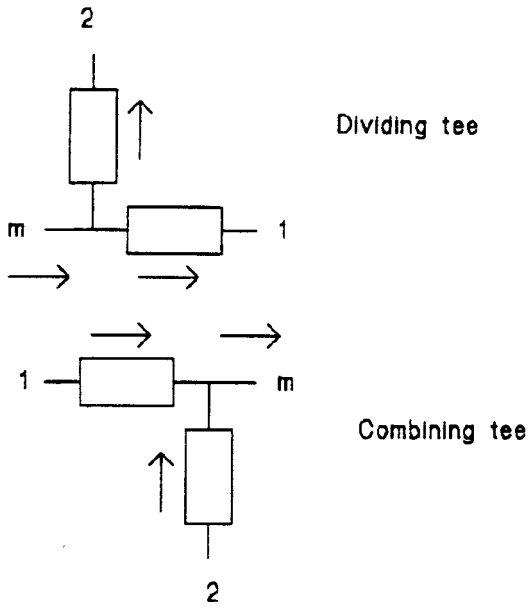

Figure 5-2
Equivalent representations of junction losses in combining and dividing tees.

Dividing tee

$$R_{h\,m\text{-}1} = 636.62\,\frac{\nu\,\rho}{d_H^3}\left[\,10.65 - 19.76\,\frac{Q_1}{Q_m} + 11.2\left(\frac{Q_1}{Q_m}\right)^2\right] \qquad \text{(eq. 5-17)}$$

$$R_{h\,2\text{-}m} = 4647.32\,\frac{\rho\,\nu}{d_H^3} \qquad \text{(eq. 5-18)}$$

For the case of a 90° elbow, the tee formulation is used with the flow rate in branch one set to zero. Hence the hydraulic resistance is simply given by the expression for $R_{h2\text{-}m}$ or $R_{hm\text{-}2}$.

5.2.2 Network Formulation

Having defined the hydraulic resistance characteristics of the required components, the network approach may now be demonstrated. A section of core-form winding is illustrated in Figure 5-3. This geometry contains each of the elements discussed in the previous section and provides a simple example of how the flow network is assembled. Note that the length to hydraulic diameter ratios for the straight ducts in this structure are relatively small (on the order of 10). This implies that some error will be introduced by the

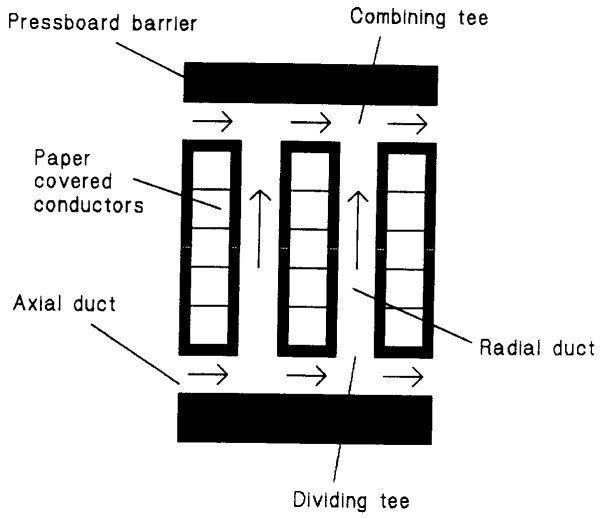

Figure 5-3
A section of core-form winding illustrating the various duct types.

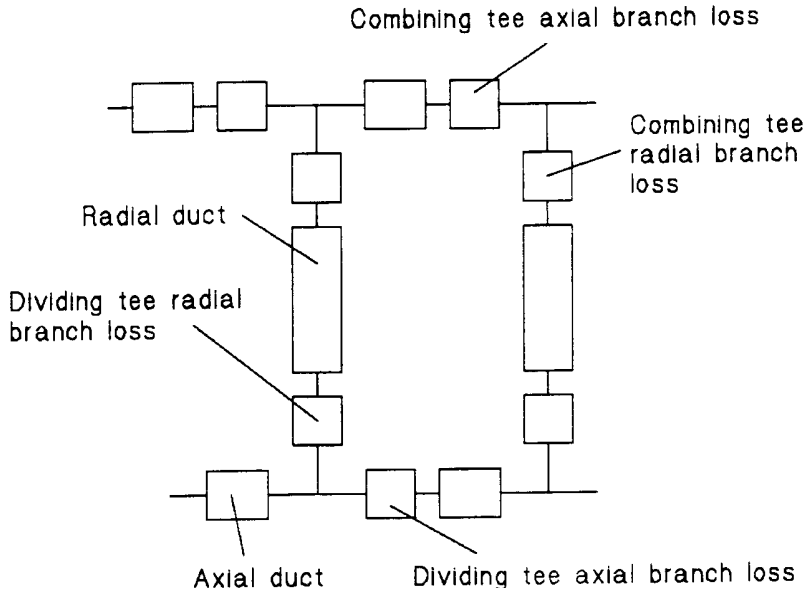

Figure 5-4
Equivalent network formulation for the geometry shown in Figure 5-3.

network. The solver was implemented in FORTRAN such that generic network data files could be read and solved. An initial iteration using Gauss elimination for a direct solution with no flow in the network was found to accelerate convergence significantly. The change in the infinite norm (117) of the pressure vector from one iteration to the next is used as the convergence criterion. The tolerance is typically selected to be less than one percent.

For the given example in Figure 5-4, the flow will divide equally between the symmetric branches of the network. This network was used as a simple test case to verify the algorithm and computer implementation. The results for a more complicated structure will be presented later in this section and compared with the findings of other investigators. The fully developed flow assumption is found to be acceptable for determining the flow rate distributions to a first order.

5.3 Electrification Model

The network generated for the flow solution has an electrification analogy which can be used to calculate the nodal charge densities. Charge transfer elements are substituted for hydraulic resistances and streaming currents replace flow rates. Using a common network for both solutions ensures that only one data file is needed to solve a given geometry. The master data file also includes the leakage resistance matrix which is superimposed upon the network such that static potentials may be calculated.

5.3.1 Single Element Electrification Models

Oil flowing through a straight duct will lose bulk charge from relaxation effects and gain charge from flow electrification. The latter effect is treated as an injected streaming current at the outlet node of the duct. These currents become the sources which drive the network. The entering mean uniform bulk charge will obey the simple relaxation law

$$q_{out} = q_{in} \exp\left(- \frac{L}{V \tau} \right) \qquad \text{(eq. 5-20)}$$

for a duct of length L. The exiting streaming current resulting from the convection of the entering charge through the duct thus becomes

$$R_h = \frac{.4429 (L \rho)^{\frac{4}{7}} \nu^{\frac{1}{7}}}{d_H^{\frac{19}{7}}} (P_1 - P_2)^{\frac{3}{7}} \qquad \text{(eq. 5-21)}$$

This relaxation factor may be augmented by field transport under energized conditions as shown previously in eq. 4-51. Under these conditions, relaxation associated with the self-field is negligible and

$$q_{out} = q_{in} \exp\left[- L \left(A + \frac{1}{V \tau} \right) \right] \qquad \text{(eq. 5-22)}$$

with A given by eq 4-51. For either case, the relaxation factors are implemented in the form

$$Q_{eff} = Q \text{ x relaxation factor} \qquad \text{(eq. 5-23)}$$

where Q_{eff} is now the effective flow rate which convects the inlet charges through the duct. These factors are used in the electrification connectivity matrix in the same manner that the hydraulic admittances are used in the flow model. The generated streaming current formulations have been described in Section 4 and their implementation is described in a later section.

As in the case of the flow model, elbows and junctions must also be considered. However, there is literally no information available to describe charge convection in these elements. As a very crude approximation, the streaming currents generated in the virtual loss elements is postulated in terms of the pressure losses by

$$I = K_E (P_1 - P_2) \qquad \text{(eq. 5-24)}$$

where the factor K_E will be entirely empirical. Initially, K_E will be set to zero to determine how critical these elements become when calibrating the network model.

The junction and elbow elements will treated as mixing regions for convected charge. In other words, the charge profile entering from a straight duct will become uniformly distributed in the mixing element downstream. This assumption is necessary in order to use the discrete element approach. Recall that the duct models in Section 4 incorporate a mean uniform inlet bulk charge density as a parameter. In addition, the network model is based on mean uniform charge densities at the inlet and outlet of each physical duct. Note that the loss elements are virtual, having no length and thus are modelled with relaxation factors of unity.

The streaming current models developed in the previous section assume fully developed channel flows. While clearly appropriate for the test duct having a length of 60 cm, this assumption raises some doubt for more realistic ducts. In an actual transformer, the length to hydraulic diameter ratio will be on the order of 10 for radial winding ducts. Fortunately, the Schmitt number

$$S = \frac{\nu}{D} \qquad \text{(eq. 5-25)}$$

is typically on the order of 10^6 for transformer oil and the momentum boundary layer will develop much faster than the charge boundary layer. In the case of laminar flow, an assessment of the error introduced by assuming developed flow may be considered for an analogous thermal problem.

The situation at hand is quite similar to the effect of an unheated starting length for convective heat transfer. For a laminar flow over a flat plate subject to a uniform heat flux, the Nusselt number as a function of position is derived by Smith (118) as

$$N u_x = .418 R_{ex}^{\frac{1}{2}} P r^{\frac{1}{3}} \left(1 - \frac{x}{x_o}\right)^{-\frac{1}{3}} \qquad \text{(eq. 5-26)}$$

where

R_{ex} = Reynolds number based on distance from leading edge

Pr = Prandtl number

x = distance from leading edge [m]

x_o = unheated starting length [m].

The solution applies only for high Prandtl number (analogous to high Schmitt number) and corresponds to Figure 5-5. The unheated starting length x_o is the distance over which the flow is allowed to develop before heat transfer begins. In a channel, a momentum boundary layer will develop on each wall. The fully developed flow will exist at the point where these boundary layers join at the center line.

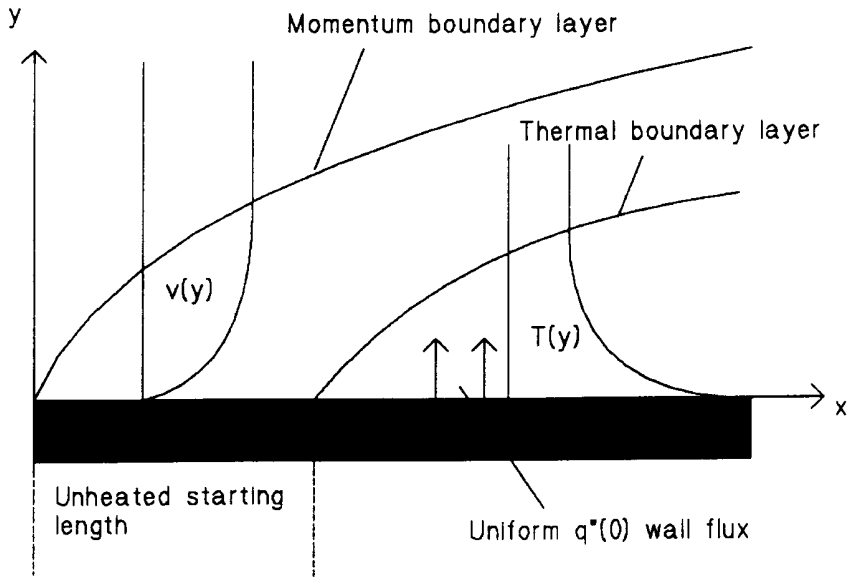

Figure 5-5
Illustration of convective heat transfer for laminar flow across a flat plate having uniform wall flux.

The momentum boundary layer is given as (113)

$$\delta_m = 4.6 \left[\frac{\nu x}{U_\infty} \right]^{\frac{1}{2}} \qquad \text{(eq. 5-27)}$$

where U_∞ is the free stream velocity. The appropriate distance for developed flow is thus approximated by

$$H = \delta_m \_ \rightarrow x = \frac{H^2 U_\infty}{21.16\nu} \qquad \text{(eq. 5-28)}$$

Recall that H is the channel half height. Comparing eq. 5-26 with $x_o = 0$ and x_o given by eq. 5-28 provides a measure of the error introduced by assuming a developed flow. The normalized Nusselt numbers are compared over the length of a 0.1 m duct in Figure 5-6.

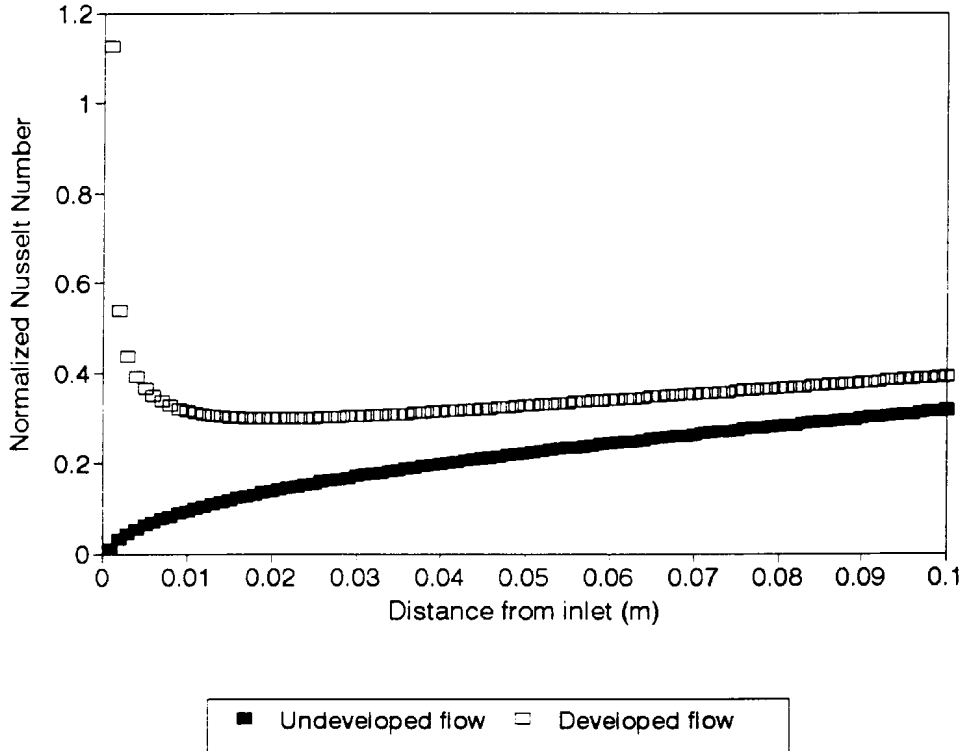

Figure 5-6
Comparison of developed and undeveloped flow Nusselt numbers for laminar flow across a flat plate with constant wall flux.

Note that the singularity in the developed flow result occurs because the analysis did not allow for axial diffusion. The Nusselt numbers were normalized in terms of fluid parameters. Neglecting the singularity in the initial millimeters of the duct and

averaging illustrates that the mean nusselt numbers differ by roughly a factor of two. This analysis assumes a channel height of 0.7 cm and a kinematic viscosity of 1.77×10^{-5} m^2/s at 25°C. The error will increase at higher temperatures but remains within an order of magnitude over the range of interest. The thermal analogy demonstrates that the assumption of fully developed flow is acceptable for an order of magnitude analysis. This justification vindicates the streaming current models for the longer radial ducts of a core-form transformer. While the axial ducts are even shorter and hence more complicated, they will primarily see well-mixed turbulent flow and will not be nearly as sensitive to flow development.

5.3.2 Network Formulation

Having created a discrete equivalent element for each piece of a transformer geometry, the network solution is determined by imposing continuity at each node. The formulation of Kirchoff's current law at a given node is illustrated for the simple geometry shown in Figure 5-7. The equivalent discrete network is shown in Figure 5-8 with arrows denoting

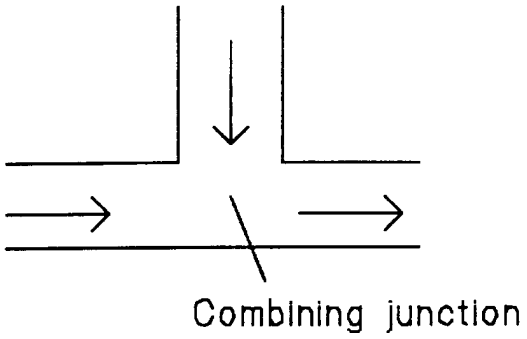

Figure 5-7
Example of a junction having entering and exiting flows.

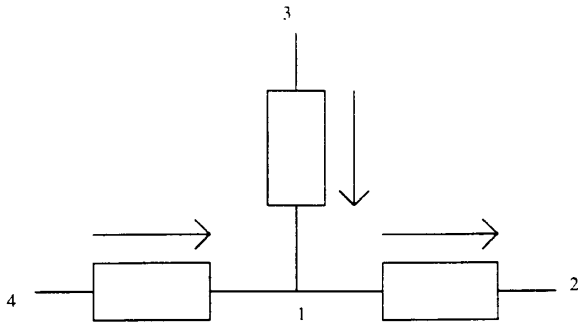

Figure 5-8
Equivalent network for demonstrating the formulation of Kirchoff's current law in terms of streaming currents.

the direction of the branch flows. At node 1, the sum of the streaming currents will be

$$- I_{41} - \quad I_{31} - q_4 Q_{41} R_{41} - q_3 Q_{31} R_{31} + q_1 Q_{12} = 0 \qquad \text{(eq. 5-29)}$$

where

I_{ij} = injected streaming current at node j due to charge generation in branch i,j

q_i = mean uniform charge density at node i

Q_{ij} = volume flow rate from node i to node j

R_{ij} = relaxation factor for duct i,j

The charge density leaving the node is convected subject to relaxation to the downstream node of the appropriate branch. In the case where a node has multiple outlet branches, the streaming currents divide according to the branch flow rates such that the total entering and exiting currents sum to zero.

Continuity equations having the form of eq. 5-29 are generated for each node in the network and the problem may be represented in matrix form as

$$[Q_{eff}]\,[q] = [I] \qquad \text{(eq. 5-30)}$$

where Q_{eff} represents the connectivity matrix with appropriate relaxation factors calculated for the network elements. The current vector represents the source injected at each node which dictates the charge density vector solution. Recognizing that the injected currents are dependent upon the inlet charge densities for each branch, the

problem is non-linear. Fortunately, the non-linearity is relatively weak and repeated solution by Gauss elimination was found to produce convergence with relatively few iterations. A tolerance of less than one percent is typically obtained without exceeding 10 iterations. The electrification solver was implemented in FORTRAN code and shares a common input file with the fluid solver discussed in the previous section.

5.3.3 Static Potential Solution

The key threat of streaming electrification is the development of large static potentials on transformer insulation surfaces. Another advantage of the network based approach is the capability for calculating these potentials. This is accomplished by overlaying a leakage resistance matrix on the given network model. In addition, the surface resistances of the network elements must be specified. The potentials are dictated by the flow of currents through the insulation structure to supply the electrification process.

As in the case of the flow and electrification models, the static potential solution requires a discrete network. A bulk leakage resistance to ground is assigned to each node as a function of geometry and material properties. Each duct element is treated in terms of a surface resistance connecting the end nodes. In this manner, the leakage of charge along insulating surfaces is recognized. The leakage currents for a given duct are defined in terms of the inlet and outlet charge densities to ensure continuity of the streaming current.

The static potential model maintains the previous assumption of a steady state with respect to time. Under this condition, the charge residing on a duct surface will have reached sufficient magnitude that the associated electric field can drive a leakage current which exactly balances accumulation. The situation is illustrated for a single duct element in Figure 5-9. The net current flowing from the oil into the wall is given by the difference between the lumped uniform relaxation and generation currents as

$$I_w = I_r - I_g \qquad \text{(eq. 5-31)}$$

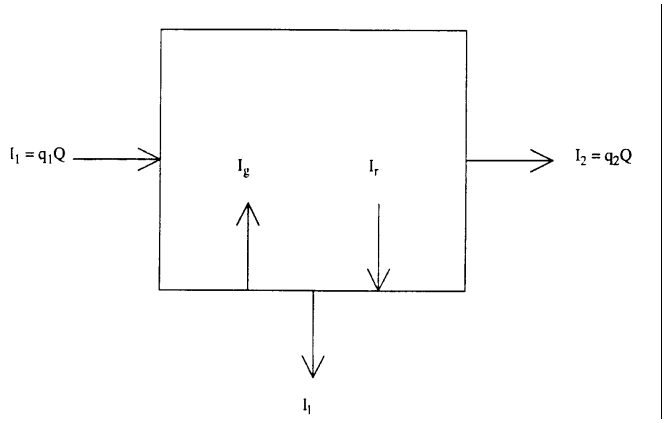

Figure 5-9
Lumped current representation of charge generation, relaxation and leakage in a duct element.

where

I_r = relaxation current [A]

I_g = generation current [A].

Recognizing that positive charges are being convected in the case of cellulose/oil system, the sign convention has been chosen such that the wall current is positive when relaxation dominates. For the steady state, continuity dictates that $I_w = I_l$ where the latter current represents leakage.

In reality, the surface charge density and hence potential will be spatially distributed through the duct. The present analysis incorporates lumped values such that uniform leakage currents and hence surface charge densities are assumed. This is justified by the requirement of computational simplicity required for the macroscopic model. Furthermore, the interpretation of a large transformer structure will not be significantly influenced by the localized charge and potential distributions. Rather, the aim of the modelling is to locate hazardous regions for a more detailed study.

The leakage current can thus be readily defined in terms of the entering and exiting mean uniform charge densities in the oil and the volume flow rate via

$$I_l = Q\,(q_{in} - q_{out}). \qquad \text{(eq. 5-32)}$$

The chosen convention shows that a negative leakage current will flow to supply charge separation and vice versa. The uniform leakage currents must now be incorporated into the static potential network model. The discrete element representation of Figure 5-9 is

shown in Figure 5-10. The leakage current has been equally divided between sources attached to the inlet and outlet nodes.

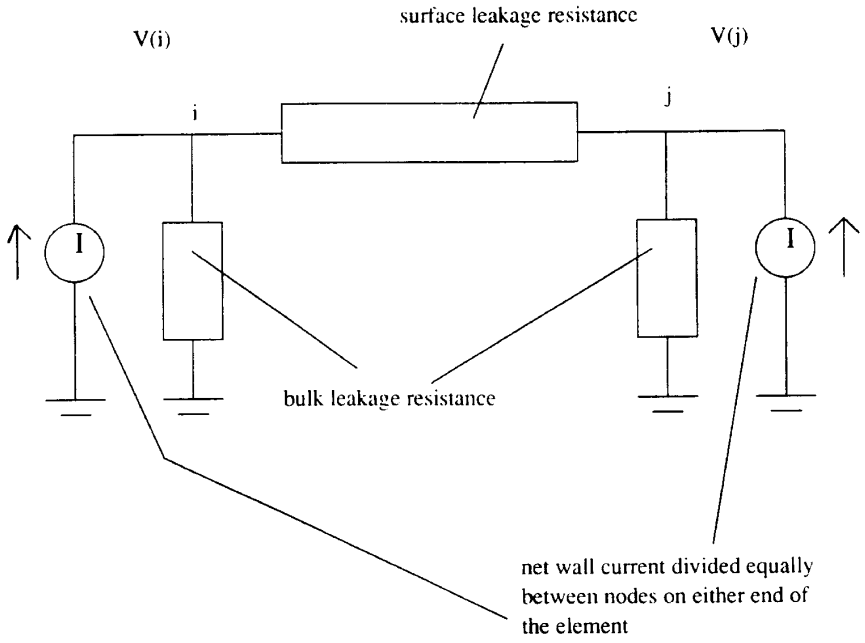

Figure 5-10
Pi-line equivalent circuit for leakage resistance and current sources in a transformer duct.

The bulk leakage resistance calculations are greatly simplified in a core-form transformer winding. As shown in Figure 5-3, at least one side of a given duct has a parallel ground plane in the form of the bundled winding conductors. Neglecting edge effects, the bulk leakage resistance for a given duct will thus be

$$R_L = \frac{l}{\sigma_P A_s} \qquad \text{(eq. 5-33)}$$

where

l = leakage distance [m]

σ_P = bulk conductivity of cellulose [S/m]

A_s = area of duct side [m_2]

For duct sides not parallel to a ground plane, the charges will flow across the pressboard/oil surfaces seeking locations of minimal bulk resistance to ground. Hence, the mean bulk resistance of a given duct is simply the parallel combination of the

resistances given by eq. 5-33 for sides adjacent to the winding conductors. The bulk resistance of the duct is equally divided between the end nodes of a branch in the same manner as the leakage current sources. This so called "pi-line" representation of the duct has been previously demonstrated in Figure 5-10.

The axial surface resistance of each duct will depend on the effective area. Adopting the nomenclature of semiconductor fabrication, the surface resistivity is expressed in ohms per square (119). The resistance is thus determined by the number of geometric squares required to bridge the axial span such that

$$R_{LS} = \frac{1}{\sigma_{PS}} N_{SQ} \qquad \text{(eq. 5-34)}$$

where N_{SQ} is the effective number of squares. Typically, core-form transformer ducts have perimeters exceeding their length and N_{SQ} is less than one.

The bulk resistivity of cellulose insulation has been well characterized (75, 76). The surface resistivity is more vague and will fall between the oil and cellulose bulk values. In general, many dielectrics exhibit surface resistivities which are roughly one order of magnitude less than their bulk values (120). Therefore, σ_{PS} will be assumed to be 10 times σ_P for present purposes. The data presented by Moser et al (75) shows that σ_{PB} is logarithmically dependent on temperature. Specific calculations of leakage resistances are presented in conjunction with the case studies for which they apply.

Having defined the streaming potential network for a single duct element, a larger geometry may be addressed. The network is formulated as

$$[R_{LS}]\,[I_L] = [V_S] \qquad \text{(eq. 5-35)}$$

where the voltage vector is the desired potential at each network node. The source current vector represents the net leakage current injected at each node via the number of connected elements. The diagonal elements of the resistance matrix represent the parallel combination of bulk resistances in all of the ducts connected to each node. The off-diagonal elements define connectivity in terms of the duct surface resistances. This network will be linear and can thus be solved directly. The solver has been implemented in FORTRAN and shares a common data file with the electrification and flow solvers.

A final note is in order regarding the influence of the transformer winding. While power frequency voltages are applied, the winding conductors are still effectively ground with respect to the static potentials resulting from electrification. The alternating voltage is assumed not to influence the leakage currents or streaming potentials in terms of a time averaged scenario. Rather, the superposition of the static

potentials upon the operating voltages is more critical for evaluating the dielectric safety margin reductions.

5.4 Calibration of Network Approach for an Actual Core-form Structure

In order to extend the network methodology to a real transformer, an intermediate level of calibration is desirable. The core-form structure of Figure 2-3 first examined by Lee and Nelson (26) is well suited to this task. Their results are incorporated along with data obtained during the moisture equilibrium experiments of Section 2. This model was fabricated by EHV Weidmann in St. Johnsbury Vermont under the guidance of Mr. W. J. McNutt.

5.4.1 Equivalent Network and Material Parameters

The core-form model may be represented in terms of the network previously shown in Figure 5-3. The first "pass" of the model is assembled by cascading these building blocks together as shown in Figure 5-11. The entire structure is comprised of two identical passes in series joined by a single duct where the total driving flow rate is achieved. Note that the ducts on the inlet/outlet side of the model are roughly 30 percent larger than those on the opposite side.

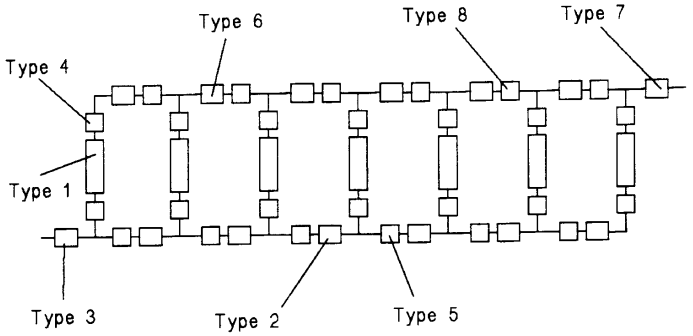

Figure 5-11
Equivalent representation of one pass of the core-form model.

The radial ducts in this structure are subdivided by two square spacers. As will be shown in the following section, these spacers are much closer together than those in an actual core-form transformer. Nevertheless, each radial duct is effectively represented by three sub-channels having different cross sectional areas. A similar situation exists for the axial ducts where single spacers run the length of the structure. One must recognize that the model is essentially a slice of a complete winding and that the spacers are required to support the conductor sections. Further difficulties are introduced by the poor tolerances observed in one of the models which was disassembled for examination.

The core-form geometry was divided into ideal elements to facilitate a network analysis. Eight different duct types were identified based on the model schematics and actual measurements. An effective cross section was derived for each type based on the parallel combination of hydraulic resistances. In this manner, the complexities presented by the support spacers are reduced and the problem reduced to a more manageable form. While this simplification is surely achieved at some cost in accuracy, the results presented later in this section demonstrate feasibility for an order of magnitude analysis.

The eight duct types are described as follows:

Type 1 - Radial straight duct (Chapter 4 model)

Type 2 - Axial duct in large manifold (Chapter 4 model)

Type 3 - Axial inlet/outlet ducts in large manifold (Chapter 4 model)

Type 4 - Radial duct junction losses (mixing model)

Type 5 - Axial duct junction losses in large manifold (mixing model)

Type 6 - Axial duct in small manifold (Chapter 4 model used)

Type 7 - Axial feed duct in small manifold (Chapter 4 model)

Type 8 - Axial junction losses in small manifold (mixing model)

The effective parameters for each duct type are listed in Table 5-1. The hydraulic diameter values are used in the fluid solver while the rectangular dimensions are used in the electrification solver. Recall that there is no physical length associated with the virtual junction loss elements.

Recall from Section 2 that all of the winding sections are energized at the same potential with respect to an external ground. Hence, field transport will augment the electrification process only in the axial ducts. The electric field at the oil/pressboard interface is estimated based on the potential drop across the oil. This voltage drop is dictated for AC by the capacitive divider action between the oil and insulating paper covering the winding conductor bundles. In the present case, the external Spauldite enclosure and pressboard walls must also be considered. A numerical analysis by Lee (26) estimates that the axial duct transverse electric fields in the model are on the order of .04 kV/mm per kV of applied voltage.

Table 5-1
Duct type geometry definitions.

Duct type	length [m]	d_h[m]	half-height [m]	width [m]
1	1.0×10^{-1}	1.4×10^{-2}	3.4×10^{-3}	7.35×10^{-2}
2	1.3×10^{-1}	2.1×10^{-2}	5.5×10^{-3}	9.0×10^{-2}
3	1.6×10^{-2}	2.1×10^{-2}	5.5×10^{-3}	9.0×10^{-2}
4	—	1.4×10^{-2}	—	—
5	—	2.1×10^{-2}	—	—
6	1.3×10^{-2}	1.6×10^{-2}	4.0×10^{-3}	9.1×10^{-2}
7	1.6×10^{-2}	1.6×10^{-2}	4.0×10^{-3}	9.1×10^{-2}
8	—	1.6×10^{-2}	—	—

Surface and bulk leakage resistances must be specified for each duct and end node in the network. The former are calculated based on squares of effective area in accordance with eq. 5-34. The bulk values are defined using eq. 5-33 with the total bulk resistance being equal to the parallel combination of two identical end resistors. The resistances for each applicable duct are shown in Table 5-2 assuming $\rho_{PB} = 1 \times 10^{15}$ at 25°C (75). Note that the surface resistances of the virtual ducts are negligible and simply taken as unity. The virtual elements have no meaningful bulk resistance to ground.

The oil parameters remain to be defined for the present problem. The kinematic viscosity for Shell Diala-A transformer oil was measured by Lee (26) as a function of temperature. Combining this characteristic with the assumptions of Section 4, the ion mobility and diffusion coefficient are inferred. Finally, oil conductivity data is available from Section 2. these parameters were fitted to the Arrhenius temperature distributions of eqs. 4-52, 4-53, 4-55 and 4-57 respectively. the corresponding activation energies and scaling constants used for the core-form calibration are presented in Table 5-3. The electrification boundary condition must be defined empirically in the same manner as for a single duct analysis.

5.4.2 Fluid Model Results

The network depicted in Figure 5-11 was solved using the methodology described in Section 5-2 over a range of flow rates. At 10 gpm (6.31×10^{-4} m^3/s) all of the flows are essentially laminar based on Reynolds number calculations at 25°C. The axial duct flows were found to be predominantly turbulent at the same temperature when the

driving flow rate was set to 40 gpm (2.52 x $10^{-3}$$m^3$/s). Turbulent flows were possible in the radial ducts

Table 5-2
Surface and bulk resistances used for core-form model.

Duct type	$R_s(\Omega)$	$R_b(\Omega)$
1	6.25×10^{13}	4.35×10^{13}
2	6.6×10^{12}	6.7×10^{14}
3	8.1×10^{12}	6.7×10^{14}
4	1	—
5	1	—
6	6.6×10^{12}	6.7×10^{14}
7	8.1×10^{12}	6.7×10^{14}
8	1	—

Table 5-3
Arrhenius parameters of transformer oil used for core-form model calibration.

Parameter	Activation energy (J)	Scaling constant (m^2/s)
ν	4.03×10^{20}	9.83×10^{10}
b	4.03×10^{20}	8.86×10^{12}
D	4.03×10^{20}	7.77×10^{10}
σ	3.97×10^{20}	6.96×10^{-8}

only at elevated temperatures where the kinematic viscosity was sufficiently reduced. Similarly, increasing the temperature also caused turbulent flow in the axial ducts at lower flow rates.

The radial duct flow rates are typically distributed as shown in Figure 5-12, which has been normalized in terms of the driving flow rate. The skewed characteristic is readily explained by the different axial duct diameters. The fluid entering the structure through the pass 1 inlet duct sees a blowing manifold having a larger hydraulic diameter than the sucking manifold. Hence, the majority of the oil remains in the larger manifold until it is forced across by the pressboard baffle separating the passes. The

converse situation exists in the second pass where the flow immediately moves through the first radial duct in route to the large sucking manifold.

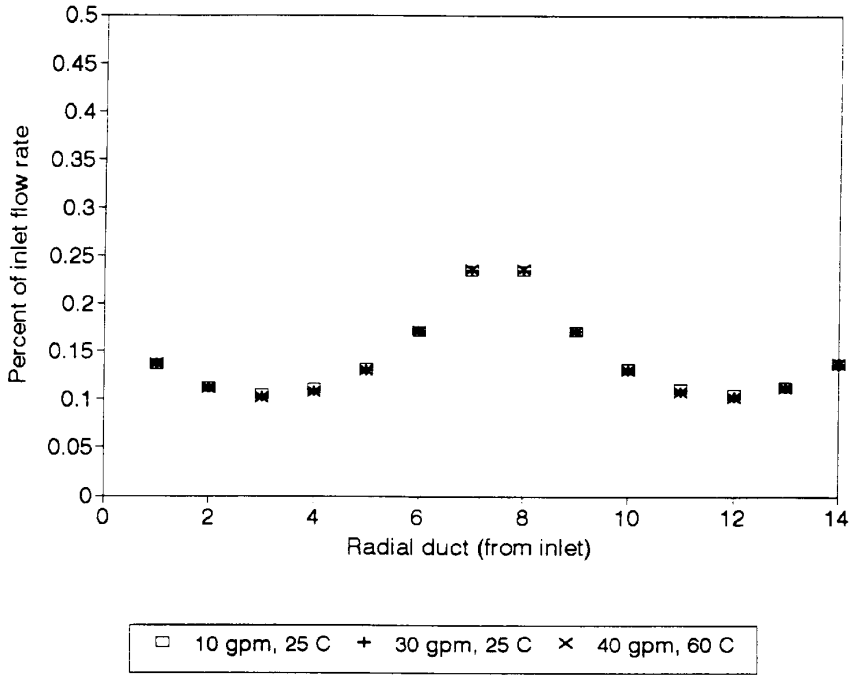

Figure 5-12
Normalized radial duct flow distribution.

The corresponding normalized axial flow distribution on the inlet/outlet side of the model is shown in Figure 5-13. The axial flows decrease along the first pass as oil is lost to the radial ducts and a minimum is achieved near the baffle. Exactly the opposite situation exists in the second pass as a result of even symmetry about the baffle. Note that the flow distributions are relatively insensitive to driving flow rate and temperature.

These results are supported by the findings of Szpiro, Allen and Richards (121) who conducted a theoretical and empirical investigation of a similar manifold structure. They were able to obtain very good agreement for various plexiglass models having different manifold dimensions. For a single pass system of five radial ducts, their radial flow distribution with the blowing manifold 50 percent larger than the sucking manifold are shown in Figure 5-14. The symmetric manifold case is also presented in Figure 5-15 for a five-duct pass. Note that the present model predicts a similar distribution under these conditions as shown in Figure 5-16. The fluid model results may thus be accepted with much greater confidence based on this comparison.

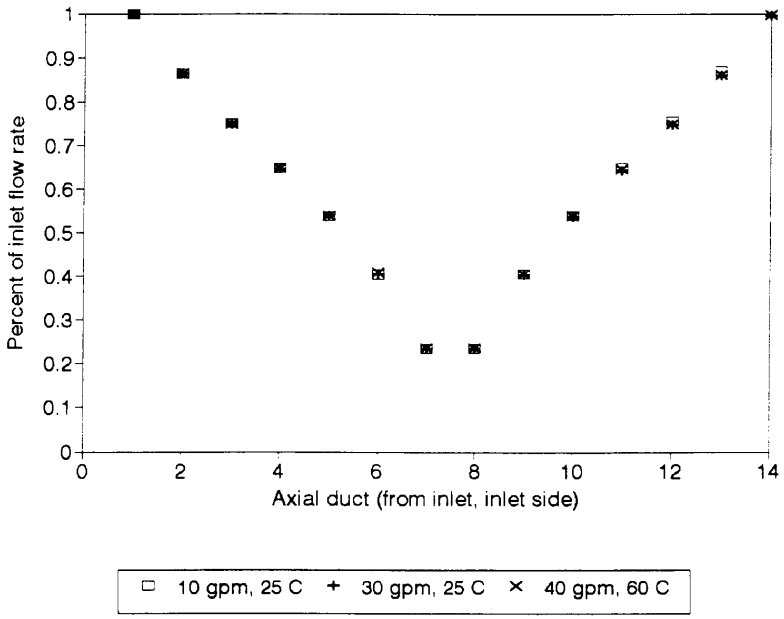

Figure 5-13
Normalized axial flow distribution on the inlet/outlet side of the model.

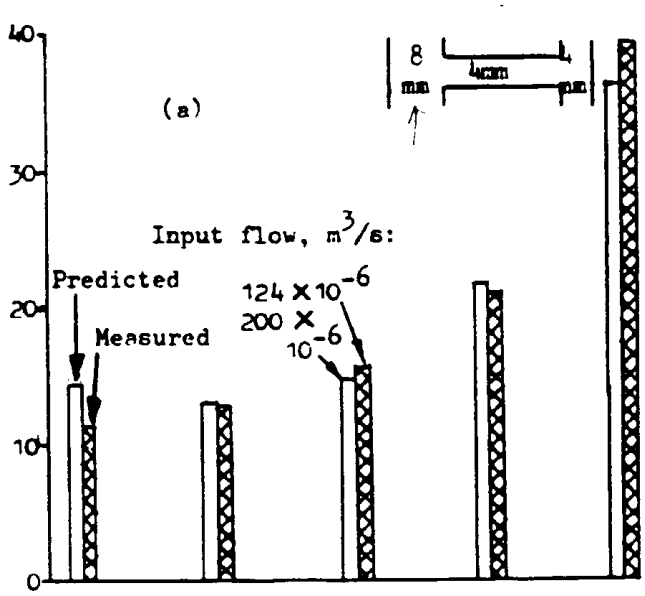

Figure 5-14
Results of Szpiro, Allen and Richards (121) for radial ducts flow distributions in asymmetric manifolds.

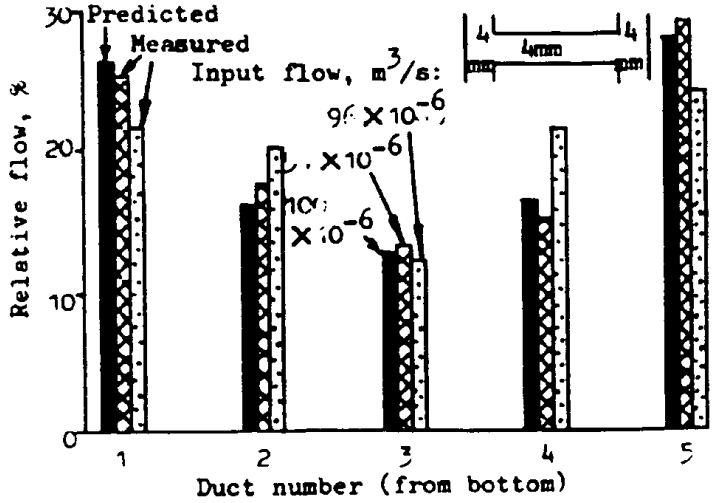

Figure 5-15
Results of Szpiro, Allen and Richards (121) for radial ducts flow distributions in a symmetric manifold.

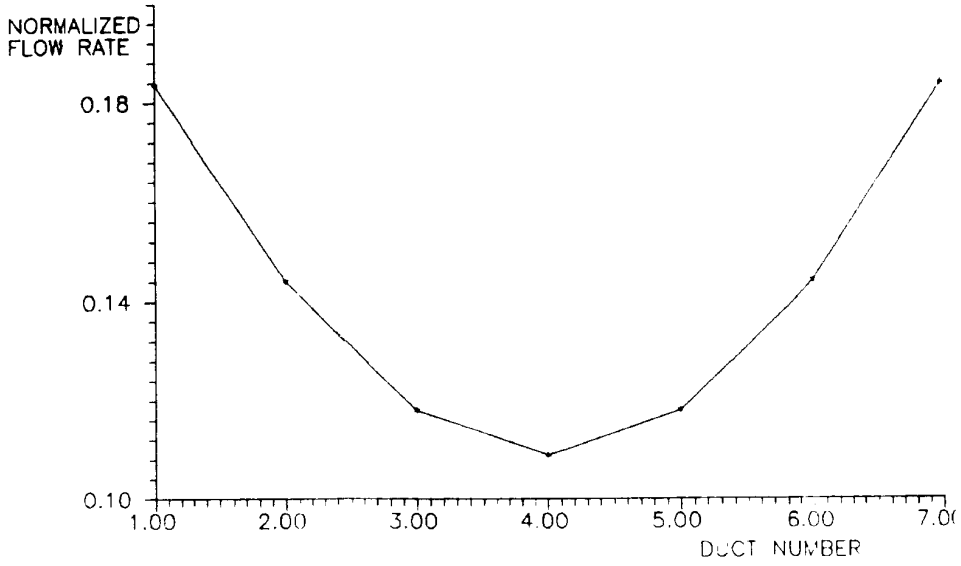

Figure 5-16
Predictions for core-form model assuming symmetric manifolds.

5.4.3 Electrification Model Calibration Results

Having defined the oil flow distributions in the core-form model, the electrification model may now be applied. The calculated charge exiting for the structure will be compared with empirical measurements using a tandem charge monitor as shown in Figure 2-2. The model parameters can thus be adjusted for correct charge density magnitudes such that the predicted and observed trends may be compared. This intermediate calibration provides critical justification of the methodology prior to examining a full-scale structure.

At 25°C with a volume flow rate of 1.26×10^{-3} m^3/s (20 gpm), the boundary condition of eq. 4-1 was defined for a = 1. A value of -700 C/m^4 for $q'(0)_o$ is required to fit the measured charge density at the model outlet. Calculations were performed using this value over the range of 6.31×10^{-4} m^3/s (10 gpm) to 2.52×10^{-3} m^3/s (40 gpm). The predicted and measured values are compared in Figure 5-17 at 25°C and 60°C. A reasonable agreement in the observed trends is clearly demonstrated. The temperature calibration of the boundary condition is discussed later in this section.

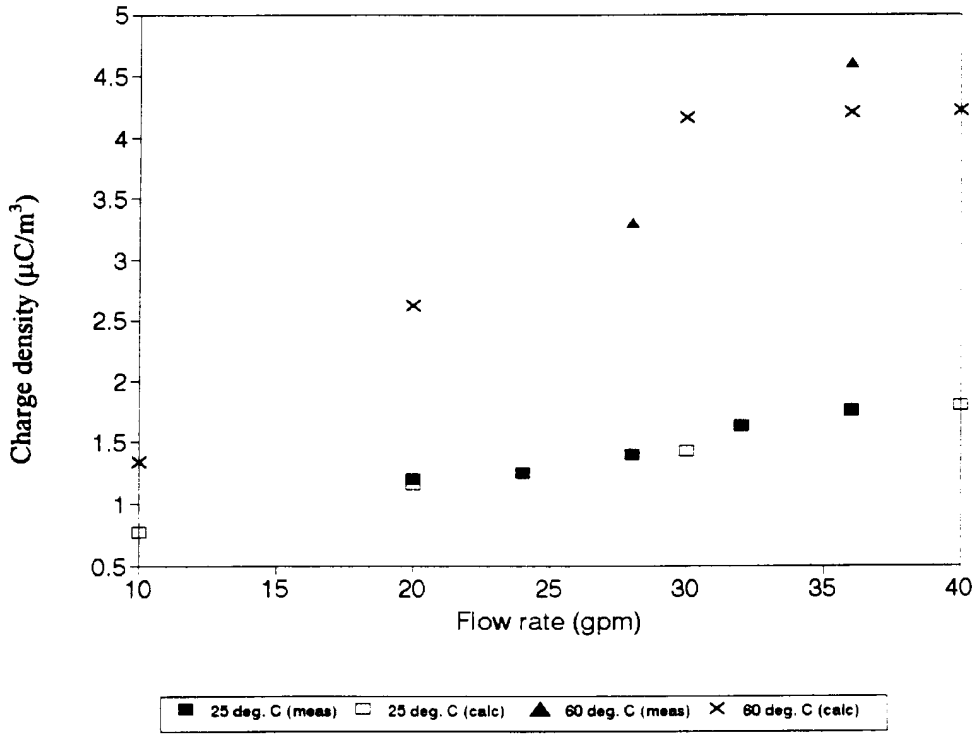

Figure 5-17
Predicted and measured charge densities exiting the model as a function of flow rate.

The next aspect of the calibration is the impact of AC energization upon the total charge exiting the structure. For laminar flow, the effect of energization is not significant. This results from the fact that only the very short axial ducts experience the electric field. In these ducts, the oil residence time is small relative to the electric field transport time for ions in the double layer. However, for turbulent flow in the axial ducts, the eddy diffusivity mechanism mixes charge into the core of the flow once they escape the diffusion sublayer. Hence, energization becomes much more important as shown in Figure 5-18. The diffusion thickness parameter was defined as 1.5×10^{-6} meters at 10 kV (4×10^{5} V/m) to fit the data at 25°C with a flow rate of 1.89×10^{-3} m^3/s (30 gpm). Recall that this parameter is multiplied by the wall charge gradient to obtain an effective volume charge at the wall which is available for field transport. Having calibrated the charge density magnitude, the response from 0 kV to 15 kV fits quite well with experimental results at different flow rates.

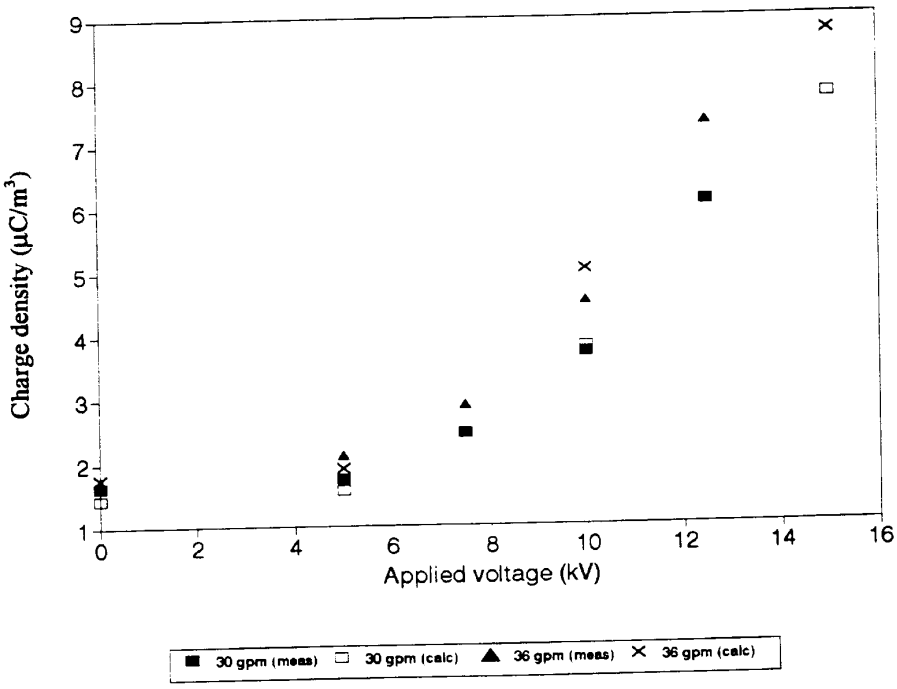

Figure 5-18
Predicted and measured charge density exiting the model as a function of applied AC voltage.

The temperature calibration of the core-form model proves to be the most difficult. While the Arrhenius distribution postulated in Section 4 was successful for a long duct, it does not fit for the present case at higher temperatures. Above 30°C, the Arrhenius model for the wall charge density gradient predicts outlet charges which exceed those measured. Recognizing that the majority of charge is generated in the ducts sustaining turbulent flow, this anomaly is tentatively explained in terms of the appropriate model. The outlet charge density is proportional to the factor

$$1 - \exp\left(- \frac{L}{V \tau} \right) \qquad \text{(eq. 5-36)}$$

where

$$\tau = \frac{\varepsilon}{\sigma} \qquad \text{(eq. 5-37)}$$

For sufficiently long ducts, the numerator of the exponential is large and expression 5-36 is nearly unity. However, for the shorter ducts in the core-form model, this term is very sensitive to the conductivity with the permittivity remaining essentially constant. As the temperature is increased, the exponential term varies dramatically via the Arrhenius dependence of the conductivity. This effect supersedes the boundary condition temperature dependence above 30°C.

This issue reiterates the need for further investigation of streaming electrification in ducts of more realistic geometry which are quite short. However, the task at hand will require a simplifying assumption. In order to complete the temperature calibration, two operating regimes will be assumed for the core-form model ducts. Up to 30°C the boundary condition will be fitted to the expected Arrhenius relationship. At higher temperatures, the conductivity dominant regime will require a new Arrhenius fit. Both regimes are illustrated in Figure 5-19 for a flow rate of 1.89 x 10^{-3} m^3/s (30 gpm). The fitted and measured outlet charge densities at this flow rate are compared in Figure 5-20. A third region should exist somewhere above 60°C where the expected Arrhenius behavior is again obtained once σ is large enough that the exponential term in eq. 5-36 becomes negligible. While somewhat artificial, the wall charge gradient temperature calibration is clearly needed in order to model an entire winding over the temperature range of interest and will be incorporated in the next main section.

5.4.4 Static Potential Model Results

The spatial potential distribution measured externally on the core-form model by Lee (26) is now compared with predicted results. Since this experiment was conducted using a different oil, the results are presented in normalized form for a flow rate of 2.27 x 10^{-3} m^3/s. The potential was scanned using a non-contacting capacitive probe in the same manner as described in Section 4. Note that the metal flanges which secure the model in the fluid loop serve to provide an additional ground path. The model assumes that the winding conductors are grounded as would be the case in a real winding. In this case, the local bulk insulation resistances enforce the potential distribution. The normalized voltages

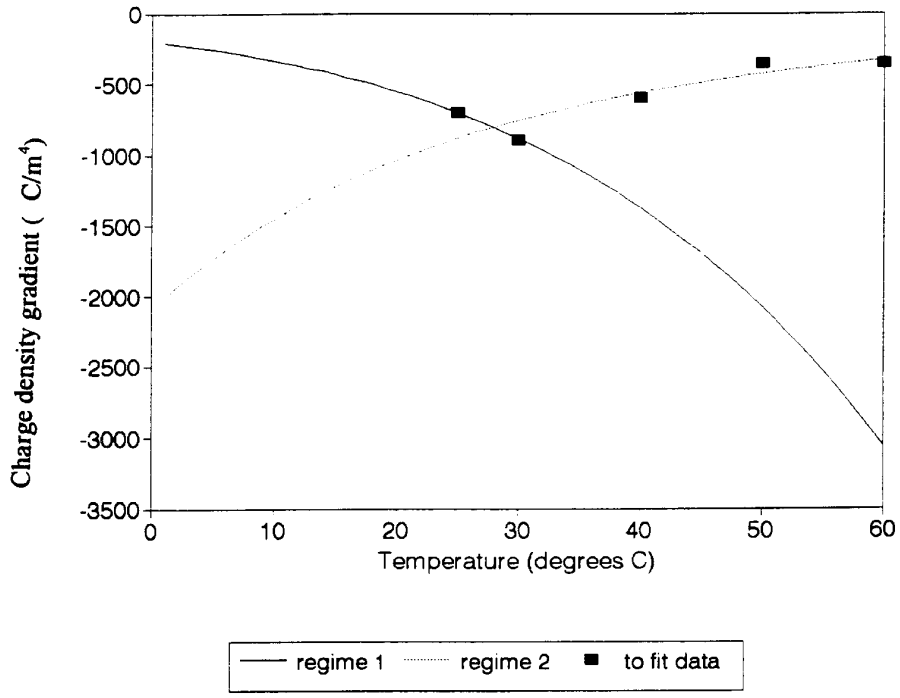

Figure 5-19
Two-region model for the wall charge gradient boundary condition as a function of temperature.

measured and predicted along the side of the model opposite the inlet and outlet ducts are presented in Figure 5-21.

As expected, the highest potential is observed in the duct which connects the two passes and hence sees the maximum flow rate. The end potentials are lower due to the close proximity of the flanges despite the high local flow velocity. The bulk resistances at the inlet and outlet were approximated as $1 \times 10^{12}\Omega$ to match the measured results at the inlet and outlet. The potential distribution along the axial duct nodes appears to correspond with the axial flow distribution of Figure 5-13. These results indicate that the static potential and hence electrification model are reasonable to a first approximation.

5.5 Summary

A network methodology for examining streaming electrification has been developed and successfully applied to an actual transformer structure. Lacking specific data points within the test model, calibration and comparison were undertaken based on empirical terminal characteristics. Having selected the boundary conditions to fit experimental data under

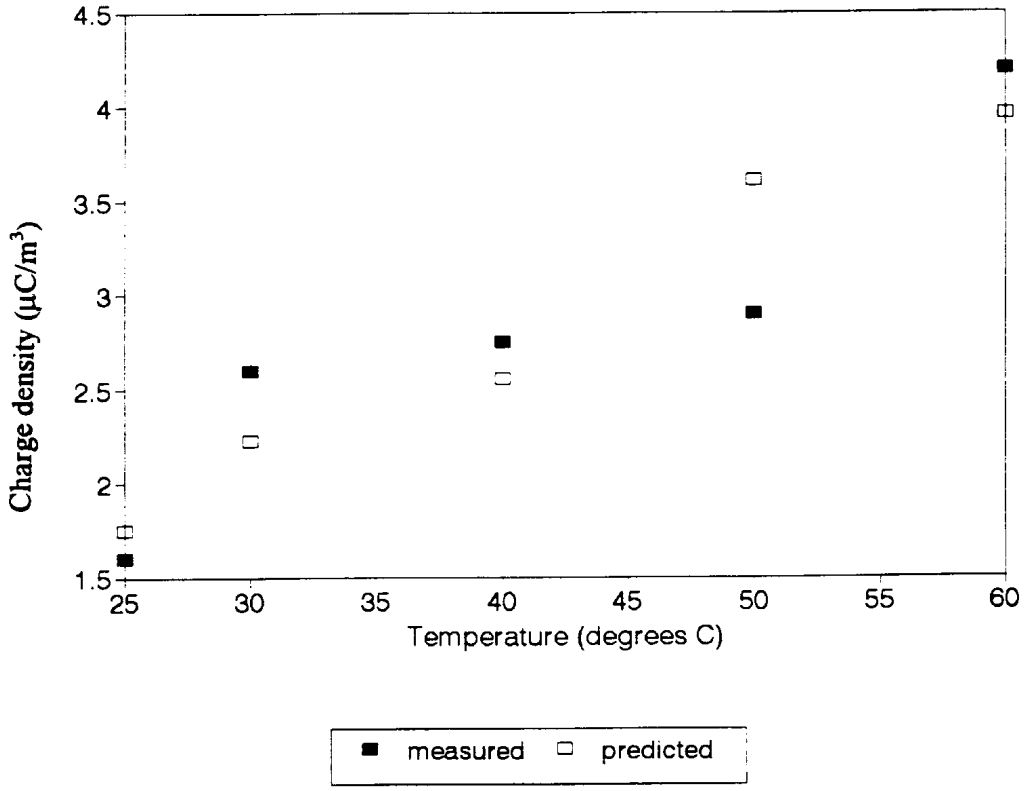

Figure 5-20
Predicted and measured charge density exiting the core-form model as a function of temperature.

specific circumstances, the trends associated with the variance of critical parameters were examined. With the exception of temperature dependence in a certain range, the duct models developed in the previous main section were successful in tracking the experimental results.

The flow and energization results are quite encouraging. They indicate that the essential physics embodied in the single duct theory are correct to a first order. In addition, the energization theory first proposed by Zahn et al (48) for low frequency AC has been verified for more realistic 60 Hz voltages. While the temperature response has been shown not to obey the simple Arrhenius distribution commonly proposed (45, 29), this result is clearly beneficial. The need for more detailed studies of realistic ducts becomes even more apparent. However, lacking this information, the purely empirical calibration data will be sufficient for present purposes.

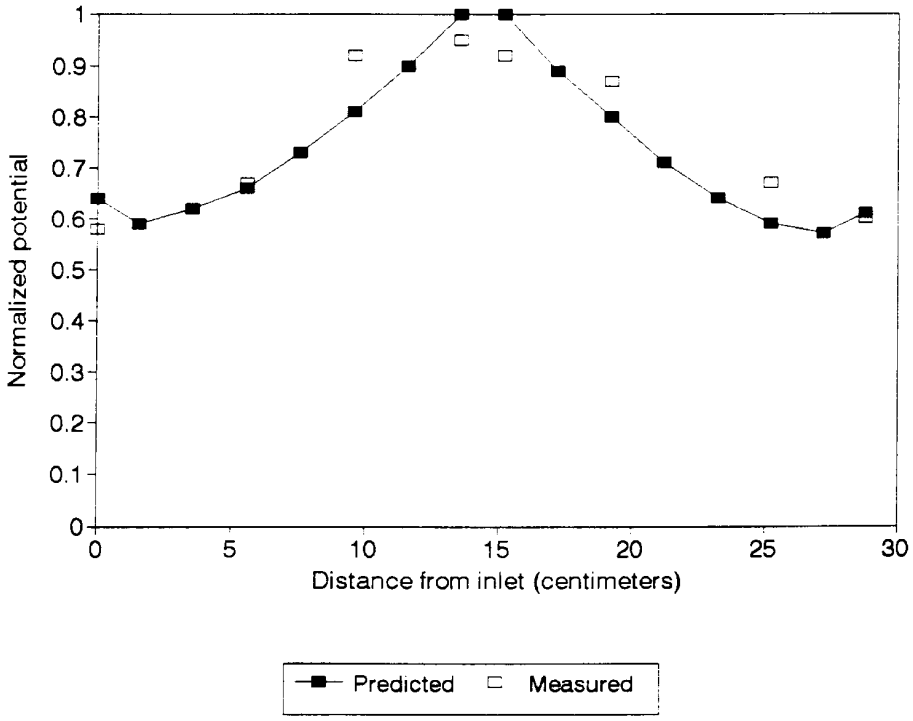

Figure 5-21
Predicted and measured axial potential distribution in the core-form model.

The calibration and verification of the network model is viewed as a necessary step in reaching the goal of this research. Having demonstrated viability of the model using a realistic structure, a macroscopic geometry can be considered with much more confidence. The empirical calibration data will facilitate the examination of an entire transformer winding with much more sophistication than has been previously attempted. Scaling effects which cannot be replicated with laboratory sized models can now be investigated using the network approach.

6

APPLICATION OF THE NETWORK-BASED STREAMING ELECTRIFICATION MODEL TO AN ACTUAL TRANSFORMER WINDING

6.1 Description of Test Case

The methodology developed in the previous two sections is now extended to a more practical situation. A complete core-form transformer winding has been specified with the assistance of Mr. W. J. McNutt (81) which is sufficiently realistic without violating proprietary restrictions. The geometry and assumptions for this test case are reviewed in this section.

The winding in question is rated for 200 kV and is comprised of duct work similar to that of Figure 2-3. Note that this is a high voltage winding with the total operating voltage applied end to end. This structure is symmetric about a leg of the core as shown in Figure 6-1. In view of this symmetry, one section defined by the radial spacers will be considered for analysis. The spacers are placed such that the ducts have a high aspect ratio and thus are readily treated by the plane channel models of Section 5.

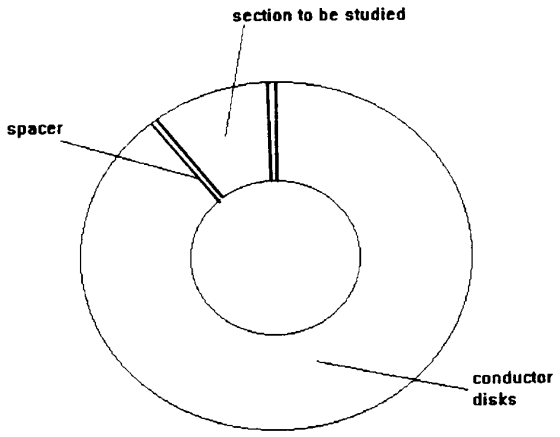

Figure 6-1
Illustration of winding symmetry about one core leg.

The test winding sections consist of eight identical passes of the form shown in Figure 6-2 and has an overall length of 2.86 meters. Each pass contains 10 conductor disk pairs for a total of 20 disks. The disk pairs are at the same potential and a uniform voltage distribution is assumed down the winding. A disk pair is detailed in Figure 6-3. Note that the annular sections are treated as having sufficiently large radii that the defining radial spacers are effectively parallel to simplify the geometry.

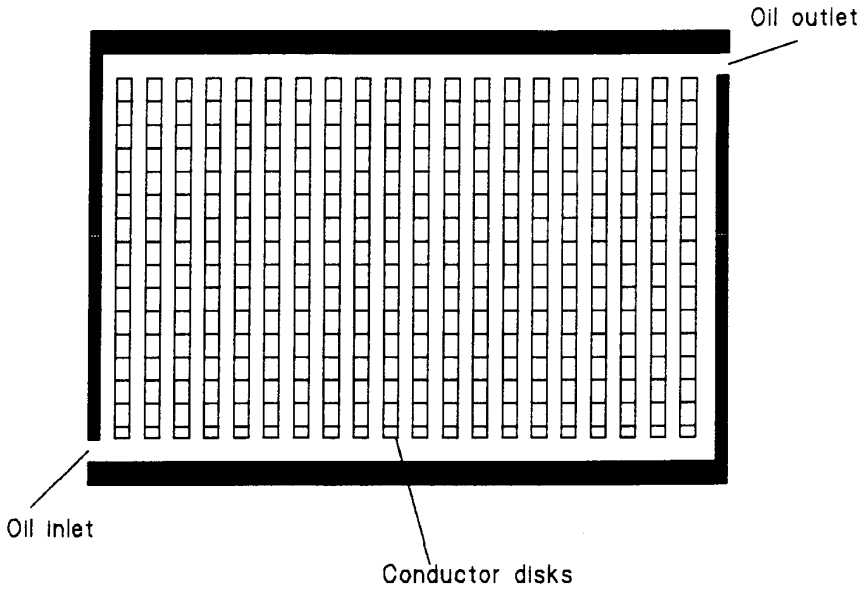

Figure 6-2
Typical pass section of the test winding.

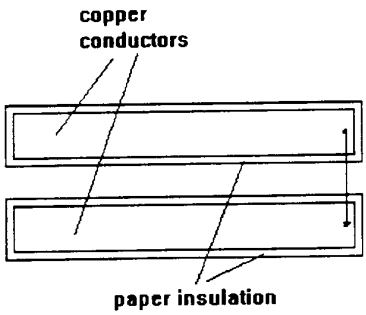

Figure 6-3
Conductor and channel details for one disk pair.

The surrounding insulation structure is detailed relative to a single pass in Figure 6-4. Ground planes are provided by the low voltage winding looking inward toward the core and the tank wall looking in the opposite direction. In each case, the axial walls of

the pass are isolated by an oil gap with an additional pressboard barrier present at the low voltage winding. The electric fields acting in the radial directions are determined by capacitive divider action assuming a linear voltage drop across the winding disk pairs.

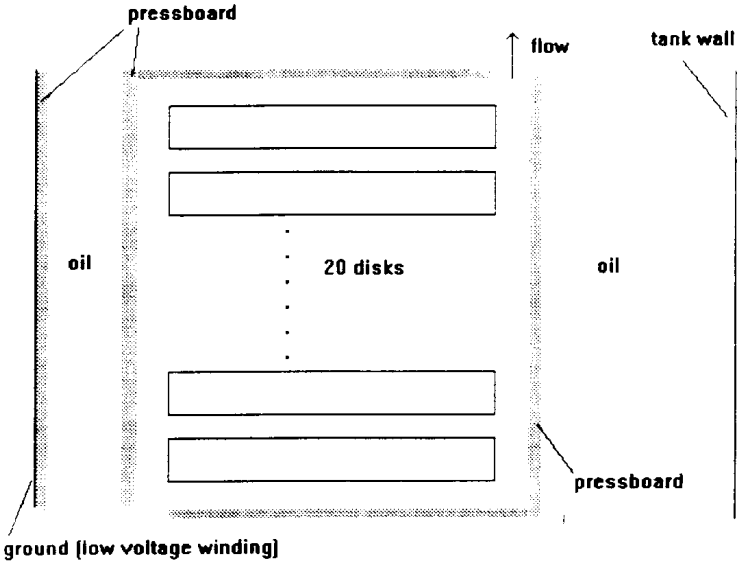

Figure 6-4
Details of the insulation structure relative to one pass of the winding.

The passes are assembled in series as illustrated in Figure 6-5. In order to force the oil flow to divide within each manifold, the pass inlets/outlets alternate between the core and tank side of the winding. Hence, each pass is a mirror image of the upstream and downstream passes. Since the axial ducts on each side are identical, only two different data files are required to account for the transposition of the inlet/outlet ducts. The flow problem is bounded by specifying the driving flow rate at the bottom of the winding (pass 1 inlet) and zero pressure at the outlet of pass 8. Note that no geometry external to the winding is considered here.

The passes are assembled using five element types as illustrated in Figure 6-6 which is a special case of Figure 5-11 in which the blowing and sucking manifolds have the same dimensions. The elements are defined as follows:

Type 1: straight radial duct

Type 2: straight axial duct

Type 3: straight inlet/outlet duct

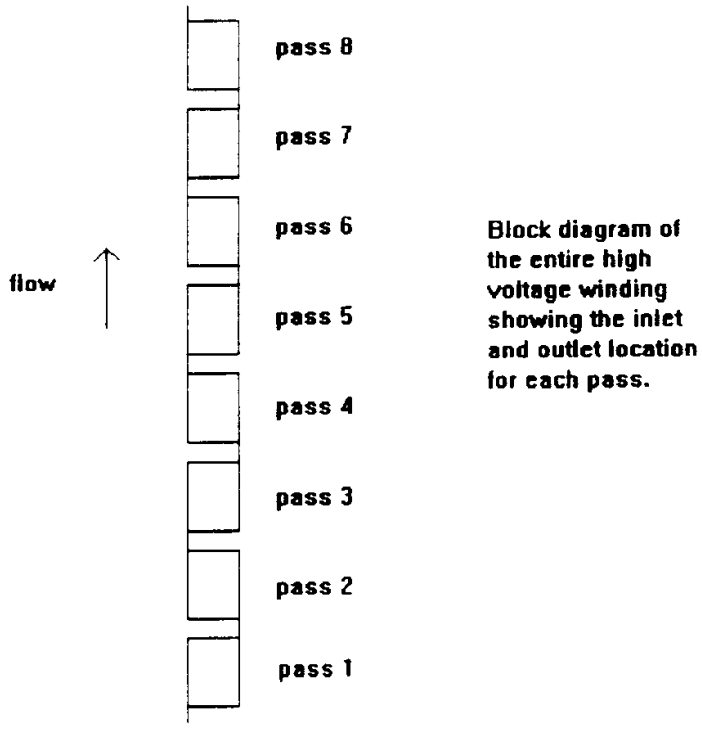

Figure 6-5
Illustration of passes connected in series to form the winding.

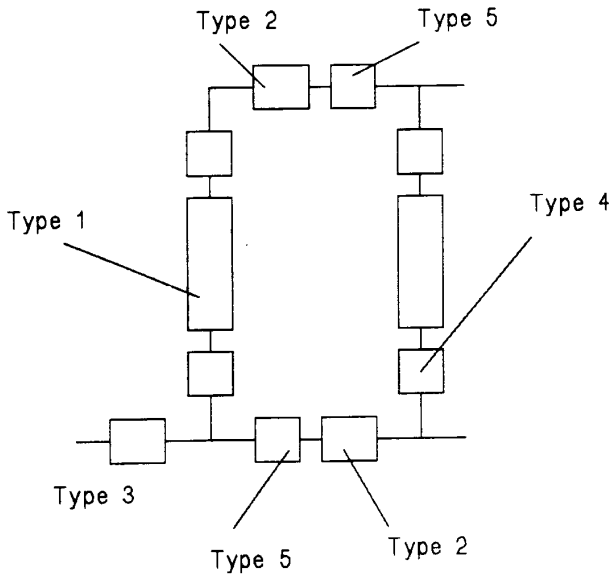

Figure 6-6
Equivalent circuit for a section of one pass showing the different duct types.

Type 4: radial duct junction losses

Type 5: axial duct junction losses

The key dimensions of each duct are provided in Table 6-1. Corresponding duct surface and bulk resistance values were also calculated using the approach of Section 5. These values are shown for all duct types at 25°C in Table 6-2. Note that the type 3 duct represents half of the true inlet/outlet section. One half is connected to the outlet of the downstream pass outlet and the other is connected to the upstream pass inlet. This is necessary to provide proper resistive coupling between the passes in the macroscopic solution.

Table 6-1
Test winding duct dimensions.

Duct type	Half Height [m]	Width [m]	Length [m]	d_H
1	2.55×10^{-3}	1.27×10^{-1}	1.0×10^{-1}	9.8×10^{-3}
2	4.75×10^{-3}	1.27×10^{-1}	1.27×10^{-2}	1.77×10^{-2}
3	4.75×10^{-3}	1.27×10^{-1}	7.94×10^{-3}	1.77×10^{-2}
4	—	—	—	9.8×10^{-3}
5	—	—	—	1.77×10^{-2}

Table 6-2
Test winding duct bulk and surface resistance at 25oC.

Duct type	R_S [Ω]	R_B [Ω]
1	3.79×10^{13}	2.52×10^{13}
2	4.60×10^{13}	8.00×10^{14}
3	2.90×10^{12}	1.60×10^{15}
4	1	—
5	1	—

The mean flow velocity in the radial ducts of this transformer will typically be on the order of 2 ft/s or 0.6 m/s (81). Hence, the flow range for analysis was chosen to be 10 gpm (3.16×10^{-3} m^{-5}/s) to 50 gpm (1.58×10^{-4} m^3/s). This corresponds to mean radial flow velocities between 1.38 ft/s (0.42 m/s) and 6.0 ft/s (2.0 m/s) which emphasizes the extreme case of higher flow rates. At 20°C, the local radial duct Reynolds numbers will range between 100 and 2000. Thus, laminar and turbulent conditions will be

investigated over this flow range. Note that the mean axial duct flow velocities are roughly a factor of five higher but will nevertheless see both flow regimes.

The axial ducts will experience the most substantial electric fields under energized conditions. On the core side, the axial ducts will see 6.9 V/m per applied volt on a given conductor disk. On the tank side, the ground plane is farther away and only 3.9 V/m will be present per applied volt on the winding disks. Recall that the voltage and hence electric field on each disk pair is calculated assuming a linear voltage drop. Obviously, there will be a voltage drop between specific conductor disks which establishes a transverse field in alternating radial ducts. This field will be independent of location in the winding under the present assumptions. However, the radial flows have relatively low Reynolds numbers over the flow range and hence the field effect will not be significant. Even under turbulent conditions, the diffusion sublayer in these ducts will remain large with respect to the field transport length at rated voltage. Initial calculations indicate that the radial duct contribution due to energization is negligible and is therefore omitted to simplify the data files.

6.2 Analysis of a Single Pass

The first step in considering the test winding is to model a single pass to determine the appropriate terminal characteristics. The flow model results are presented at the minimum and maximum flow rates in Figures 6-7 and 6-8 for the radial and axial ducts respectively. In the former case, the distribution is symmetric since the blowing and sucking manifolds have identical hydraulic diameters. As expected, the axial flow rates on the blowing side decline over the pass to reach a minimum at the downstream block washer. These results seem quite reasonable for a symmetric manifold in light of other findings (121).

The charging behavior of a single pass is illustrated with respect to flow rate and inlet charge density in Figure 6-9. As expected, the charge density exiting the pass increases with flow velocity. The large step between 10 and 15 gpm occurs as the axial flows transition into turbulence. Note that these results were obtained at 25°C with no applied voltage. The slope of the outlet charge density versus flow curve is observed to decrease as the driving flow rate increases. This is the result of charge relaxation becoming significant with respect to generation. The relaxation mechanism ensures that as the flow rate is raised, the charge relaxed will eventually balance the charge separated such that an upper limit is defined. When the inlet charge density is less significant than that generated in the pass, it is effectively superimposed upon the outlet charge density result subject to relaxation as experimentally verified in Section 3.

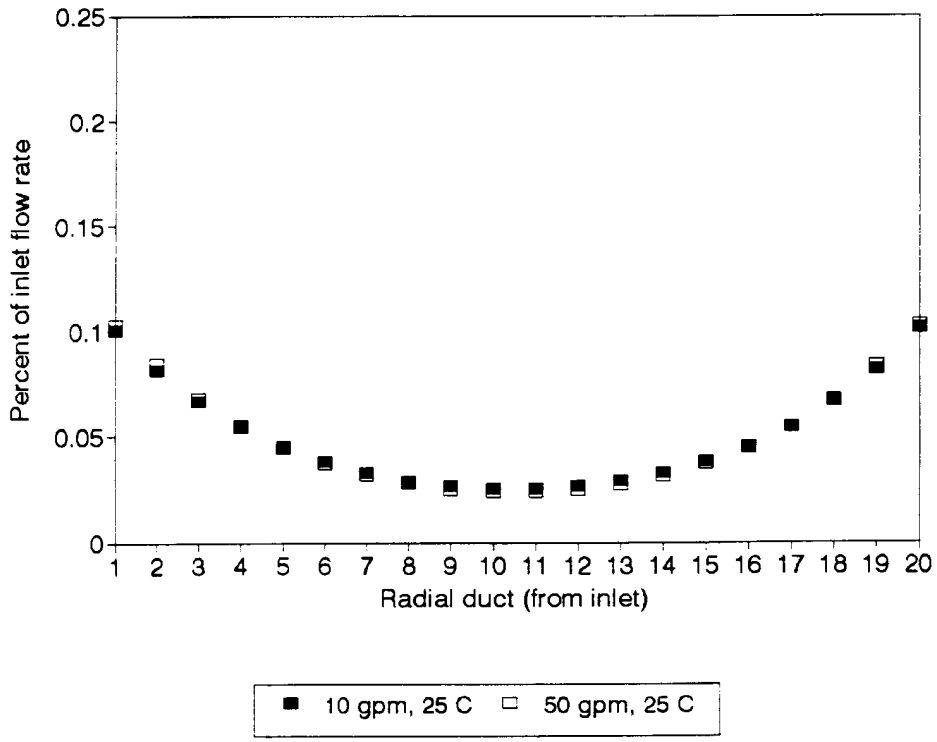

Figure 6-7
Radial flow rate distribution for a single pass of the test winding.

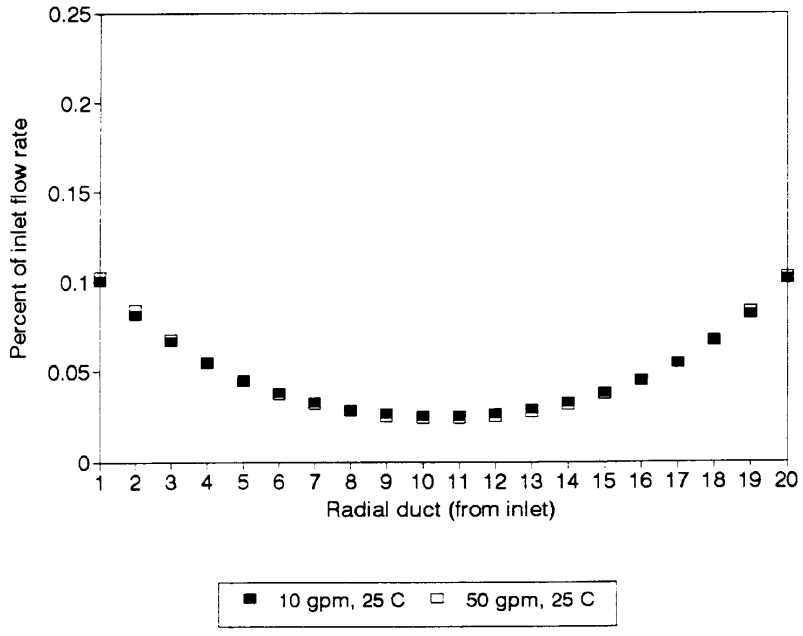

Figure 6-8
Axial flow rate distributions for a single pass of the test winding.

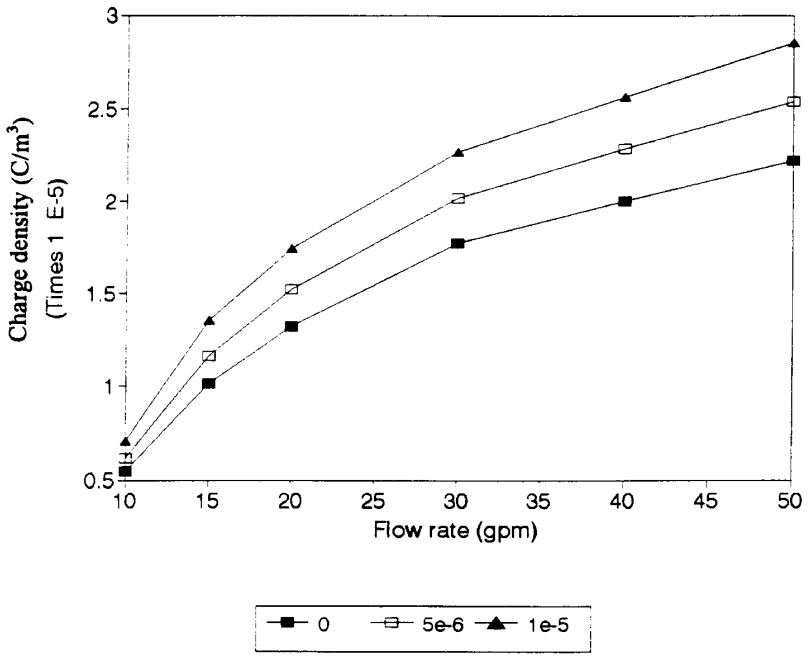

Figure 6-9
Terminal charging characteristics for one pass of the test winding (note legend values are inlet charge density in C/m^3).

This concept is further illustrated by Figure 6-10 which presents a three-dimensional view of the pass charging behavior. This data provides a terminal characteristic by which the pass can be reduced to a single lumped element at 25°C without energization. As the inlet charge density is increased, the outlet charge becomes insensitive to generation within the pass. As will be illustrated in the following sections, further increasing the influent charge can lead to a relaxation dominated solution where the outlet charge is actually less than the inlet charge. The incorporation of such equivalent elements into a macroscopic solution is detailed in the next section.

The effect of energizing the pass conductors is illustrated in Figure 6-11. The temperature is set at 25°C and the applied voltage is dropped linearly across the conductor disk pairs with the inlet charge set to zero. At the lowest flow rate where the duct flows are laminar,the effect of energization is not significant. However, at higher flows where the axial ducts become turbulent, substantial field transport of charge is observed. The outlet charge density is determined under these conditions by the diffusion sublayer thickness relative to the energizing field magnitude and oil residence time. As the velocity is increased, the sublayer is compressed and field transport into the turbulent core becomes evident at lower voltages. The upper limit where generation balances relaxation is also apparent for this case.

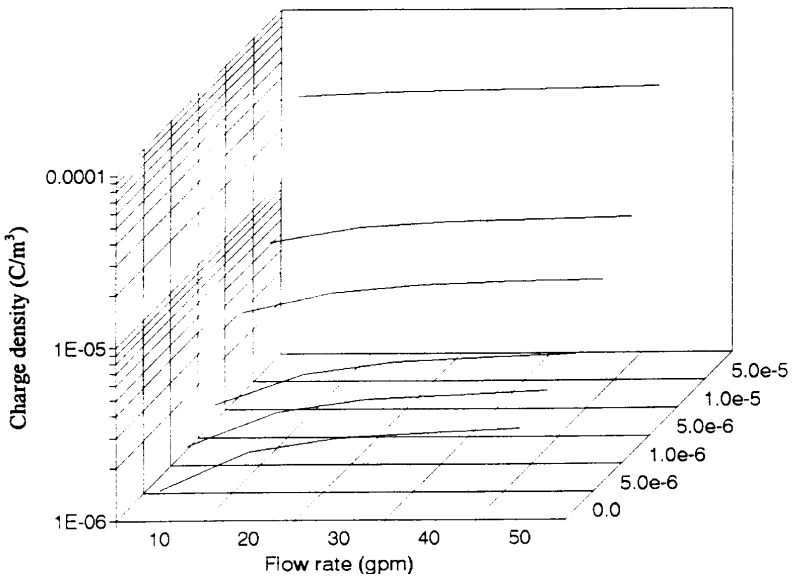

Figure 6-10
Charging characteristic of a single pass as a function of flow rate and influent charge (z-axis values are in C/m^3).

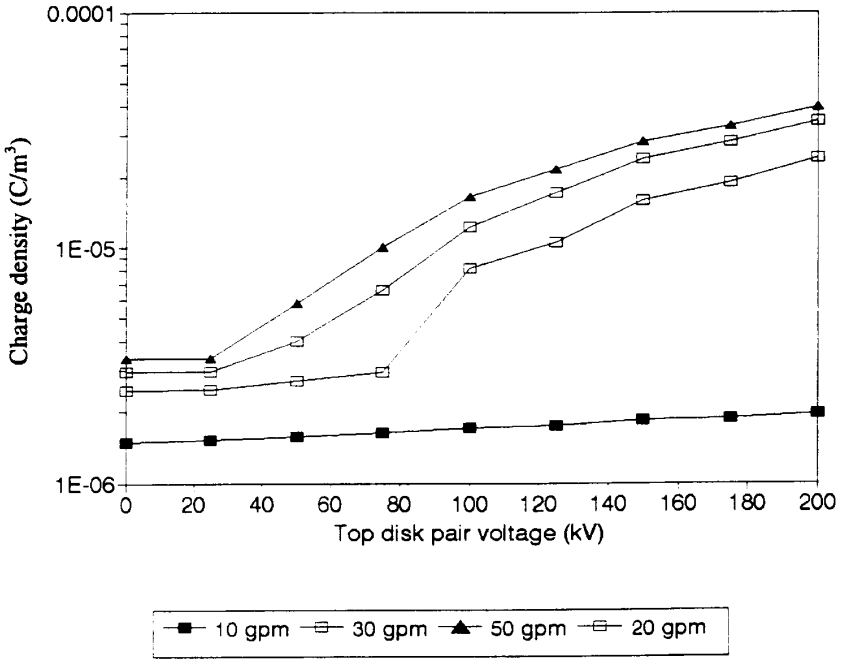

Figure 6-11
Impact of flow rate and top conductor energizing voltage on outlet charge for a single pass.

The corresponding pass eight characteristic for energized conditions is shown in Figure 6-12. A large jump in the outlet charge is observed at rated voltage as the axial ducts become turbulent. The saturation effect of inlet charge becomes noticeable once an entering charge density exceeding $5\mu C/m^3$ is achieved. Notice that the required charge for generation to be counterbalanced by relaxation is higher under these conditions than for the unenergized case of Figure 6-10.

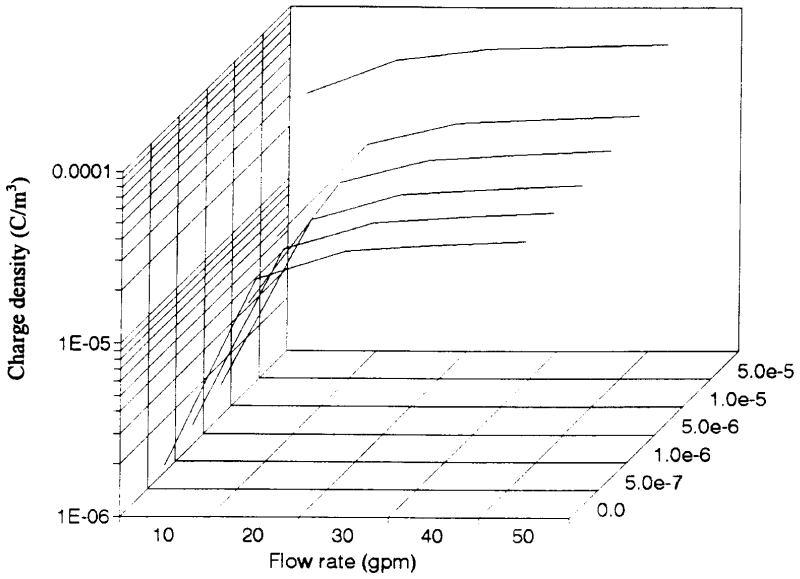

Figure 6-12
Charging characteristic for pass eight at rated voltage subject to flow rate and inlet charge density (z-axis values are in C/m^3).

6.3 Incorporation of Pass Characteristic Into Complete Winding Model

Having classified the charging characteristics of the passes which make up the winding, a complete model may now be visualized. For the case of interest, the problem now consists of eight series elements as shown in Figure 6-5. Hydraulic admittance characteristics of the form given in Figure 6-13 are required in addition to the charging characteristics of the form shown in Figure 6-10.

The computer algorithms described in the previous main section may be readily incorporated for the present case. Rather than calculating the hydraulic resistance, the correct operating point is interpolated from the admittance data based on the pressure drop. Similarly, the streaming current generated in a given element is now interpolated from the

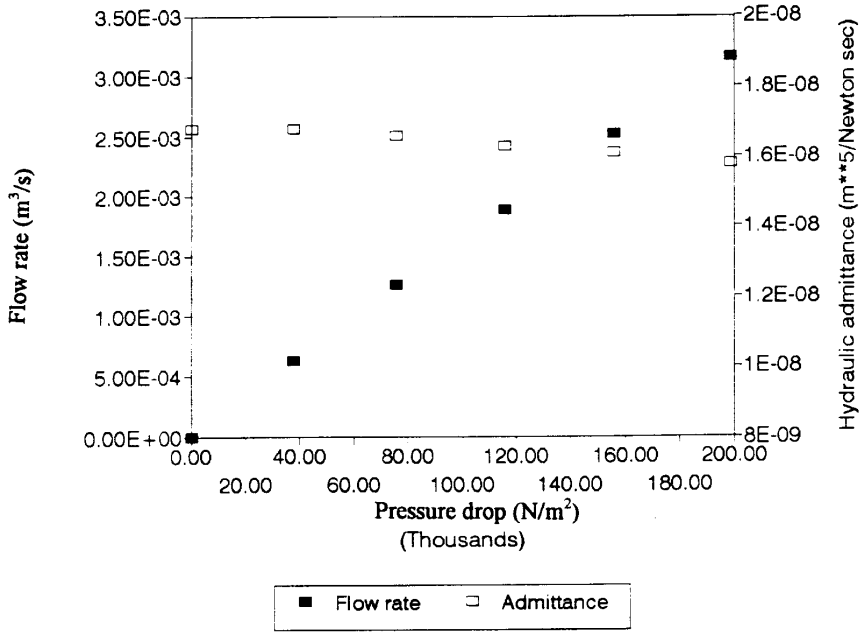

Figure 6-13
Hydraulic admittance characteristic for a single pass.

appropriate three-dimensional characteristic relating inlet charge and flow rate to outlet charge. Exactly the same solvers may be used with the input files modified to provide look up tables for the various elements. Hence, equivalent lumped models must always be generated at the pass level before implementing the macroscopic solver.

The required modifications were made to allow solution of generic networks by reduction to equivalent elements. However, in the present case, a significant simplification is possible. Since the passes are connected in series, they can be solved sequentially with each pass result providing boundary conditions for the next pass. In the case of the flow model, only one pass must be analyzed as all passes have the same flow distributions recognizing the transposition of the inlet and outlet ducts. For electrification, the outlet charge from pass one enters pass two and so forth up to the pass eight outlet. Hence, the complication of generating pass characteristics can be simply incorporated into the solution process.

A final note is in order with regard to the static potential calculation. In principle, this solution might not be accurate on a single pass basis since the leakage paths could extend into neighboring passes. However, since the conductor disks represent a DC ground, the static potentials are only dependent upon the local leakage resistances. Hence, the leakage currents generated in a given duct will not travel very far to find ground potential. This results from the fact that the bulk radial duct leakage resistances are low due to the larger relative area. Currents will thus only be forced to flow along insulating surfaces until a radial duct is reached.

The reason for splitting the inlet/outlet ducts in half lengthwise now becomes apparent. The total leakage currents generated within the ducts must divide equally between the upstream and downstream passes which represent identical parallel resistances to ground. By attaching half of the duct to each pass and solving on an individual basis for the flow and electrification models, the proper current distribution is maintained. The inlet/outlet ducts must be considered carefully since they have the highest flow rates and low surface resistances such that current will leak to the attached passes. For all other ducts, the close proximity of low bulk resistances to ground via the radial ducts effectively localizes the process. Voltage distributions were calculated on a single pass with varied bulk resistances at the inlet and outlet. The results showed that the chosen analysis method is accurate to better than 10 percent with the passes solved individually.

6.4 Full Winding Macroscopic Results

Having specified and solved a single pass, the entire winding is now considered with appropriate coupling between the passes. The charge density observed at three different pass outlets is shown in Figure 6-14. These results were obtained with no applied voltage or inlet charge at 25°C. As expected, the final pass exhausts the highest charge density due to the contributions of the downstream stages. Furthermore, the passes farther from the inlet are also observed to produce more outlet charge per increase in flow rate. This is the result of an integral effect over the particular pass and the upstream passes which all generate more charge with increased flow.

Under energized conditions, the voltage distribution in the winding modifies this behavior somewhat. As shown at rated voltage in Figure 6-15, the pass outlet charges maintain a similar characteristic on a logarithmic scale. The transition to turbulence is evident in each of the three passes by a jump in outlet charge. In the second pass, the fields are much lower and the effect of energization is correspondingly much less. The fifth and eighth passes show the influence of higher conductor voltages in addition to the integral effect of upstream passes noted without applied voltage.

The next logical step is to consider the effect of influent charge upon the previous cases. A more detailed characteristic showing the volume charge density exiting from each pass is presented in Figure 6-16 with no inlet charge. This graph shows the fully laminar and fully turbulent extremes with and without energization at 25°C. As demonstrated previously, the low flow rate case shows the charge in the oil increasing as the winding is traversed. However, the effect of energization is relatively slight. Under turbulent conditions, much more charge is present with and without the voltage applied. In the former case, the combination of field transport and turbulence provides a dramatic increase in charge density. The slope is observed to be much steeper due to the higher voltages in the passes farthest from the inlet.

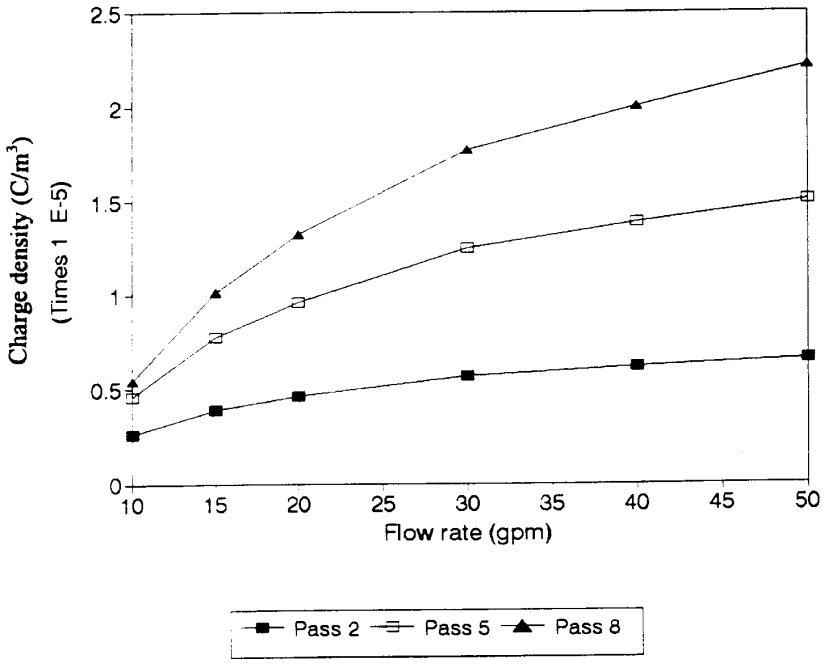

Figure 6-14
Charge density at three passes as a function of flow rate at 25°C with no applied voltage or inlet charge.

The impact of 10μC/m^3 provided at the inlet of pass one is demonstrated in Figure 6-17. For laminar flow, relaxation completely dominates and the charge entrained in the oil decreases during passage through the winding. As with no inlet charge, the effect of energization remains minuscule for laminar flow. The turbulent case approaches the balance between generation and relaxation with no voltage applied. The slope of the curve has been reduced from the previous case of Figure 6-16. However, energization at rated voltage still dominates the electrification process under turbulent conditions. Moving away from the inlet, the pass voltages become sufficient to overwhelm the relaxation mechanism and realize the characteristic obtained with no entering charge.

The effect of temperature on the charge density in the winding is illustrated for three passes in Figure 6-18. These curves were obtained at 40 gpm with no applied voltage or inlet charge. The slight discontinuity in the responses at 40°C is the result of the empirically defined boundary condition for temperature from the previous main section. In the third pass, the outlet charge density is shown to increase with temperature in the same manner as for the core-form model used for calibration (see Figure 5-19). However, closer to the top

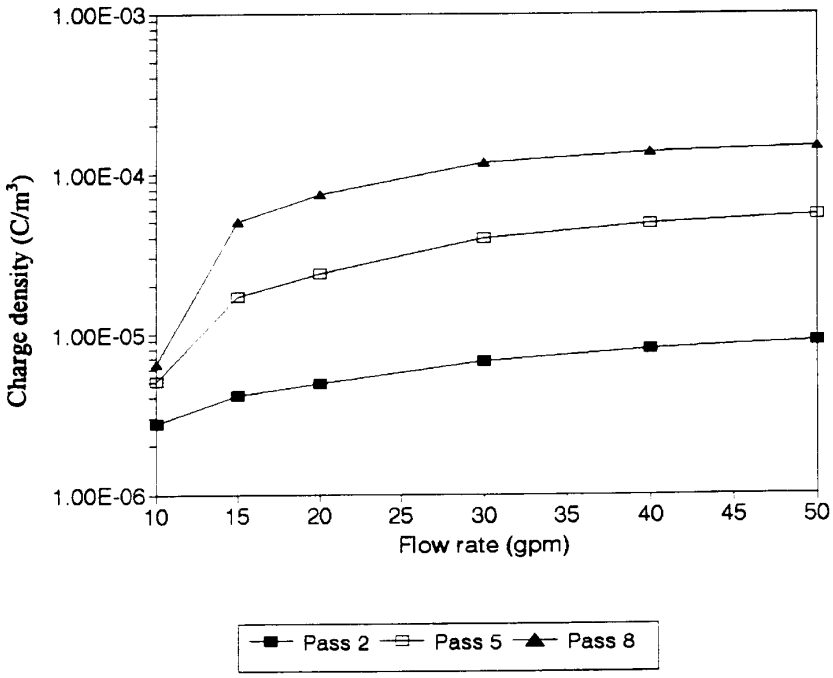

Figure 6-15
Charge density at three passes as a function of flow rate at 25°C with rated voltage and no inlet charge.

of the winding, the charge density peaks at 50°C and begins to decay. This result is very significant and demonstrates a critical volumetric effect. Temperature peaks have been observed in actual transformer measurements of streaming current (21) (see Figure 2-18). However, this behavior has not been documented for laboratory scale experiments with the single exception of the duct results given by Tanaka et al (29).

The reason for the temperature peak is once again the competing relaxation and generation mechanisms. Charge separation is enhanced initially by the increase in wall charge flux and higher turbulence as the kinematic viscosity drops. The conductivity increases exponentially with temperature such that the charge relaxation time for the oil is greatly reduced. Note that the conductivity also reduces the development length for turbulent charging via eq. 4-61. Ultimately, the relaxation effect dominates at higher temperatures which indicates that a lesser amount of charge may be entrained in the oil before generation is completely balanced by relaxation. The volume effect is thus that the oil residence time in the winding is sufficient to reach this saturation point. This is a case of comparatively longer residence times with the oil still flowing sufficiently fast to provide optimal charge separation. Hence, in smaller structures, this situation does not have sufficient space to develop and temperature responses typically mimic the behavior of pass three.

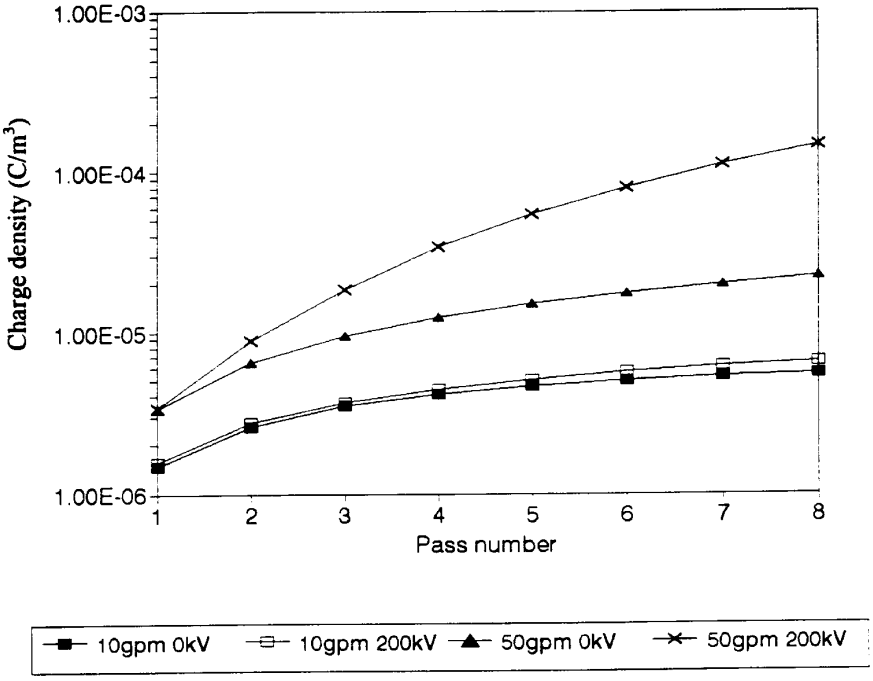

Figure 6-16
Charge density exiting from each pass as a function of flow rate and energization with no influent charge.

While the charge generation within the winding increases with temperature over a certain range, the static potential hazard does not. This is expected in terms of the pressboard resistivity temperature relationship. The resistivity values were estimated using the results of Moser et al (75, 76) shown in Figure 6-19. The logarithmic drop in leakage resistance completely overwhelms the effect of temperature enhanced electrification as demonstrated in Figure 6-20. These results were obtained at 40 gpm with no energization and illustrate the potential at the outlet of the first pass. Based on the results of Figure 6-18, the charge generation near the winding inlet is expected to increase over this temperature range. Hence, Figure 6-20 provides a good measure of the worst case competition between leakage and generation.

6.5 Full Winding Detailed Results

Up to this point, the winding has been considered from the perspective of the various pass terminals. Having gained insight from the analysis of the previous two sections, the internal workings of the passes may now be examined. The relationship between the inlet and outlet terminals may thus be better understood in terms of the detailed charge density and static potential distributions. The microscopic phenomena are found to be effectively superimposed upon the macroscopic characteristics of the structure.

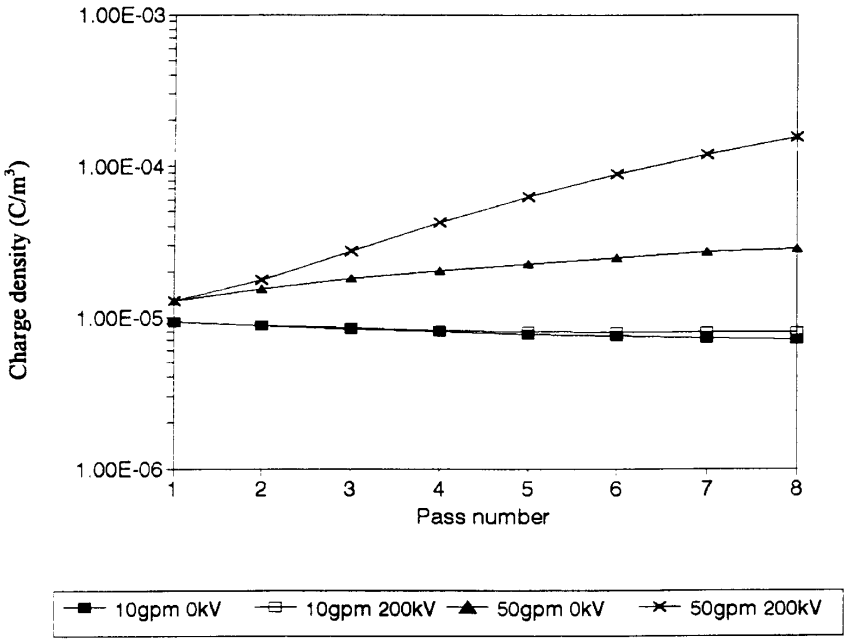

Figure 6-17
Charge density exiting from each pass as a function of flow rate and energization with 10μC/m^3 at the inlet.

6.5.1 Effect of Flow Regime and Influent Charge

The fully laminar case is first considered with no energization or inlet charge density. Figure 6-21 illustrates the core side and tank side axial distributions of charge for 10 gpm and 25°C. The charge density follows the general trend demonstrated previously in Figure 6-16. However, the added detail within the passes demonstrates two interesting effects. The first is the spatial phasing of the charge density distribution which results from the alternating placement of the inlet/outlet ducts. Since the first pass inlet is on the core side, the tank side characteristic effectively lags by exactly one pass. Note that there are 40 axial nodes per pass.

The second effect of interest is the transitions in the charge density characteristics. These abrupt discontinuities occur on both sides of the winding and indicate transition from one pass to the next. Following the core-side characteristic through the first pass, the charge is observed to start from zero and peak at nearly 1μC/m^3. The final node is adjacent to the blocking washer which separates the phases and sees the lowest axial flow rate. Moving to the other side of the washer, the charge density is found to be nearly twice as large. This is the result of the total charge generated in the first pass flowing into the second pass augmented by significant generation in the ducts near the inlet/outlet. Recalling Figure 6-7,

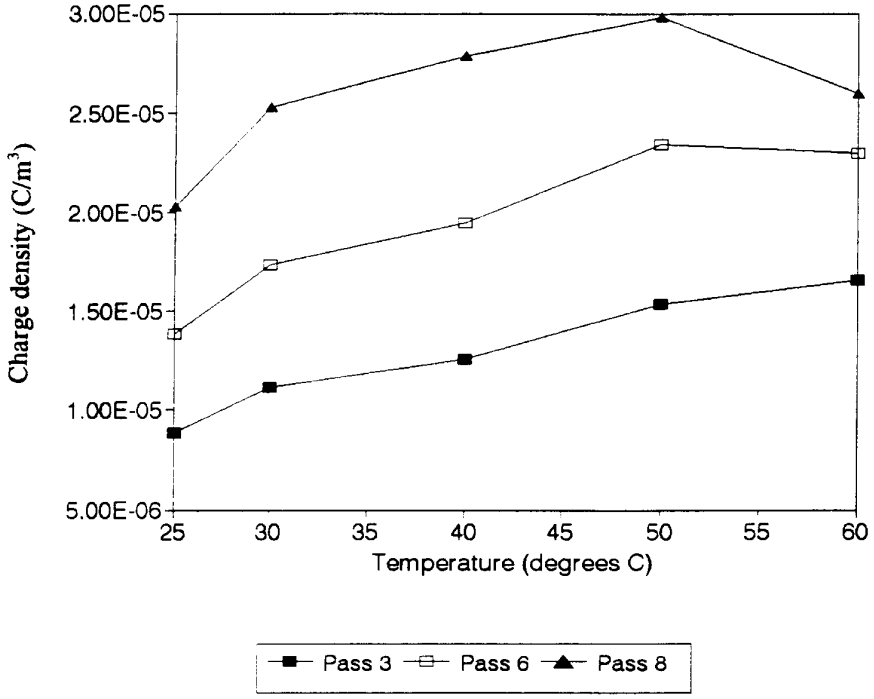

Figure 6-18
Influence of temperature on charge density with no inlet charge or energizing voltage.

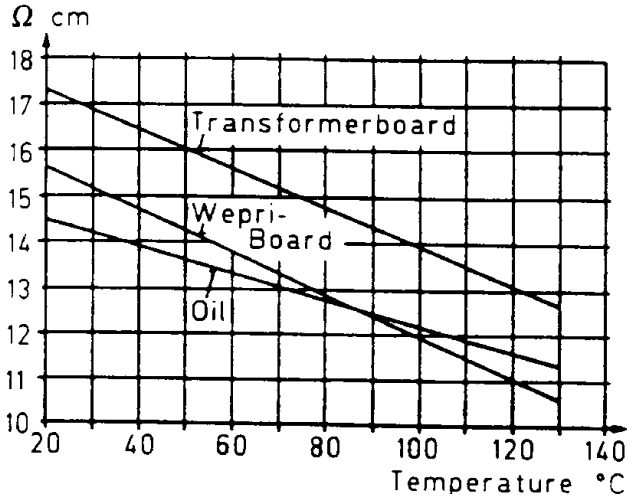

Figure 6-19
Log resistivity of cellulose insulation as a function of temperature as presented by Moser et al (76).

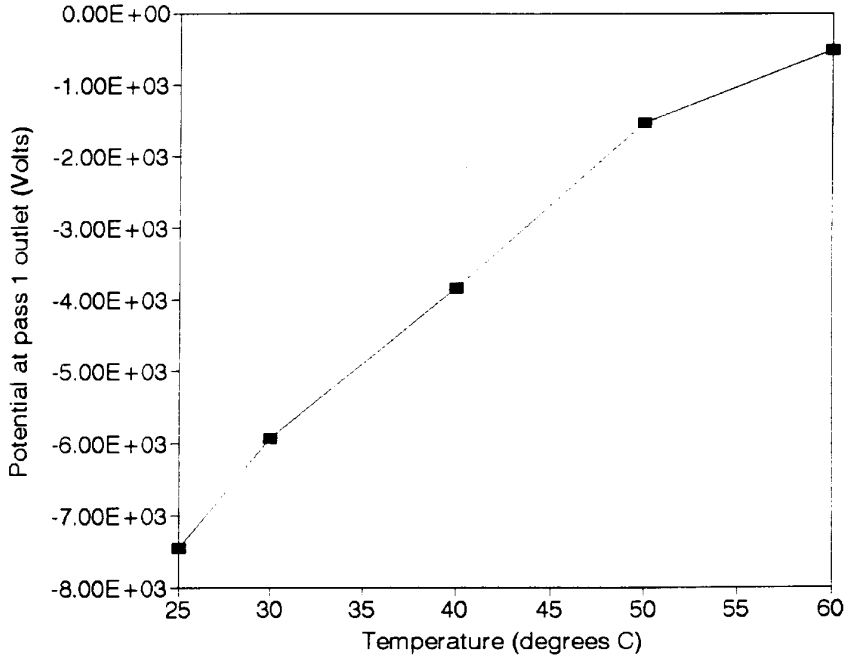

Figure 6-20
Static potential at the outlet of pass one as a function of temperature at 40 gpm with no applied voltage or inlet charge.

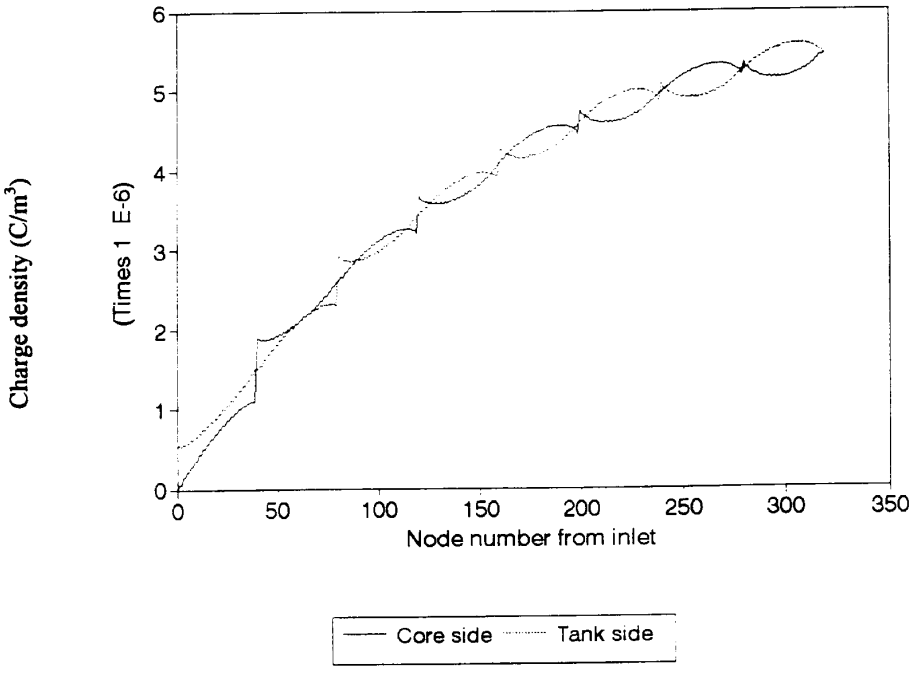

Figure 6-21
Charge density distributions under laminar conditions at 25°C without energization or influent charge.

the first radial duct will carry the highest of the radial flow rates and hence convects substantial charge to the first core side axial node. In addition, the first radial duct will also internally separate charge to further enhance the charge density at this location.

A similar effect is observed on the tank side in the first pass. The first axial node is observed to have $0.5\mu C/m^3$ and transitions abruptly from zero such that the first radial duct makes the most important contribution. Note that no influent charge is present at the pass one inlet to augment this value. Returning to the core side and continuing through the second pass, the charge density initially drops and then increases as the outlet is approached. The drop results from relaxation and the increase follows the flow rate distribution shown in Figure 6-8. As the oil enters the third pass, the substantial generation in the inlet/outlet duct coupled with the convected charge from the last radial duct in pass two provides another peak on the core side axial distribution.

Throughout the remainder of the winding, the preceding explanation holds for both the core and tank side distributions. However, as the charge saturation level where generation and relaxation balance is achieved, the pass behavior is modified. This becomes noticeable in the top half of the winding where the slope of the macroscopic curve begins to flatten out. As the charge density in the oil becomes larger, relaxation within the passes becomes more apparent. The saturation effect is nicely demonstrated as the core and tank side ducts begin to relax and generate charge out of phase from one another so as to provide a cancelling effect.

The charge density distributions of Figure 6-21 are directly manifested in the corresponding static potential results shown in Figure 6-22. However, additional considerations are introduced by the net leakage currents subject to flow rate and local lumped resistances to ground. Voltage peaks are present at each pass inlet/outlet due to the high flow rates and hence generation in these ducts. As in the case of charge density, the core and tank side distributions are exactly one pass out of phase. The macroscopic distribution begins to asymptotically approach zero as charge saturation is achieved and the local leakage currents diminish.

Secondary voltage peaks are observed at the same axial locations as the larger peaks described above. This results from the surface leakage resistances connecting the various nodes. The significant leakage currents generated in the vicinity of the inlet/outlet ducts will flow to ground at the nearest convenient radial duct offering a low bulk resistance to the winding conductors. Hence, the axial nodes on the opposite side of the pass will be forced to higher values of voltage. Note that relaxation is significant in the axial ducts opposite the inlet/outlet ducts which serves to reduce the local potentials. As in the case of charge density, the static potential distributions are effectively periodic in space with the tank side lagging the core side by one pass.

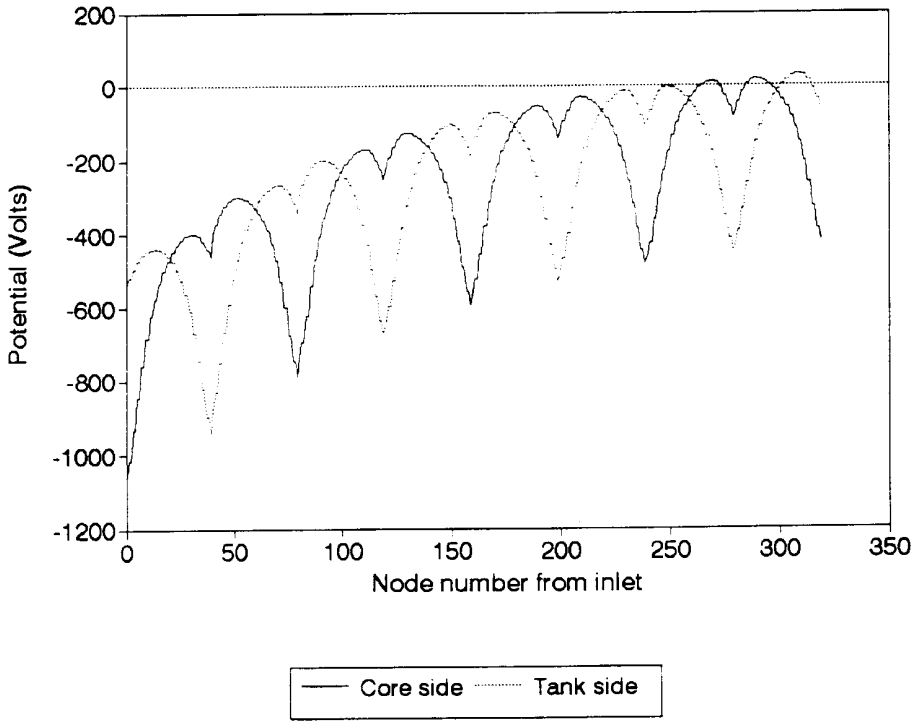

Figure 6-22
Static potential distributions under laminar conditions at 25°C without energization or inlet charge.

The charge density distributions at 50 gpm are given in Figure 6-23 with all other conditions the same as for the 10 gpm case. While the spatially periodic behavior is again observed, the faster flow rate does alter the results. In this case, the macroscopic characteristic remains linear throughout the entire winding. Furthermore, the charge distributions within the passes also exhibit a more linear behavior instead of the exponential shapes seen in Figure 6-21. This is explained by recalling the exponential form of the relaxation model from eq. 5-21. In this case, the $V\tau$ product is large relative to the duct lengths and significantly less charge is lost to relaxation. Hence, while the turbulent flows separate more charge, the oil residence times are reduced and relaxation is less efficient.

The static potential distributions for the 50 gpm case are presented in Figure 6-24. The voltages are an order of magnitude higher than the 10 gpm case with the peak value nearly reaching 10 kV. As for laminar flow, voltage maxima are observed at the pass inlet/outlet ducts sustaining the highest oil velocities. The core and tank side distributions are again periodic and exhibit a linear rather than exponential decay. Due to the domination of the charge generation mechanism, the relaxation of charge in the top passes is unable to reduce the voltage magnitude below 3.0 kV. Recall that with the slower driving flow rate, the oil residence times were sufficient to effectively neutralize the static potential at the top of the winding.

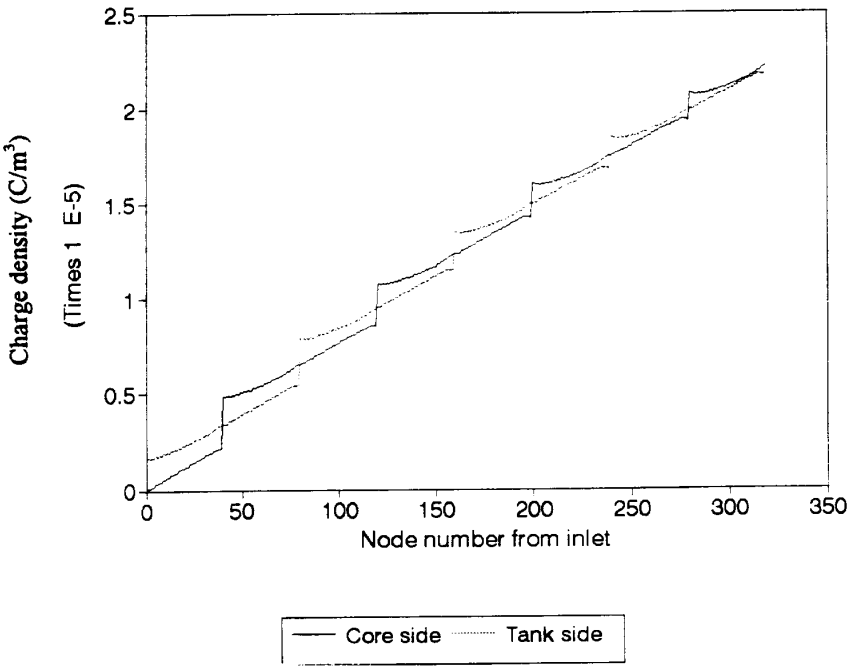

Figure 6-23
Charge density distributions under turbulent conditions at 25°C without energization or inlet charge.

For additional perspective, the laminar and turbulent cases are revisited under the same conditions with a non-zero charge density entering the winding. This situation is quite realistic since the external pumps and/or coolers are known to separate charge (110). The 10 gpm charge density distributions are shown in Figure 6-25 with a charge density of 10 $\mu C/m^3$ entering the first pass. From the macroscopic viewpoint of the pass terminals, relaxation was shown to completely dominate throughout the structure in Figure 6-17. In the final pass, the characteristics begin to level off as the saturation limit is approached.

On a local level, some degree of charge generation is evident. In the first pass, the core side distribution shows a minute increase in the faster flows near the inlet. As the blocking washer is approached, the axial flows are reduced and relaxation becomes more apparent. Moving into the second pass, a large drop is observed due to relaxation in the radial ducts which have longer residence times. Near the outlet of the second pass, the core side axial flow rates increase to augment generation and reduce relaxation. Moving up through the winding, generation becomes more significant as the inlet charge decays. As before, the tank side axial duct results show the same distribution lagging one pass behind the core side with both characteristics having a spatial period of two passes. Near the top of the winding, relaxation in one side is balanced by generation on the other side as the saturation limit is achieved. Note that in this case, saturation was approached from having excess charge whereas with no inlet charge the converse case of insufficient charge is observed.

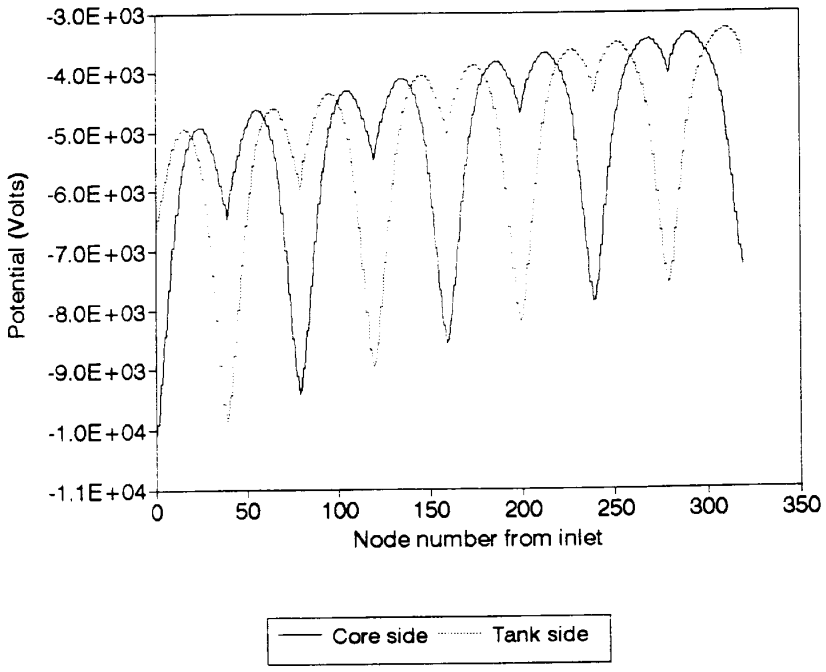

Figure 6-24
Static potential distributions under turbulent conditions at 25°C without energization or inlet charge.

As for the case of no inlet charge, the static potential curves follow the charge distributions as shown in Figure 6-26. With relaxation dominating, the voltage near the inlet is observed to be positive rather than negative. Near the inlet/outlet ducts, the strong separation of positive charge is evident as the negative countercharges reduce the positive surface potentials. Once sufficient inlet charge has relaxed from the oil, local generation dominance is apparent via negative potential peaks. Note that the average potential distributions will approach zero in the saturation limit while local potentials are sustained subject to flow velocity and leakage resistance.

The effect of inlet charge is much less impressive for the case of turbulent flow. The charge distributions remain linear as shown in Figure 6-27 on both the core and tank sides. Due to superposition of the influent 10 $\mu C/m^3$, the net gain of charge in the winding is effectively reduced as previously demonstrated in Figures 6-16 and 6-17. The detailed charge distributions show essentially the same behavior with and without the presence of inlet charge. A minor drop in the charge is apparent approaching the block washers at the end of each pass. However, in the former case, a higher degree of relaxation is evident in the axial ducts of the seventh and eighth passes where the core side and tank side values merge. This effect is evident in the corresponding voltage distributions shown in Figure 6-28. Both results are reduced in magnitude from Figure 6-24 due to relaxation and this

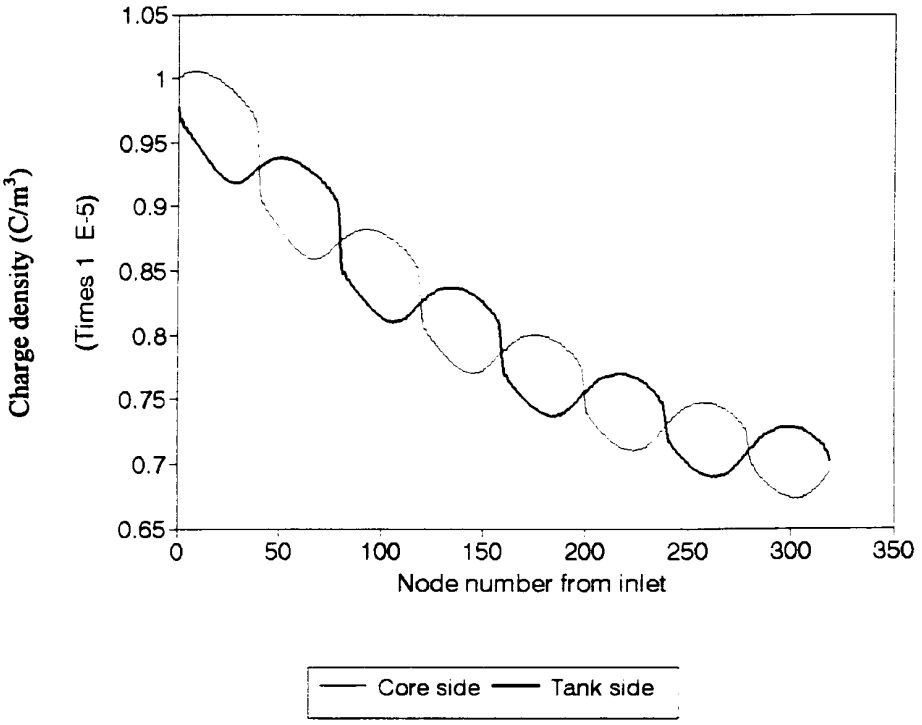

Figure 6-25
Charge density distributions under laminar conditions at 25°C with 10 μC/m^3 at the inlet and no applied voltage.

effect is pronounced in the last two passes. While the nature of the distributions in the seventh and eighth passes are somewhat different, their average values still fit the general trend.

The results of this section demonstrate that the effect of charge convected into the winding can dramatically influence streaming electrification. While the generation of charge in the external cooling loop is traditionally considered a hazard, these findings indicate the opposite. Provided the influent charge is of the appropriate sign, substantial reduction of streaming potentials in the winding may be obtained subject to the oil residence time. Independent of flow conditions and inlet charge, the electrification process will attempt to approach a limit where relaxation and generation balance one another. This situation is more readily observed with slower flow rates where generation is less appreciable. Furthermore, the saturation limit may be approached from having either surplus or insufficient charge density in the oil. Once the limit is achieved, local potential maxima are possible, but the average voltage decays to zero.

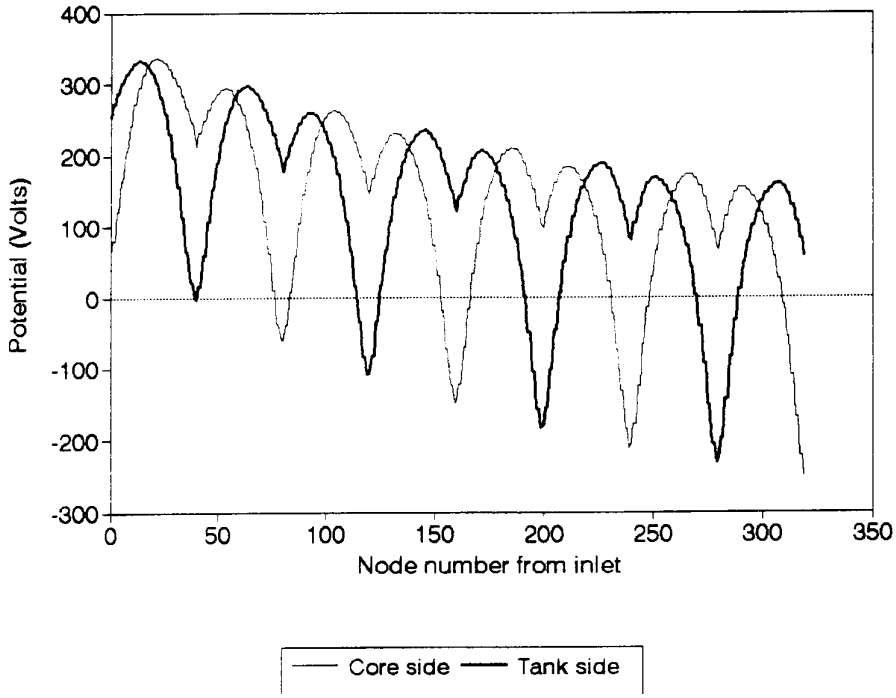

Figure 6-26
Static potential distributions under laminar conditions at 25°C with 10 μC/m^3 at the inlet and no applied voltage.

6.5.2 Influence of Operating Temperatures

A test case is presented at a fixed flow rate of 40 gpm with no applied voltage or inlet charge density over a range of temperatures. With this flow rate at 25°C, the axial ducts are turbulent and the charge density distributions shown in Figure 6-29 are similar to the 50 gpm results of Figure 6-23. The corresponding static potential distributions are presented in Figure 6-30 and also bear a strong resemblance to the 50 gpm case (see Figure 6-24). As expected, the lower flow rate gives less charge generated and hence smaller static potentials. In the top half of the winding, the characteristics of the voltage minima do change somewhat. This effect was previously observed in Figure 6-27 for 50 gpm with inlet charge and results from relaxation. At 40 gpm, this effect occurs even without influent charge since the smaller $V\tau$ product ensures longer residence times for relaxation in the axial ducts approaching the block washers.

Increasing the temperature to 40°C causes a significant change in the electrification results. The reduction of kinematic viscosity increases the Reynolds numbers in the radial ducts such that they become turbulent. As demonstrated in Sections 4 and 5, charge generation in the ducts is expected to increase with temperature. However, these enhancements to the charge generation process are effectively countered by increased relaxation as shown in

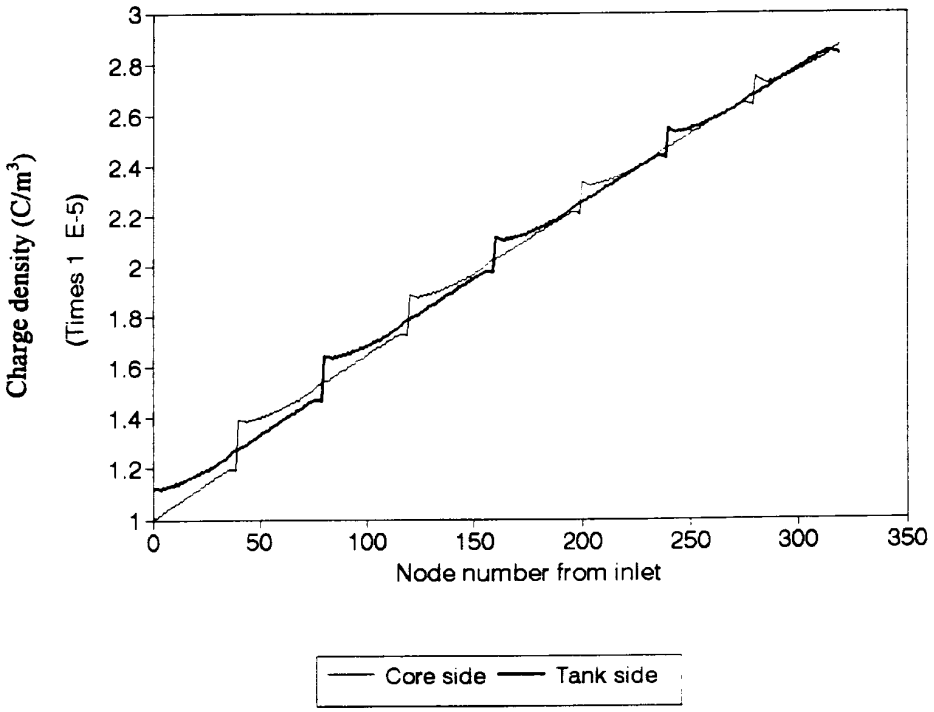

Figure 6-27
Charge density distributions under turbulent conditions at 25°C with 10 μC/m^3 at the inlet and no applied voltage.

Figure 6-31. This figure demonstrates where charge relaxation dominates within the passes. As explained in the previous section, a large jump in the charge density is observed across the block washers separating the passes. The core side charge distribution shows essentially a linear increase in the first pass. In the first axial duct of the second pass, a peak is achieved due to convected charge and generated charge from the first radial duct. Moving through the second pass, relaxation decay is evident until the increasing flows near the outlet restore the generation dominance. In the passes near the top of the winding, a large degree of relaxation is apparent due to the higher influent charge densities. Note that once again, the same behavior is observed on the tank side of the winding subject to a one pass spatial delay.

The static potential results for 40°C are presented in Figure 6-32. Due to the decrease in cellulose resistivity, the peak voltage is reduced by more than 10 kV from the 25°C case. Another interesting change is that the core and tank side voltage peaks are closer in magnitude at a given axial location due to the decrease in connecting surface resistance. The mean voltage characteristics still show a linear decay while the pass distributions are modified near the top of the winding. Once again, these changes occur in the axial flows approaching the block washers in low flow regions which are relaxation dominated. As the

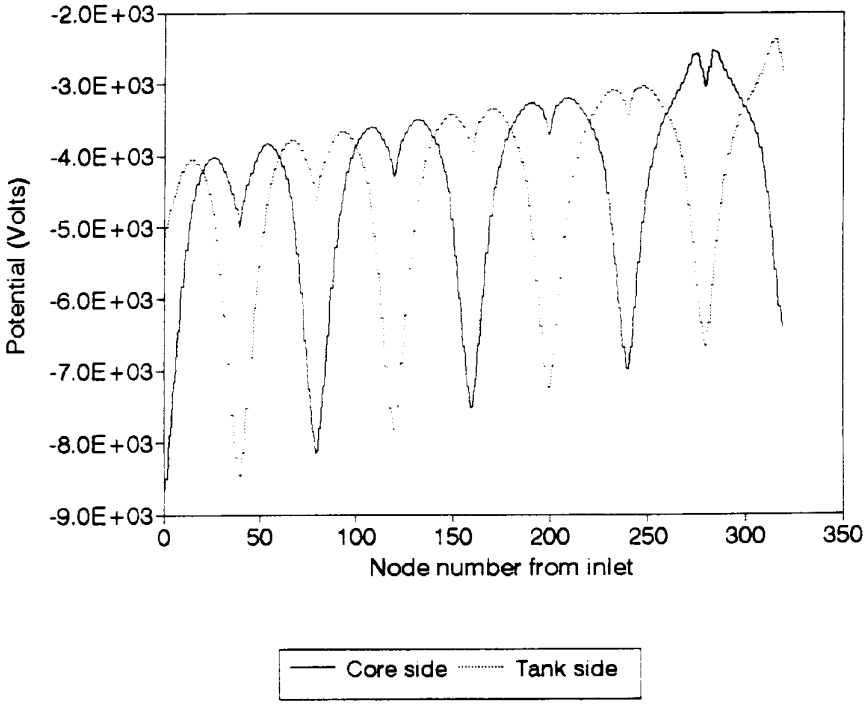

Figure 6-28
Static potential distributions under turbulent conditions at 25°C with 10 μC/m^3 at the inlet and no applied voltage.

charge density decays become more pronounced near the top of the winding, the potentials in these regions are more noticeably reduced and the voltage distributions modified accordingly.

The previous scenario is now reconsidered with the temperature raised to 60°C. As shown in Figure 6-33, the impact upon the charge density distributions is quite dramatic. The local charge distributions are shown to be modified as both generation and relaxation are augmented by the further increase in temperature. As in the 40°C case, the core side charge density increases linearly through the first pass and jumps significantly at the beginning of the second pass. However, in the present case, the saturation limit is nearly achieved in the second pass where turbulent generation balances temperature enhanced relaxation. A minor amount of relaxation is observed and then the charge increases through most of the third pass. However, the ultimate dominance of relaxation via enhanced conductivity becomes evident as the mean distribution begins to flatten at the top of the winding. The exponential decay of the charge within the passes becomes significant over generation as the saturation limit is achieved.

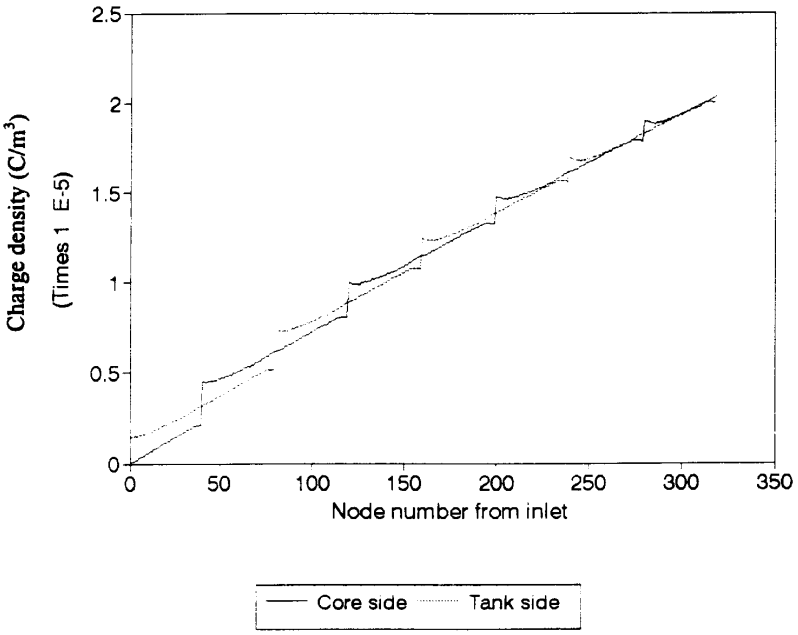

Figure 6-29
Charge density distributions at 40 gpm and 25°C without energization or inlet charge.

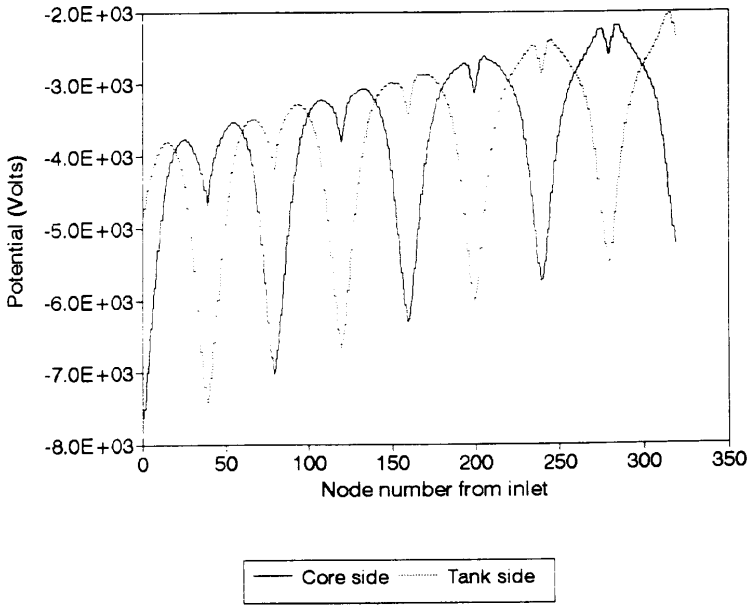

Figure 6-30
Static potential distributions at 40 gpm and 25°C without energization or inlet charge.

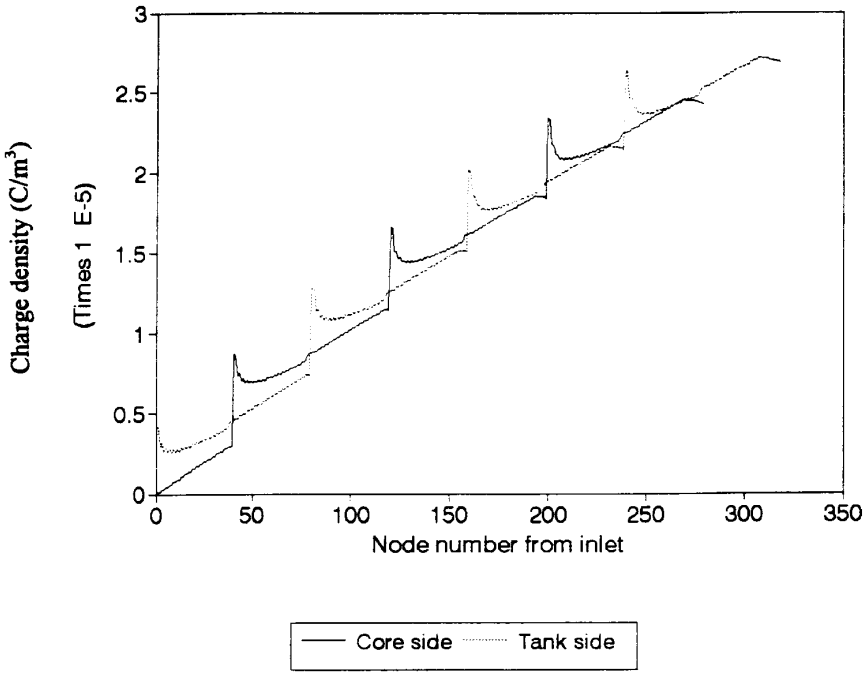

Figure 6-31
Charge density distributions at 40 gpm and 40°C without energization or inlet charge.

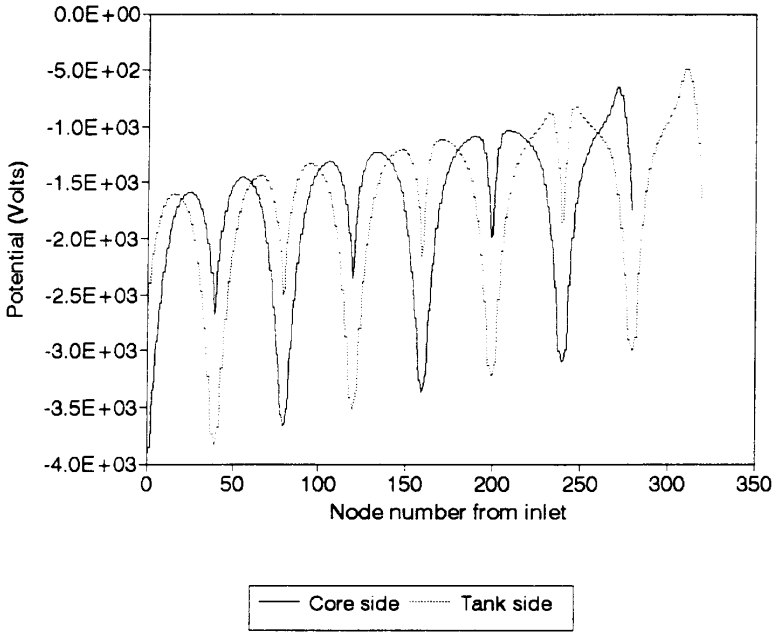

Figure 6-32
Static potential distributions at 40 gpm and 40°C without energization or inlet charge.

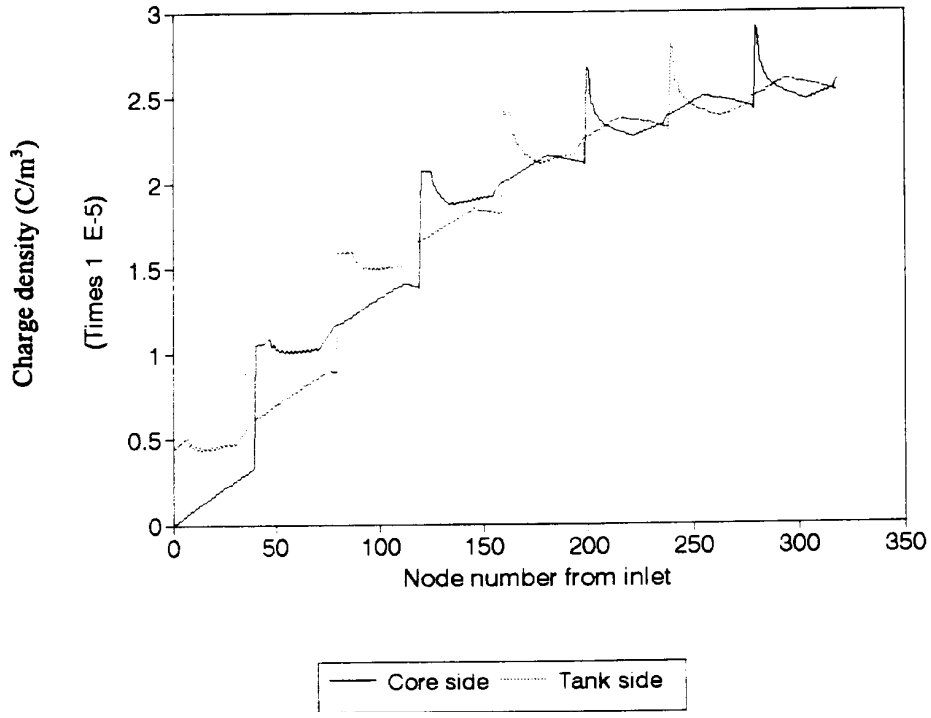

Figure 6-33
Charge density distributions at 40 gpm and 60°C without energization or inlet charge.

The logarithmic drop in pressboard resistivity becomes further evident in the voltage distributions as the temperature is raised to 60°C. As shown in Figure 6-34, the peak static voltage is reduced by nearly an order of magnitude from the previous case. Near the top of the winding, relaxation dominated ducts sustain small excursions to positive potential. As previously shown for 10 gpm (see Figure 6-26), the potential exponentially decays to zero in the top of the winding as saturation is achieved. In this case, the reduced surface resistances coupling the core and tank side ducts leaves the respective potential distributions within 100 V of one another. As a final point of interest, observe that the pass voltage distortions previously observed only at the top of the winding have been shifted to the middle passes. However, the mean distributions still follow the expected exponential trend.

This section illustrates that temperature will significantly alter streaming electrification in a transformer. The primary effect from the viewpoint of charge density comes from the Arrhenius variation of the oil conductivity. The resulting enhancement in both relaxation and generation effectively scales the effective residence time (or volume) required to achieve the charge saturation balance. The 40 gpm curves for 25°C and 60°C of Figures 6-29 and 6-33 serve to illustrate this point. At the lower temperature, the macroscopic apparent charge characteristic increases with nearly constant slope

through the winding. In the latter case, an exponential approach to the saturation limit is evident in the passes near the top of the winding.

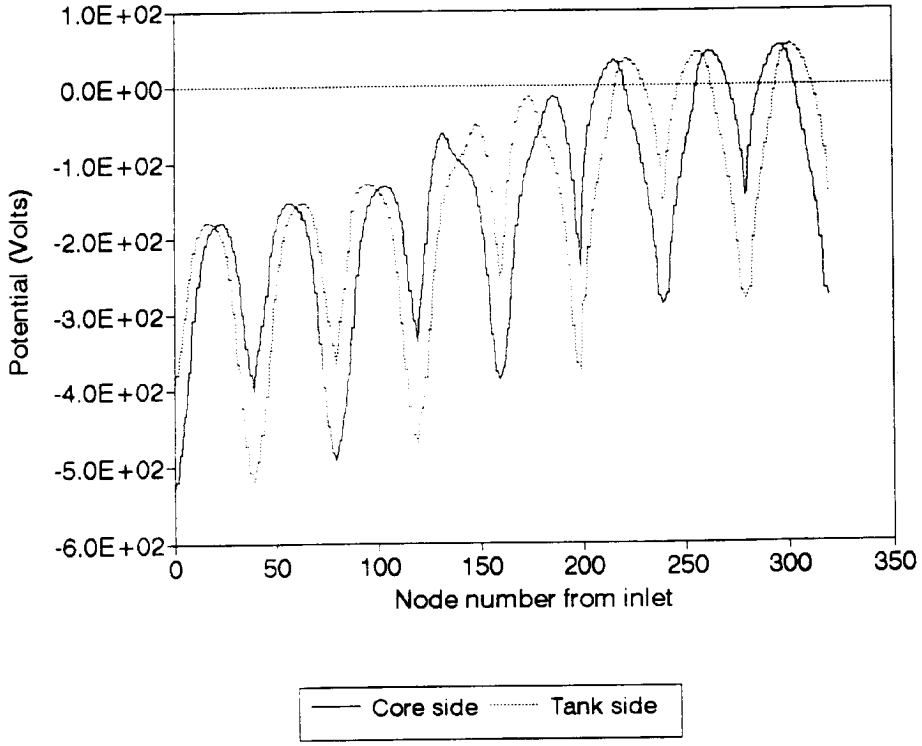

Figure 6-34
Static potential distributions at 40 gpm and 60° without energization or inlet charge.

These results reiterate the profound importance of the factor

$$1 - \exp\left(-\frac{x}{V\tau}\right) \qquad \text{(eq. 6-1)}$$

which has been incorporated in some form by numerous researchers (29, 13, 66). The relationship between the $V\tau$ factor and effective volume factor $x = L$ determines the shape of the charge characteristic within the structure of interest. With the mean velocity V fixed, temperature variations in the relaxation time τ via conductivity simply scale the saturation limit in or out of the space window defined by L. This scaling occurs in terms of the length constant and amplitude since the saturation limit varies directly with conductivity. The temperature peak observed for actual transformers may thus be readily explained by the associated large L values. The spatial window is sufficiently large that higher temperatures will make the saturation limit visible and reduce the amount of volume charge density required. In smaller laboratory structures,

L may be orders of magnitude less and saturation cannot be achieved over the same temperature range.

While the temperature variation of electrification is quite interesting, the transformer hazard is ultimately dictated by the leakage resistances. Noting that the cellulose resistivity drops exponentially with temperature, the static potentials must also decay. As previously demonstrated in Figure 6-20, the leakage resistance completely overwhelms the temperature increase in charge separation. Furthermore, the voltages are also reduced by enhanced relaxation of countercharges from the oil. Therefore, a cooler transformer is probably at greatest risk which has been the case for a number of field failures.

6.5.3 Influence of AC Energization

Having investigated flow and temperature effects, the impact of anticipated operating voltage must be considered. A worst case scenario of maximum (50 gpm) turbulent flow rate is investigated at two temperature extremes. At 25°C, the energized charge density characteristics are depicted in Figure 6-35. As expected, energization dramatically changes the charge distribution in the oil. The core and tank side values are no longer identical and out of phase due to the larger electric fields on the core side. However, both characteristics increase in a similar fashion moving toward the higher alternating voltages present at the top of the winding. Within the first pass, the charge density increases linearly since the radially directed fields in the axial ducts are not large enough to transport charge across the diffusion sublayer.

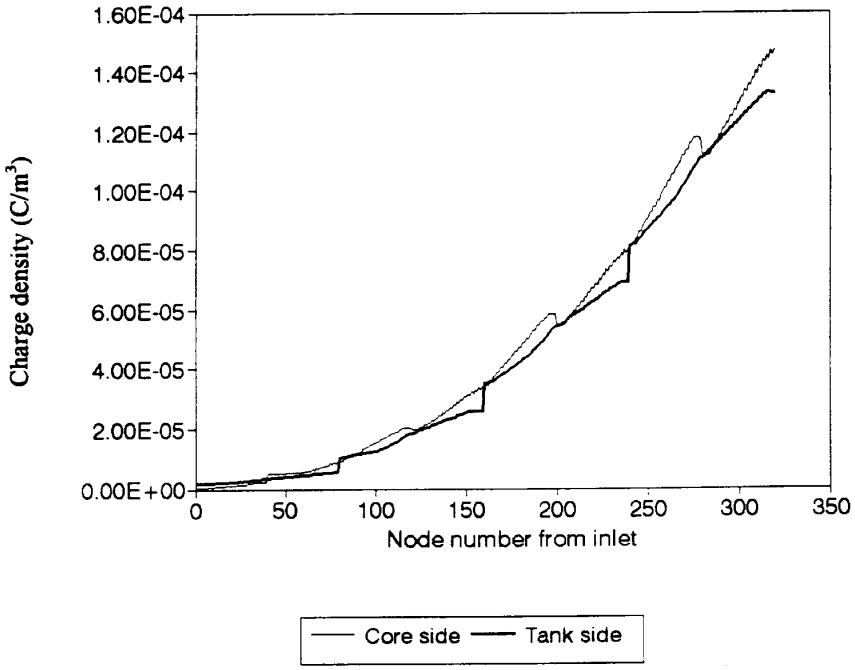

Figure 6-35
Charge density distributions at 50 gpm and 25°C with rated voltage and no inlet charge.

The core and tank side distributions behave in the manner originally discussed until the end of the second pass is reached and field transport becomes significant. Beyond this point, the core and tank side results are shown to drop across the block washers. In contrast, the tank side results exhibit increases at these locations. This occurs due to the difference in the core and tank side transverse electric fields. The core side fields are larger so the net outlet charge from an even numbered pass subject to radial convection augments the tank side charge. Exiting the odd numbered passes, the opposite is true and the core side characteristic initially drops. Note that the charge density exiting from the winding is an order of magnitude higher under energized conditions. Field transport dominates the electrification process substantially and the saturation limit is not approached.

Following the charge density behavior, the static potential distributions also increase toward the eighth pass as shown in Figure 6-36. Once again, the more efficient charge separation in the higher core side electric fields is apparent. Voltage peaks are obvious in the inlet outlet ducts where the Reynolds numbers are highest and the diffusion sublayers at a minimum. The axial ducts dominate and the voltage distributions within the passes effectively follow the corresponding flow rate curves of Figure 6-8. Within the size of the winding, relaxation effects are unable to reduce the potentials significantly. Notice that the peak potential now exceeds 100 kV in magnitude which is a factor of 10 higher than that with no applied voltage.

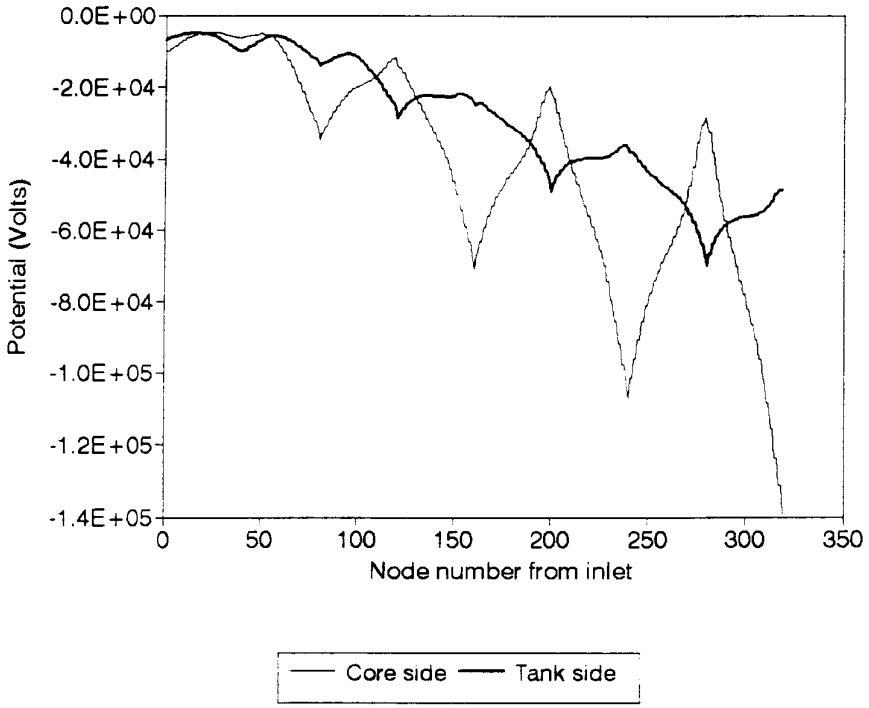

Figure 6-36
Static potential distributions at 50 gpm and 25°C with rated voltage and no inlet charge.

With the operating temperature increased to 60°C, the charge density characteristic are not significantly altered. As shown in Figure 6-37, the charge densities obey the same distribution with roughly a 50 percent increase in magnitude. This increase results from the decrease in kinematic viscosity and hence diffusion sublayer thickness with temperature and is augmented by the enhanced ion mobilities. The voltage distributions are illustrated in Figure 6-38 and are clearly similar to the previous case. However, the decreased leakage resistances are sufficient to reduce the peak voltage magnitude below 6.0 kV. Even at high temperature there is still no sign of the saturation limit and field transport in the axial ducts still dominates the relaxation process.

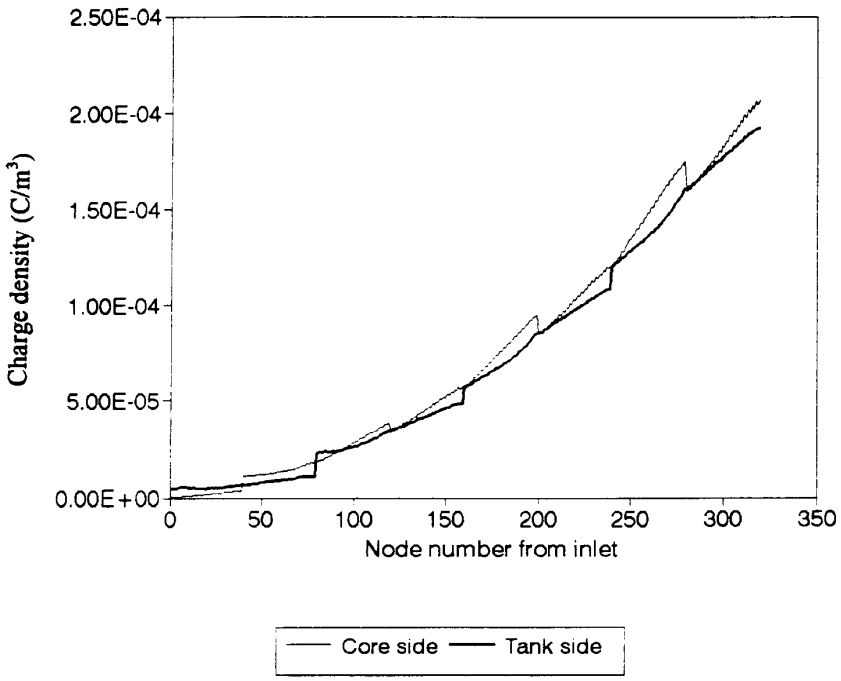

Figure 6-37
Charge density distributions at 50 gpm and 60°C with rated voltage and no inlet charge.

This section illustrates that under normal operating conditions, field transport of ions from the interfacial double layer is the dominating process. While the generated static potentials decrease when the temperature is raised, relaxation of charge from the oil is unable to noticeably counter generation. Extremely large static potentials are predicted in the passes near the top of the winding when operating at lower temperature. The implications of these results are discussed in the following section.

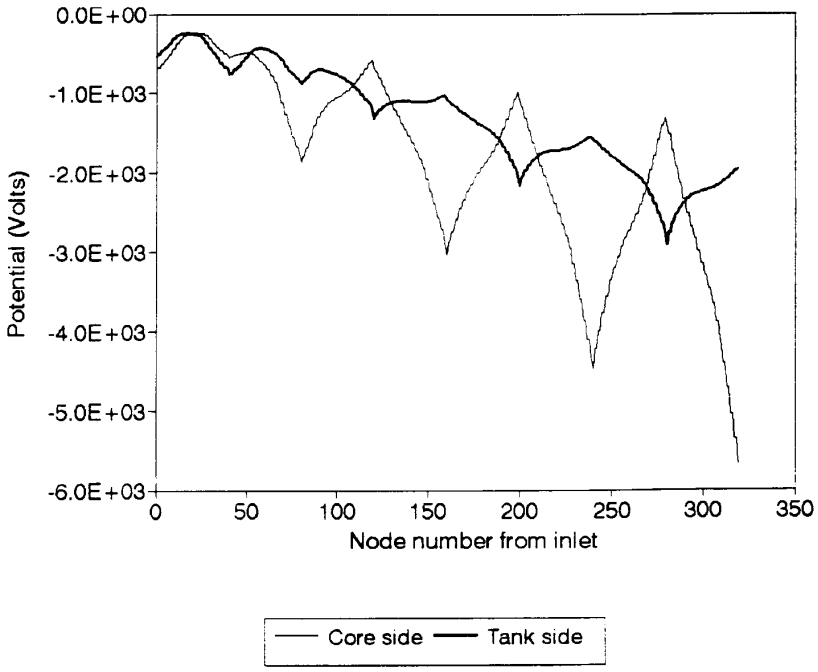

Figure 6-38
Static potential distributions at 50 gpm and 60°C with rated voltage and no inlet charge.

6.6 Practical Consideration of Results

Having performed a parametric analysis of streaming electrification in a realistic transformer winding, the results must now be analyzed from the operation standpoint. The salient findings are summarized below:

1. The static potentials resulting from electrification will be highest when the transformer is at low temperature even though charge generation will increase with temperature.

2. The saturation limit ultimately determines the amount of charge generation which is possible before relaxation becomes sufficient to prevent further increase.

3. The saturation limit is always approached to some degree whether the oil charge density is greater or less than the required value.

4. Modifying the temperature and/or flow rate can bring the saturation limit within the spatial volume of interest.

5. Influent charge density of the correct sign will relax and hence decrease the static potentials within the winding.

6. AC energization giving rise to sufficiently large electric fields can completely dominate the electrification process.

The task is now to consider the static electric field magnitudes required to compromise the dielectric integrity of a transformer.

The lumped value approach adopted here stipulates that nodal voltages are uniformly distributed on the corresponding duct end surfaces. Hence, the only fields within the bulk oil will result from total contained charge. In general, application of Gauss's law demonstrates that the static fields resulting from the bulk oil charge are not a threat. Looking at the highest generated charge density of $2.0 \times 10^{-4} C/m^3$ in a large radial duct, the associated field is more than an order of magnitude below the breakdown strength of transformer oil. Therefore, the focus should be upon the surface potentials and corresponding fields along the oil/cellulose interfaces and within the bulk cellulose.

The bulk insulation case is more readily considered and the paper insulation covering the winding conductors will see the greatest static stress. The paper covering is 0.64 mm thick and the DC breakdown strength can be as high as 140 kV/mm (76). The required static potential for breakdown is thus on the order of

$$V_{BD} = 90 \text{ kV} \qquad \text{(eq. 6-2)}$$

without superposition of operating AC fields. In the context of the present results, such magnitudes are obtained only under energized conditions. However, the predictions do indicate that this order of potential could also be obtained purely due to higher flows at temperatures approaching $0^{\circ}C$. As previously mentioned, some suspected electrification failures have occurred on cold startup when the leakage resistances were high. The possibility of damaging partial discharges at voltages well below 90.0 kV should also be recognized with the application of alternating voltage.

The scenario of high fields along insulation surface is more difficult to investigate. This situation may be very dependent upon the actual voltage distributions within a given duct. The present model supplies only inlet and outlet values which provide at least some measure of tangential surface fields. The maximum radial voltage drop occurs under energized conditions and provides a field on the order of

$$E = \frac{5.0 \times 10^4}{0.1} \text{ V/m} = 0.5 \text{ kV/mm} \qquad \text{(eq. 6-3)}$$

which is well below the breakdown strength of acceptable transformer oil(10 kV/mm) which is the weaker half of the oil/cellulose interface. Axial surface fields will be even less since the low surface resistances ensure that inlet and outlet voltages are similar.

The meaning of the present results is enhanced by comparison with other work, particularly large-scale transformer measurements. The only analytical results available for full-scale transformers are those of Roach and Templeton (66) who address the shell-form design. While detailed comparison is clearly not useful due to dramatic

geometry differences, it is gratifying to observe that their model also predicts a temperature peak at 50°C. The streaming current predicted at the top of the winding by Roach and Templeton is presented in Figure 6-39 and compares nicely with Figure 6-18. A comparison of charge density calculations can be made at 40°C and 40 gpm with no voltage applied (see Figure 6-31). The average velocity in the winding ducts is on the order of 5.52 ft/s (1.68 m/s) and the present model predicts 25 μC/m^3 at the pass outlet. Roach and Templeton's results are extrapolated to obtain 20 μC/m^3 from the outlet of a pancake coil duct with the same oil temperature. While this comparison is clearly not direct, it does provide some added comfort in interpreting the results.

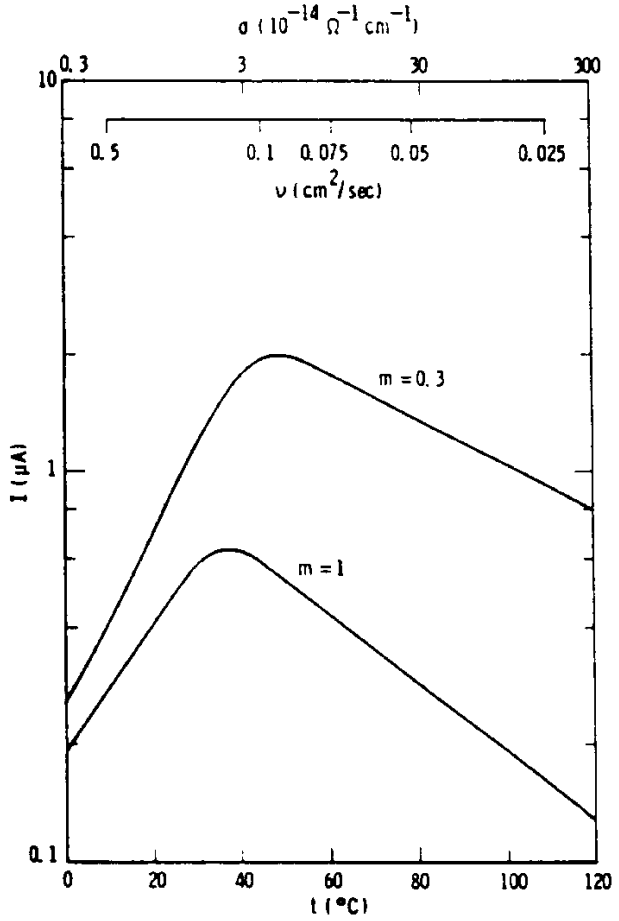

Figure 6-39
Streaming current vs oil temperature calculation at the outlet of a shell-form transformer coil duct by Roach and Templeton (66).

The only published experimental results for streaming electrification in core-form transformers is provided by Japanese researchers. Measurements by Higaki et al (22) illustrate a temperature peak at around 50°C for streaming currents in an actual transformer. Corresponding potential calculations predict on the order of -20 kV at the bottom of the high voltage winding at four times rated flow rate without applied

voltage. This corresponds fairly well with the static potential predictions shown in Figure 6-23 for similar conditions. Unfortunately, the majority of Japanese large-scale experiments address shell-form transformer geometries. Furthermore, most measurements involve leakage currents from specific transformer components which do not give insight regarding the internal charge distributions. Note that the previously discussed temperature peak is commonly observed in most large structure studies which supports the volumetric relaxation arguments made earlier.

Having demonstrated that the model results appear reasonable with respect to the admittedly limited findings of other investigators, the transformer failure mode must be further discussed. As explained in Section 3, the shell-form failures where electrification is suspected usually involve static discharging in the lower plenum where the oil enters the coils. While core-form failures are not as well documented, there is some evidence of similar static damage (99, 81). This is consistent with the model findings where no inlet charge is assumed and the windings are not energized. However, the present results predict that in the steady state with voltage applied, the largest static potentials will be present at the top of the windings where the highest electric fields are found.

This discrepancy may be explained in terms of the complete transformer hydraulic circuit and perhaps also the dynamics involved in reaching steady state. The cooling oil exiting the windings in the upper plenum will be directed through external radiators into the lower plenum. The model results thus far have not allowed for recirculating flow simply due to lack of empirical data for the additional components. Rather, complete relaxation in the upper plenum was assumed with the possibility of a specified inlet charge density generated by the cooling pumps. However, if significant recirculation did occur, the winding surface charge in the steady state might well be neutralized in the manner of Figure 6-26.

Many suspected transformer failures have occurred shortly after start up under dynamic conditions. Hence, the possibility of a stable operating regime at high temperatures where the transformer is "self-neutralized" should be considered. Static electrification would thus pose a threat in route to the steady state or if the stable mode were disturbed by some parametric change. This seems quite plausible , particularly in the former case where the initial temperature and hence insulation conductivity could be relatively low. Furthermore, some utilities apparently run the cooling pumps for several hours prior to bringing their transformers on-line. The bottom end of the winding (or inlet region) could thus begin to discharge before energization. The enhancement of AC stress could lead to further damage and possible failure before the insulation is heated sufficiently to limit the static potentials. Hence, the energized situation of Figure 6-38 might never be reached in a transformer which suffers an electrification induced failure. Rather, if the unit safely achieves a steady state condition, the recirculation (and generation) of charge through external components will provide a sufficiently neutralized operating regime to prevent problems.

The present model could readily be extended to simulate the charge feedback effect pending empirical data to calibrate the required element models. A complete hydraulic circuit for a shell-form transformer is provided by Roach and Templeton (66) in Figure 6-40. Each additional component would require a generation and relaxation model similar to the duct models described in Sections 4 and 5. The upper and lower plenums would probably serve as relaxation volumes due to their large size and slower oil velocities. Charge generation will most likely occur in the pumps and cooling radiators where the oil flow is expected to be very turbulent. The more complicated geometry of a transformer having multiple cooling loops could be treated using parallel network elements. Similarly, the remaining pass sections about each leg of the core would be parallel lumped element networks much like the ones used for a single pass. Closing the loop to provide charge feedback will require more iterations in the solver, but should be possible with the existing computer code.

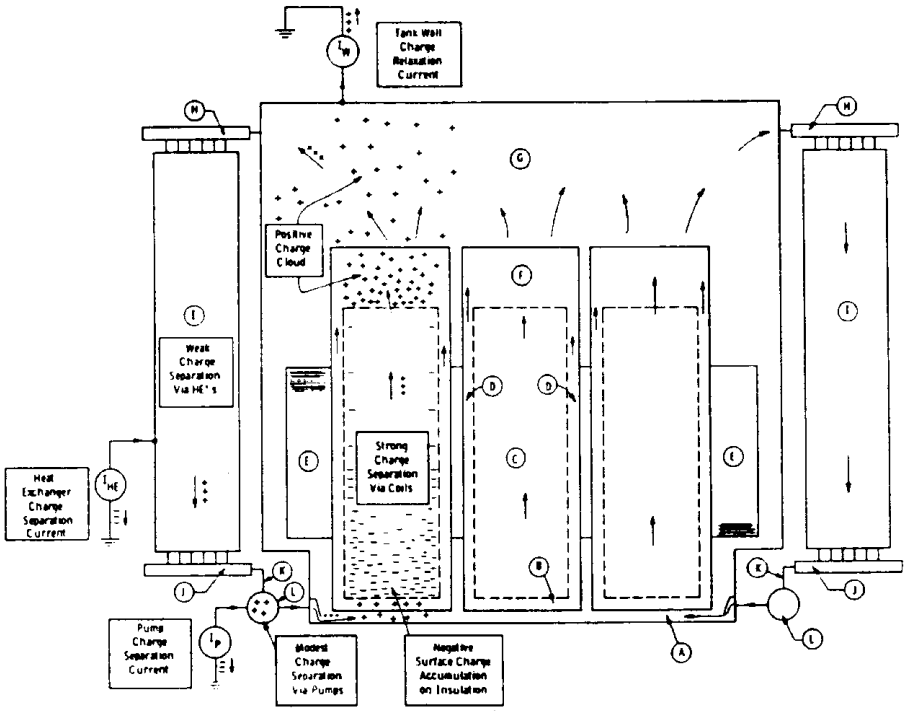

FIG. 1—*Model of three-phase transformer for flow electrification analysis. KEY: A = lower plenum, B = insulation entrance; C = coils; D = leakage ducts; E = core; F = insulation exit, bridge; G = upper plenum; H = pipe to HE; I = heat exchanger (HE); J = pipe from HE; K = pipe to pump; L = pump.*

Figure 6-40
Complete shell-form transformer flow network of Roach and Templeton (66).

The final aspect of making the model more realistic is to develop mathematical descriptions of particular sections of geometry. Both the core and shell-type transformers will have an inlet region where oil is transitioned into the windings from a plenum after passing through the cooling banks. In either case, the oil flow will experience dramatic velocity enhancements as a result of the substantial flow area

reduction. A predicted singularity in transverse velocity components is expected and excessive charge separation may occur in these regions. Shell-form failure analysis has clearly indicated the presence of static alleged discharge damage on the insulation near the winding inlet ducts (23, 99). The inlet problem is quite complicated and realistic large-scale experiments will probably be required to understand the local charging behavior. The theoretical model presented here could easily include the inlet region if an empirical model were developed.

A final note is in order with regard to transformer operations. In addition to proper oil selection and insulation processing, some steps can be taken to reduce electrification problems. The most critical issue is unnecessary oil circulation at low temperatures. Pumps should be brought on-line only as required to control the winding temperature so as to prevent thermal damage. The results of this section show that static potential buildup is most likely to occur where the insulation structure is cold. Furthermore, operating the absolute minimum number of pumps needed will reduce the effective oil velocities in the winding. This will serve to increase the oil residence time and allow the charge saturation limit to be more readily achieved so as to take advantage of self-neutralization. These suggestions will be most important during the initial transient phase of operation where many electrification failures are believed to have occurred. The path taken to reach steady state may be quite critical to avoid the pitfall(s) which lead to static charging problems.

The results of this section serve to illustrate the usefulness of modeling streaming electrification in a realistic structure. The importance of scale has been demonstrated with regard to the charge saturation limit and the predictions appear reasonable based on the limited data available. A parametric study has provided an indication of how major variables such as flow rate, temperature and energization influence streaming electrification within the winding. This methodology provides a coupling between the real transformer and the more readily investigated laboratory model. All of the experimental work presented in earlier sections has illustrated the importance of scale.

7

CONCLUSIONS

7.1 Experimental Results

Experiments were performed to investigate the impact of moisture dynamics upon streaming electrification in both shell-form and core-form transformer geometries. In each case, the process of moisture equilibration between the oil and cellulose did not dramatically influence charge separation. However, at very low moisture contents, charge separation did appear to decline with decreasing oil moisture which is opposite of the behavior reported for high oil moisture levels. This suggests that two different oil moisture regimes exist with regard to electrification and the transition is estimated to occur at approximately 5.0 ppm. While this is quite interesting, moisture dynamics per se does not appear to dramatically influence electrification within the context of these experiments.

The moisture dynamics experiments also serve to demonstrate that the Norris curves may not be precise in defining equilibrium levels in the oil and cellulose. While the curves are believed to be correct at higher levels under steady-state conditions, extrapolation into the low ppm/percent range does not agree with experimental findings. This is believed to result primarily from a moisture profile existing within the cellulose insulation. A relatively thin surface layer of the cellulose is believed to govern the equilibration process. However, this layer may be much wetter than the bulk cellulose being measured and therefore the actual moisture content in the oil will be higher than expected. This was consistently observed in both the core and shell-form experiments.

Additional experiments were performed using a shell-form transformer model to examine the impact of charge separation or dielectric integrity. Partial discharge measurements indicated two distinct regimes of behavior. At low applied voltage, the discharges were sporadic and indicated the long charging time constant characteristic of streaming electrification. At higher voltages, AC discharging became much more apparent in both magnitude and repetition rate. Note that flow electrification over time was found to reduce the AC inception voltage for partial discharge. Given the small size of the model, leakage of charge prevented sufficient accumulation to cause damaging discharges.

Further experiments were carried out using a special test cell to determine the impact of deposited charge on the surface breakdown strength of cellulose samples. Even with the charge injection and relaxation schemes optimized for maximum surface deposition, the effect of surface charge was very minimal within the experimental statistics under impulse conditions. This experiment was fundamentally limited by impulse generator capability which dictated small sample sizes in order to establish a base case. The leakage of deposited charge to ground prevented significant electric fields from being generated.

A final experiment was performed using the shell-form model to determine the impact of cumulative charging on static electrification. The fluid loop was modified such that the relaxation tank could be switched in or out with the hope that charged oil could be forced into the model. Unfortunately, the charge generated in the model was able to relax almost completely in the connecting pipes and the only inlet charge was supplied by the pump. Furthermore, frictional heating with the removal of the relaxation tank was sufficient to enhance charging in the model. However, with the given influent charge level available, charge generation in the model was not affected. This result is quite important in that treating relaxation and generation of charge by superposition appears to be correct. This assumption was critical for the development of the theoretical model.

In reviewing the experimental work, the importance of scale is clearly demonstrated. Even using the realistic shell-form transformer model, the structure was not large enough to demonstrate damaging effects of streaming electrification. The leakage paths from the insulating surfaces were not long enough to prevent substantial charge loss. This effect was also clear in the surface breakdown experiments. Hence, the importance of considering a structure of realistic proportions becomes clear and provides further justification for large-scale modelling. The data provided by these experiments was incorporated into the development of the network-based streaming electrification model.

7.2 Theoretical Work

A boundary layer approach for charge separation in a transformer duct was developed and empirically calibrated. The use of a boundary layer to provide a length scale for defining the appropriate physical model was shown to be reasonable to a first order. Based on previous experiments, the duct model successfully treats different flow regimes in conjunction with temperature and energization. A constant derivative charge flux at the duct wall was found to be an acceptable boundary condition. The velocity dependence of the boundary condition has been justified by considering solid/liquid interface as a supply region having finite thickness.

The single duct model was incorporated into a network model so as to approximate the core-form laboratory structure. Each duct was defined as a specific element type in terms of hydraulic resistance, charge relaxation, charge generation and surface leakage resistance. Virtual loss elements were used to treat the hydraulic problems introduced by confluence points in the structure. The flow model solutions were determined to be reasonable based on comparison with previous work and the oil flow distribution was found to be similar over a wide range of flow rates. The electrification boundary condition was empirically determined based on the net charge exiting from the core-form structure. The flow and energization dependence of the outlet charge was found to be predicted by the model to a first order after calibration. The temperature calibration required the incorporation of an artificial boundary condition dependence at high temperatures for the short ducts in the core-form model. The static potential model was demonstrated to provide a reasonable voltage distribution based on previous data.

Having completed an intermediate calibration of the network model using empirical results for the core-form structure, the model was extended to a complete transformer winding. The results provide very useful insight into electrification in large transformers. The importance of scale is quite clear and the large-scale model was found to predict some of the effects observed in real transformers but not measured at the laboratory scale. A temperature peak was predicted in the charge density exiting from the winding as the oil conductivity becomes sufficient to relax charge near the outlet pass. Ultimately, the charge and hence potential distribution in the winding was shown to depend on the product of the oil velocity and relaxation time. The $V\tau$ product determines whether the saturation limit where relaxation and generation balance is achieved within the winding.

With no applied AC voltage, the highest static potentials were observed at the winding inlet. The potential declines along the winding as charge in the oil relaxes to neutralize the surface. At the higher flow rates, the saturation limit is not as apparent and a negative potential exists in all of the ducts. However, at lower flow rates, saturation is achieved at the top of the winding and the average static potential becomes zero. Note that the saturation limit was always approached regardless of influent charge or velocity. While the charge generation tends to increase with temperature, the logarithmic decrease in cellulose resistivity was found to dominate. Hence, the worst case static potentials were always observed at lower temperatures.

The application of AC voltage effectively inverted the charge and potential distributions relative to the un-energized case. This occurs due to the highest voltages and hence electric fields being present at the top conductor disks. Note that this would not be the case in a shell-form transformer where the coil-to-coil voltage drops are transverse to the primary flow axis. The impact of field transport was apparent in the extremely high values of charge predicted at rated voltage. While high temperature increases the efficiency of the charge injection process, the leakage resistance still dominates with

regard to static potentials. As previously stated, the worst case surface potentials were always found at low temperature.

The network-based streaming electrification model has been demonstrated to a first order. The full-scale simulation results appear very reasonable and provide critical perspective which cannot be obtained in smaller structures. The single element and core-form network empirical calibrations provide a justification for the approach and results obtained. Having established the methodology, new theoretical and experimental information may now be readily incorporated and evaluated in the context of an actual power transformer.

7.3 Implications for the Utility Industry

This work indicates that the static electrification threat to power transformers may be reduced through modified operating procedures. In terms of static potentials on insulating surfaces, cold temperatures are clearly the worst case. Even with relatively low levels of charge separation, substantial surface charge may result given the extremely high leakage resistance. This may give rise to discharging which will cause local insulation damage and also introduce carbon particles and gas bubbles into the oil. The low temperature situation will be much worse for the case of high flow rate even with no applied voltage.

As a general practice, it is recommended to run the cooling pumps only when necessary. When a transformer is cold and the pumps are run prior to energization, a significant static potential distribution may be present when the AC voltage is finally applied. However, if the unit were energized and heated under load, the insulation temperatures would be higher when the pumps became necessary to prevent thermal damage. Hence, the static potential levels would be limited by the reduced leakage resistances and the electrification threat minimized.

Another interesting aspect of the large-scale modelling is the possible effect of charge feedback. In all cases, the effect of influent charge was to reduce the static potential levels within the test winding. This suggests that perhaps a self-neutralized state exists once the transformer has achieved a stable operating point. Hence, the electrification threat might be most severe just after energization which is suggested by several failures very early in service life. If the electrification can be controlled by following the above guidelines, perhaps the safe operating situation with charge feedback minimizing the static potentials can be achieved.

7.4 Future Work

While a great deal has been accomplished in the present work, much more research needs to be done in this area. With regard to moisture dynamics, an improved method

for profiling moisture in cellulose would be invaluable. A technique which could measure on-line and eliminate the complications of sampling would be especially useful. The Norris curves could then be generated accurately for the low moisture regime where many transformers operate. With sufficiently accurate equilibrium curves, oil moisture readings from transformers in the field would be much more meaningful.

One strong conclusion from this work is that further experiments must be performed on a larger or even full-scale. The surface charge breakdown tests should be run using a larger cell such that more significant surface charge may be obtained. In addition to using larger structures, some thought should also be given to geometry. For example, many of the simple laboratory structures which are readily analyzed are much different from reality. The shell-form transformer inlet region is an important structure which may never be understood without good empirical data. Similarly, the corners and junctions in a core-form manifold have yet to be considered on an individual basis.

In conjunction with large-scale empirical work, the fundamental aspects of electrification need further investigating. In particular, boundary conditions which have an electrochemical basis would be useful. While more detailed analysis may require more sophisticated modelling (i.e. finite elements) the results could be readily adapted into the existing model. By defining terminal characteristics for a duct using a new method, it could be incorporated into the network approach developed in this work. Perhaps by continuing with large-scale experiments and improved analytical models, the problem can be even better understood and eliminated.

8

REFERENCES

1. Crofts, D. W., "The Static Electrification Phenomenon in Power Transformers", IEEE Trans. Elec. Insul., Vol. 23, No. 1, 1988,pp 137-146.

2. Lee, M. J. and Nelson, J. K., "Flow-Induced Electrification and Partial Discharge Measurements in Transformer Duct Structures", IEEE Trans. Elec. Insul. Vol. 26, No. 4, August 1991, pp 739-748.

3. Helmholtz, H., Physik und Chemie, Vol. 243, 1879, pp 337-382.

4. Chapman, D. L., "A Contribution to the Theory of Electrocapillarity", Phil. Mag. Vol. 25, 1913, pp 475-481.

5. Gouy, G., J. Phys. Chem. Vol. 9, 1910, pg 457.

6. Robinson, R. A. and Stokes, R. H., *Electrolyte Solutions*, Butterworth's Publications Ltd., London, 1959.

7. Stern, O., "Zur Theorie der Electrolytischen Doppelschicht", Z. Elektrochem., Vol. 30,1924, pg 508.

8. Grahame, D.C., "The Electrical Double Layer and the Theory of Electrocapillarity", Chem. Rev. Vol. 41, 1947, pp 441-501.

9. Bockris, J. O'M., Devanathan, M. A. V., and Müller, K., "On the Structure of Charge Interfaces", Proc. Roy. Soc., Vol. A274, 1963, pp 55-79.

10. Hunter, R. J., *Zeta Potential in Colloid Science*, Academic Press, New York, 1981.

11. Quarmby, A. and Anand, R. K., "Axisymmetric Turbulent Mass Transfer in a Circular Tube", J. Fluid Mech., Vol. 38, Part 3, 1969 pp 433-455.

12. Gasworth, S. M., Melcher, J. R. and Zahn, M., "Electrification Problems Resulting from Liquid Dielectric Flow", EL-4501, Research Project 1536-7, Final Report to EPRI, April 1986.

13. Abedian, B. and Sonin, A. A., "Theory for Electric Charging in Turbulent Pipe Flow", J. Fluid Mech., Vol. 120, 1982, pp 199-217.

14. Klinkenberg, A., *Advances in Petroleum Chemistry and Refining*, Vol. 8, Chapt. 2, Edited by McKetta, J. J., Interscience Publishers, 1964.

15. Hughes, J. F., and Bright, A. W., "Electrostatic Hazards Associated with Powder Handling in Silo Installations", IEEE Trans. Ind. Appl., January/February 1979, pp 100-103.

16. Gemant, A., *Liquid Dielectrics*, Wiley, New York, 1933.

17. Klinkenberg, A., and Van der Minne, J. L., *Electrostatics in the Petroleum Industry*, Elsevier, The Netherlands, 1958.

18. Ginsburgh, I., "The Static Charge Reducer", J. Colloid and Interface Sci., Vol. 32, No. 3, March 1970, pp 424-432.

19. Huber, P. W. and Sonin, A. A., "Theory for Electric Charging in Liquid Hydrocarbon Filtration", J. Colloid and Interface Sci., Vol. 61, No. 1, August 1977, pp 109-125.

20. Yasufuku, S., Ise, T., Inoue, Y., and Ishioka, Y., "Electrokinetic Phenomena in Electrical Insulating Oil/Impregnated Cellulosic Pressboard Systems", IEEE Trans. Elec. Insul., Vol. EI-12, No. 5, October 1977, pp 370-375.

21. Shimizu, S., Murata, H., and Honda, M., "Electrostatics in Power Transformers", IEEE Trans. Power Appar. and Sys., Vol. PAS-98, No. 4, July/August 1979, pp 1244-1250.

22. Higaki, M., Kako, Y., Moriyama, M., Hirano, M., Hiraishi, K., and Kurita, K., "Static Electrification and Partial Discharges Caused by Oil Flow in Forced-Oil-Cooled Core-Type Power Transformers", IEEE Trans. Power Appar. and Sys., Vol. PAS-98, No. 4, July/August 1979, pp 1259-1267.

23. Moore, H. R., "Inspection of Transformer at Palo Verde Nuclear Plant", Proc. 3rd EPRI Workshop on Static Electrification in Power Transformers, San Jose, California, January 1992.

24. Tamura, R., Miura, Y., Watanabe, T., Ishii, T., Yamada, N., and Nitta, T., "Static Electrification by Forced-Oil Flow in Large Power Transformers", IEEE Trans. Power Appar. and Sys., Vol. PAS-99, No. 1, January/February 1980, pp 335-343.

25. Lee, M. J. and Nelson, J. K., "Electrokinetic Effects in Power Transformers", EL/ER-6880, Research Project 8000-1, Interim Report to EPRI, June 1990.

26. Lee, M. J. and Nelson, J. K., "Electrokinetic Effects in Power Transformers", TR-101216, Research Project 1499-12, Interim Report to EPRI, November, 1992.

27. Zahn, M., Melcher, J. and Lyon, D., "Flow Electrification in Transformer Oil/Cellulosic Systems", CEIDP Annual Report, 1986, pp 257-265.

28. Higaki, M., Miyao, H., Endou, K., and Ohtani, H., "A Calculation of Potential Distribution Caused by Static Electrification Owing to Oil Flow in an Oil-Paper Insulating System and its Application to Partial Discharge Phenomenon in Oil", IEEE Trans. Power Appar. and Sys., Vol PAS-98, No. 4, January/February 1979, pp 1275-1282.

29. Tanaka, T., Yamada, N., and Yasojima, Y., "Characteristics of Streaming Electrification in Pressboard Pipe and the Influence of an External Electric Field", J. Electrostatics, Vol. 17, 1985, pp 215-234.

30. Stannett, A. W., "The Conductivity of Hydrocarbon Transformer Oil Containing Water and Solid Conducting Particles", British J. Appl. Phys., Vol. 2, April 1951, pp 110-114.

31. Oommen, T. V., "Static Electrification Control in Power Transformers", EPRI Final Report, 1989.

32. Theodossiou, G., Nelson, J. K., Lee, M. J., and Odell, G. M., "The Influence of Electrohydrodynamic Motion on the Breakdown of Dielectric Liquids", J. Phys. D: Appl. Phys., Vol. 21. , 1988, pp 45-50.

33. Boumans, A. A., "Streaming currents in Turbulent Flows and Metal Capillaries", Physica, Vol. 23, 1957, pp 1038-1046.

34. Boumans, A. A., "Streaming Currents in Turbulent Flows and Metal Capillaries", Physica, Vol. 23, 1957, pp 1047-1055.

35. Rutgers, A. J., De Smet, M. and Rigole, W., "Streaming Currents in Nonaqueous Solutions", J. Coll. Sci., Vol. 14, 1959, pp 330-337.

36. Schön, G., "Elektrostatische Aufladunsvorgänge und ihre Zündgefahren", Chemie. Ing. Techn., Vol. 24, No. 6, January 1962, pp 432-436.

37. Goodfellow, H. D., and Graydon, W. F., "Electrostatic Charging Current Characteristics for Different Fluid Systems", Chem. Eng. Sci., Vol. 23, 1968, pp 1267-1281.

38. Gibson, N. and Lloyd, F. C., "Electrification of Toluene Flowing in Large-Diameter Metal Pipes", J. Phys. D:Appl. Phys., Vol. 3, 1970, pp 563-573.

39. Gibson, N., and Lloyd, F. C., "Effect of Contamination on the Electrification of Toluene Flowing in Metal Pipes", Chem. Eng. Sci., Vol. 25, 1970, pp 87-98.

40. Carruthers, J. A., and Marsh, K. J., "Charge Relaxation in Hydrocarbon Liquids Flowing Through Conducting and Non-conducting Pipes", J. Inst. Petrol., Vol. 48, No. 462, June 1962, pp 169-179.

41. Shafer, M. R., Baker, D. W., and Benson, K. R., "Electric Currents and Potentials Resulting from the Flow of Charged Liquid Hydrocarbons Through Short Pipes", J. Research, NBS-C Eng. and Inst., Vol. 69C, No. 4, October/December 1965, pp 307-317.

42. Carruthers, J. A. and Wigeley, K. J., "An Estimation of Electrostatic Potentials, Fields and Energies in a Rectangular Metal Tank Containing Charged Fuel", J. Inst. Petrol., Vol. 48, No., 462, June 1962, pp 180-195.

43. Ito M. and Ueda, M., "Electric Potential and Charge Density in Insulating Liquid Generated by Liquid Flow", E. E. Japan, Vol. 90, No. 4, 1970, pp 68-75.

44. Lauer, J. L. and Antal, P. G., "Electrostatic Charge Separation During Nonuniform Flow of Hydrocarbons Through Porous Insulators", J. Coll. Interface Sci., Vol. 32, No.n3, March 1970, pp 407-423.

45. Oommen, T. V. and Lindgren, S. R., "Streaming Electrification Study of Transformer Insulating System Using a Paper Tube Model", IEEE Trans. Power Delivery, Vol. 5, No. 2, April 1990, pp 972-983.

46. Radwan, R. M., El-Dewieny, R. R., and Metwally, I. A., "Investigation of Static Electrification due to Transformer Oil Flow in Power Apparatus", IEEE Trans. Elec. Insul., Vol. 27, No. 2, April 1992 , pp 278-286.

47. Miyao, H., Higaki, M., and Kamata, Y., "Influence of AC and DC Fields on Streaming Electrification of Transformer Oil", IEEE Trans. Elec. Insul., Vol. 23, No. 1, 1988, pp 129-135.

48. Morin, A. J., Zahn, M. and Melcher, J. R., "Fluid Electrification Measurements of Transformer Pressboard/Oil Insulation in a Couette Charger", IEEE Trans. Elec. Insul., Vol. 26, No. 5, October, 1991, pp 870-901.

49. Kedzia, J., "Investigation of Transformer Oil Electrification in a Spinning Disk System", IEEE Trans. Elec. Insul., Vol. 24, No. 1, February 1989, pp 59-65.

50. Kedzia, J., "Measurement of Electrification of Liquids in a Rotating Cylinder System", J. Electrostatics, Vol. 20, 1988, pp 305-312.

51. Kedzia, J., "Electrostatic Properties of Aged Transformer Oil", IEEE Trans. Elec. Insul., Vol. 24, No. 2, April, 1989, pp 175-178.

52. Oommen, T. V., and Petrie, E. M., "Electrostatic Charging Tendency of Transformer Oils", IEEE Trans. Power Appar. and Sys., Vol. PAS-103, No. 7, July 1984.

53. Yasuda, M., Goto, K., Okubo, H., Ishii, T., Mori., E. and Masunaga, M., "Suppression of Static Electrification of Insulating Oil for Large Power Transformers", Proc. IEEE Winter Power Meeting, Paper WM197-2 1982.

54. Ieda, M., Goto, K., Okugo, H., Miayamoto, T., Tsukioka, H., and Kohno, Y., "Suppression of Static Electrification of Insulating Oil for Large Power Transformers", IEEE Trans. Elec. Insul., Vol. 23, No. 1, 1988, pp 153-157.

55. Ieda, M., Yanari, T., Miyamoto, T. and Higaki, M., "Investigation of Static Electrification in Large Power Transformers in Japan", Proc. 3rd EPRI Workshop on Static Electrification in Power Transformers, San Jose, California, January 1992.

56. Griffin, P. J. and Christie, J., "Effects of Water and Benzotriazole on Electrostatic Charge Generation in Mineral Oil/Cellulose System", Proc. 3rd. EPRI Workshop on Static Electrification in Power Transformers, San Jose, California, January 1992.

57. Lee, M. J. and Nelson, J. K., "Tandem Charge Density Monitor", IEEE Trans. Elec. Insul., Vol. EI-25, 1990, pp 399-404.

58. Denbow, N. and Bright, A. W., "The Design and Performance of Novel On-Line Electrostatic Charge Density Monitors, Injectors and Neutralisers for Use in Fuel Systems", Inst. Phys. Conf. Ser. No. 48, 1979pp 171-180.

59. Zahn, M., Morin, A. J., Melcher, J. R., and Otten, D., "An Absolute Charge Sensor for Fluid Electrification Measurements", IEEE Trans. Elec. Insul., Vol. 26, 1991, pp 181-199.

60. Abedian, B. and Miaoulis, I. N., "A Passive Probe for Electrostatic Charge Density Measurements", Rev. Sci. Inst., Vol. 61, No. 11, November, 1990, pp 3416-3420.

61. Gavis, J. and Koszman, I., "Development of Charge in Low Conductivity Liquids Flowing Past Surfaces: A Theory of the Phenomenon in Tubes", J. Coll. Sci., Vol. 16, 1961, pp 375-391.

62. Koszman, I. and Gavis, J., "Development of Charge in Low Conductivity Liquids Flowing Past Surfaces", Chem. Eng. Sci., Vol. 17, 1962, pp 1013-1022.

63. Koszman, I. and Gavis, J., "Development of Charge in Low Conductivity Liquids Flowing Past Surfaces - Experimental Verification and Application of the Theory Developed for Tube Flow", Chem. Eng. Sci., Vol. 17,1962, pp 1023-1040.

64. Gavis, J., "Transport of Electric Charge in Low Dielectric Constant Fluids", Chem. Eng. Sci., Vol. 19, 1964, pp 237-252.

65. Glasstone, S., Laidler, K. J. and Eyring, H., *The Theory of Rate Processes*, McGraw-Hill Book Company Inc., 1941, New York and London

66. Roach, J. F. and Templeton, J. B., "An Engineering Model for Streaming Electrification in Power Transformers", *Electrical Insulating Oils*, STP 998, H. G. Erdman, Ed., American Society for Testing and Materials, Philadelphia, 1988, pp 119-135.

67. Walmsley, H. L. and Woodford, G., "The Generation of Electric Currents by the Laminar Flow of Dielectric Liquids", J. Phys. D:Appl. Phys., Vol. 14, 1981, pp 1761-1782.

68. Walmsley, H. L., "The Generation of Electric Currents by the Turbulent Flow of Dielectric Liquids: I. Long Pipes", J. Phys. D:Appl. Phys., Vol. 15, 1982, pp 1907-1934.

69. Walmsley, H. L., "The Generation of Electric Currents by the Turbulent Flow of Dielectric Liquids: II. Pipes of Finite Length", J. Phys. D:Appl. Phys., Vol. 16, 1983, pp 553-572.

70. Pribylov, V. N. and Chernyi, L. T, "Electrization of Dielectric Liquids Flowing in Tubes", Fluid Dynamics, Vol. 14, 1979, pp 844-849.

71. Touchard, G., "Streaming Currents Developed in Laminar and Turbulent Flows Through a Pipe", J. Electrostatics, Vol. 5, 1978, pp 463-476.

72. Touchard, G., Benyamina, M., Borzieux, J. A. G., and Romat, H., "Static Electrification by Laminar Flows Through Artificially Roughed Pipes", IEEE Trans. Ind. Appl., Vol. 25, No. 6, November/December, 1989, pp 1067-1072.

73. Norris, E. T., "High Voltage Power Transformer Insulation", Proc. IEE, Vol. 110, No. 2, February 1963, pp 428-440.

74. Fabre, J. and Pichon, A., "Deteriorating Processes and Products of Paper in Oil. Application to Transformers", CIGRE paper 137, 1960.

75. Moser, H. P., *Transformerboard*, Scientia Electrica, 1979.

76. Moser, H. P. and Dahinden, V., *Transformerboard II*, Scientia Electrica, 1987.

77. Kennedy, W., "Resistivity of Oil and Pressboard Insulation and Their Effect on Transformer Design", Proc. 3rd EPRI Workshop on Static Electrification in Power Transformers, San Jose, California, 1992.

78. Moser, H. P., Krause, C., Praxl, G., Spandonis, G, Stonitsch, R., and Brechna, H., "Influence of Transformerboard and Nomex™ Board on the Electrification of Power Transformers", Proc. 3rd EPRI Workshop on Static Electrification in Power Transformers, San Jose, California, 1992.

79. Oommen, T. V., "On-line moisture sensing in Transformers", Proc. 20th Electrical/Electronics Insul. Conf., Boston, Ma, October 1991, pp 236-241.

80. Mitsubishi CA-06 Coulometric Moisture Meter Operation Manual.

81. McNutt, W. J., Berkshire Transformer Company, Personal Communication.

82. Franchek, M., EHV Weidmann, Personal Communication.

83. Adamczewski, I., *Ionization, Conductivity and Breakdown in Dielectric Liquids*, Barnes and Noble Inc., New York, 1969.

84. Gemant, A., *Ions in Hydrocarbons*, Interscience Publishers, New York, 1967.

85. Lamarre, C., Crine, J.P and Duval, M., "Influence of Oxidation on the Electrical Properties of Inhibited Napthenic and Paraffinic Transformer Oils", IEEE Trans. Elec. Insul., Vol EI-22, No. 1, February, 1987, pp 57-62.

86. Froix, M. F. and Nelson, R., "The interaction of Water with Cellulose from Nuclear Magnetic Resonance Relaxation Times", Macromolecules, Vol. 8, No. 6, November/December 1975, pp 726-730.

87. Roto, M. A., Johnson, J. F., Damon, D. H., and Engelhardt, J. S., "Analysis of Moisture in Oil-Impregnated Paper Tapes", IEEE Trans. Elec. Insul., 1983, pp 354-358.

88. Gervais, P., Duval, M., Merabet, M. and Bose, T. K., "The state of Water in Oil Impregnated Paper Insulation", Conf. Rec., IEEE Int. Symp. Elec. Insul., June 3-6, Toronto, Canada, 1990, pp 65-67.

89. Zahn,M., Massachusetts Institute of Technology, Personal Communication, 1992.

90. Oommen, T. V., "Moisture Equilibrium in Paper-Oil Insulation Systems", Proc. 16th Electrical/Electronics Insul. Conf., Chicago, Il, Oct. 3-6, 1983, pp 162-166.

91. Howe, A. F., "Diffusion of Moisture Through Power Transformer Insulation", Proc. IEE, Vol. I25, No. 10, October 1978, pp 978-986.

92. von Guggenberg, P. A., and Melcher, J. R., "Moisture Dynamics in Paper/Oil Systems Subject to Thermal Transients", Public Service Electric and Gas of New Jersey/EPRI Workshop on Static Electrification in Transformers, November, 15-17, Princeton, NJ, 1989.

93. Guidi, W. W. and Fullerton, H. P., "Mathematical Methods for Predicting Moisture Take-Up and Removal in Large Power Transformers", Paper C74 242-4, IEEE Winter Power Meeting, 1974.

94. Kuffel, E., and Zaegl, W. S., *High Voltage Engineering Fundamentals*, Pergamon Press, New York, 1984.

95. Gallagher, T. J. and Pearmain, A. J., *High Voltage Measurements, Testing and Design*, Wiley Interscience Publishers, New York, 1983.

96. Kreuger, F. H., *Discharge Detection in High Voltage Equipment*, Temple Press Books Ltd., London, 1964.

97. IEEE C57.113 "Trial Use Guide for Partial Discharge Measurement in Liquid Filled Power Transformers and Shunt Reactors".

98. IEC 76 "Power Transformers Part 3: Insulation Levels and Dielectric Tests".

99. H. Moore, Harold Moore and Associates, Private Communication 1994.

100. Atten, P. and Haidara, M., "Electrical Conduction and EHD Motion of Dielectric Liquids in a Knife-Plane Electrode Assembly", IEEE Trans. Elec. Insul., Vol EI-20, No. 2, April 1985, pp 187-198.

101. Lewis, T. J., "Basic Processes of Conduction in Dielectric Liquids", Proc. 11th ICDL, July, 1993, pp 32-41.

102. Greenwood, A., *Electrical Transients in Power Systems*, Wiley Interscience, New York, 1971.

103. Creed, F. C., *The Generation and Measurement of High- Voltage Impulses*, Center Book Publishers Inc., 1989.

104. Bradwell, A., *Electrical Insulation*, Peter Peregrinus Ltd., London, 1983.

105. Kelley, E. E., Hebner, R. E., Anderson, W. E., Lechner, J. A. and Blue, J. L., "The Effect of an Oil-Paper Interface Parallel to an Electric Field on the Breakdown Voltage at Elevated Temperature", IEEE Trans. Elec. Insul., Vol. 23, No. 2, April 1988, pp 249-259.

106. Anker, M. U., "The Effect of Test Geometry, Permittivity Matching and Metal Particles on the Flashover Voltage of Oil/Solid Interfaces", IEEE Trans. Power Appar. and Sys., Vol. PAS-102, No. 12, December 1983, pp 3796-3802.

107. Ragheveer, M. R., Kolaczkowski, Z, Weifang, J. and Kuffel, E., "Surface Electric Strength of Processed Pressboard and Under Composite AC and DC and Conventional Stresses", IEEE Trans. Elec. Insul., Vol. 25, No. 2, April 1990, pp 341-350.

108. Pheiffer, P. E., *Probability for Applications* Springer-Verlag Inc., New York, 1990.

109. Jia-Xiang, Y., Xio-Chun, C., Li-Jian, D., Zhong-Hua, L. and Chong-Jun, J., "Influence of Streaming Electrification on Creep Discharge of Oil-Paper Insulation System", IEEE Int. Symp. Elec. Insul., June 5-8, 1994, Pittsburgh, PA, pg 538.

110. Howells, E., Zahn, M. and Lindgren, S. R., "Static Electrification Effects in Transformer Oil Circulating Pumps", IEEE Trans. Power Delivery, Vol. 5, No. 2, April 1990, pp 1000-1005.

111. Washabaugh, A. P. and Zahn, M., "Charge Density Enhancement Due to Recirculatory Flow", IEEE DEIS, Vol. 1, No. 1, February 1994, pp 38-52.

112. Schlicting, H., *Boundary Layer Theory*, McGraw-Hill Classic Textbook Reissue.

113. Kays, and Crawford, *Convective Heat Transfer*, McGraw-Hill Classic Textbook Reissue.

114. Jaimison, D. K. and Villemonte, J. R., "Junction Losses in Laminar and Transitional Flows", J. American Soc. Civ. Eng. 1971, 97(HY7), pp 1045-1061.

115. Oliver, A. J., "Estimation of Transformer Winding Temperatures and Coolant Flows Using a General Network Method", IEE Proc. Vol 127, Pt.C, No. 6, November 1980.

116. Allen, P.H.G. and Childs, E.P., "Conjugated Heat Transfer in Disk-Type Power Transformer Windings", Proc. 8th Int. Heat Transfer Conf., San Francisco, CA, 1986.

117. Burden, P.L. and Fairs, J.D., *Numerical Analysis* 4th ed, PWS-Kent Publishing Company, Boston, MA, 1989.

118. Smith, W., Rensselaer Polytechnic Institute, Private Communication, Spring 1992.

119. Jaeger, R.C., *Introduction to Microelectromic Fabrication, Volume 5, Modular Series on Solid State Devices*, ed by G.W. Neudeck and R.F. Pierret, Addison-Wesley Publishing Company, 1988.

120. Shugg, *Handbook of Electrical and Electronic Insulating Materials*, Van Nostrand, 1986.

121. Szpiro, O., Allen, P.H.G, and Richards, C.W., "Coolant Distribution in Disc-Type Transformer Winding Horizontal Ducts and its Influence on Heat Transfer", Proc. 8th Int. Heat Transfer Conf., Munich 1982.

122. Howells, E., "Acoustic Emission Detection of Partial Discharges in Power Transformers", EPRI-EL-4009, Project 426-1, Final Report, August 1985.

A

COMPARISON OF CHARGE DENSITY METERS

During the early stages of this project, experiments were performed to evaluate the tandem charge monitor (TCM) and absolute charge sensor (ACS). The experiments took place at three different facilities to provide an unbiased comparison of the instruments. Initial measurements were taken in a large-scale fluid loop at J. W. Harley Inc. with both meters installed in the same axial location along a 0.152 m diameter pipe. Further tests were carried out using the smaller oil flow systems available at RPI and MIT.

Over a wide range of conditions, the ACS was found to read higher charge densities than the TCM. Table A-1 provides a comparison of typical results from the three tests. Note that the calculated values are based on measured streaming currents and volume flow rates. The internal flow rates of the TCM and ACS were identified as the most likely causes of calibration error. In the latter case, the flow meter had been factory calibrated for water rather than oil. The flow meter is of the ball gauge type and hence will be very dependent upon fluid viscosity. A flow calibration experiment was performed to determine the extent of this problem.

Table A-1
Comparison of charge density measurements in different test facilities.

	J.W. Harley	RPI	MIT
T (^{o}C)	40	25	25
Q (GPM)	720	60	8.5
TCM ($\mu C/m^3$)	12	2.5	30
ACS ($\mu C/m^3$)	38	8.6	100
Calculated ($\mu C/m^3$)	11.2	6.9	100

The TCM pump was connected to transfer oil from a temperature controlled reservoir through the flow meter into a graduated cylinder. This allowed true measurements of the volume flow rate over a range of temperatures. The results are presented in Figure A-1 which demonstrates the importance of viscosity calibration in the lower temperature range. At 25^{o}C, the correction factor for the TCM is 3.4 which nicely

explains the discrepancy with the ACS during the RPI and MIT experiments. With regard to the J. W. Harley results, the flow correction of the TCM gives better agreement with the ACS, but a difference of 14μC/m^3 persists. This may be explained by the effects of higher operating pressures on the ACS bellows. One should also note that the calculated charge values may not be accurate if there are alternate leakage paths for the streaming current. In any case, the results of Figure A-1 have been incorporated to correct all TCM readings reported in this report.

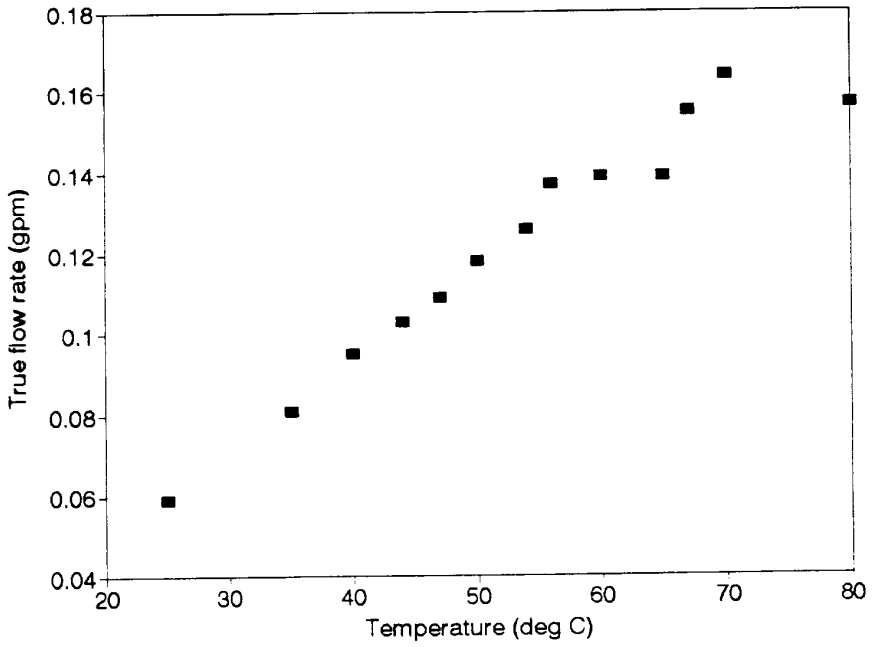

Figure A-1
TCM true volume flow rate curve as a function of temperature with flow meter adjusted to read 0.2 GPM.

B

ACOUSTIC PARTIAL DISCHARGE MEASUREMENTS

At the request of the project sponsors, acoustic partial discharge (PD) measurements were attempted in the shell-form model during the experiments documented in Section 3.2. Model R15I acoustic transducers purchased from Physical Acoustics Corporation were used. These sensors consist of a quartz crystal mechanically coupled to a ceramic contact shoe. A DC voltage is supplied to power an internal amplifier which provides 60 dB of gain to the signal generated by the vibrating element. This type of sensor is commonly used for PD measurement in power equipment (122).

Measurements were taken using one sensor at different locations on the shell-form model casing as illustrated in Figure B-1. The side locations were selected to eliminate problems with pickup from the AC source when the sensor was close to the model bushings. The contact shoe was mounted to the model housing using an ultrasonic coupling gel to maximize transmittance of acoustic energy. Additional sensitivity was obtained using a Tektronixs 125 pre-amplifier with type-O op-amps configured to provide 60 dB of gain at a center frequency of 150 kHz. The sensor output signals were displayed on a Nicolet model 204 digital oscilloscope as shown in Figure B-2. Without flow or AC energization, the measurement system was found to be quite sensitive to small signals induced by gently tapping any part of the fluid loop with a metal object.

Preliminary experiments were undertaken with no oil flow to investigate detection of AC discharging. With the sensor at location one (see Figure B-1), discharges were evident at 15 kV rms. Based on Figure 3-4, these discharges were probably on the order of 600 pC which is comparable to the sensitivity level reported by Howells et al (122). A typical acoustic PD response is shown in Figure B-3 which has a frequency close to 150 kHz. Similar signals having smaller magnitudes were detected at locations two, three, four and five. No reliable signal was measured from sensor location six during these tests. Variations in the model casing surface may have led to poor contact in this case.

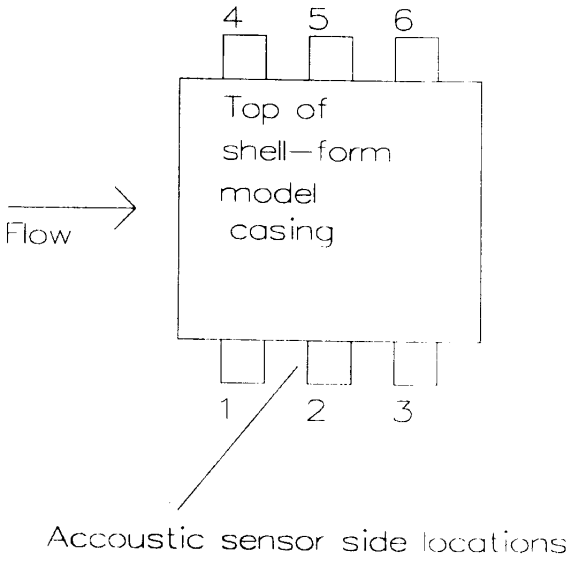

Figure B-1
Different locations for acoustic sensor on shell-form model casing.

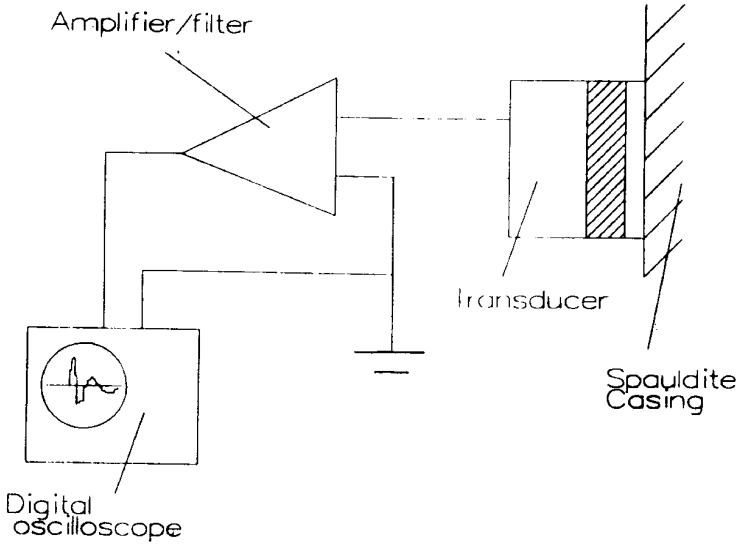

Figure B-2
Test arrangement for acoustic PD measurement.

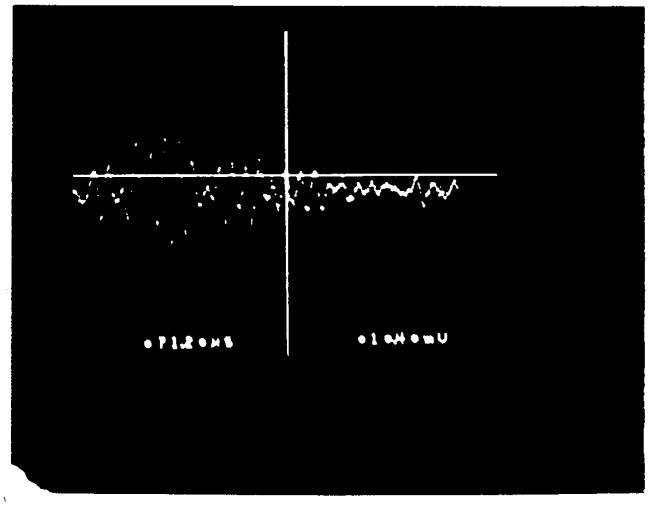

Figure B-3
Typical acoustic response to PD at 15 kV with no oil flow.

With the pump running, substantial signals were present in the frequency range of interest without any applied voltage. This may be attributed to mechanical vibrations from the pump or possibly the collapse of gas bubbles in the flowing oil. In any case, PD signals could not be reliably detected with the oil flowing using this measurement scheme. Use of multiple sensors to locate electrification discharges was therefore abandoned. This would have been quite difficult even with detectable signals due to the small size of the model and the complexity of the structure.

C

GOVERNING EQUATIONS FOR LAMINAR FLOW

C.1 Flow equations for plane channel geometry

For laminar flow in the plane channel defined in Figure 4.3, the critical Navier-Stokes Equations will be continuity given as

$$\frac{\partial v_x}{\partial x} + \frac{\partial v_y}{\partial y} = 0 \qquad \text{(eq. C-1)}$$

with the x-momentum and y-momentum equations

$$p\, v_x \frac{\partial v_x}{\partial x} + p\, v_y \frac{\partial v_x}{\partial y} = -\frac{d P}{d x} + \mu \left(\frac{\partial^2 v_x}{\partial y^2} + \frac{\partial^2 v_x}{\partial x^2} \right) \qquad \text{(eq. C-2)}$$

and

$$p\, v_x \frac{\partial v_y}{\partial x} + p\, v_y \frac{\partial v_y}{\partial y} = -\frac{d P}{d y} + \mu \left(\frac{\partial^2 v_y}{\partial y^2} + \frac{\partial^2 v_y}{\partial x^2} \right) - \rho\, g \qquad \text{(eq. C-3)}$$

where

P	=	pressure [N/m^2]
x	=	longitudinal distance [m]
y	=	transverse distance across channel [m]
μ	=	absolute viscosity [kg/ms]
ρ	=	fluid density [kg/m^3]
v_x	=	fluid velocity in x-direction [m/s]
v_y	=	fluid velocity in y-direction [m/s]
g	=	gravity acceleration [m/s^2]

Note that steady state, incompressible flow has been assumed. If further assumptions are made stipulating parallel flow and the effects of hydrostatic pressure ignored, the y-momentum and continuity Equations are not required. The velocity distribution may thus be obtained by solving

$$0 = \left(-\frac{dP}{dx} \right) + \mu \frac{\partial^2 v}{\partial y^2}. \qquad \text{(eq. C-4)}$$

This result is easily integrated to obtain the x-directed velocity profile

$$v = \frac{-1}{2\mu}\left(-\frac{dP}{dx} \right) y^2 + \frac{1}{\mu} C_1 y + C_2. \qquad \text{(eq. C-5)}$$

Assuming no slip at the channel walls, the boundary conditions will be

$$v(0) = 0 \qquad \text{(eq. C-6)}$$

$$v(2H) = 0 \qquad \text{(eq. C-7)}$$

where H is the channel half-height. Solving for the integration constants and rearranging gives

$$v(y) = \left(-\frac{dP}{dx} \right) \frac{1}{\mu} \left[H y - \frac{1}{2} y^2 \right]. \qquad \text{(eq. C-8)}$$

The volume flow rate is determined by integrating the velocity profile result

over the channel cross section to obtain

$$Q = \frac{W}{\mu}\left(-\frac{dP}{dx} \right) \frac{2}{3} H^3 \qquad \text{(eq. C-9)}$$

where W is the channel width. Recognizing that $Q = VA_c$ where A_c is the channel cross section given by the product of the width and height and V is the mean flow velocity, the pressure gradient can be expressed in terms of flow rate. Substituting back into eq. C-8 provides an expression of the velocity profile in terms of the mean flow velocity as

$$v(y) = \frac{3V}{H^2} \left[H y - \frac{1}{2} y^2 \right]. \qquad \text{(eq. C-10)}$$

C.2 Laminar Relaxation Equation

The behavior of charge in an insulating medium will be governed by a relaxation Equation which ensures conservation of charge as various physical mechanisms compete. The total current density in a control volume containing some ionic concentration will be

$$\hat{J} = \hat{j}_+ + \hat{j}_- \qquad \text{(eq. C-11)}$$

which represents the sum of current density resulting from both negative and positive ions. The currents associated with the positive and negative ion fluxes are given as

$$\hat{j}_+ = - D_+ F Z_+ \nabla C_+ + \sigma_+ \hat{E} + \hat{v} C_+ F Z_+ \qquad \text{(eq. C-12)}$$

and

$$\hat{j}_- = D_- F Z_- \nabla C_- + \sigma_- \hat{E} + \hat{v} C_- F Z_- \qquad \text{(eq. C-13)}$$

respectively. The subscripts indicate which ionic species is associated with the given parameters which are defined as follows:

C	=	ion concentration [mol]
$\hat{j}$	=	current density vector [A/m^2]
D	=	ion diffusion coefficient [m^2/s]
F	=	Faraday constant [C/mol]
Z	=	ion valency
σ	=	conductivity for ions [S/m]
$\hat{v}$	=	velocity vector [m/s]
$\hat{E}$	=	background electric field vector [V/m]

Recognizing that the electric field can be represented in terms of the potential by

$$\hat{E} = - \nabla \phi \qquad \text{(eq. C-14)}$$

The total ionic current equation thus becomes

$$\hat{J} = - D_+ Z_+ F \nabla C_+ + D_- Z_- F \nabla C_- - (\sigma_+ + \sigma_-) \nabla \phi + \hat{v} F (C_+ Z_+ - C_- Z_-) . \qquad \text{(eq. C-15)}$$

Assuming that the ions in question are univalent such that $Z_- = Z_+ = 1$ and defining the free bulk charge q as the difference in species concentrations given by

$$q = F(C_+ - C_-) \qquad \text{(eq. C-16)}$$

the current density expression is simplified to

$$\hat{J} = - D \nabla q - \sigma \nabla \phi + \hat{v} q \qquad \text{(eq. C-17)}$$

Note that the positive and negative species diffusion coefficients have been assumed equal and a net conductivity defined by $\sigma = \sigma_- + \sigma_+$ introduced to consider the contributions of both species.

The net current density vector must obey conservation of charge as stated in Maxwell's Equations by

$$\nabla \bullet \hat{J} - \frac{\partial q}{\partial t} = 0 . \qquad \text{(eq. C-18)}$$

Neglecting the time derivative in the steady state and substituting the expression for current density gives

$$\nabla \bullet (- D \nabla q - \sigma \nabla \phi + \hat{v} q) = 0 \qquad \text{(eq. C-19)}$$

which is further simplified by vector identity to

$$- D \nabla^2 q - \sigma \nabla^2 \phi + \nabla \bullet \hat{v} q = 0 . \qquad \text{(eq. C-20)}$$

The potential can now be expressed in terms of the charge density using Laplace's Equation

$$\nabla^2 \phi = - \frac{q}{\varepsilon} \qquad \text{(eq. C-21)}$$

to obtain the general linear relaxation equation

$$- D \nabla^2 q + \frac{\sigma}{\varepsilon} q + \nabla \bullet \hat{v} q = 0 . \qquad \text{(eq. C-22)}$$

Further simplification is possible to fit the plane channel geometry specified in the previous section. The first term becomes

$$- D \nabla^2 = - D \frac{\partial^2 q}{\partial x^2} - D \frac{\partial^2 q}{\partial y^2} \qquad \text{(eq. C-23)}$$

and the third term works out to be

$$(\nabla \bullet \hat{v}) q = \frac{\partial}{\partial x} (v_x q) + \frac{\partial}{\partial y} (v_y q) . \qquad \text{(eq. C-24)}$$

Recognizing that convection in the x-direction will be far more significant than diffusion and assuming parallel flow in the same direction, the final form of the relaxation equation becomes

$$- D \frac{\partial^2 q}{\partial y^2} + \frac{1}{\tau} q + \frac{\partial}{\partial x} (v_x q) = 0 . \qquad \text{(eq. C-25)}$$

Note that the charge relaxation time

$$\tau = \frac{\varepsilon}{\sigma} \qquad \text{(eq. C-26)}$$

has been incorporated into the final form of the plane channel equation.

D

TURBULENT FLOW EQUATIONS

While the same governing equations apply to turbulent channel flow, the laminar result is no longer appropriate for this case. The charge density and velocity variables must now be expressed in terms of a mean value and turbulent fluctuating quantity as follows:

$$v_x = \overline{v_x} + v_x' \qquad \text{(eq. D-1)}$$

$$v_y = \overline{v_y} + v_y' \qquad \text{(eq. D-2)}$$

$$q = \bar{q} + q' \qquad \text{(eq. D-3)}$$

Note that the average quantities are indicated by horizontal bars while the fluctuating components are primed. The y-component of fluid velocity has been retained to describe eddy diffusivity.

Inserting the turbulent parameters into the general eq. C-22 yields

$$- D \frac{\partial^2 \bar{q}}{\partial y^2} - D \frac{\partial^2 q'}{\partial y^2} + \frac{1}{\tau} \bar{q} + \frac{1}{\tau} q' + \frac{\partial}{\partial x} [\overline{v_x q} + \bar{q} v_x + \overline{v_x} q' + v_x q'] + \frac{\partial}{\partial y} [\overline{v_y q} + \bar{q} v_y' + \overline{v_y} q' + q' v_y'] = 0 . \qquad \text{(eq. D-4)}$$

This expression is now averaged using the following rules specified by Kays and Crawford (113):

$$A = \overline{A} + a'$$

$$\overline{\frac{\partial A}{\partial x}} = \frac{\partial \overline{A}}{\partial x}$$

$$\overline{\overline{A}} = \overline{A}$$

$$\overline{a'} = 0$$

$$\overline{Aa'} = 0$$

Applying these rules to the terms of equation D-4 yields the following results:

Term 1 $\overline{D\frac{\partial^2 \overline{q}}{\partial y^2}} = -D\frac{\partial^2 \overline{q}}{\partial y^2}$

Term 2 $\overline{D\frac{\partial^2 q'}{\partial y^2}} = 0$

Term 3 $\overline{\frac{1}{\tau}\overline{q}} = \frac{1}{\tau}\overline{q}$

Term 4 $\overline{\frac{1}{\tau}q'} = 0$

Term 5 $\overline{\overline{v_x q}} = \overline{v_x q}$

Term 6 $\overline{\overline{q}\, v_{x'}} = 0$

Term 7 $\overline{\overline{v_x} q'} = 0$

Term 10 $\overline{\overline{q}\, v_{y'}} = 0$

Term 11 $\overline{\overline{v_y} q'} = 0$

The eighth term $\overline{v_x 'q'}$ is neglected relative to the fifth term which provides a much more significant term in the x-direction. In addition, the ninth term $\overline{\overline{v_y q}}$ is neglected for channel flow in the x-direction such that $\overline{v_y}$ goes to zero.

The final term $\overline{q' v_y}'$ cannot be neglected and should be treated using a turbulent diffusivity (13) as

$$\overline{q' v_{y'}} = - D_T \frac{\partial \bar{q}}{\partial y} \qquad \text{(eq. D-5)}$$

where $D_T = D_T(y)$ represents the diffusivity. With subsequent substitution and rearrangement, the final relaxation equation for turbulent flow becomes

$$- \frac{\partial}{\partial y} \left[(D + D_T) \left(\frac{\partial \bar{q}}{\partial y} \right) \right] + \frac{\bar{q}}{\tau} + \frac{\partial}{\partial x} (\overline{v_x q}) = 0 . \qquad \text{(eq. D-6)}$$

E

LIST OF SYMBOLS AND NOTATIONS

Note that the notation used in referenced articles has been faithfully reproduced and defined in this report. The variables defined here are used consistently throughout the document and are defined as follows:

a	=	empirical exponent for wall charge density gradient
A	=	turbulent electric field transport constant [m^{-1}]
A_2	=	second turbulent field transport constant [m^{-1}]
A_c	=	cross sectional area of a duct [m^2]
A_s	=	area of bulk cellulose leakage path [m^2]
b	=	ionic mobility [m^2/Vs]
b_o	=	Arrhenius scaling constant for mobility [m^2/Vs]
C	=	ion concentration [mol/m^3]
C_1	=	impulse generator lumped capacitance [F]
C_2	=	specimen capacitance [F]
C_B	=	blocking capacitance for PD measurements [F]
C_M	=	moisture concentration in cellulose [mol/m^3]
C_q	=	coupling capacitance for PD calibration [F]
C_s	=	specimen terminal capacitance of test object [F]
d	=	thickness of charge layer available for field transport [m]
d_H	=	hydraulic diameter [m]

D	=	molecular diffusion coefficient [m^2/s]
D_p	=	diffusion coefficient for water in cellulose [m^2/s]
D_T	=	turbulent diffusivity [m^2/s]
D_o	=	Arrhenius diffusion scaling constant [m^2/s]
e^-	=	electronic charge (1.6×10^{-19}) [C]
E	=	electric field [V/m]
E_o	=	peak value of AC electric field [V/m]
$\hat{E}$	=	electric field vector [V/m]
f	=	dimensionless charge boundary layer thickness [m]
F	=	Faraday constant [C/mol]
H	=	half-height of a plane channel [m]
I	=	streaming current [A]
$[I]$	=	nodal injected streaming current vector [A]
$[I_L]$	=	nodal leakage current vector [A]
$\hat{j}$	=	current density due to one ion species [A/m^2]
$\hat{J}$	=	total current density [A/m^2]
k	=	Boltzmann constant (1.38×10^{-23}) [$J/^oK$]
k1,k2,k3	=	dimensionless boundary layer transform constants
K	=	constant relating mobility to viscosity [m^4/Vs^2]
K_E	=	empirical constant for charge generation [A/m^2N]
L	=	transformer duct length [m]
L_d	=	laminar flow development length [m]

m	=	constant for determining diffusion sublayer thickness
N_{SQ}	=	number of squares in surface leakage path
Nu_x	=	Nusselt number based on x
P	=	fluid pressure [N/m^2]
$[P]$	=	nodal pressure vector [N/m^2]
Pr	=	Prandtl number
q	=	volume charge density [C/m^3]
q_B	=	bulk volume charge density [C/m^3]
q_W	=	wall volume charge density [C/m^3]
q_{eff}	=	effective charge density available at the wall for field transport [C/m^3]
q_o	=	charge density in the Debye layer [C/m^3]
q^*	=	net charge contained in the fluid per unit of wall surface area [C/m^3]
$q'(0)$	=	volume charge density gradient at the wall [C/m^4]
$q'(0)_o$	=	scaling constant for volume charge density gradient at the wall
$q'(0)_\infty$	=	Arrhenius scaling constant for wall charge density gradient scaling constant
$[q]$	=	nodal charge density vector [C/m^3]
Q	=	volume flow rate [m^3/s]
Q_{eff}	=	effective volume flow rate which accounts for charge relaxation [m^3/s]
$[Q]$	=	nodal driving flow rate vector [m^3/s]
$[Q_{eff_1}$	=	connectivity matrix for effective volume flow rate between each node [m^3/s]
r	=	radial distance from axis in cylindrical coordinates [m]
R	=	radius of a circular duct [m]

R_e = hydraulic Reynolds number

R_{ex} = Reynolds number based on x distance from inlet

R_h = hydraulic resistance [Ns/m^5]

R_L = bulk leakage resistance for cellulose [Ω]

R_{LS} = surface leakage resistance for cellulose [Ω]

$[R_{LM}]$ = complete nodal connectivity leakage resistance matrix [Ω]

R_1 = front resistor in impulse circuit [Ω]

R_2 = tail resistor in impulse circuit [Ω]

R_{ij} = relaxation factor for charge convected between nodes i and j

S = Schmitt number

t_c = time to crest for impulse waveform [s]

t_1 = time for field transported ions to move into the fluid[s]

t_2 = time for field transported ions to approach the wall[s]

T = temperature [^oK]

U_∞ = free stream velocity [m/s]

v = fluid velocity along duct axis [m/s]

$\hat{v}$ = velocity vector [m/s]

v^* = friction velocity for turbulent flow [m/s]

V = mean fluid velocity along duct axis [m/s]

$[V_S]$ = nodal static potential vector [V]

V_{BD} = breakdown voltage [V]

W = width of rectangular duct [m]

W_b = activation energy for mobility [J]

W_D = activation energy for diffusion coefficient [J]

W_ν = activation energy for kinematic viscosity [J]

W_σ = activation energy for conductivity [J]

W_q = activation energy for wall charge density gradient [J]

x = distance along duct length (rectangular coordinates) [m]

x_t = location where laminar charge boundary layer crosses diffusion sublayer [m]

x_o = unheated starting length for heat transfer [m]

y = transverse distance from the wall (rectangular coordinates) [m]

$[Y_h]$ = hydraulic impedance connectivity matrix [m^5/Ns]

z = axial distance in cylindrical coordinate system [m]

Z = ion valency number

β = slope of velocity profile near the wall [s^{-1}]

δ = charge boundary layer thickness [m]

δ_e = electric field transport length [m]

δ_m = momentum boundary layer thickness [m]

Δ = diffusion sublayer thickness [m]

ε = fluid permittivity [F/m]

ζ = zeta potential [V]

η = dimensionless distance variable for charge boundary layer transformation

θ = dimensionless normalized charge density profile

λ = Debye length [m]

λ_f = Blasius friction factor

λ_T = turbulent Debye length [m]

μ = fluid viscosity [Ns/m]

ν = fluid kinematic viscosity [m^2/s]

ν_o = Arrhenius scaling constant for kinematic viscosity [m^2/s]

ρ = fluid density [kg/m^3]

ρ_{PB} = bulk resistivity for cellulose [Ω/m]

σ = fluid conductivity [S/m]

σ_o = Arrhenius scaling constant for conductivity [S/m]

σ_P = bulk cellulose conductivity [S/m]

σ_{PS} = surface conductivity of cellulose [square/Ω]

τ = fluid relaxation time [s]

τ_w = wall shear stress due to viscous flow [N/m^2]

ω = frequency of alternating voltage [s^{-1}]

Note that for turbulent conditions, the given variables are used with a bar indicating an average quantity and a prime indicating a fluctuating quantity.